Purdue University
Purdue e-Pubs

Open Access Dissertations | Theses and Dissertations

8-2016

Ultraviolet and Infrared Spectroscopy of Synthetic Foldamers, Aib Homopeptides, and Solvated 1,2-Diphenylethane in the Gas Phase

Joseph R. Gord
Purdue University

Follow this and additional works at: https://docs.lib.purdue.edu/open_access_dissertations

 Part of the Analytical Chemistry Commons, and the Physical Chemistry Commons

Recommended Citation
Gord, Joseph R., "Ultraviolet and Infrared Spectroscopy of Synthetic Foldamers, Aib Homopeptides, and Solvated 1,2-Diphenylethane in the Gas Phase" (2016). *Open Access Dissertations*. 763.
https://docs.lib.purdue.edu/open_access_dissertations/763

This document has been made available through Purdue e-Pubs, a service of the Purdue University Libraries. Please contact epubs@purdue.edu for additional information.

Graduate School Form 30
(Updated 11/20/2014)

PURDUE UNIVERSITY
GRADUATE SCHOOL
Thesis/Dissertation Acceptance

This is to certify that the thesis/dissertation prepared

By Joseph R. Gord

Entitled ULTRAVIOLET AND INFRARED SPECTROSCOPY OF SYNTHETIC FOLDAMERS, AIB HOMOPEPTIDES, AND SOLVATED 1,2-DIPHENYLETHANE IN THE GAS PHASE

For the degree of Doctor of Philosophy

Is approved by the final examining committee:

Timothy Zwier

Graham Cooks

Garth J. Simpson

Scott A. McLuckey

To the best of my knowledge and as understood by the student in the Thesis/Dissertation Agreement, Publication Delay, and Certification/Disclaimer (Graduate School Form 32), this thesis/dissertation adheres to the provisions of Purdue University's "Policy on Integrity in Research" and the use of copyrighted material.

Timothy Zwier

Approved by Major Professor(s): _____

_____

Approved by: Timothy Zwier 06/30/2016

Head of the Department Graduate Program Date

ULTRAVIOLET AND INFRARED SPECTROSCOPY OF SYNTHETIC FOLDAMERS, AIB HOMOPEPTIDES, AND SOLVATED 1,2-DIPHENYLETHANE IN THE GAS PHASE

A Dissertation

Submitted to the Faculty

of

Purdue University

by

Joseph R. Gord

In Partial Fulfillment of the

Requirements of the Degree of

Doctor of Philosophy

August 2016

Purdue University

West Lafayette, Indiana

For my family.

ACKNOWLEDGEMENTS

Kirsten, your love and support over the last three years have been of immeasurable value. I am eternally grateful for your presence in my life, and I am so looking forward to marrying you. You are more than I could ever hope for.

Mom, Dad, Michael, and Jeffrey, your unwavering encouragement and love is a perpetual source of strength. Dad, Mrs. White was correct. Thank you for helping me to do more things, see more things, and have more things explained to me than any other kid in the class (at every grade level). You are undoubtedly the reason I have come this far. Joe and Melliavee Gardner, P. Ronald and Kay Gord (Grandpas and Grandmas), your love, support, and encouragement mean so much. I am truly blessed to have grandparents like you!

Tim, my favorite nickname for you is definitely "Bone-Dog". I'm not sure how this name came to be though. It is likely an extension of the more traditional "T-Bone". Regardless, I know without question that I could not have selected a better graduate advisor for whom to work. You are a fantastic teacher, a wonderful mentor, and the highest example of integrity and service for all of us. Thank you for your wisdom and guidance.

Khan (Patrick Walsh), Snacob (Jacob Dean), My-Buddy-Craig (Craig Caswell), and Dan (Hewett), your friendship along this road has carried me in good times and in

not-so-good times. Also, Pat… casserole is delicious. Anthony Tomaine and Christopher Haskins, thank you for your friendship. I've enjoyed staying up past my bedtime to play video games and eat pizza with you. To the rest of the group, working with you all has certainly been an experience, but given the chance, I wouldn't have traded any of you.

Rob Reason, Betty Dexter, Betty Hatfield, Debbie Packer, Lynn Rider, Darci DeCamp, Suzy Gustafson, Trisha Herrera, Mark Carlsen, and certainly not least, Tim Selby, I'm so thankful to have had the opportunity to work in the department that you run. You are undoubtedly the grease, the keeps the wheels rolling. You are also the wheels, transmission, and engine. Without you nothing happens, and without you, my experience at Purdue would lack the exceptional richness that you have all contributed.

Prof. Matt Kubasik, you have been a wonderful collaborator and friend. I have learned much from you and enjoyed our many Skype calls. Thank you for providing a wealth of Aib samples, incredible content and editorial support, and for showing me around on my first trip to NYC!

To the Zwier group, past and present, it has been an honor. You don't know what you've got until it's about to be gone. Cherish your time here.

Remember the words of Neil Peart, sung by the great Geddy Lee, "Science, like nature, must also be tamed, with a view toward its preservation. Given the same state of integrity, it will surely serve us well."

TABLE OF CONTENTS

Page

Page

Page

LIST OF TABLES

LIST OF FIGURES

Figure Page

Figure Page

Figure Page

Figure Page

Figure Page

ABSTRACT

Gord, Joseph R. Ph.D., Purdue University, August 2016. Ultraviolet and Infrared Spectroscopy of Synthetic Foldamers, Aib Homopeptides, and Solvated 1,2-Diphenylethane in the Gas Phase. Major Professor: Timothy S. Zwier.

The work presented here implements a supersonic jet expansion source to funnel the population of model peptides and solvated-bichromophore clusters into their low lying structural minima and to collisionally cool these minima to their respective zero-point vibrational levels. Single-conformation ultraviolet and infrared spectroscopy techniques are then used to probe these systems and investigate their electronic properties and uncover their intrinsic conformational preferences in the gas phase.

Model β/γ-peptides known as synthetic foldamers and aminoisobutyric acid (Aib) homopeptides incorporate structural constraints that are designed/known to impose particular structural motifs. Here the ability of a β/γ-dipeptide to replicate the backbone length of an α-tripeptide and subsequently form the first portion of an α-helix is presented. Additionally, tests of the propensity for $(Aib)_n$ homopeptides to form 3_{10}-helices, in spite of accumulation of a macrodipole moment are shown. In fact, Aib is a strong 3_{10}-helix former, but there appears to be a point around n = 6 where competing forces funnel the population into a competing conformational family.

1,2-Diphenylethane (DPE) is a model, flexible bichromophore comprising two phenyl rings bound by an ethane bridge. By complexing DPE with $(H_2O)_n$ (n = 1-3) the effects of step-wise solvation on the electronic spectroscopy (i.e. the impact of water on

vibronically coupled chromophores) and the conformational preferences of both the DPE monomer and the $(H_2O)_n$ structures were investigated. In three of the four resultant clusters, the water molecule(s) were found to bind symmetrically to the DPE host, and an S_0-S_2 origin transition was not observed. However, in the fourth case, in which the *anti* conformation of the DPE monomer serves as host, localization is observed, and the S_0-S_2 origin is detected. Also of note is that the water-trimer, which almost always adopts a cycle geometry, was found to exclusively adopt a chain-geometry in the presence of DPE.

CHAPTER 1 INTRODUCTION

1.1 Motivation: Understanding Peptides and Bichromophore-Solvation in the Complexity Gap

Many modern spectroscopic efforts, enabled by the development and improvement of techniques and tools such as frequency comb spectroscopy, hyperspectral imaging, and two-dimensional IR spectroscopy, are focused on understanding the spectroscopy of macromolecular systems such as proteins and other biologically active species. These investigations, however, which are often performed under solvated conditions at room temperature, suffer from decreased spectral resolution as well as complicating environmental elements, such as solvation, crystal packing, and other intermolecular interactions. Consequently, interpretation of data collected in these experiments often requires substantial modeling efforts, as well as simplifying assumptions about the species and experiments. Simultaneously, advances in high resolution spectroscopy and computational theory are enabling more quantitative results to be determined on small, model systems. This results in a substantial complexity gap between simple, single coordinate systems with few minima on the potential energy surface and expansive systems having hundreds to thousands of minima accessible through 3N-6 degrees of freedom in a system having N atoms; in proteins, N can be in the 10^3 or greater.

Spectroscopy in the complexity gap focuses on understanding the nature of hydrogen bonding, vibronic coupling, electronic energy transfer, population transfer, and

isomerization dynamics of molecules in a size regime that falls between the two extremes described above and advances the frontier of computational chemistry, but is still accessible to diagnostic spectroscopy experiments in the ultraviolet and infrared.[1,2] By combining supersonic expansion sources capable of cooling molecules down to the zero-point levels of their low energy conformations with single- and double-resonance spectroscopy techniques, investigators have been able to elucidate the intrinsic properties of complexity-gap species. Many studies of particular relevance to this work have been focused on understanding the structural preferences of biologically relevant molecules, based on the common understanding that structure informs function.[3]

Obvious targets for these early studies were the amino acids phenylalanine, tryptophan, and tyrosine, all of which possess a "built-in" chromophore to enable spectroscopic investigation.[4-14] The next step after studying these was to investigate amino acid derivatives and oligomers containing multiple amino acid residues.[9,15-18] The use of appropriate capping groups further enabled researchers to interrogate species that lack built-in chromophores. More recently, advances in laser spectroscopy and mass spectrometry, such as widely tunable, high resolution IR sources and cold ion instruments designed for spectroscopic investigation of model systems[19-23], have enabled studies to interrogate larger oligomers and peptides, charged species, water-bound species, as well as non-natural amino acids specifically designed to adopt particular structures, known as synthetic foldamers.[20,22,24-40]

Another area of research bridging into the complexity gap is focused on better understanding the behavior of multichromophore systems within the gas phase.[41-46] Of specific interest is the ability of water to influence the electronic and conformational

properties of these antenna-like systems.[47-50] Recently, work on the solvation of 1,2-diphenoxyethane (DPOE) and 2,2,2-paracyclophane (TCP) has sought to understand the ability of water to localize the, otherwise coupled, S_0-S_1 and S_0-S_2 electronic origins within these systems. Efforts have similarly endeavored to understand the influence exerted on the structural preferences of the water clusters by the host molecule.[41,46-50] This is another area in which structure plays an integral role, both for its own sake and also as a mechanism of influence on secondary structure of biological systems, e.g. in instances of hydrogen bonding with highly polar side chains and in circumstances involving the collapse of hydrophobic regions within larger peptides seeking reprieve from interaction with water.

By probing the intrinsic structural and spectroscopic properties of molecules in this size regime, and by actively seeking out larger and more complex systems as part of a "bottom-up" approach, researchers are wading into the complexity gap and providing valuable feedback on the ways in which particular functional groups, backbone and sidechain constraints, and amino acid sequences impact the folding propensities and structural preferences of localized segments of biomolecules.[38-40] These efforts also provide new tests of computational models to predict structure and spectroscopic features such as Fermi resonance, vibronic coupling, and Amide group coupling in the Amide I and II regions.[51-54] Ideally, a day will come when an amino acid sequence can be input, and the entire potential energy surface can be computed.[55-62]

1.2 Organization

The work presented in this thesis falls into two categories. The first focuses on understanding the impact of backbone and sidechain constraints on the conformational preferences of non-coded amino acid oligomers in the absence of collisions and interactions with solvent molecules. The second focuses on understanding the impact of step-wise hydration on both the solute and solvent in a series of complexes comprising a model, flexible bichromophore and "n" H_2O molecules (n = 1-3) in order to understand water's impact on conformation and excitonic localization within the complexes.

1.2.1 Investigative Approach

Chapter 2 introduces the principles and equipment that enable single-conformation spectroscopy of cold, isolated molecules. It lays out the mechanism of collisional cooling within a supersonic expansion, and then discusses the pertinent single- and double-resonance laser systems and techniques used to probe the cooled species of interest. After describing the experimental techniques, a brief explanation of the conformational searching process that enables direct comparison between the collected experimental data and calculated spectra to aid in the structural assignment of each conformation is presented.

1.2.2 Synthetic Foldamers and Aib-Homopeptides

Recent efforts in a long-standing collaboration with Prof. Samuel Gellman of the University of Wisconsin—Madison[28,29,33,35,63-68] have sought to understand the behavior of mixed oligomers containing constrained β- and γ-foldamers.[30-32,36] Walsh and co-workers first elucidated the nature of hydrogen bonding interactions in the highly constrained, pure γ-foldamers, Ac-γ_{ACHC}-NHBn and Ac-γ_{ACHC}-γ_{ACHC}-NHBn, each of which was found to adopt just a single conformation, incorporating a C9 hydrogen bonded ring between nearest neighbor amide groups for Ac-γ_{ACHC}-NHBn, and a C14 hydrogen bonded ring between next-nearest neighbor amide groups in Ac-γ_{ACHC}-γ_{ACHC}-NHBn.[39]

Quite different from the pure constrained γ-amino acids, Kusaka, et al. investigated the folding propensities of two α/γ-foldamers which incorporated the same highly constrained γ-amino acid, $\gamma_{ACHC,}$ and the naturally occurring α-amino acid, alanine, in a system engineered to form one segment of a 12-helix incorporating sequential C12 hydrogen bonded rings. In their work on Ac-γ_{ACHC}-Ala-NHBn and Ac-Ala-γ_{ACHC}-NHBn, they observed a wealth of conformations in addition to the C12 rings that were anticipated. In fact, four and six different conformations were observed for γα and αγ, respectively.[38]

In Chapter 3 of this thesis, the effort to characterize these non-natural, constrained foldamers is continued; the folding propensities of two highly constrained β/γ-foldamers, Ac-β_{ACPC}-γ_{ACHC}-NHBn, and Ac-γ_{ACHC}-β_{ACPC}-NHBn, have been investigated to determine how the factors of additional C atoms between the NH and C=O groups of a residue as well as cyclic, backbone constraints impact hydrogen bonding and the preferred

conformations. Interestingly, the β/γ-dipeptide replicates the number of backbone C atoms in an α-tripeptide. The preferred conformations of these foldamer species are presented and discussed.

Chapters 4 and 6 discuss the results of a new collaboration forged between the Zwier group and Prof. Matthew A. Kubasik of Fairfield University in Fairfield, CT. Helices are one of the principal elements of secondary structure, and while the majority of naturally occurring helices are α-helices, approximately 10% of all naturally occurring helices are 3_{10}-heices. Numerous efforts have sought to characterize 3_{10}-helix inducing capacity of aminoisobutyric acid (Aib), a non-coded amino acid having a dimethylated C_α.[69] Expanding on solution and crystal phase data, as well as a study from the Mons research group exploring the ability of a single Aib residue to impact the folding propensities of a gas phase tetramer, the first gas phase spectra on homopeptides containing sequential Aib residues (up to $(Aib)_6$) are presented.

1.2.3 Solvation of a Flexible Bichromophore

Flexible, multichromophore systems have been a subject of interest in the Zwier group for quite some time.[42,43,51] The influence and mechanism of solvation have been a focus for even longer, beginning with the study of benzene•H_2O clusters and expanding to larger systems.[1,70-77] Recently, a body of work has been presented probing the behavior and solvation of the multichromophore systems 2,2,2-paracyclophane (TCP) and 1,2-diphenoxyethane (DPOE). These multichromophore systems have been shown to be highly susceptible to the effects of excitonic localization in the presence of

asymmetrically bound water molecules. Additionally, they have been shown to perturb the preferred structures of self-associated water clusters.[37,41,46-50] 1,2-diphenylethane (DPE) is of interest as it is a falls between the benzene•H_2O species and the larger TCP•H_2O system, having one and three chromophores, respectively. The spectroscopy of the DPE monomer has been carried out to identify two conformations; the first adopts a *gauche*-orientation of the phenyl rings and has C_2 symmetry, while the second adopts the *anti*-orientation of the rings and has C_{2h} symmetry.[41] Chapter 5 continues the investigation of DPE and explores the IR and UV spectroscopy of the solvated clusters DPE•H_2O, DPE•$(H_2O)_2$, and DPE•$(H_2O)_3$. The ability of water to localize excitation on one or the other of the rings in DPE is probed, as is the perturbative impact of DPE on the associated water clusters. Comparisons with benzene•H_2O and TCP•H_2O are presented.

1.3 References

(1) Zwier, T. S. *Journal of Physical Chemistry A* 2001, *105*, 8827.

(2) Zwier, T. S. *Journal of Physical Chemistry A* 2006, *110*, 4133.

(3) Creighton, T. E. *Proteins: Structure and Molecular Properties*; Second ed., 1993.

(4) Martinez, S. J.; Alfano, J. C.; Levy, D. H. *Journal of Molecular Spectroscopy* 1992, *156*, 421.

(5) Snoek, L. C.; Robertson, E. G.; Kroemer, R. T.; Simons, J. P. *Chemical Physics Letters* 2000, *321*, 49.

(6) Snoek, L. C.; Kroemer, R. T.; Hockridge, M. R.; Simons, J. P. *Physical Chemistry Chemical Physics* 2001, *3*, 1819.

(7) Grace, L. I.; Cohen, R.; Dunn, T. M.; Lubman, D. M.; de Vries, M. S. *Journal of Molecular Spectroscopy* 2002, *215*, 204.

(8) Weber, G. *Biochem. J.* 1960, *75*, 335.

(9) Creed, D. *Photochemistry and Photobiology* 1984, *39*, 537.

(10) Rizzo, T. R.; Park, Y. D.; Peteanu, L. A.; Levy, D. H. *Journal of Chemical Physics* 1986, *84*, 2534.

(11) Rizzo, T. R.; Park, Y. D.; Levy, D. H. *Journal of Chemical Physics* 1986, *85*, 6945.

(12) Philips, L. A.; Webb, S. P.; Martinez, S., J., III; Fleming, G. R.; Levy, D. H. *J. Am. Chem. Soc.* 1988, *110*, 1352.

(13) Cable, J. R.; Tubergen, M. J.; Levy, D. H. *J. Am. Chem. Soc.* 1988, *110*, 7349.

(14) Boyarkin, O. V.; Mercier, S. R.; Kamariotis, A.; Rizzo, T. R. *J. Am. Chem. Soc.* 2006, *128*, 2816.

(15) Peteanu, L. A.; Levy, D. H. *Journal of Physical Chemistry* 1988, *92*, 6554.

(16) Sipior, J.; Sulkes, M. *Journal of Chemical Physics* 1988, *88*, 6146.

(17) Cohen, R.; Brauer, B.; Nir, E.; Grace, L.; Vries, M. S. d. *Journal of Physical Chemistry A* 2000, *104*, 6351.

(18) Fricke, H.; Gerlach, A.; Unterberg, C.; Rzepecki, P.; Schrader, T.; Gerhards, M. *Physical Chemistry Chemical Physics* 2004, *6*, 4636.

(19) Inokuchi, Y.; Boyarkin, O. V.; Kusaka, R.; Haino, T.; Ebata, T.; Rizzo, T. R. *Journal of Physical Chemistry A* 2012, *116*, 4057.

(20) Inokuchi, Y.; Boyarkin, O. V.; Kusaka, R.; Haino, T.; Ebata, T.; Rizzo, T. R. *J. Am. Chem. Soc.* 2011, *133*, 12256.

(21) Nagornova, N. S.; Guglielmi, M.; Doemer, M.; Tavernelli, I.; Rothlisberger, U.; Rizzo, T. R.; Boyarkin, O. V. *Angewandte Chemie-International Edition* 2011, *50*, 5383.

(22) Nagornova, N. S.; Rizzo, T. R.; Boyarkin, O. V. *J. Am. Chem. Soc.* 2010, *132*, 4040.

(23) Rizzo, T. R.; Stearns, J. A.; Boyarkin, O. V. *International Reviews in Physical Chemistry* 2009, *28*, 481.

(24) Stearns, J. A.; Boyarkin, O. V.; Rizzo, T. R. *Chimia* 2008, *62*, 240.

(25) Stearns, J. A.; Seaiby, C.; Boyarkin, O. V.; Rizzo, T. R. *Physical Chemistry Chemical Physics* 2009, *11*, 125.

(26) Svendsen, A.; Lorenz, U. J.; Boyarkin, O. V.; Rizzo, T. R. *Review of Scientific Instruments* 2010, *81*.

(27) Appella, D. H.; Christianson, L. A.; Karle, I. L.; Powell, D. R.; Gellman, S. H. *J. Am. Chem. Soc.* 1996, *118*, 13071.

(28) Krauthauser, S.; Christianson, L. A.; Powell, D. R.; Gellman, S. H. *J. Am. Chem. Soc.* 1997, *119*, 11719.

(29) Chung, Y. J.; Christianson, L. A.; Stanger, H. E.; Powell, D. R.; Gellman, S. H. *J. Am. Chem. Soc.* 1998, *120*, 10555.

(30) Baquero, E. E.; James, W. H.; Choi, S. H.; Gellman, S. H.; Zwier, T. S. *J. Am. Chem. Soc.* 2008, *130*, 4784.

(31) Baquero, E. E.; James, W. H.; Choi, S. H.; Gellman, S. H.; Zwier, T. S. *J. Am. Chem. Soc.* 2008, *130*, 4795.

(32) James III, W. H.; Baquero, E. E.; Shubert, V. A.; Choi, S. H.; Gellman, S. H.; Zwier, T. S. *J. Am. Chem. Soc.* 2009, *131*, 6574.

(33) Guo, L.; Chi, Y. G.; Almeida, A. M.; Guzei, I. A.; Parker, B. K.; Gellman, S. H. *J. Am. Chem. Soc.* 2009, *131*, 16018.

(34) James III, W. H.; Muller, C. W.; Buchanan, E. G.; Nix, M. G. D.; Guo, L.; Roskop, L.; Gordon, M. S.; Slipchenko, L. V.; Gellman, S. H.; Zwier, T. S. *J. Am. Chem. Soc.* 2009, *131*, 14243.

(35) Guo, L.; Almeida, A. M.; Zhang, W.; Reidenbach, A. G.; Choi, S. H.; Guzei, I. A.; Gellman, S. H. *J. Am. Chem. Soc.* 2010, *132*, 7868.

(36) James III, W. H.; Buchanan, E. G.; Guo, L.; Gellman, S. H.; Zwier, T. S. *J. Phys. Chem. A.* 2011, *115*, 11960.

(37) Buchanan, E. G., Purdue University, 2014.

(38) Kusaka, R.; Zhang, D.; Walsh, P. S.; R., G. J.; Fisher, B. F.; Gellman, S. H.; Zwier, T. S. *J. Phys. Chem. A.* 2013, *117*, 10847.

(39) Walsh, P. S.; Kusaka, R.; Buchanan, E. G.; James III, W. H.; Fisher, B. F.; Gellman, S. H.; Zwier, T. S. *J. Phys. Chem. A.* 2013, *117*, 12350.

(40) Gord, J. R.; Walsh, P. S.; Fisher, B. F.; Gellman, S. H.; Zwier, T. S. *The Journal of Physical Chemistry B* 2014.

(41) Buchanan, E. G.; Dean, J. C.; Zwier, T. S.; Sibert III, E. L. *J. Chem. Phys.* 2013, *138*.

(42) Pillsbury, N. R.; Stearns, J. A.; Muller, C. W.; Plusquellic, D. F.; Zwier, T. S. *Journal of Chemical Physics* 2008, *129*, 114301.

(43) Stearns, J. A.; Pillsbury, N. R.; Douglass, K. O.; Muller, C. W.; Zwier, T. S.; Plusquellic, D. F. *Journal of Chemical Physics* 2008, *129*.

(44) Rodrigo, C. P.; Mueller, C. W.; Pillsbury, N. R.; James, W. H., III; Plusquellic, D. F.; Zwier, T. S. *Journal of Chemical Physics* 2011, *134*.

(45) Pillsbury, N. R.; Muller, C. W.; Meerts, W. L.; Plusquellic, D. F.; Zwier, T. S. *Journal of Physical Chemistry A* 2009, *113*, 5000.

(46) Buchanan, E. G.; Walsh, P. S.; Plusquellic, D. F.; Zwier, T. S. *J. Chem. Phys.* 2013, *138*, 204313.

(47) Walsh, P. S.; Buchanan, E. G.; Gord, J. R.; Zwier, T. S. *J. Chem. Phys.* 2015, *142*, 154304.

(48) Walsh, P. S.; Buchanan, E. G.; Gord, J. R.; Zwier, T. S. *J. Chem. Phys.* 2015, *142*, 154303.

(49) Buchanan, E. G.; Zwier, T. S. *J Phys Chem A* 2014, *118*, 8583.

(50) Buchanan, E. G.; Gord, J. R.; Zwier, T. S. *J. Phys. Chem. Lett.* 2013, *4*, 1644.

(51) Nebgen, B.; Emmert, F. L., III; Slipchenko, L. V. *Journal of Chemical Physics* 2012, *137*.

(52) Kopec, S.; Ottiger, P.; Leutwyler, S.; Koeppel, H. *Journal of Chemical Physics* 2012, *137*.

(53) Choi, J. H.; Ham, S. Y.; Cho, M. *Journal of Physical Chemistry B* 2003, *107*, 9132.

(54) Buchanan, E. G.; James III, W. H.; Choi, S. H.; Guo, L.; Gellman, S. H.; Müller, C. W.; Zwier, T. S. *J. Chem. Phys.* 2012, *137*, 094301.

(55) Oakley, M. T.; Wales, D. J.; Johnston, R. L. *Journal of Physical Chemistry B* 2011, *115*, 11525.

(56) Klenin, K.; Strode, B.; Wales, D. J.; Wenzel, W. *Biochimica Et Biophysica Acta-Proteins and Proteomics* 2011, *1814*, 977.

(57) Prentiss, M. C.; Wales, D. J.; Wolynes, P. G. *Plos Computational Biology* 2010, *6*.

(58) Malolepsza, E.; Strodel, B.; Khalili, M.; Trygubenko, S.; Fejer, S. N.; Wales, D. J. *Journal of Computational Chemistry* 2010, *31*, 1402.

(59) Prentiss, M. C.; Wales, D. J.; Wolynes, P. G. *Journal of Chemical Physics* 2008, *128*.

(60) Despa, F.; Wales, D. J.; Berry, R. S. *Journal of Chemical Physics* 2005, *122*.

(61) Evans, D. A.; Wales, D. J. *J. Chem. Phys.* 2003, *118*, 3891.

(62) Wales, D. J. *Energy Landscapes*; Cambridge University Press: Cambridge, 2003.

(63) Pomerantz, W. C.; Grygiel, T. L. R.; Lai, J. R.; Gellman, S. H. *Organic Letters* 2008, *10*, 1799.

(64) Horne, W. S.; Gellman, S. H. *Acc. Chem. Res.* 2008, *41*, 1399.

(65) Rathore, N.; Gellman, S. H.; de Pablo, J. J. *Biophysical Journal* 2006, *91*, 3425.

(66) Peelen, T. J.; Chi, Y. G.; English, E. P.; Gellman, S. H. *Organic Letters* 2004, *6*, 4411.

(67) Appella, D. H.; Christianson, L. A.; Klein, D. A.; Powell, D. R.; Huang, X. L.; Barchi, J. J.; Gellman, S. H. *Nature* 1997, *387*, 381.

(68) Gellman, S. H. *Accounts of Chemical Research* 1998, *31*, 173.

(69) Toniolo, C.; Benedetti, E. *Trends in Biochemical Sciences* 1991, *16*, 350.

(70) Gotch, A. J.; Garrett, A. W.; Severance, D. L.; Zwier, T. S. *Chemical Physics Letters* 1991, *178*, 121.

(71) Gotch, A. J.; Zwier, T. S. *Journal of Chemical Physics* 1992, *96*, 3388.

(72) Gruenloh, C. J.; Carney, J. R.; Arrington, C. A.; Zwier, T. S.; Fredericks, S. Y.; Jordan, K. D. *Science* 1997, *276*, 1678.

(73) Gruenloh, C. J.; Carney, J. R.; Hagemeister, F. C.; Zwier, T. S.; Wood, J. T.; Jordan, K. D. *Journal of Chemical Physics* 2000, *113*, 2290.

(74) Pribble, R. N.; Garrett, A. W.; Haber, K.; Zwier, T. S. *Journal of Chemical Physics* 1995, *103*, 531.

(75) Pribble, R. N.; Zwier, T. S. *Science* 1994, *265*, 75.

(76) Pribble, R. N.; Zwier, T. S. *Faraday Discussions* 1994, *97*, 229.

(77) Zwier, T. S. *Annual Review of Physical Chemistry* 1996, *47*, 205.

CHAPTER 2
TECHNIQUES AND METHODS

2.1 Introduction and Chamber Description

Data presented in this thesis were recorded using an experimental setup comprising a supersonic jet expansion source and a differentially pumped Wiley-Mclaren time of flight mass spectrometer equipped with a 25 mm microchannel plate (MCP) detector. The chamber, shown in Figure 2.1, has two differentially pumped regions. The source region, maintained at a pressure of 1.0×10^{-7} mbar, is pumped by an 880 l/s turbomolecular pump (Pfeiffer Vacuum, TMU 1001), while the detector region is maintained at a pressure of 1.0×10^{-9} mbar using a smaller 220 l/s turbomolecular pump (Pfeiffer Vacuum, TMU 261). The significantly smaller chamber volume and decreased gas load in the detector region enable achievement of lower pressures, even while using a smaller pump. Single- and double-resonance spectroscopy experiments performed using a suite of Nd:YAG pumped IR and UV lasers are used to interrogate molecules of interest. In a typical experiment, gas-phase sample molecules are co-expanded with an inert, carrier gas, through a pulsed-valve and into the vacuum chamber, forming a supersonic jet expansion. Sample molecules undergo collisions with buffer gas atoms in the expansion and are cooled down to their respective zero-point vibrational levels. The coldest part of the supersonic expansion passes through a 3 mm skimmer and forms a molecular beam which is then interrogated using single- and double-resonance laser

methods in the extraction region of the (TOF) mass spectrometer. This chapter will serve to quickly introduce the principles and equipment enabling these experiments. Only the most salient details will be provided here, as these methods have been described in exceptional detail elsewhere.[1-3]

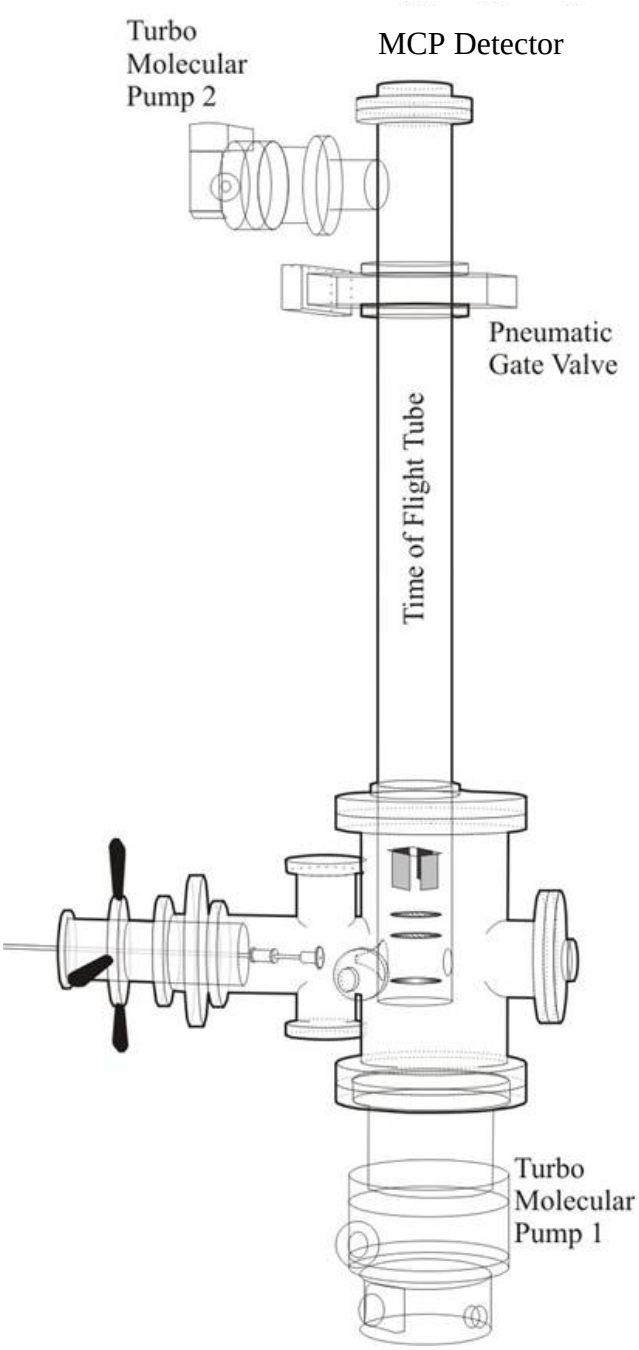

Figure 2.1: Schematic representation of the “NSF” chamber.

2.2 Supersonic Expansions and Molecular Beams

Implementation of a supersonic expansion, depicted in Figure 2.2, allows the lowest energy conformations of a sample to be studied under cold, collision-free conditions. In our experiments, a pulsed supersonic expansion is implemented in order to reduce the gas load on our pumping equipment. A pulsed expansion also synchronizes nicely with our pulsed lasers systems, discussed later.

To generate a supersonic jet, an atomic gas, most commonly He, Ne, or Ar, seeded with a small fraction of sample molecules is held in a reservoir, behind the nozzle, at a stagnation pressure, p_0, of 2-5 bar. This pre-expansion gas mixture is characterized by a Maxwell-Boltzmann distribution of conformational isomers, and has a mean free path, λ, that is very small. This mixture is then expanded through a solenoid-based pulsed valve at a flow rate ranging from 5-10 standard cubic centimeters/minute (SCCM). The nozzle opening has a 500-800 μm diameter, D. As the gas mixture flows through the orifice and into the vacuum chamber, sample molecules and buffer-gas atoms experience an enormous number of two- and three-body collisions, proportional to p_0D and p_0^2D, respectively. As this takes place, the random motion of the Boltzmann-distributed pre-expansion mixture is transformed, via enthalpy-reducing collisions, into a directed mass flow. When the average velocity of the flow exceeds the local speed of sound, the expansion is considered supersonic.[4]

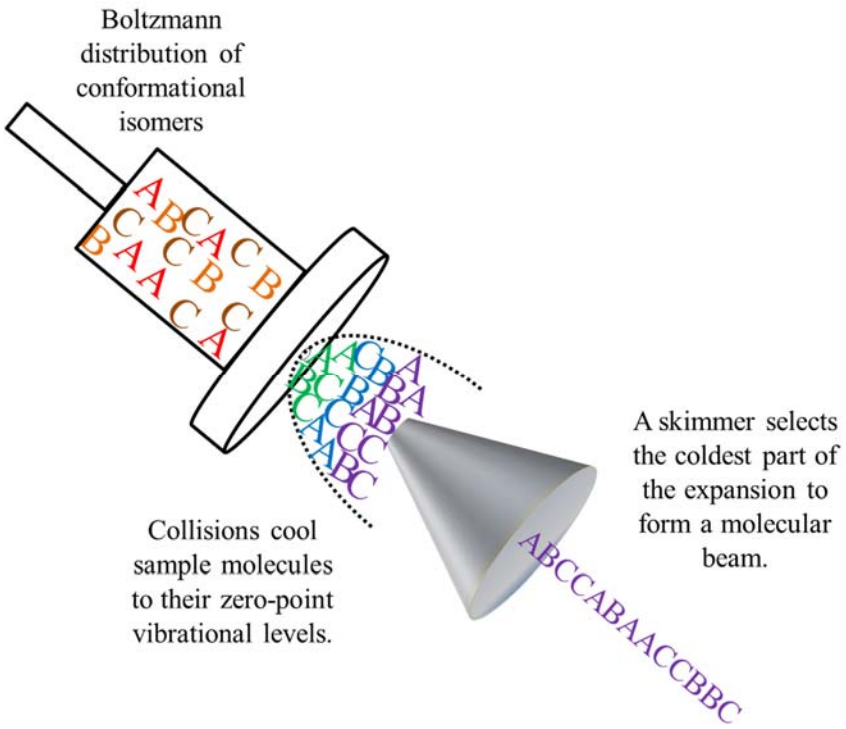

Figure 2.2: Cartoon representation of the supersonic expansion process.

Two-body collisions between sample molecules and buffer-gas atoms result in the transfer of energy out of the vibrational and rotational degrees of freedom of the sample molecules and into the translational degree of freedom of the carrier-gas atoms. As the gas pulse moves further downstream from the orifice, the velocity distribution of the seeded beam narrows as collision frequency falls off, and the temperature of the beam drops dramatically.[5] This process cools the atoms and molecules in the gas pulse to translational, rotational, and vibrational temperatures on the order of ~1 K, ~2-5 K, and ~10-15 K, respectively. Cooling the rotational and vibrational degrees of freedom out of the sample molecules greatly reduces the spectral congestion by dramatically decreasing the inhomogeneous broadening induced by higher temperatures and interactions with

solvent and other solute molecules.[6] Additionally, the low vibrational and rotational temperatures allow vibronic transitions to be resolved having full-widths at half maximum (FWHM) of ~1-2 cm^{-1} and greatly reduce the occurrence of hot and sequence bands.

2.3 Sample Preparation Methods

In order to implement the supersonic expansion source described above, it is necessary to coax the sample molecules out of the solid or liquid phase and into the gas phase. Under ideal circumstances a given molecule of interest would have a sufficiently high vapor pressure that the required number density could be achieved without additional treatment. Unfortunately, the large sizes of the molecules discussed in this work often precluded ideal circumstances, and either heating or laser desorption was necessary to achieve the required vapor pressure.

2.3.1 Heating

When the thermal stability of a sample allows, the preferred method for increasing the vapor pressure behind the nozzle is simply by heating the sample in an inline, stainless steel chamber. This is accomplished by wrapping the stainless steel sample chamber, gas-line, solenoid, and nozzle assembly with a resistively heated rope. The working end of a k-type thermal couple is captured between the outer wall of the sample chamber and the heater rope, thereby allowing the local, equilibrated temperature of the sample to be monitored in real time. Temperature control is achieved by changing the voltage applied to the heater rope using a Variac. Heating temperatures for a given

sample typically start 20º below the melting point and are then increased until appreciable signal is detected. (Some samples may require temperatures higher than the melting point.) To guard against thermal decomposition, solid samples are typically wrapped in glass wool and placed in a specially designed glass cup that fits inside the sample holder and prevents the sample from making direct contact with the stainless steel walls. Whenever possible, heating is the preferred method for increasing vapor pressure, however there are cases in which the thermal stability of a sample prohibits heating.

2.3.2 Laser Desorption

Under circumstances in which the sample cannot be heated, a somewhat more gentle method is used to coax the sample molecules into the gas phase. To perform laser desorption, shown in Figure 2.3[7], a solid- or semi-solid sample is first mechanically incorporated into the surface of a small graphite rod, measuring approximately 5 mm wide, by 2.5 mm thick, by 50 mm long. This graphite rod is supported by an aluminum boat attached to the end of a stainless steel rod. Using a load-lock port on the side of the vacuum chamber, this assembly is inserted such that its long axis is orthogonal to the molecular beam axis. The rod is then positioned in the Z-axis so that its surface is directly below the orifice of the pulsed-valve. A 6 ns, 3-5 mJ, pulse of 1064 nm light from a Continuum, MiniLite, Nd:YAG laser operating at 20 Hz enters the chamber through a CaF window located directly above the graphite rod. The laser pulse strikes the sample-impregnated graphite, and causes the sample molecules to be popped up into the gas phase where they are entrained in the gas pulse coming from the valve.

Care must be taken to ensure that the distribution of sample on the graphite rod is even, in order to avoid sample-rich hot spots or sample-lean bare spots. Graphite rods should be replaced regularly, and as such, only the smallest amount of sample capable of producing acceptable signal levels should be used. Users should pay attention to the behavior of the signal coming off of the rod. At times, signal is highly stable, and a slow translation speed can be used. At other times, the signal can be highly unstable, and increased rod translation speeds are necessary.

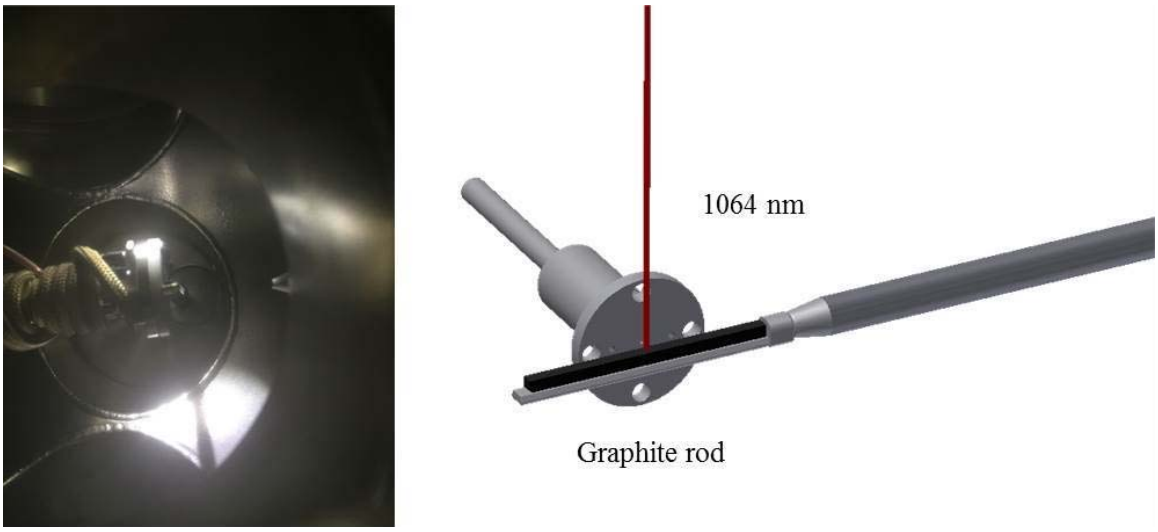

Figure 2.3: Laser desorption scheme used to more gently coax heavy or fragile molecules into the gas phase.

When implementing laser desorption, it is necessary that argon be used as the buffer-gas for two primary reasons. First, the laser desorption process has the capacity to impart additional energy to the sample molecules. Indeed, this energy transfer has been

responsible for the appearance of conformations within the cooled molecular beam that have higher than usual relative energies.[8] This additional energy needs to be cooled away in order to reach the zero-point vibrational level of each low energy conformation. The increased mass of Ar relative to Ne or He grants it a greater cooling capacity and makes it desirable in situations, such as when implementing laser desorption, in which the molecules of interest may have increased internal energy. Additionally, in laser desorption the sample molecules are not efficiently entrained within the gas pulse until a point down-stream from the valve opening. The relationship of decreasing collision frequency with increasing distance from the expansion source dictates that by the time the sample molecules have been entrained in the gas pulse, the number of energy-transferring collisions has already decreased significantly. The combined factors of higher initial internal energy and decreased collision frequency require the collisions that do occur to remove a larger amount of energy in order for sample molecules to be effectively cooled to the vibrational zero-point levels of their low energy conformations. Consequently, argon is used in all laser desorption experiments. Additionally, the number of collisions can be enhanced by increasing the stagnation pressure, p_0, based on the proportionality of two-body collision frequency to p_0D

2.3.3 Water Cluster Formation

At times, the influence of individual water molecules on the structure and spectroscopy of a particular sample molecule are of interest. In these cases, it is desirable to perform well-controlled addition of individual water molecules to form clusters with sample molecules. In order to accomplish this, a gas manifold has been assembled that

allows a partial pressure of H_2O to be incorporated into the carrier gas in a controlled way. The manifold splits the gas supply line coming from the cylinder into three parallel lines equipped with dedicated flow meters as well as inlet and outlet valves. The central, primary line provides a direct pathway to the sample-holder and the backside of the pulsed valve. Secondary sample-lines on the left and right side of the primary gas line each pass through a sample vessel designed to hold a substantial amount of liquid soaked cotton (e.g. H_2O or C_6H_6). By controlling the backing pressure and the relative flow through each portion of the gas manifold according to Equation 2.1, the desired partial pressure can be achieved.[9]

$$\frac{\text{Sample Flow}}{\text{Total Flow}} \; x \; \frac{\text{Sample Vapor Pressure}}{\text{Backing Pressure}} \; x \; 100\% = \% \text{ Sample} \qquad \text{Equation 2.1}$$

2.4 Laser Methods

2.4.1 Laser Radiation Sources

Laser light is generated in the ultraviolet (UV) and the infrared (IR) using Nd:YAG pumped dye lasers and optical parametric oscillator/optical parametric amplifier (OPO/OPA) systems, respectively. UV light is generated by doubling the output of a dye laser (RadiantDyes, Narrowscan or LambdaPhysik, ScanMate) which is pumped by either the second (532 nm, 150 mJ/pulse) or third (355 nm, 80-90 mJ/pulse) harmonic of a Continuum Surelite II, Nd:YAG laser, depending on the nature of the dye being used (e.g. 355 nm pump for Coumarin 540A or 532 nm pump for Rhodamine 6G).

IR light is generated using sum- and difference-frequency mixing in a LaserVision OPO/OPA system (Figure 2.4). Briefly stated, 1064 nm light (~600-650 mJ/pulse) from a seeded Nd:YAG (Continuum, SureLite EX & NP Photonics SI-2000 Injection Seeder) enters the OPO/OPA box (Figure 2.4), is telescoped to the appropriate beam size, and is subsequently divided by a 70/30 beam splitter. 70% of the 1064 nm light is passed on to the OPA stage, while the remaining 30% of the 1064 nm light is directed through a KTP doubling crystal to generate 532 nm light which is injected into the OPO stage. Two phase-matched KTP crystals compose the OPO stage in which the 532 nm photon having 18794 cm^{-1} of energy is split into signal (~12500 cm^{-1}) and idler (~6200 cm^{-1}) photons whose energies can be adjusted by angle tuning the OPO crystals, but whose sum is always equal to 18794 cm^{-1}. The OPO stage benefits from implementation of a grating/tuning mirror pair that serves as the rear mirror of the cavity and greatly increase the resolution of the OPO. The idler photon from the OPO stage seeds the OPA stage, which comprises four KTA crystals, and is difference frequency mixed with the remaining 70% of the 1064 nm light. The OPA stage outputs signal and idler photons, and the idler photon is selected using a “stack-of-plates” silicon polarizer. Pulse energies are on the order of ~ 12-15 mJ/pulse of idler light.

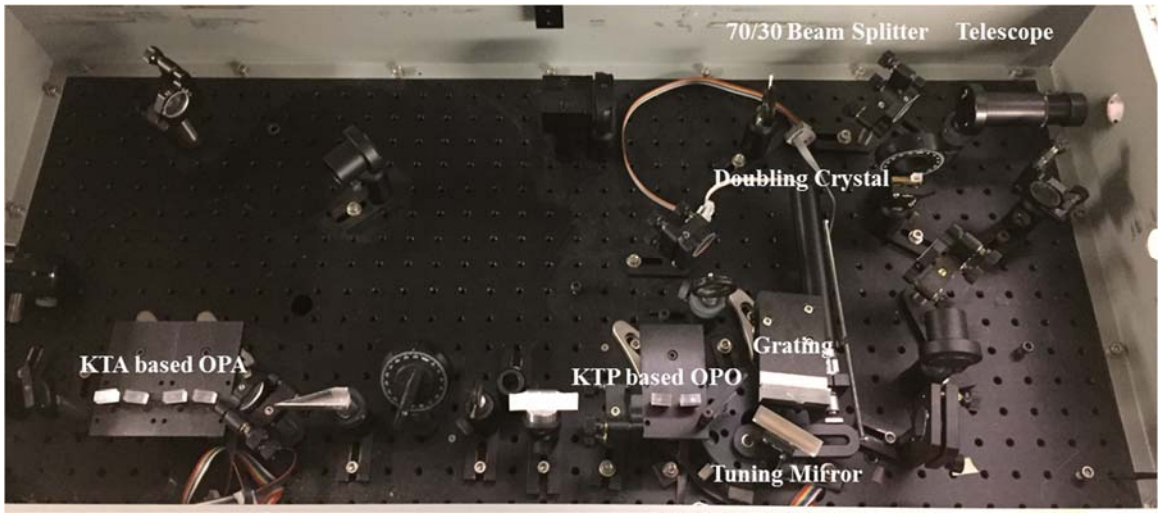

Figure 2.4: Layout of the LaserVision OPO/OPA system: Major components have been labeled.

In some cases, light in the Amide I and II (1400 cm^{-1} – 1800 cm^{-1}) regions of the IR spectrum was required. In order to generate this light both the signal and idler beams from the OPA stage are difference frequency mixed down field in a $AgGaSe_2$ crystal. Typical output power in these regions was on the order of 500-1000 μJ/pulse.

2.4.2 Resonant 2-Photon Ionization (R2PI)

Resonant two-photon ionization (R2PI), shown schematically in Figure 2.5, is used to record the electronic excitation spectra for the molecules of interest. In R2PI, the UV laser is scanned in a portion of the spectrum appropriate for the specific sample. When the laser is resonant with a vibronic transition between the S_0 and S_1 (or S_n) states of a given conformation, absorption occurs. The first resonant photon absorbed promotes the molecule of interest to the excited state, and then, upon absorption of a second photon having the same wavelength, the molecule is ionized. Both photons are absorbed nearly

coincidentally. An alternate form of R2PI, known as two-color 2C-R2PI is used when the energy of the S_0-S_1 transition is less than half of the energy needed to ionize the molecule. In 2C-R2PI, the ionizing photon (provided by a second dye laser) is tuned to a higher frequency, thus guaranteeing sufficient energy to ionize the molecule of interest. By tuning the UV laser over a range of wavelengths characteristic of each molecule's chromophore, the vibronic spectrum of all conformations present in the jet can be recorded. R2PI and 2C-R2PI are forms of action spectroscopy in which absorption is not detected by directly measuring the difference in photon flux before and after light interacts with the sample, but rather by observing the production of ions that are only generated when absorption of light by the molecules of interest occurs. Because it produces signal on top of a low background, action spectroscopy can be much more sensitive than direct absorption measurements.

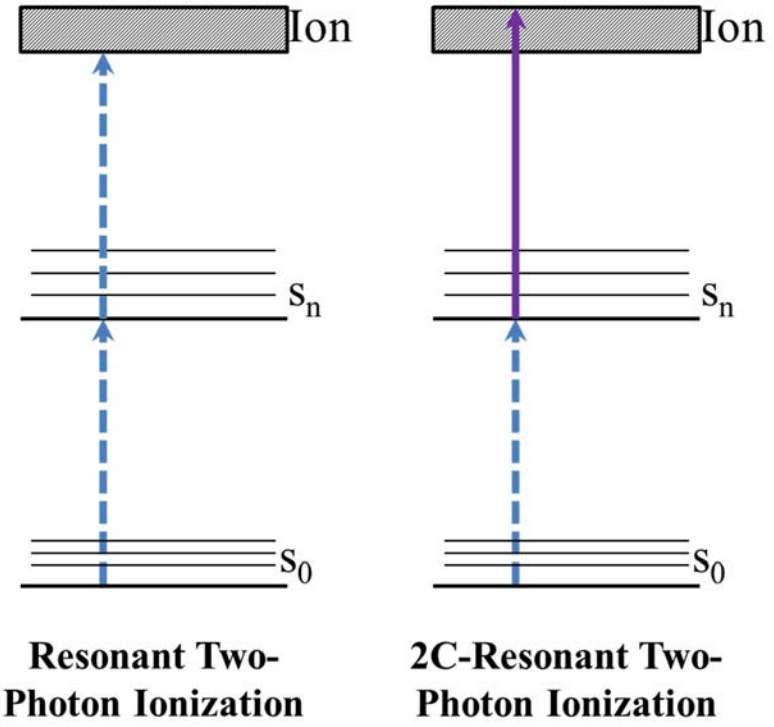

Figure 2.5: Energy level diagrams for resonant two-photon ionization (R2PI) and 2-Color R2PI.

2.4.3 Resonant Ion-Dip Infrared Spectroscopy

Resonant ion-dip infrared spectroscopy (RIDIRS) is utilized to record conformer-specific IR spectra across a broad range of IR frequencies. In RIDIRS, the UV laser, running at 20 Hz, is tuned to a particular vibronic transition observed in the R2PI spectrum belonging to a specific conformation in order to produce a constant level of ion signal. A 10 Hz, infrared beam, generated using the LaserVision OPO/OPA discussed above, is spatially overlapped with the UV beam. The timing between the two laser pulses is adjusted so that the IR laser pulse interacts with the gas pulse ~200 ns prior to the arrival of the UV laser pulse. The enormous disparity between the speed of light and the velocity of the gas pulse ensure that both laser pulses, even though separated in time,

interact with the same portion of the same gas pulse. When the IR beam is resonant with a vibrational transition belonging to the same conformation being monitored by the UV laser, some of the population is promoted out of the vibrational, zero-point level into a vibrationally excited level within the ground electronic state, and a dip in the total ion signal is observed. By performing active baseline subtraction to determine the difference between each pair of "IR on" and "IR off" peaks in real-time using a Stanford Research Systems gated integrator (SR250), a spectrum can be recorded in which the fractional depletion of ion signal is plotted as a function of IR frequency. This is shown below in Figure 2.6. The LaserVision OPO/OPA system enables spectra to be collected in the Amide II, Amide I, alkyl CH stretch, NH stretch, and OH stretch regions.[10] These regions are of particular importance when determining the structural parameters of small peptide-based systems.

2.4.4 IR-UV & UV-UV Hole-Burning Spectroscopy

Once the R2PI and RIDIR spectra have been recorded, IR-UV or UV-UV hole-burning spectroscopy can be used to separate the UV spectrum into components belonging to individual conformations. To collect these spectra the IR laser (in the case of IR-UV hole-burning) is fixed on a vibrational transition belonging to a specific conformation, and the UV laser is scanned. By operating the IR laser at 10 Hz and the UV laser at 20 Hz and performing active baseline subtraction in a gated integrator, the fractional depletion of the ion signal as a function of UV frequency can be recorded yielding a single-conformation UV spectrum. In the case of UV-UV hole-burning spectroscopy, a second UV laser, designated as the hole-burn laser, is spatially

overlapped with the probe UV laser, and relative timing is adjusted to ensure the hole-burn laser pulses arrives approximately 200 ns ahead of the probe pulse. By running the hole-burn laser at 10 Hz, and the probe laser at 20 Hz and performing active baseline subtraction, as discussed above, the vibronic spectrum of a specific conformation present in the supersonic jet expansion can be collected. This scheme is shown in Figure 2.6.

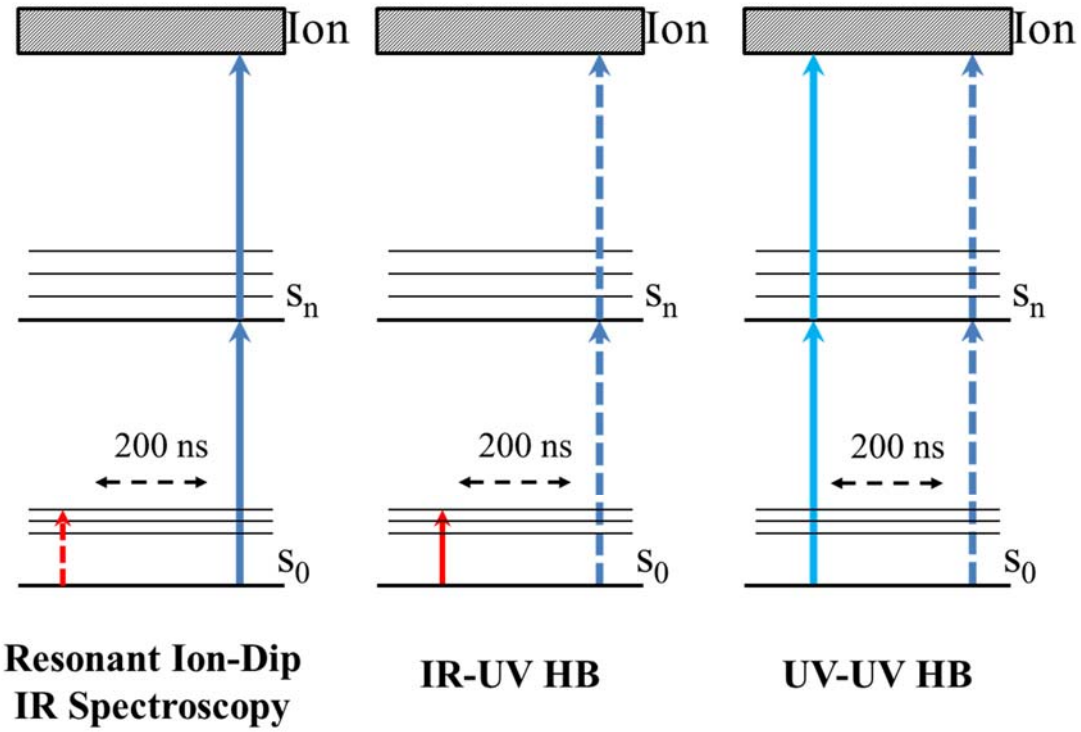

Figure 2.6: Double-Resonance Laser Schemes: Resonant Ion-Dip IR Spectroscopy, IR-UV Hole-burning, UV-UV Hole-burning. Dashed lines indicate that the frequency of the laser light is scanned. Solid lines indicate that the laser light is tuned to a particular frequency and is not scanned.

2.5 Signal Detection

Ions generated via the single- and double-resonance laser schemes described above are detected using a time-of-flight mass spectrometer. In the NSF chamber, the molecular beam enters a Wiley McLaren ion source which is held at a constant potential by the repeller plate and the draw-off-grid which are set to +4270 VDC and +3950 VDC, respectively. Upon laser-ionization, sample molecule cations are accelerated along a 1m flight tube to impact the microchannel plate (MCP, R. M. Jordan, Co.) detector and generate a cascade of electrons. The resulting current is converted to voltage and subsequently amplified 25x by a 300 MHz amplifier (Stanford Research Systems SR 445). The output voltage is monitored using a Tektronix 3032B oscilloscope; signal is pulled off of the scope using home-built LabView data acquisition programs and saved.

The most significant advantage of detecting signal in this way is the single AMU resolution afforded by the TOF mass spectrometer. Mass selection allows the signal of a particular species to be monitored in spite of any possible fragmentation, clustering, or impurity within the sample. By monitoring the mass channel belonging to the species of interest, contaminants of any variety can be filtered out.

2.6 Computational Methods

The results of DFT calculations are used to assist in making structural assignments of the observed IR spectra. To obtain these computational results, a conformational search is performed at the force field level using Amber* or a similar force field within MacroModel, a Schrödinger product.[11,12] A starting structure is

submitted to a force field level conformational search performed within an energy window of up to100 kJ/mol. The lowest energy outputs of the force field level search are re-optimized to calculate geometries and harmonic IR frequencies and intensities at the DFT level, implementing an appropriate functional and basis set (e.g. M052x/6-31+g(d)[13]), using Gaussian09.[14] The outputs of these calculations are scaled according to well established, functional-specific scale factors. The resultant stick spectra can then be compared directly to measured experimental spectra to aid in assigning structural features and spectroscopic signatures.

2.7 References

(1) James III, W. H. 2009.

(2) Dean, J. C., Purdue University, 2014.

(3) Buchanan, E. G., Purdue University, 2014.

(4) Morse, M. D. *Experimental Methods in the Physical Sciences* 1996, *29*, 21.

(5) Lubman, D. M.; Rettner, C. T.; Zare, R. N. *Journal of Physical Chemistry* 1982, *86*, 1129.

(6) Levy, D. H. *Annual Review of Physical Chemistry* 1980, *31*, 197.

(7) Meijer, G.; Vries, M. S. d.; Hunziker, H. E.; Wendt, H. R. *Appl. Phys. B* 1990, *51*, 395.

(8) Dean, J. C.; Buchanan, E. G.; Zwier, T. S. *J. Am. Chem. Soc.* 2012, *134*, 17186.

(9) Gruenloh, C. J., Purdue University, 1999.

(10) Zwier, T. S. *Journal of Physical Chemistry A* 2001, *105*, 8827.

(11) Weiner, P. K.; Kollman, P. A. *Journal of Computational Chemistry* 1981, *2*, 287.

(12) Mohamadi, F.; Richards, N. G. J.; Guida, W. C.; Liskamp, R.; Lipton, M.; Caufield, C.; Chang, G.; Hendrickson, T.; Still, W. C. *J. Comput. Chem.* 1990, *11*, 440.

(13) Zhao, Y.; Truhlar, D. G. *Journal of Chemical Theory and Computation* 2008, *4*, 1849.

(14) Gaussian 09, R. A., Frisch, M. J.; Trucks, G. W.; Schlegel, H. B.; Scuseria, G. E.; Robb, M. A.; Cheeseman, J. R.; Scalmani, G.; Barone, V.; Mennucci, B.; Petersson, G. A.; Nakatsuji, H.; Caricato, M.; Li, X.; Hratchian, H. P.; Izmaylov, A. F.; Bloino, J.; Zheng, G.; Sonnenberg, J. L.; Hada, M.; Ehara, M.; Toyota, K.; Fukuda, R.; Hasegawa, J.; Ishida, M.; Nakajima, T.; Honda, Y.; Kitao, O.; Nakai, H.; Vreven, T.; Montgomery, Jr., J. A.; Peralta, J. E.; Ogliaro, F.; Bearpark, M.; Heyd, J. J.; Brothers, E.; Kudin, K. N.; Staroverov, V.N.; Kobayashi, R.; Normand, J.; Raghavachari, K.; Rendell, A.; Burant, J. C.; Iyengar, S. S.; Tomasi, J.; Cossi, M.; Rega, N.; Millam, N. J.; Klene, M.; Knox, J. E.; Cross, J. B.; Bakken, V.; Adamo, C.; Jaramillo, J.; Gomperts, R.; Stratmann, R. E.; Yazyev, O.; Austin, A.J.; Cammi, R.; Pomelli, C.; Ochterski, J. W.; Martin, R. L.; Morokuma, K.; Zakrzewski, V. G.; Voth, G. A.; Salvador, P.; Dannenberg, J. J.; Dapprich, S.; Daniels, A. D.; Farkas, Ö.; Foresman, J. B.; Ortiz, J.V.; Cioslowski, J.; Fox, D. J. Gaussian, Inc., Wallingford CT, 2009.

CHAPTER 3
MIMICKING THE FIRST TURN OF AN α-HELIX WITH AN UNNATURAL BACKBONE: CONFORMATION-SPECIFIC IR AND UV SPECTROSCOPY OF CYCLICALLY CONSTRAINED β/γ-PEPTIDES

3.1 Introduction

One of the primary goals of the field of synthetic foldamers is to build into the peptidomimetic structures folding propensities that either mimic those of naturally occurring α-peptides, or differ from them in controllable ways that can be used in constructing new folding or binding paradigms. Among the most studied and promising classes of foldamers are β- and γ-peptides, which incorporate either two (β) or three (γ) backbone carbons between adjacent amide groups.[1] The lengthened carbon backbone, relative to α-peptides, brings the potential for forming many conformations. However, the additional inter-amide carbons create the possibility of imposing conformational constraints by incorporating backbone carbon-carbon bonds into rings.

While foldamers comprised purely of β- or pure γ-amino acid residues serve as important starting points for exploring the conformational properties of unnatural oligomers, heterogeneous backbones, containing more than one type of residue, offer even greater possibilities for fine-tuning secondary structures and the positions of the side chains, thereby enabling foldamers to interact in specific ways with biomacromolecular targets.[1e] β/γ-Peptides in which the β and γ residues alternate have a numerical

congruency with α-peptides in that an α-tripeptide (ααα) segment has the same number of backbone atoms as a β/γ-dipeptide (βγ or γβ) segment.[2] The α-helix features a characteristic *i+4→i* N-H···O=C H-bonding pattern, and one of these 13-atom H-bonds can be formed by a capped α-tripeptide (e.g., Ac-ααα-NHMe). An analogous 13-atom N-H···O=C *i+3→i* H-bond can be formed by a capped β/γ-dipeptide (e.g., Ac-βγ-NHMe or Ac-γβ-NHMe). This H-bond similarity has led to an interest in 1:1 β/γ-peptides with an alternating backbone pattern as potential structural mimics of an α-helix.[3]

Some efforts to mimic α-helical turns with β/γ segments have involved flexible subunits,[2, 4] but Guo et al. have described β/γ-peptides in which both the β and γ subunits are cyclically constrained. This study included crystallographic analysis of a pentameric β/γ-peptide that displayed only C13 H-bonds in the solid state.[5] NMR data for an analogous hexameric β/γ-peptide in a non-polar solvent suggested a similar helical conformation. Vasudev et al. have described the crystal structure of a heterogeneous tripeptide displaying a C13 H-bond across a βγ-dipeptide unit, but other gabapentin-containing oligomers were found to display different H-bonding patterns.[6]

The present work involves the study of the single-conformation spectroscopy of the two prototypical, cyclically-constrained, capped β/γ-dipeptides, shown in Figure 3.1, in the gas phase. The goal of this work is to determine whether the preorganization in these small oligomers is sufficient to enable formation of the first C13 H-bond, or whether alternative structures containing different H-bonds are favored instead. By studying these molecules under jet-cooled conditions in the gas phase, the inherent conformational preferences in the absence of solvent can be observed, and a direct

comparison with calculations on isolated molecules can be made. Incorporation of an aromatic ring in the C-terminal benzyl cap enables the use of double-resonance laser spectroscopy to record single-conformation spectra both in the IR and UV regions.

This conformational analysis of β/γ-peptides in the gas phase builds on earlier studies of a similar nature focused on unconstrained β-peptides,[7] γ-peptides,[8] and mixed α/β-peptides.[1b] In these cases, the simple backbone substitutions provided little in the way of strict steric constraints for the peptide backbone, producing a large number of conformational isomers that spanned a wide range of H-bonding patterns, including single-ring, sequential double-ring, and bifurcated double-ring structures. A sub-set of these conformers representing the full range of structures was used to create a test set of conformers for which the uncoupled site frequencies and amide I/I and amide II/II couplings could be determined.[9]

More recently, we have studied a series of small, peptidic foldamers that contain cyclically constrained β or γ residues, like those incorporated into the model foldamers considered here, including α/β-peptides[10], γ-peptides[11], and mixed α/γ-peptides.[1b, 7-8, 10, 12] In each case, an aromatic ring was incorporated in the structure to provide an ultraviolet chromophore for double-resonance spectroscopy. In the α/β-peptides, this was accomplished by a Phe side chain in the α-peptide subunit, while in the constrained γ- and α/γ-peptides and in the present study on constrained β/γ-peptides, the phenyl ring is a part of the C-terminal benzyl cap (Figure 3.1). This position of the phenyl cap at the end of the backbone enables a clearer look at the conformational preferences of the

constrained backbones, an especially important aspect of the present work where cyclic constraints are built into both the β and γ subunits.

The β-amino acid *trans*-2-aminocyclopentanecarboxylic acid (ACPC) has the Cα-Cβ bond incorporated into a cyclopentyl ring. This cyclic constraint in our β/γ-peptides is intended to elicit a strong preference for an interior dihedral ζ in the 80-95° range for the Cα-Cβ bond.[13] With this constraint, the ACPC residue produces a *gauche*-like configuration for the two adjacent amide groups, thereby pre-organizing the formation of a turn in the foldamer backbone. In the γ subunits, the Cβ-Cγ bond is incorporated into a cyclohexyl ring. This cyclic constraint in combination with the ethyl side chain at the Cα position (γ^2, Figure 3.1) predisposes the θ and ζ dihedral angles of the γ subunit to prefer *gauche*$^+$ configurations; the sequence of two consecutive *gauche*$^+$ torsion angles leads to a strong local turn-forming propensity.[14]

While the α/β- and α/γ-peptides containing ring-constrained β or γ residues showed some conformational diversity, a degree of preorganization was evident. The large C11 (α/β) and C12 (α/γ) single-rings that represent the first H-bonded turn of an 11-helix or 12-helix were among the structures observed, but these were in competition with conformers having different H-bonding architectures. In the recent study of γ-peptides with constrained residues, the corresponding capped triamide (γγ) was almost entirely folded into a C14 single-ring structure that represents the first H-bonded turn of a 14-helix. Indeed, the peptide backbone of this C14 structure was calculated to be nearly identical to that of a di-γ-peptide segment within the 14-helix observed in the crystalline form of a constrained γ-peptide hexamer.[11, 15] As shown below, the two cyclically-

constrained β/γ-peptides studied in the present work are almost entirely folded into C13 structures, thereby forming the H-bonded first turn of the β/γ-peptide analogue of the α-helix. The properties of this α-helix analogue will be considered in some detail relative to its natural counterpart.

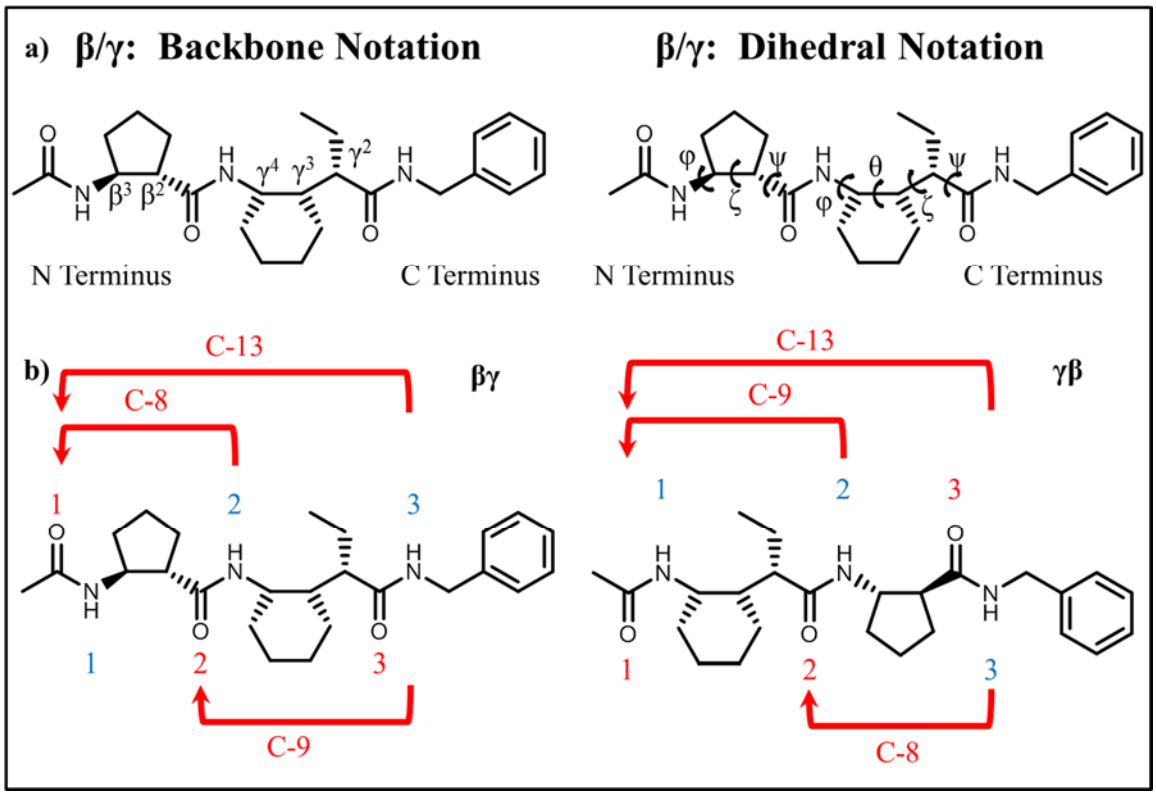

Figure 3.1: Schematic representation of the molecules to be studied in this work. a) backbone and dihedral notation. b) potential H-bonding patterns for βγ and γβ.

3.2 Experimental

Solid samples of the molecules of interest were placed in an oven located directly behind a pulsed valve with a 500 μm orifice diameter. Samples were heated to

approximately 220 ºC in order to generate the required vapor pressure. The sample was entrained in pure neon (~3 bar), and the pulsed valve was operated at a rate of 20 Hz. The supersonic expansion passed through a 3 mm conical skimmer forming a molecular beam which was subsequently interrogated in the ionization region of a 1-meter, linear time of flight (TOF) mass spectrometer.

The methods used here have been reported in detail elsewhere, so only a cursory explanation will be provided.[16] Electronic excitation spectra were obtained using resonant two-photon ionization (R2PI), by crossing the molecular beam at 90º in the ionization region of the Wiley-McLaren[17] linear time-of-flight mass spectrometer using the doubled output of a Radiant Dyes Narrowscan dye laser (<1 mJ/pulse) pumped by the third harmonic of a Continuum Surelite II Nd:YAG laser. The ions arriving in the parent mass channel (m/z = 427) were detected with a microchannel plate ion detector. Action spectra were generated in which the mass-resolved ion signal was plotted as a function of wavelength. These spectra contained contributions from all the conformational isomers present in the expansion.

Single-conformation UV spectra were then obtained using UV-UV hole-burning (UVHB) spectroscopy. In this case, UVHB spectra were obtained by counter-propagating the doubled output of a second dye laser (Lambda-Physik Scanmate) operated at 10 Hz, with the output from the 20 Hz probe laser. The two beams were spatially overlapped and temporally separated such that the hole-burn laser preceded the probe laser by 200 ns. The wavelength of the hole-burn laser was fixed on a specific vibronic transition identified in the R2PI spectrum, while the probe laser was scanned through the S_0-S_1 origin region. Depletion was monitored using the active baseline

subtraction mode of a gated integrator (Stanford Research) to record the difference in ion intensity created by the hole-burn laser as the probe laser was tuned. When the probe laser was scanned to a vibronic transition originating from the same zero-point level as the isomer interrogated by the hole-burn laser, depletion in ion signal was recorded.

Single-conformation infrared spectra were recorded via resonant ion-dip infrared (RIDIR) spectroscopy, a second double-resonance hole-burning technique, in which the hole-burning laser, now in the infrared, is produced by an optical parametric converter (LaserVision). In this case, the IR laser was tuned, while the UV probe laser was fixed on a transition identified as being due to a particular conformational isomer. When the IR laser was resonant with a ground-state vibrational transition sharing the same ground-state level as that interrogated by the probe, molecules were removed from the ground-state, and depletion was detected in the ion signal generated by the UV pulse. The difference in ion signal between sequential IR "on" and IR "off" pulses was recorded as a function of wavenumber. Spectra in the NH stretching region from ~ 3300 to 3500 cm^{-1} were obtained with pulse energies of 3-10 mJ/pulse. Spectra in the amide I and II regions were obtained by frequency mixing the signal and idler outputs in an additional $AgGaSe_2$ crystal in the final mixing stage to generate mid-IR output having ~ 300-500 μJ/pulse.

Computational predictions to spectra and geometry optimizations were determined by first performing a conformational search within the AMBER* force field using MacroModel[18] and a 100 kJ/mol energy window with no torsion check. The structures of approximately fifty of the lowest energy conformations from each search were then optimized with Gaussian09[19] using Density Functional Theory (DFT) at the

M05-2X/6-31+G(d) level of theory.[20] Additional parameters were "int=grid=ultrafine" and "scf=tight". The harmonic vibrational frequencies and infrared intensities were calculated for all conformers, and compared with experiment, after scaling the NH stretch region by 0.94 and the amide I/II region by 0.96.[21] The scaled, calculated spectra most closely matching the intensity and frequency patterns in the observed, experimental spectra were used to assign calculated structures to the experimental spectra. The relative energies of the calculated structures were then used as a sanity check to ensure that only energetically realistic structures were selected for assignments.

3.2.1 Nomenclature

The nomenclature used to label different conformations is based on that used in our previous studies of constrained γ-peptides[11] and α/γ-peptides[12b]. The various conformations are grouped into families that differ from one another first and foremost by their different H-bonding arrangements. Hydrogen bonds formed between amide NH and C=O groups are characterized primarily by the number of atoms in the cycle that is formed between the donor H and acceptor O group. This is done using a C*n* notation where *n* indicates the number of atoms in the cycle.[9] At times, a given size C*n* ring can be formed from peptide backbones that differ in one or more of the backbone dihedral angles, with four unique angles (ϕ, θ, ζ, ψ) describing the γ-peptide subunit and three dihedrals (ϕ, ζ, ψ) for the β-peptide subunit, as indicated in Figure 3.1(a). The orientation of the ethyl side chain on the γ-peptide and the phenyl ring on the benzyl cap are also incorporated into the labeling scheme. The C_{β}-C_{γ}-$C_{ethyl,\alpha}$-$C_{ethyl,\beta}$ dihedral for the

ethyl group or the C-N-C-C_{phenyl} dihedral for the phenyl ring are labeled as *anti (a)*, *gauche$^+$(g+),* or *gauche$^-$(g-)* for dihedral angles of nominally ±180º, +60º, and -60º, respectively. A fully named structure would include the base name of the peptide, the hydrogen bonding pattern, and then the orientation of the ethyl and phenyl rings, for example, βγ C8/13, (*a*, *g*-).

3.3 Results

3.3.1 Ac-β_{ACPC}-γ_{ACHC}-NHBn (βγ)

The R2PI spectrum of βγ from 37240-37750 cm^{-1} is shown as the top trace in Figure 3.2, with a series of UV-UV hole-burning spectra below it. Asterisks in the UVHB spectra indicate the transitions used for hole-burning in recording each spectrum. The R2PI spectrum is characterized by two clear sets of progressions, which the UVHB spectra below it identify as belonging to different conformational isomers. Conformer A has its S_0-S_1 origin transition at 37420 cm^{-1} and has members of the Franck-Condon progression separated by ~ 18 cm^{-1}. This progression is due to a low frequency torsional mode involving motion of both the ACPC and phenyl rings. The set of transitions assigned to conformer B begins 66 cm^{-1} to the red of A, with its S_0-S_1 origin at 37353 cm^{-1} and a somewhat shorter progression in a 20 cm^{-1} mode. The Franck Condon activity in these low-frequency modes indicates some degree of interaction between the phenyl ring and the rest of the molecule.

Transitions due to a third, minor conformer (conformer C) begin at 37345 cm^{-1}. This peak was initially thought to be a hot band, but several attempts to induce intensity via warming of the expansion by modifying expansion conditions (backing pressure, etc.) were unsuccessful, allowing us to tentatively assign it to an origin transition of a third minor conformer. However, due to its weak intensity, no further investigation was carried out on it. It should be noted that the progression significantly blue-shifted from the origin is due to incomplete subtraction from the spectrum of conformer A.

The top traces in Figure 3.3(a) show spectra obtained for conformations A (red) and B (blue) of βγ in the amide I (1600-1800 cm^{-1}) and amide II regions (1450-1600 cm^{-1}), while Figure 3.3(b) shows the analogous RIDIR spectra in the 3300-3500 cm^{-1} region associated with the amide NH stretch fundamentals. Only two of the three C=O stretch transitions are resolved in conformer A, while all three can be seen in B, with a closely spaced pair appearing at 1698 and 1705 cm^{-1}. Interestingly, in these spectra the transitions in the amide II region (nominally NH bend fundamentals) are significantly more intense than their amide I C=O stretch counterparts. In many circumstances, just the reverse is found[9]. Several small bands found in the 1400-1480 cm^{-1} region are tentatively assigned to CH bend fundamentals. The amide I/II regions of the two conformers are very similar to one another, suggesting that they are members of the same H-bonded family.

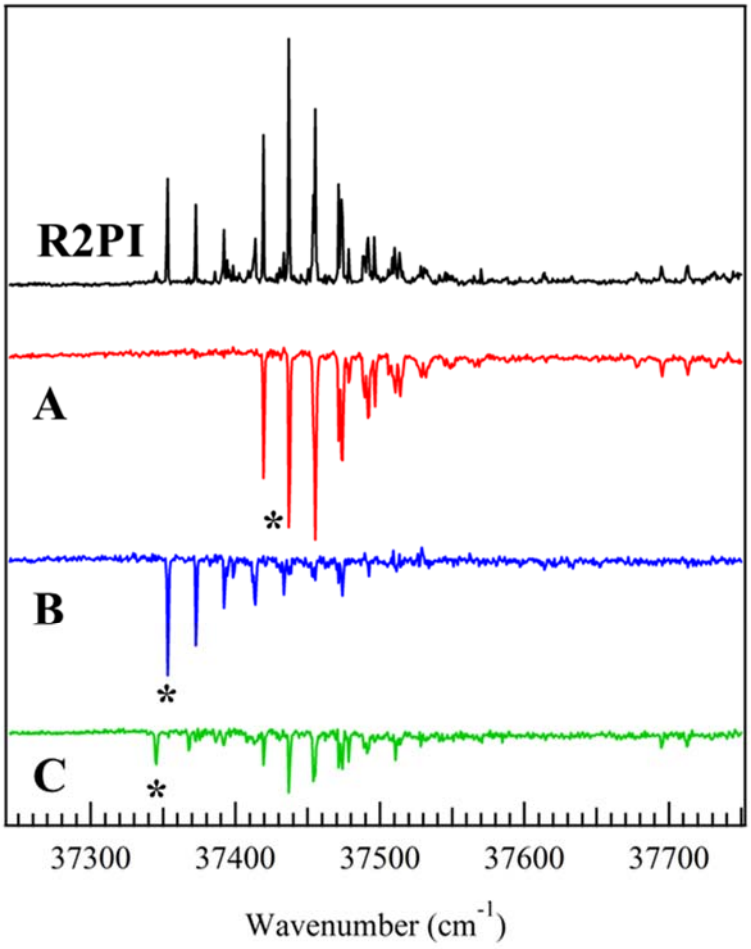

Figure 3.2: R2PI (black) and UVHB (red, blue, green) spectra taken in the S_0-S_1 region of βγ. Asterisks in A, B, and C indicate the vibronic transitions to which the hole-burn laser was set to collect UVHB spectra.

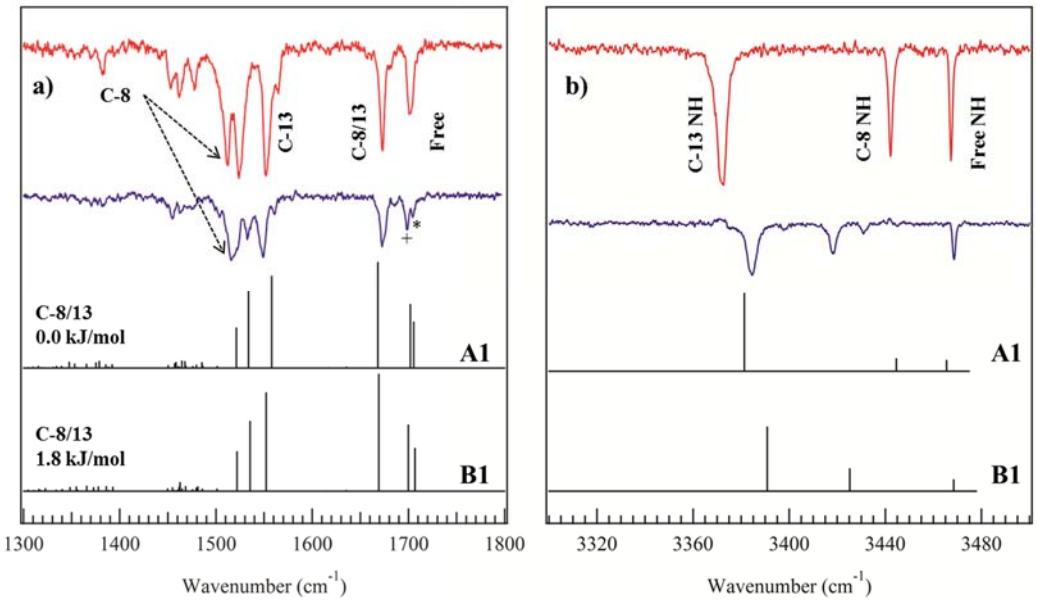

Figure 3.3: RIDIR spectra of conformers A (in red) and B (in blue) of βγ in the (a) amide I/II and (b) NH stretch regions. Scaled, calculated harmonic vibrational frequencies and IR intensities are given in the stick spectra. Harmonic frequencies were calculated at the DFT M05-2X/6-31+G(d) level of theory. Structural assignments of the transitions in each region are indicated. The scale factor in the amide I and II region (a) is 0.96, and the scale factor in the NH stretch region (b) is 0.94.

As expected based on the number of amide groups, there are three NH stretch fundamentals present in the spectrum of A, with a free amide NH stretch at 3467 cm^{-1}, a weakly H-bonded NH stretch at 3442 cm^{-1}, and a more strongly H-bonded NH stretch at 3372 cm^{-1}. That the 3467 cm^{-1} is due to a free NH stretch is borne out by comparison with the free amide NH stretch fundamentals in the constrained γ-peptides[11] and α/γ-peptides[12b] studied previously, which appear within a few cm^{-1} of this frequency. The NH stretch region of conformer B is generally similar to that of A, but differs most substantially in having its lowest frequency fundamental shifted up in frequency (3385 cm^{-1}) and its middle transition shifted down in frequency (3418 cm^{-1}) relative to A. The

two spectra are quite similar in appearance, and have a similar trade-off in frequency shifts as the two C9/C12 bifurcated double-ring structures of $\alpha\gamma^{12\beta}$.

Figure 3.3 also presents a comparison of the experimental RIDIR spectra with the predictions of DFT, M05-2X/6-31+G(d) calculations for the best-fit vibrational frequencies and infrared intensities, shown as stick spectra below. The structures associated with these simulated IR spectra are shown in Figure 3.4. All three structures are C8/C13 bifurcated double-rings that differ in subtle ways from one another. Structural pairs A1/A2 and B1/B2 differ along the 1/2 designation primarily in having different ethyl group orientations, while the A structures differ from the B structures in the length of the C8 and C13 H-bonds, with a shorter C13 (by ~ 0.06 Å) and longer C8 (by ~ 0.2 Å) bonds in A than in B.

The close correspondence between experiment and calculation enables assignment of the observed infrared bands to particular aspects of the C8/C13 bifurcated double-ring structures responsible for them. In the NH stretch region (Figure 3.3(b)), the highest frequency NH stretch transitions of both conformers of βγ are due to a free NH stretch of the N-terminal NH[1] group. The middle transition is due to NH[2], which forms a C8 H-bonded ring with C=O[1], while the lowest frequency, most intense NH stretch transition is due to NH[3], which forms a C13 H-bond to the same C=O[1] group in closing the second segment of the bifurcated C8/C13 double-ring structure. The larger frequency shift and greater intensity of the C13 NH stretch transition relative to the C8 fundamental reflects the short, strong H-bond formed by the C13 ring.

The fact that C=O[1] is acting as a double-acceptor while the other two C=O groups are free is also borne out by the appearance of the spectrum in the amide I region. Amide I fundamentals due to the two free C=O groups appear at nearly identical frequencies, just above 1700 cm^{-1}. The transition due to C=O[1] appears at 1673 cm^{-1}, shifted down in frequency, as is characteristic of such bifurcated double-ring acceptors[9].

Finally, the amide II region shows reflection symmetry with respect to the NH stretch region. The highest frequency amide II fundamental (1552 cm^{-1}) is associated with the strong C13 H-bond, as anticipated based on a stiffening of the NH bend in the presence of a linear H-bond.[9] The free and C8 NH bends are close in frequency, reflecting the unusually weak nature of the C8 H-bond. Figure 3.4 shows the H-bond distances, NH···O=C, in the calculated structures. In the global minimum structure, assigned to conformer βγ(A), the C13 H-bond length is 2.01 Å, while the C8 H-bond is 2.44 Å. As anticipated, the lower frequency of the C13 NH stretch fundamental arises in part because of the short, strong H-bond formed.

The most striking difference between the spectrum of conformer βγ(B) relative to that of βγ(A) is the shift to lower frequency of the C8 NH stretch fundamental, and a corresponding shift to higher frequency for the C13 NH stretch transition. Shifts which are properly captured by both the B1 and B2 structures, differing only in the ethyl group orientation, and between which we cannot distinguish with certainty. The structural changes accompanying these shifts are consistent with a strengthening of the C8 H-bond, which is shortened from 2.44 to 2.24 Å, and a corresponding, but smaller, weakening in the C13 H-bond, which is elongated from 2.01 to 2.07 Å. On the basis of energetics, it is

likely that the A1 and B1 structures are observed experimentally, but these structural differences are inconsequential relative to the firmly established C8/C13 bifurcated double-ring that constitutes the first turn of a 13-helix.

The assigned structures make possible a clearer interpretation of the Franck-Condon activity observed in the R2PI spectrum. The long progressions in the R2PI/UVHB spectra involve the lowest frequency modes of the molecules, in which the entire framework of the helix cycle rocks back and forth. The assigned structures lack a specific π H-bond with the ring (as evidenced by the IR spectra), and therefore the interaction with the π cloud is via van der Waals interactions, which are unlikely to have a major effect on the relative energies of the structures even if the benzyl cap was removed.

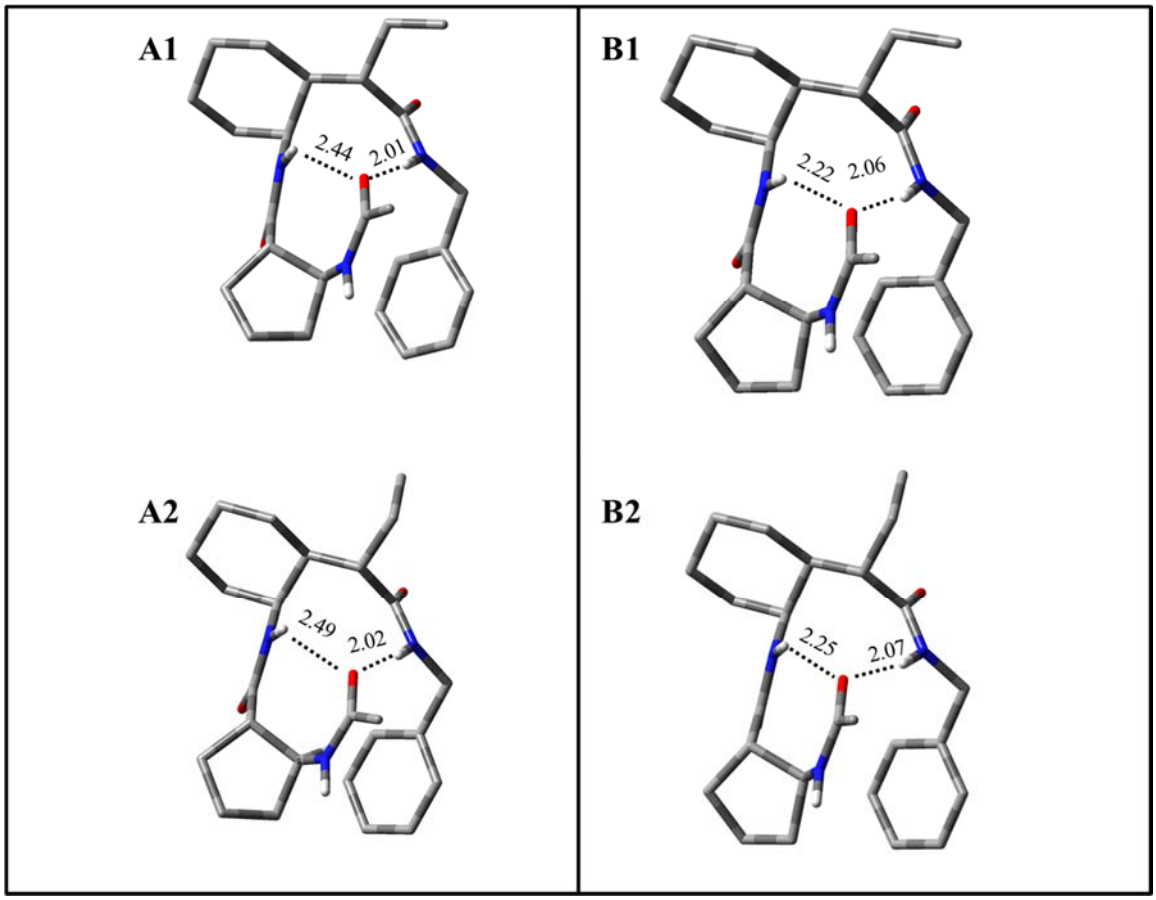

Figure 3.4: Assigned structures (hydrogens removed) based on computational fits to the RIDIR spectra of Ac-βACPC-γACHC-NHBn. Hydrogen bonds are indicated with dashed lines, and lengths are given in Å. Conformer A1 was determined to be the global minimum. Conformers B1 and B2 are distinct from conformer A1 and A2 based on their H-bonding pattern. Pairs 1/2 differ from each other primarily in the position of the ethyl group, anti and gauche, respectively, for both A and B.

3.3.2 Ac-γ_{ACHC}-β_{ACPC}-NHBn (γβ)

The R2PI spectrum of γβ from 37380-37750 cm^{-1} is shown as the top trace in Figure 3.5. The UVHB spectrum, shown below it, was recorded with UVHB laser fixed on the transition marked by an asterisk in the figure, at 37483 cm^{-1}. All transitions in the R2PI spectrum burn together, indicating that all the transitions in this region are vibronic

transitions due to a single conformational isomer of γβ, with its S_0-S_1 origin at 37483 cm^{-1}. The extent of this Franck-Condon activity indicates substantial involvement of the aromatic ring with other parts of the molecule, with electronic excitation changing the geometry along these low frequency modes in the excited state. Three progressions were identified in the spectrum, involving low frequency modes with frequency 21, 31, and 37 cm^{-1}, labeled as Z, Y, and X, respectively, in Figure 3.5.

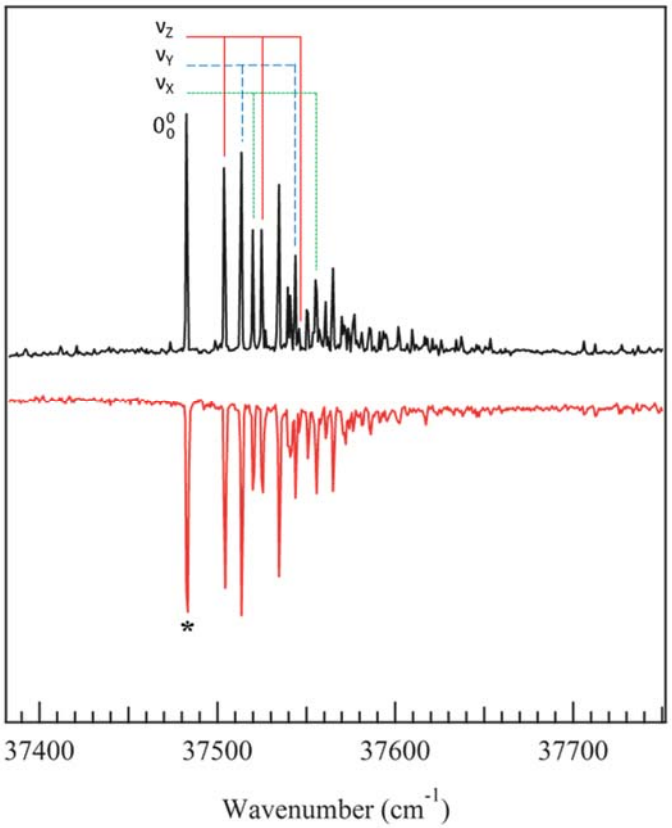

Figure 3.5: R2PI and UVHB spectra for Ac-γ_{ACHC}-β_{ACPC}-NHBn in the S_0-S_1 region of γβ collected by monitoring ion signal in the monomer mass channel. The asterisk indicates the transition to which the laser was set to collect the hole-burn spectrum. Progressions have been marked Z, Y, and X corresponding to low frequency modes of 21, 31, and 37 cm^{-1}, respectively.

Figures 3.6(a) and 3.6(b) show RIDIR spectra of the single conformer of γβ in the amide I/II and NH stretch regions, respectively. In the spectrum for the amide I region, all three C=O stretch fundamentals are now well-resolved, while only a pair of transitions are resolved in the amide II region. The broadening on the low frequency transitions at 1532 cm^{-1} suggests the possibility that a pair of unresolved transitions contributes to this breadth. The NH stretch region looks very similar to that of conformer B of βγ (Figure 3.3(b)), having a free NH stretch fundamental at 3472 cm^{-1} and H-bonded NH stretch transitions at 3412 cm^{-1} and 3370 cm^{-1}. The resemblance of the RIDIR spectrum of the single conformer of γβ with the pair of conformers observed for βγ argues that it belongs to a similar bifurcated double-ring conformational family.

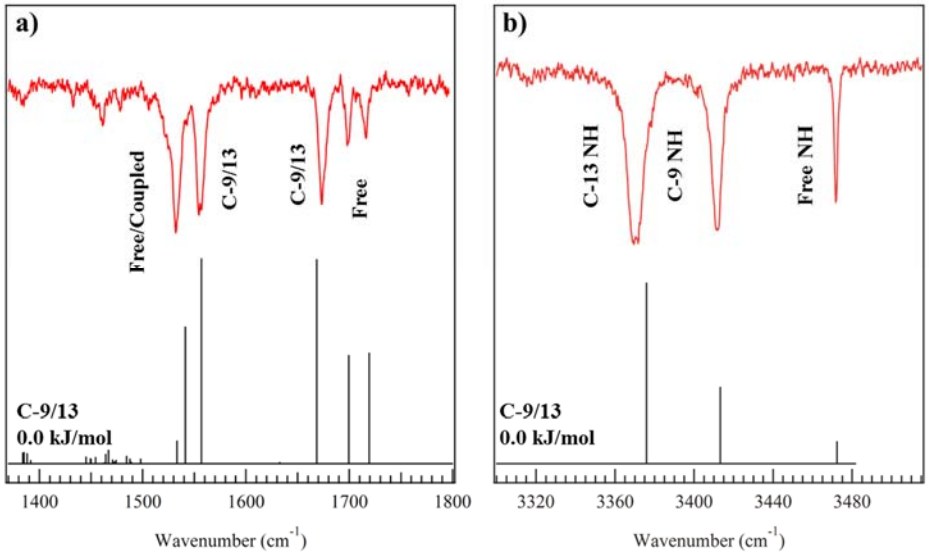

Figure 3.6: RIDIR spectra and scaled, calculated harmonic vibrational frequencies and IR intensities of γβ are given in the stick spectra which were calculated at the DFT, M05-2X/6-31+G(d) level of theory. Structural assignments of the transitions in each region are indicated. The scale factor in the amide I and II region (a) is 0.96, and the scale factor in the NH stretch (b) region is 0.94.

This is borne out by the calculated IR spectrum of the global minimum structure for γβ, which is shown as a stick diagram in Figure 6. The fit to experiment is excellent. As anticipated, the γβ structure is a bifurcated double-ring, here a C9/C13 rather than a C8/C13 structure because the reversal of the β-peptide and γ-peptide subunits produces a C9 nearest-neighbor H-bond across the γ-peptide as the first segment of the bifurcated ring in γβ, rather than the C8 associated with the β-peptide subunit in βγ. The best-fit structure, shown in Figure 3.7, is also calculated to be the global minimum. As we might expect, similar to βγ, there is a pair of calculated structures that share the same backbone conformation, but differ only in the ethyl group orientation. However, in γβ, the energy cost is significantly higher (~ 12 kJ/mol). This can be seen in Table 1. Again though, there is a negligible impact on the calculated IR spectrum, making an assignment to the C9/C13 H-bonding architecture firm. Based on energetics, in what follows we refer to structure γβ(A1) as the assigned structure for γβ.

The NH stretch fundamentals due to the C9 (NH[2]) and C13 (NH[3]) hydrogen bonded rings have transitions appearing at 3412 and 3370 cm^{-1} respectively. The C13 NH stretch is very near its value in the two conformers of βγ. However, as with their C8/C13 counterparts, the frequency of the C9 H-bond is almost 100 cm^{-1} above its value in an isolated C9 ring[11]. This is a consequence of longer H-bond distance (2.13 Å vs. 1.93 Å in γ) and the weakening associated with formation of a bifurcated double-ring.

Spectra of γβ in the amide I and II regions, (Figure 3.6(b)), are also similar in appearance to their βγ counterparts. However, in this case the two free C=O stretch transitions are well-separated from one another at 1716 cm^{-1} (C=O[3]) and 1698 cm^{-1}

(C=O[2]). In the amide II region, the calculations predict that only two of the three NH bend fundamentals have appreciable intensity. In this case, the amide II vibrations are quite mixed, with significant amplitude on two of the three NH groups. The highest frequency transition at 1554 cm^{-1} is assigned to an in-phase mixture of C13 and C9 NH motion. The band at 1532 cm^{-1} is primarily the free NH[1] bend, while the weak transition a few cm^{-1} below this (unresolved in the experimental spectrum) has out-of-phase contributions from the C9 NH[2] counter-acted by out-of-phase motion of the C13 and free NH groups, leading to a near cancellation in its intensity.

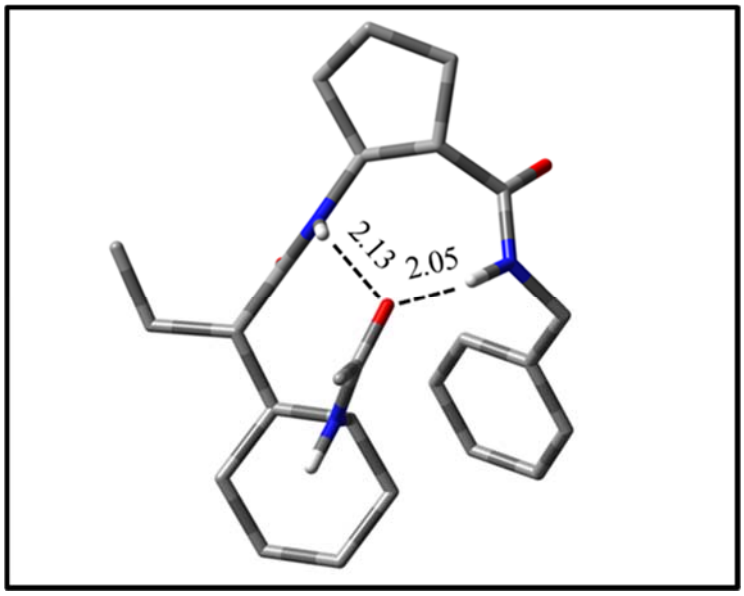

Figure 3.7: Assigned structure for Ac-γ_{ACHC}-β_{ACPC}-NHBn. Hydrogen bonds are indicated by dashed lines and NH···O distances are given in Å.

It is worth noting that the assigned structure has its three lowest frequency modes calculated at 28, 32, and 37 cm^{-1}, in good correspondence with the progressions observed in the R2PI spectrum to modes Z, Y, and X, respectively. All three of these modes

involve substantial motion of the cyclohexyl and phenyl rings relative to one another, as the single turn positions the two in close proximity to one another. Upon excitation of the π-π* transition, the structure distorts along these low-frequency modes, giving rise to the observed Franck-Condon activity.

3.4 Discussion

3.4.1 Conformational Preferences of βγ and γβ

The present results on two prototypical β/γ-peptide dimers provide a first look at the conformational preferences of the β/γ-peptide backbone in the gas phase. Unlike many of the early studies from our group on other homogeneous[7-8, 11-12] and heterogeneous[1b, 10, 12b] foldamers, both the β and γ subunits studied are conformationally constrained by incorporation of a ring into the backbone, cyclopentyl in the β subunit or cyclohexyl in the γ subunit. As previously observed for other small foldamers containing ring-constrained subunits, the number of conformations observed in the expansion-cooled sample is small. In γβ the conformational population is dominated by a single conformational isomer. In βγ two conformers are observed, but these two structures belong to the same conformational family, with only minor differences between them.

Independent of the order of β and γ subunits, the major intramolecular H-bond occurs in a 13-atom ring. This structure is secondarily stabilized by an additional NH···O=C H-bond involving NH[2] and C=O[1], forming either a C8 (βγ) or C9 (γβ) H-bonded ring, which in concert with the C13 H-bond results in bifurcated double-ring

structures. The C13 H-bond distance calculated for the assigned C9/C13 structure is almost identical to the C13 H-bond distance seen in both C8/C13 conformers A and B in βγ.

The different subunit order in βγ vs. γβ leads to some interesting effects on the foldamer backbones and the dihedral angles they support (Table 3.1). Both the C8/C13 and C9/C13 bifurcated double-ring structures orient all three amide groups so that they point in the same direction, with the acceptor C=O on the N-terminal acyl cap accepting H-bonds from donor NH groups on the interior and C-terminal NHBn caps (Figure 3.1).

Table 3.1: Structural and energetic comparison of low-energy conformers of foldamers βγ and γβ.

βγ Molecule	**ΔE (kJ/mol)**	**φ_β**	**ζ_β**	**ψ_β**	**φ**	**θ**	**ζ**	**ψ**	**C13 (Å)**	**C8 (Å)**
βγ-C8/13 (*a*, *g*-) [**A1**]	0.00	-68	132	-103	-168	59	51	-122	2.01	2.44
βγ-C8/13 (*g*-, *g*-)[**A2**]	5.92	-68	133	-104	-166	57	53	-131	2.02	2.49
βγ-C8/13 (*a*, *g*-) [**B1**]	1.78	-70	127	-92	-171	58	48	-121	2.06	2.22
βγ-C8/13 (*g*-, *g*-) [**B2**]	7.60	-70	126	-95	-168	57	51	-128	2.07	2.24
βγ-C8/13 (*a*, *g*-)	0.32	-65	134	-103	-161	58	46	-115	1.97	2.4
βγ-C8/13 (*a*, *a*)	1.40	-64	118	-128	-142	58	51	-112	1.93	2.94
βγ-C8/13 (*g*-, *a*)	7.81	-66	135	-102	-161	57	49	-120	1.98	2.45

γβ Molecule	**ΔE (kJ/mol)**	**φ**	**θ**	**ζ**	**ψ**	**φ_β**	**ζ_β**	**ψ_β**	**C13 (Å)**	**C9 (Å)**
γβ-C9/13 (*a*, *g*-) [**A1**]	0.00	-110	62	75	-115	-140	90	-90	2.04	2.13
γβ-C9/13 (*g*+, *g*-) [**A2**]	11.78	-109	64	73	-117	-138	91	-90	2.04	2.14
γβ-C13 (*a*, *g*-)	2.16	-153	59	61	-113	-114	95	-112	1.97	N/A
γβ-C13 (*a*, *g*-)	6.53	-141	53	35	70	65	83	-127	1.95	N/A
γβ-C13 (*g*-, *g*-)	10.27	-155	59	58	-117	-103	93	-117	1.97	N/A

Table 3.1 Continued

Additional Molecules	Family	φ_β	ζ_β	ψ_β	φ	θ	ζ	ψ
$\beta_{ACPC}\alpha$[b]	C7/C8a	~ -70	~ 130	~ -60				
β-γ-β-γ-β[c]								
β_1	α-Helix	-108	93	-128				
γ_2					-135	60	60	-121
β_3	α-Helix	-134	114	-86				
γ_4					-147	58	47	-130
β_5	C-9	-168	141	-155				
γ[d]					-106	66	75	-103
γγ (1)[d]	C-14				-158	61	67	-115
γγ (2)[d]	C-14				-161	59	56	-132
γα[e]	F/C9/C12				-105	62	71	-126
αγ[e]	C5/F/C9				-103	66	76	-103

[a]Dihedral angles are given in Figure 3.1. [b]Reference 18 (several structures, see reference) [c]Reference 11, [d]Reference 19, [e]Reference 21

In βγ, the cyclopentyl bridges between amide groups involved in a C8 H-bonded ring, with the γ residue C=O group oriented toward the benzyl cap NH. This arrangement produces a central ζ_β torsion angle (Cα-Cβ) near 130°, which is unusually large relative to ACPC residues in helical conformations.[13] In contrast, the ACPC residue in γβ spans two amide groups that both act as NH donors, leading to ζ_β near 90°, which is in the range typically seen for ACPC residues within helical secondary structures.

The γ residue displays distinct dihedral preferences in response to the donor/acceptor nature of the neighboring amide groups. In contrast to the ACPC

residues, the γ residues display central (θ, ζ) dihedral angles that are always near their optimal values of 60-70º, whether they are involved in a C9 H-bond or not. However, the ϕ angle varies as a result of different sequence contexts for the γ residues, near -110º in γβ conformations that form a C9 ring, by opening up to values near -160º to -170º when both NH groups are involved in H-bonds, as in the C8/C13 double rings in βγ.

In assessing the degree to which our two constrained β/γ-peptides are locked into structures that support C13 H-bonds, we must compare the relative energies of the C13 structures with the energies of other structures that feature different H-bonding patterns. To that end, we have carried out an exhaustive search of the potential energy surface and optimized all conformational minima in the first ~ 40 kJ/mol at the DFT M05-2X/6-31+G(d) level of theory. The calculated relative energies of all conformational minima, grouped by conformational family, are summarized in the energy level diagrams for βγ and γβ shown in Figure 3.8(a) and 3.8(b), respectively. Calculated structural families include bifurcated double-rings, sequential double-rings, single-rings, and single-ring/amide stacked composites. Analogues of these H-bonding patterns have been observed previously in both α-peptides and synthetic foldamers[9], but for βγ and γβ they are expanded to ring sizes appropriate for the β/γ-peptides.

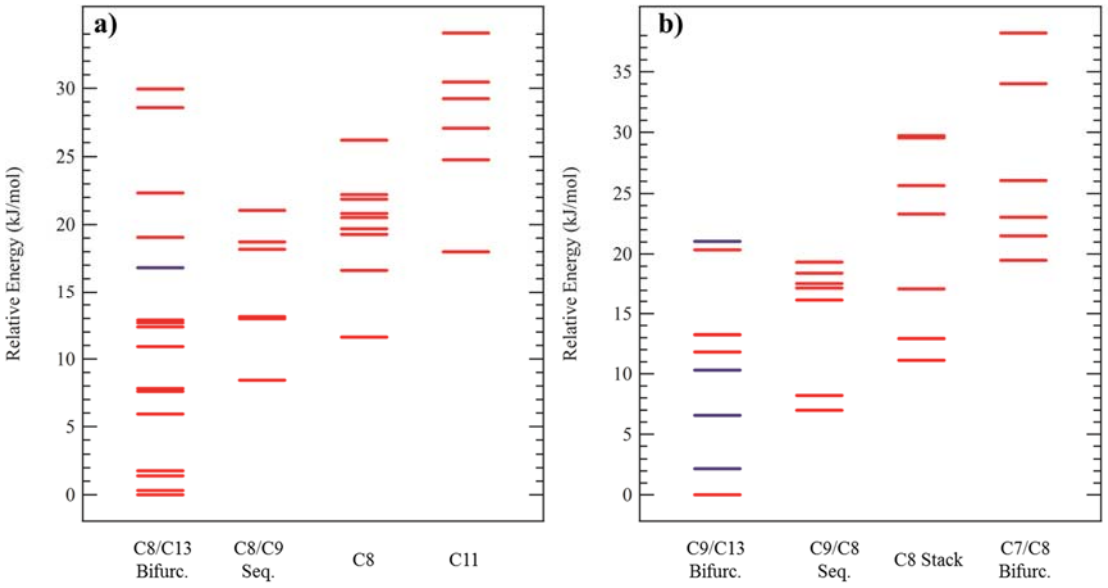

Figure 3.8: Energy level diagrams for the conformational minima of (a) βγ and (b) γβ, calculated at the DFT M05-2X/6-31+G(d) level of theory. Columns are sorted by family. Bifurc. = Bifurcated double-ring, Seq. = Sequential double-ring, and Stack = amide stacked. The markers given in blue indicate a structure that only contains a C13 H-bond, but otherwise has the characteristics of the C8/C13 Bifurcated or C9/C13 Bifurcated families.

As Figure 3.8 nicely illustrates, structures that incorporate a C13 H-bond are clearly preferred over all alternatives, with energy at least 7 kJ/mol lower than those of the most stable C8/C9 or C9/C8 sequential double-rings. The large number of low-energy C8/C13 structures for βγ (Figure 3.8(a)) reflects the presence of two structural types (A and B) that differ in the strength of two H-bonds that share a common amide C=O acceptor group in what is otherwise a similar H-bonding architecture. In addition, for each backbone dihedral configuration, there are several conformations that differ in the position of the ethyl side chain, the orientation of the phenyl ring, and the cycle conformation.[10] The different phenyl ring orientations have energies spread over ~ 2-5

kJ/mol, while reconfiguration of the ethyl group from its preferred *anti* to a *gauche*$^-$ orientation raises the energy of the conformer by ~ 5.8 kJ/mol for βγ, while the analogous rotation of the ethyl group from *anti* to *gauche*$^+$ in γβ comes at the cost of ~ 12 kJ/mol.

In Figure 3.8(b), we have combined the C9/C13 and single-ring C13 structures into a single column (the latter colored in blue). The fact that these single-ring structures are near in energy to their C9/C13 counterparts illustrates clearly how weak and non-optimal the C9 H-bond is relative to its isolated counterpart (e.g., that in γ, Table 3.1).[11] The orientation most suited to the formation of the additional C9 H-bond occurs when the ϕ dihedrals of the β and γ subunits approach 180º and -60º positions, respectively In the cases where only a C13 H-bond is formed, these dihedral values are switched.

The C8/C9 and C9/C8 sequential double rings might be anticipated to compete effectively with the C13-containing structures, which are held together principally by a single H-bond. The H-bond lengths of the C8/C9 rings are in the 1.9-2.0 Å range, in a range similar to their distances in the absence of the cyclic constraints. In order to explore the role played by the cyclic constraints in dictating the preference for C8/C13 bifurcated rings over C8/C9 sequential rings, we have optimized and compared the relative energies of each structural type with and without the cyclic constraints present, replacing these groups when appropriate with methyl groups. In the cases tested (Table 3.2), the C8/C9 structures were always at least 7 kJ/mol higher in energy than their C8/C13 counterparts, indicating that the bifurcated structure is intrinsically more stable than the C8/C9 double-ring structures. This conclusion is somewhat surprising given the

stability and prevalence of similar C7/C8 double-ring structures seen in work on α/β-peptides.[1b, 10]

Table 3.2. Table showing the results from comparison of bifurcated double-ring structures with sequential double-ring structures for βγ.

Molecule	Ala Position	Energy Δ (kJ/mol)
βγ-C8/C9 (a, g+)	Cβ in γ-residue, Cα in β-residue	7.29
βγ-C8/13 (a, g-) [A]	Cβ in γ-residue, Cα in β-residue	0.00
βγ-C8/C9 (a, g+)	Cα in β-residue	7.00
βγ-C8/13 (a, g-) [A]	Cα in β-residue	0.00
βγ-C8/C9 (a, g+)	Cβ in γ-residue	9.76
βγ-C8/13 (a, g-) [A]	Cβ in γ-residue	0.00

Interestingly, one of the conformational families observed in γβ is a hybrid structure that incorporates a C8 ring across the β subunit with an amide-stacked conformation across the γ subunit. Previous work showed that an amide stacking conformation in unconstrained γ-peptides was nearly as stable as C9 structures because of combined effects of minimal steric strain involving the γ-peptide backbone and an energetically optimal antiparallel approach of the two amide groups engaged in the stacking interaction.[8, 12a, 21] While the C8/stack combination is about 10 kJ/mol less stable than the C9/C13 global minimum, it is nonetheless interesting to see that amide

stacking leads to stable minima not far above the global minimum, even in the presence of the cyclic constraint associated with the γ subunit employed in our studies. The C8/stack structure differs from the C8/C13 global minimum in having the N-terminal amide group of the γ residue rotated 180° from its C8/C13 values, as a result of differences in dihedral angles ψ and ζ. Reorientation of the amide group leads to a dipole moment for the C8/stacked structure of ~ 5 D, nearly 4 D less than the dipole moment of the C8/C13 counterpart, which has all amide groups pointing in the same direction.

3.4.2 Constrained γ-peptide Series: α/γ-, β/γ-, and γ-peptides

The results presented here on constrained β/γ-peptides complete a series of studies that includes the ring-constrained γ-peptide, α/β-peptide, and α/γ-peptide analogues. As a result, we can compare and contrast the type of conformational preferences imposed by the cyclohexyl ring and ethyl side chain constraints among the different peptidic backbones, and the degree to which these constraints enforce a preference for a particular conformation.

The homogeneous constrained γ-peptides studied by Walsh et al. have the same constraints as the γ subunit in the present work. This γ residue constraint led to clear and specific folding preferences among the γ-peptides previously examined. In the capped γ-diamide Ac-γ_{ACHC}-NHBn (labeled in shorthand simply as γ), all conformations contained a C9 H-bonded ring. In the capped triamide Ac-γ_{ACHC}-γ_{ACHC}-NHBn (labeled γγ), the lone observed conformer contained a single C14 ring that constituted the first turn of a 14-helix. As Table 3.1 shows, the central two dihedral angles, θ and ζ, of the γ-peptide

backbone are locked into angles near 60° (g_+), producing a turn in the backbone. When combined in succession, the two turns bring the *i+3* NH group into close proximity with the *i* C=O, forming an *i+3*→*i* C14 H-bond.

In the cyclically constrained α/β-peptides[10] and α/γ-peptides[12b], the α subunit, which cannot have a cyclic constraint without losing H-bond donor sites, was free to adopt multiple configurations with little energetic variation. Thus, while the cyclic constraint imposed restrictions on the γ or β subunit, several conformational families were observed for the heterogeneous α/β and α/γ backbones. C5/C8 bifurcated double rings were formed by α/β-peptide $\alpha_L\beta_{ACPC}$, while in $\beta_{ACPC}\alpha_L$, both C8/$C7_{eq}$ sequential double rings and C11 single-rings were observed.[10] In the α/γ-peptide analogues Ac-Ala-γ_{ACHC}-NHBn and Ac-γ_{ACHC}-Ala-NHBn (labeled simply as αγ and γα), a total of ten conformations were observed, most of which contained a C9 ring across the γ subunit. Among them were three structures that incorporated a C12 ring, the first step in forming a 12-helix. By comparison, the β/γ-peptides studied in this work benefit from the restrictions imposed on the backbone by both the β and γ subunits. As a result, the preference for C13 structures in βγ and γβ appears to be as robust as the preference for C14 rings among fully constrained γ-peptides.

3.4.3 Comparison of the Single Turn C13 with the 13-helix in β/γ- and α-peptides

The present study allows us to compare in detail the structure of a prototypical turn of a β/γ-peptide 13-helix, with the more fully-formed 13-helix in longer β/γ-peptides and the α-helix formed by α-peptides. While there are no experimental data on βγ and γβ

in solution or in crystalline form, previous studies by Guo et al[5] on longer constrained β/γ-peptides provide a point of reference. The X-ray structure for the pentameric (β-γ-β-γ-β) foldamer reveals that some backbone dihedral angles vary along the backbone rather significantly. Nevertheless, the structural constraints imposed by the γ subunit appear to be quite robust, since the θ, ζ, and ψ angles in the pentamer crystal structure agree quite well with those found in the present gas phase studies (Table 3.1).[5] The ϕ angles in the pentamer crystal structure (-135°, -147°) are intermediate between those found in βγ and γβ, and are more consistent with the dihedral angles predicted for the single-ring C13 structures of γβ (Table 3.1), which lack the distortions induced by the presence of a second H-bond (C8 or C9) imposed by the bifurcated double-ring.

The dihedral angles for the β subunits in the crystalline pentamer show much greater variability than those of the γ subunits, a trend that is consistent with the significant differences among ϕ_β, ζ_β, and ψ_β dihedral angles found in the β subunits of γβ relative to those of βγ (Table 3.1). Figure 3.9 presents an overlay of the βγ(**A**) C8/C13 structure determined in this work with the $\beta_3\gamma_4$ portion of the helical β/γ-pentapeptide from Guo et al. The choice of this comparison is based on the dihedral angles of the βγ(**A**) structure most closely aligning at this point on the pentamer helix. As one can see, the C8/C13 structure differs from the more well-formed β/γ 13-helix primarily in the reorientation of the N-terminal amide group in order to form a C8 H-bond with the interior amide group, but is still able to maintain a similar C13 H-bond distance.

Even with the adjustments noted above for the accommodation of the additional C8 H bond, the dihedral angles calculated for the experimentally observed βγ and γβ

structures are in surprisingly good agreement with computational predictions for the β/γ hexapeptide 13-helix obtained by the Hofmann group in Germany.[3] The agreement is particularly noteworthy given that the calculations were conducted with β/γ-peptide oligomers completely lacking in side chains. Note that the signs of each dihedral angle are switched in the Hofmann study relative to our work because the computational work involved helices with opposite handedness, formed from an achiral backbone, relative to the helical conformations specified by the subunit chirality in βγ and γβ.

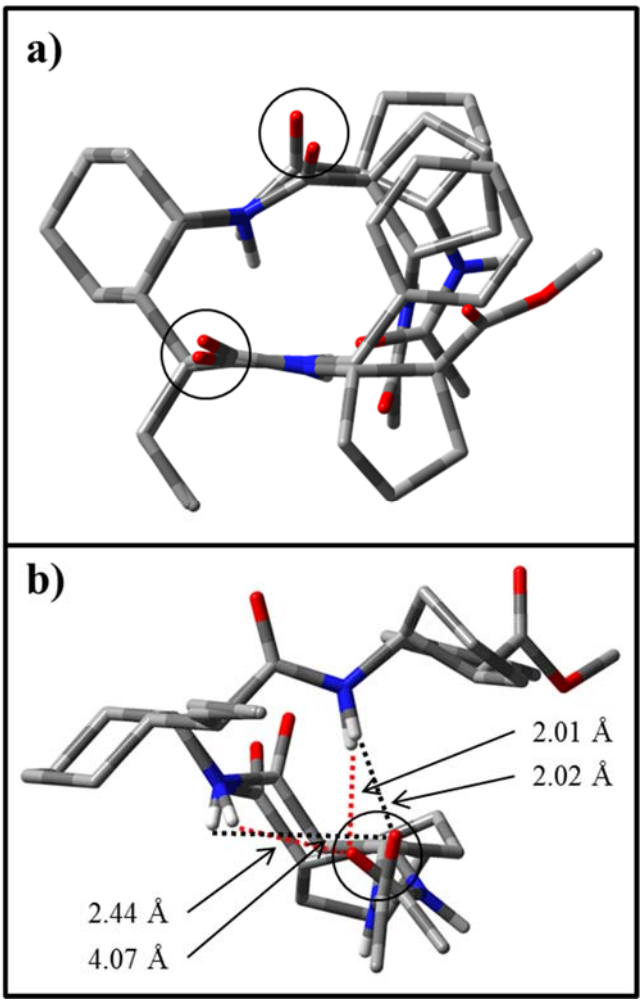

Figure 3.9: a) Axial, and b) side view of the structures of βγ (A) and the $\beta_3\gamma_4$ segment of the β/γ pentamer from Guo et al.[5] overlapped at the ACHC constraint to demonstrate the differences between the backbone dihedral angles of the two structures. The principle difference is found in the orientation of the N-terminal amide group, whose C=O acceptor reconfigures to accommodate the C8 H-bond in βγ(A). Red and black dashed lines mark both the C8 and C13 hydrogen bonds formed in β/γ (A) and the $\beta_3\gamma_4$ segment, respectively. Associated bond lengths are listed and labeled.

Based on their pentamer crystal structure, Guo et al. determined that the 13-helix formed from β/γ-peptides has a pitch (5.4 Å/turn) and radius (2.5 Å) very similar to the α-helix formed from α-peptides (pitch of 5.4 Å per turn, radius of 2.3 Å). Of course, the

two helices differ significantly in the number of residues per turn (3.6 for the α-helix versus 2.6 for the β/γ-peptide 13-helix), since a β/γ dipeptide has the same number of backbone atoms as an α tripeptide. Figure 3.10 compares two views of the β/γ- and α-peptide 13-helices viewed down the helical axes. In Figure 3.10, the side chains are removed in order to better view the β/γ-peptide (Figure 3.10(a)) and α-peptide (Figure 3.10(b)) backbones. In an α-helix, the amide groups are evenly spaced and rotated ~ 100^{o} relative to one another (3.6 x 100^{o} = 360^{o} per turn). This arrangement in the α-helix causes the side chains to fan out around the helix periphery in a regularly spaced pattern, as shown in the bottom view of Figure 3.10(b). By comparison, the backbone amide arrangement in the β/γ-peptide 13-helix must be less regular than in the α-helix, because the foldamer helix is comprised of two different types of subunit, with the γ-peptide subunit responsible for a larger angular change (~ 160^{o}, semicircular arrow) than its β-peptide counterpart (~ 90^{o}).

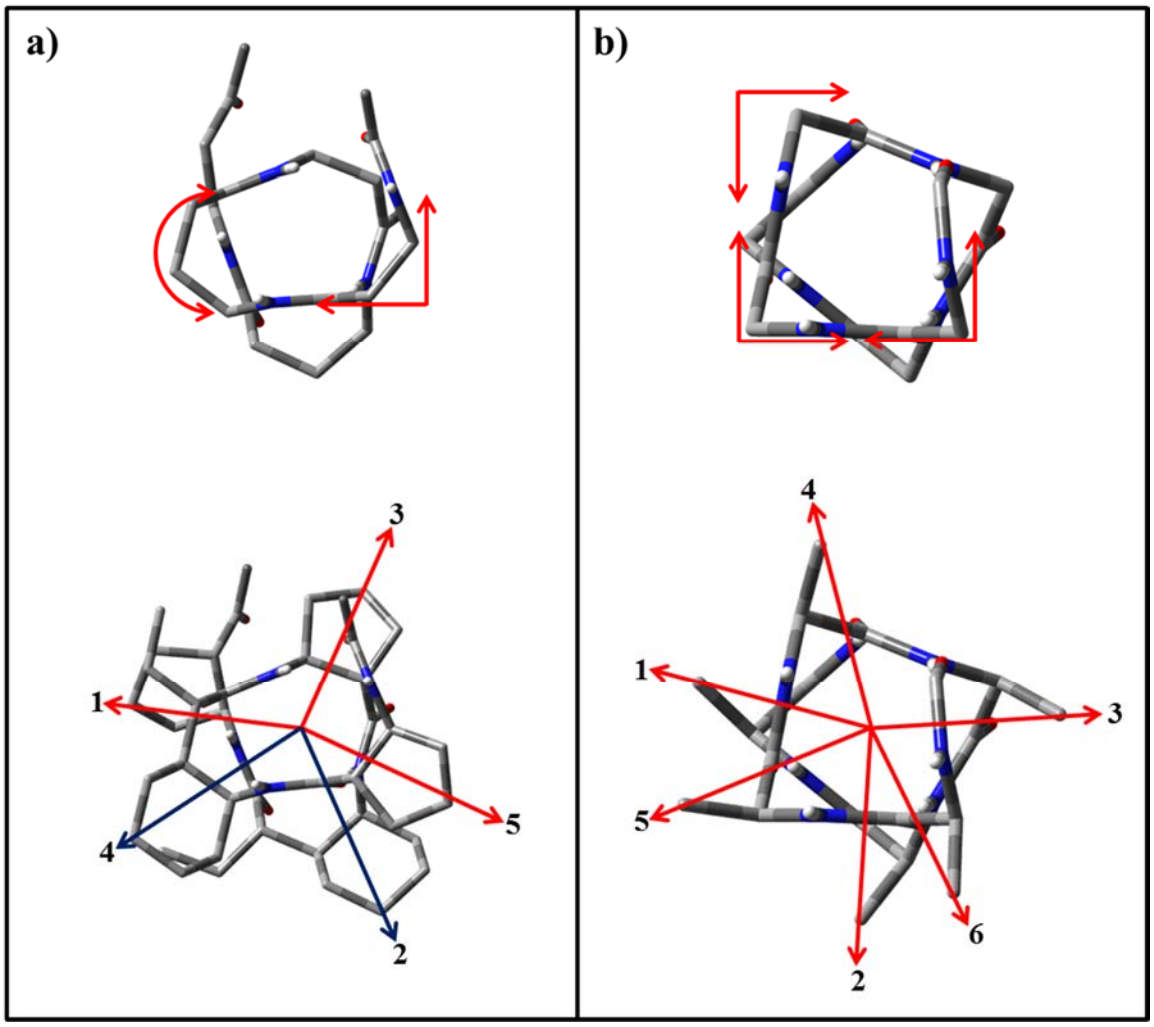

Figure 3.10: Comparison of the backbone (top) and side chain (bottom) arrangements in the β/γ-peptide 13-helix (a) and the α-helix (b). The numbering reflects the side chain sequence from N-terminal to C-terminal. The arrows in the lower portion of both a) and b) show the arrangement of the side chain groups. In the bottom portion of a) the red arrows indicate the position of ACPC groups and the black arrows indicate the position of the ACHC groups.

3.5 Conclusion

Single-conformation spectroscopy of two prototypical β/γ-peptides in the gas phase has provided direct evidence that, in the absence of solvent or intermolecular effects, the inherent structural preferences imposed by the cyclic constraints present in βγ

and γβ are sufficient to lock in the population entirely in a structure held together principally by a single C13 H-bond. This conformation represents the first turn of a β/γ-peptide 13-helix that is closely analogous to the α-helices formed by α-peptides. It will be interesting in future work to extend the gas phase studies to longer β/γ-peptides, in which the combined effects of successive C13 rings show their effects in the NH stretch, amide I, and amide II regions, where they can be compared with the α-helix analogues. The effects of H_2O complexation on the conformational preferences and H-bonded networks formed also would be interesting subjects of future studies. Studies of β/γ-peptide analogues lacking residues with cyclic constraints should reveal the roles played by these constraints in determining the conformational preferences of this heterogeneous foldameric backbone.

3.6 References

1. Ramesh, V. V. E.; Puranik, V. G.; Sanjayan, G. J., Carbohydrate-derived conformationally restricted bicyclic dipeptides as potentilal hetero foldamer building blocks. *Tetrahedron: Asymmetry* 2012, *23*, 1400-1404.

2. James III, W. H.; Baquero, E. E.; Shubert, V. A.; Choi, S. H.; Gellman, S. H.; Zwier, T. S., Single-Conformation and Diastereomer Specific Ultraviolet and Infrared Spectroscopy of Model Synthetic Foldamers: alpha/beta-Peptides. *J. Am. Chem. Soc.* 2009, *131* (18), 6574-6590.

3. Karle, I. L., Hydrogen bonds in molecular assemblies of natural, synthetic and 'designer' peptides. *J. Mol. Str.* 1999, *474*, 103-112.

4. Seebach, D.; Gardiner, J., β-Peptidic Peptidomimetics. *Acc. Chem. Res.* 2008, *41* (10), 1366–1375.

5. Horne, W. S.; Gellman, S. H., Foldamers with Heterogeneous Backbones. *Acc. Chem. Res.* 2008, *41* (10), 1399-1408.

6. Bouillere, F.; Thetiot-Laurent, S.; Kouklovsky, C.; Alezra, V., Foldamers Containing γ–Amino Acid Residues or Their Analogues: Structural Features and Applications. *Amino Acids* 2011, *41*, 687-707.

7. Karle, I. L.; Pramanik, A.; Banerjee, A.; Bhattacharjya, S.; Balaram, P., ω-Amino Acids in Peptide Design. Crystal Structures and Solution Conformations of Peptide Helices Containing a β-Alanyl-γ-Aminobutyryl Segment. *J. Am. Chem. Soc.* 1997, *119* (39), 9087-9095.

8. Baldauf, C.; Gunther, R.; Hofmann, H. J., Helix formation in alpha,gamma- and beta,gamma-hybrid peptides: Theoretical insights into mimicry of alpha- and beta-Peptides. *J. Org. Chem.* 2006, *71* (3), 1200-1208.

9. Araghi, R. R.; Jackel, C.; Colfen, H.; Salwiczek, M.; Volkel, A.; Wagner, S. C.; Wieczorek, S.; Baldauf, C.; Koksch, B., A beta/gamma Motif to Mimic alpha-Helical Turns in Proteins. *Chembiochem* 2010, *11* (3), 335-339.

10. Nyakatura, E. K.; Araghi, R. R.; Mortier, J.; S., W.; Baldauf, C.; Wolber, G.; Koksch, B., An Unusual Interstrand H-Bond Stabilizes the Heteroassembly of Helical αβγ-Chimeras with Natural Peptides. *ACS Chem. Biol.* 2013, *Just Accepted*.

11. Guo, L.; Almeida, A. M.; Zhang, W.; Reidenbach, A. G.; Choi, S. H.; Guzei, I. A.; Gellman, S. H., Helix Formation in Preorganized beta/gamma-Peptide Foldamers: Hydrogen-Bond Analogy to the alpha-Helix without alpha-Amino Acid Residues. *J. Am. Chem. Soc.* 2010, *132* (23), 7868-+.

12. Vasudev, P. G.; Chatterjee, S.; Shamala, N.; Balaram, P., Gabapentin: A Stereochemically Constrained gamma Amino Acid Residue in Hybrid Peptide Design. *Acc. Chem. Res.* 2009, *42* (10), 1628-1639.

13. Baquero, E. E.; James, W. H.; Choi, S. H.; Gellman, S. H.; Zwier, T. S., Single-conformation ultraviolet and infrared spectroscopy of model synthetic foldamers: beta-peptides Ac-beta(3)-hPhe-NHMe and Ac-beta(3)-hTyr-NHMe. *J. Am. Chem. Soc.* 2008, *130* (14), 4784-4794.

14. Baquero, E. E.; James, W. H.; Choi, S. H.; Gellman, S. H.; Zwier, T. S., Single-conformation ultraviolet and infrared spectroscopy of model synthetic foldamers: beta-peptides Ac-beta(3)-hPhe-beta(3)-hAla-NHMe and Ac-beta(3)-hAla-beta(3)-hPhe-NHMe. *J. Am. Chem. Soc.* 2008, *130* (14), 4795-4807.

15. Buchanan, E. G.; James, W. H., III; Gutberlet, A.; Dean, J. C.; Guo, L.; Gellman, S. H.; Zwier, T. S., Single-conformation spectroscopy and population analysis of model gamma-peptides: New tests of amide stacking. *Faraday Discuss.* 2011, *150*, 209-226.

16. James, W. H., III; Buchanan, E. G.; Mueller, C. W.; Dean, J. C.; Kosenkov, D.; Slipchenko, L. V.; Guo, L.; Reidenbach, A. G.; Gellman, S. H.; Zwier, T. S., Evolution of Amide Stacking in Larger gamma-Peptides: Triamide H-Bonded Cycles. *J. Phys. Chem. A.* 2011, *115* (47), 13783-13798.

17. Buchanan, E. G.; James III, W. H.; Choi, S. H.; Guo, L.; Gellman, S. H.; Müller, C. W.; Zwier, T. S., Single-conformation infrared spectra of model peptides in the amide I and amide II regions: Experiment-based determination of local mode frequencies and inter-mode coupling. *J. Chem. Phys.* 2012, *137*, 094301.

18. James III, W. H.; Baquero, E. E.; Choi, S. H.; Gellman, S. H.; Zwier, T. S., Laser Spectroscopy of Conformationally Constrained alpha/beta-Peptides: Ac-ACPC-Phe-NHMe and Ac-Phe-ACPC-NHMe. *J. Phys. Chem. A.* 2010, *114* (3), 1581-1591.

19. Walsh, P. S.; Kusaka, R.; Buchanan, E. G.; James III, W. H.; Fisher, B. F.; Gellman, S. H.; Zwier, T. S., Cyclic Constraints on Conformational Flexibility in γ–Peptides: Conformation Specific IR and UV Spectroscopy. *J. Phys. Chem. A.* 2013, *117*, 12350-12362.

20. James III, W. H.; Buchanan, E. G.; Guo, L.; Gellman, S. H.; Zwier, T. S., Competition between Amide Stacking and Intramolecular H Bonds in gamma-Peptide Derivatives: Controlling Nearest-Neighbor Preferences. *J. Phys. Chem. A.* 2011, *115* (43), 11960-11970.

21. Kusaka, R.; Zhang, D.; Walsh, P. S.; R., G. J.; Fisher, B. F.; Gellman, S. H.; Zwier, T. S., Role of Ring-Constrained Gamma-Amino Acid Residues in Alpha/Gamma-Peptide Folding: Single-Conformation UV and IR Spectroscopy. *J. Phys. Chem. A.* 2013, *117*, 10847-10862.

22. Choi, S. H.; Guzei, I. A.; Spencer, L. C.; Gellman, S. H., Crystallographic characterization of helical secondary structures in alpha/beta-peptides with 1 : 1 residue alternation. *J. Am. Chem. Soc.* 2008, *130* (20), 6544-6550.

23. Choi, S. H.; Guzei, I. A.; Spencer, L. C.; Gellman, S. H., Crystallographic Characterization of Helical Secondary Structures in 2:1 and 1:2 α/β-Peptides. *J. Am. Chem. Soc.* 2009, *131*.

24. Choi, S. H.; Guzei, I. A.; Spencer, L. C.; Gellman, S. H., Crystallographic Characterization of 12-Helicsl Secondary Structure in β-Peptides Containing Side Chain Groups. *J. Am. Chem. Soc.* 2010, *132*.

25. Guo, L.; Chi, Y. G.; Almeida, A. M.; Guzei, I. A.; Parker, B. K.; Gellman, S. H., Stereospecific Synthesis of Conformationally Constrained gamma-Amino Acids: New Foldamer Building Blocks That Support Helical Secondary Structure. *J. Am. Chem. Soc.* 2009, *131* (44), 16018-+.

26. Guo, L.; Zhang, W.; Reidenbach, A. G.; Giuliano, M. W.; Guzei, I. A.; Spencer, L. C.; Gellman, S. H., Characteristic Structural Parameters for the gamma-Peptide 14-Helix: Importance of Subunit Preorganization. *Angew. Chem. Int. Ed.* 2011, *50* (26), 5843-5846.

27. Shubert, V. A.; Baquero, E. E.; Clarkson, J. R.; James, W. H.; Turk, J. A.; Hare, A. A.; Worrel, K.; Lipton, M. A.; Schofield, D. P.; Jordan, K. D.; Zwier, T. S., Entropy-driven population distributions in a prototypical molecule with two flexible side chains: O-(2-acetamidoethyl)-N-acetyltyramine. *J. Chem. Phys.* 2007, *127* (23).

28. Wiley, W. C.; McLaren, I. H., Time-of-Flight Mass Spectrometer with Improved Resolution. *Rev. Sci. Instrum.* 1955, *26* (12), 1150-1157.

29. Mohamadi, F.; Richards, N. G. J.; Guida, W. C.; Liskamp, R.; Lipton, M.; Caufield, C.; Chang, G.; Hendrickson, T.; Still, W. C., Macromodel - an Integrated Software System for Modeling Organic and Bioorganic Molecules Using Molecular Mechanics. *J. Comput. Chem.* 1990, *11* (4), 440-467.

30. Frisch, M. J.; Trucks, G. W.; Schlegel, H. B.; Scuseria, G. E.; Robb, M. A.; Cheeseman, J. R.; Scalmani, G.; Barone, V.; Mennucci, B.; Petersson, G. A.; Nakatsuji, H.; et al. *Gaussian 09*, Revision A.2 Gaussian, Inc., Wallingford CT, 2009.

31. Zhao, Y.; Truhlar, D. G., Density functionals for noncovalent interaction energies of biological importance. *Journal of Chemical Theory and Computation* 2007, *3* (1), 289-300.

32. James III, W. H.; Muller, C. W.; Buchanan, E. G.; Nix, M. G. D.; Guo, L.; Roskop, L.; Gordon, M. S.; Slipchenko, L. V.; Gellman, S. H.; Zwier, T. S., Intramolecular Amide Stacking and Its Competition with Hydrogen Bonding in a Small Foldamer. *J. Am. Chem. Soc.* 2009, *131* (40), 14243-14245.

CHAPTER 4
CONFORMATION-SPECIFIC SPECTROSCOPY OF CAPPED, GAS-PHASE AIB OLIGOMERS: TESTS OF THE AIB RESIDUE AS A 3_{10}-HELIX FORMER

4.1 Introduction

The intrinsic conformational propensities of amino acid residues for promoting (or disrupting) helical secondary structure have been examined computationally[1,2] and experimentally. [3-6] The great majority of proteinaceous helices determined in X-ray crystal structures are right-handed α-helices[7,8], characterized by 3.6 residues per turn and hydrogen-bonded rings of 13 atoms (3.6_{13}-helices) closed by backbone hydrogen-bonding pairs between residues $i + 4 \rightarrow i$ and Ramachandran angles of $\phi, \psi = -60^{o}, -45^{o}$.[7] About 10% of helices found in protein structures are more tightly-wound 3_{10}-helices, with 3.0 residues per turn and rings of 10 atoms closed by $i + 3 \rightarrow i$ backbone hydrogen-bonding partners and Ramachandran angles of $\phi, \psi = -57^{o}, -30^{o}$.[8-10] Although the α-helix is the most commonly found secondary structure, it accounts for only about 30% of residues in protein X-ray structures.[8] Clearly, the forces that favor the development of well-defined helical structures, such as intramolecular hydrogen bonding and inter-residue side-chain packing, are competing against other conformational imperatives. In fact, the balance between these forces can sometimes be tipped by the presence of even a single residue.[11,12]

Aminoisobutyric acid (Aib) is a naturally occurring amino acid containing two side chain methyl groups. The symmetric dimethylation of the α-carbon renders Aib

achiral, similar to glycine. In stark contrast to glycine, which is known to be the residue least supportive of helical structure[1,3-6,10,13], Aib residues are strongly helicogenic; oligomers of Aib are known to induce formation of the 3_{10}-helix in solution and in the condensed phase.[13-16] The Aib residue is found singly and contiguously (up to Aib_4) in the naturally occurring peptaibol family of antimicrobial peptides. The helicogenicity of contiguous Aib residues is believed to allow peptaibols to form helical transmembrane pores essential to their mechanism of antimicrobial activity.[13,15,17]

The vibrational modes of the polar amide functional groups are sensitive to the local electrostatic environment and are consequently diagnostic of protein and peptide secondary structural features such as intramolecular hydrogen bonding. Toniolo and coworkers monitored the onset of helical secondary structure in a series of Aib homopeptides, Z-$(Aib)_n$-OtBu (n = 1-12), by examining the NH stretch (Amide A) region of the infrared.[14] Solvated in deuterochloroform, Z-$(Aib)_n$-OtBu exhibits two Amide A spectral bands, assigned to "free" and "intramolecularly hydrogen bound" NH stretches. With increasing n, the "hydrogen bound" spectral band grows at the expense of the "free" spectral band, converging to a limit of two free NH stretches, characteristic of a 3_{10}-helical bonding pattern.

In a more recent study, Toniolo and Ge employed 2D IR spectroscopy to investigate the C=O stretch (Amide I) spectroscopic features of a series of Aib oligomers (Z-$(Aib)_n$-OtBu, n = 3, 5, 8, 10) dissolved in $CDCl_3$.[18] Although individual modes are not resolvable in $CDCl_3$, estimates of local Amide I frequencies and coupling constants have been obtained through fits of the 2D IR spectral contours. The 2D IR spectra indicate that Amide I spectral features characteristic of 3_{10}-helices emerge as early as n =

5.[18] The isotope-edited Amide I region linear infrared spectra of Kubasik and coworkers, employing ^{13}C-enriched Z-(Aib)$_6$-OtBu isotopologues, reveal localized ^{13}C=O Amide I modes as distinct spectral features at reduced frequencies—an improvement over the broad, unresolved ^{12}C=O Amide I band.[19] These isotope-edited spectra confirm a 3_{10}-helical hydrogen-bonding pattern for Z-(Aib)$_6$-OtBu, since the lowest frequency ^{13}C-localized Amide I oscillators are those that, within a 3_{10} helical hydrogen-bonding pattern, are both hydrogen bond acceptors (at the carbonyl oxygen) and hydrogen bond donors (at the amide group hydrogen). Although ^{13}C-enrichment shifts a ^{13}C-Amide I band to lower frequency, the spectral features in the Amide I and Amide A regions are still inherently broadened by solvent effects.

Under jet-cooled conditions, gas phase spectroscopic studies of peptides offer superior spectral resolution as compared to solvent-broadened condensed phase efforts. Additionally, gas phase studies examine the intrinsic conformational propensities of amino acid residues and peptides by removing subtle structure-supporting aspects of a solvent environment. In a recent study of the glycine homopeptide series Z-(Gly)$_n$-OH with n = 1, 3, 5 and Z-(Gly)$_5$-NHMe, Dean et al. showed that both of the n = 5 oligomers folded exclusively into 14/16 mixed helices in which the C14 and C16 H-bonds point in opposite directions along the peptide backbone. The observed structures exhibit calculated permanent dipole moments of only 2.6 and 2.8 D for the -OH and -NHMe structures, respectively,[20] effectively "canceling" the dipole moments of the individual peptide units, each estimated at 3.46 D. The conformational flexibility of the glycine residue allowed the backbone to adopt a configuration capable of supporting this mixed-

helical architecture, with C7 ($i + 2 \rightarrow i$) H-bonds serving as spacers between the remote C14 and C16 H-bonds.

Gas phase studies have also been carried out to evaluate the competition among different hydrogen-bonding motifs in a series of tetrapeptides capable of forming a variety of intramolecular hydrogen bonds.[21] Mons and coauthors saw competition among structures involving C10 and C7 hydrogen-bonded rings, NH•••π hydrogen-bonded interactions, and 2_7-ribbon structures in their study of Ac-Phe-Ala-Ala-NH_2, Ac-Ala-Ala-Phe-NH_2, and Ac-Ala-Phe-Ala-NH_2.

Additionally, the Mons group has examined a tetrapeptide containing a phenylalanine residue flanked by two Aib residues (Ac-Aib-Phe-Aib-NH_2) under jet-cooled conditions.[22] Two conformers were observed, both of which contained NH stretch transitions due to a pair of C10 H-bonds that are indicative of an incipient 3_{10}-helix. The transitions assigned to the two C10 H-bonds appeared at 3374 cm^{-1} and 3405 cm^{-1} in one conformer, and 3374 cm^{-1} and 3408 cm^{-1} in the other, all lower in frequency than a typical free amide NH (~3470 cm^{-1}).[20,22,23]

The goal of the present study is to investigate more fully the folding propensities and spectroscopic signatures of the series of capped Aib homopeptides shown in Figure 4.1, under cold, isolated conditions in the gas phase. These structures will be referred to in short-hand as Z-$(Aib)_n$-X (n = 1, 2, 4 and X = OH [for n = 1 only] or OMe). The benzyloxycarbonyl (Z) cap provides the necessary UV chromophore for carrying out single-conformation spectroscopy, while retaining a pure Aib homopeptide backbone. The present work examines the intrinsic conformational propensities of the Aib residue and contiguous Aib units, elaborated as short homo-oligomers. By cooling the molecule

in a supersonic expansion, the present work probes the lowest energy conformations of these homopeptides in their isolated form, unperturbed by solvent or solid state intermolecular interactions. Single-conformation IR spectra are compared to the predictions of DFT calculations, leading to assignments that identify the preferred conformations of the molecules in this series, and spectroscopically characterize them in the ultraviolet (UV) and infrared (IR).

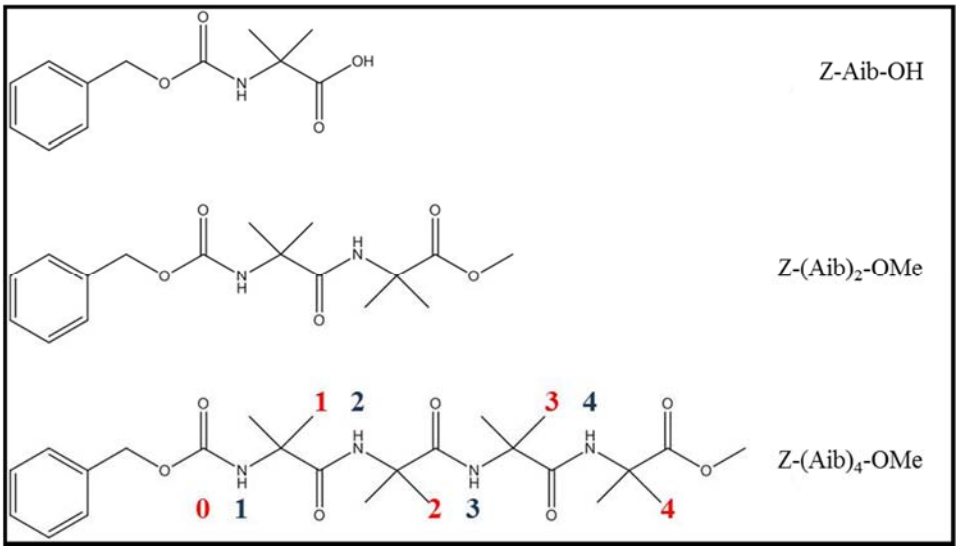

Figure 4.1: The complete series of capped Aib homopeptides investigated in this study. C=O groups have been numbered in red and NH groups have been numbered in blue, in both cases from N- to C-terminus with 0 indicating the C=O in the Z-cap.

4.2 Methods

4.2.1 Experimental Methods

Samples were laser desorbed into the gas phase from the surface of a graphite rod using the 1064 nm output from a Nd:YAG laser (Continuum MiniLite).[24] Laser pulses were approximately 6 ns in duration with 3-5 mJ of energy per pulse. The desorption rod

was translated linearly using a pusher motor during data collection to ensure that fresh sample was available throughout each scan. This laser desorption scheme has been described in detail elsewhere.[20,25] After being desorbed, the gas-phase sample molecules were entrained in an expansion of argon gas coming from a Parker Fluidics, Series 9 general valve with a 500-800 μm nozzle diameter operating at 20 Hz with approximately 5.5 bar of backing pressure. Sample molecules were then collisionally cooled in a supersonic expansion, funneling their population into the zero-point vibrational energy levels of the most stable conformers.[26-28] Downstream, the seeded expansion was passed through a 3 mm skimmer to form a molecular beam which was interrogated using single- and double-resonance laser schemes in the ionization region of a Wiley McLaren, time-of-flight mass spectrometer.[29]

Resonant two-photon ionization (R2PI) was used to record the electronic excitation spectra for the molecules of interest. Scans over the 35,000 cm^{-1} to 38,000 cm^{-1} region were recorded using the doubled output of a Radiant Dyes, NarrowScan dye laser pumped by 355 nm light from a Continuum, SureLite II, Nd:YAG laser. When UV light from the dye laser is resonant with a vibronic transition between the S_0 and S_1 states of a given conformation, a first photon is absorbed which promotes the molecule to the excited state; upon immediate absorption of a second photon, the molecule is ionized. By tuning the UV laser over a range of wavelengths characteristic of the Z-cap UV chromophore, the vibronic spectrum of all conformations present in the jet can be recorded.

A KTP/KTA-based infrared parametric converter (LaserVision) was used to generate IR light in the NH and OH stretch regions (3200 cm^{-1} to 3700 cm^{-1}) with typical

output energies on the order of 12-15 mJ/pulse. When desired, a $AgGaSe_2$ crystal was used to difference frequency mix into the mid-infrared, in order to generate light in the 1600 cm^{-1} to 1800 cm^{-1} region which encompasses the Amide I (C=O stretch) fundamentals.[30] Typical output energies in the Amide I region were on the order of 500-1000 μJ/pulse.

Single-conformation IR spectra were recorded using resonant ion-dip IR spectroscopy (RIDIRS).[30,31] In RIDIRS, the UV laser, operating at 20 Hz, has its wavelength fixed on a vibronic transition belonging to a single conformer, selected from the R2PI spectrum, in order to generate a constant level of ion signal. The 10 Hz, infrared beam is spatially overlapped with, but temporally precedes the UV beam. When the IR laser is resonant with a vibrational transition belonging to the same conformation that is being pumped with the UV laser, some of the population is moved out of the vibrational zero-point level and promoted to a vibrationally excited level within the ground electronic state, thus the total number of molecules available for the UV laser to ionize is decreased, and a dip in the total ion signal is observed. By performing active baseline subtraction on each pair of "IR on" and "IR off" peaks with a Stanford Research Systems gated integrator (SR-250), a spectrum can be recorded in which the fractional depletion in ion signal is plotted as a function of IR frequency.

Once the R2PI and RIDIR spectra have been recorded, IR-UV hole-burning (HB) spectroscopy can be used to separate the R2PI spectrum into a set of conformer-specific UV spectra.[30] To collect these IR-UV HB spectra, the wavelength of the IR laser is fixed on a vibrational transition belonging to a specific conformation, and the wavelength of the UV laser is scanned. By implementing the same timing and overlap schemes

described in RIDIRS, and performing active baseline subtraction, the fractional depletion of the ion signal versus UV frequency can be recorded to obtain single-conformation UV spectra.

4.2.2 Computational Methods

The results of DFT calculations are used to assist in making structural assignments of the observed IR spectra. To obtain these computational results, a starting structure is submitted to a conformational search performed at the Amber* force field[32] level within a 100 kJ/mol energy window using MacroModel (Schrödinger, Inc.).[32,33] The lowest energy outputs of the conformational search are re-optimized to calculate geometries and harmonic IR frequencies and intensities at the DFT level in Gaussian09[34] using the M05-2X functional and a 6-31+G(d) basis set.[35] The outputs of these calculations are scaled according to well established, functional-specific scale factors of 0.940 in the NH and OH stretching regions and 0.960 in the Amide I region, to account for anharmonic effects.[20,36-38]

4.2.3 Synthetic Methods

Commercially available starting materials Aib (Acros), Z-Aib-OH (Bachem) and HCl•Aib-OtBu (Bachem) were used as received. HCl•Aib-OMe was prepared from MeOH and trimethylsilyl chloride.[39] Aib dimers, Z-$(Aib)_2$-OtBu and Z-$(Aib)_2$-OMe, were prepared using EDCI as a coupling reagent at 60°C in a CEM Discover SP microwave reactor for 30 minutes.[40] These two dimers were used to prepare Z-$(Aib)_4$-

OMe via literature methods.[14] Z-$(Aib)_2$-OMe and Z-$(Aib)_4$-OMe were purified via flash silica gel chromatography.

4.2.4 Nomenclature

Analysis of the single-conformation data employs the amide group numbering scheme shown in Figure 4.1. In this scheme, NH groups are labeled 1-4 and C=O groups are numbered from 0-4 beginning at the N-terminal carbamate group of the Z-cap and extending to the C-terminus. Hydrogen-bonded rings are named according to the number of atoms in the cycle closed by the H-bonding interaction. For example, a ten-atom cycle formed by an intramolecular hydrogen bond is labeled as 'C10'. To describe the hydrogen-bonding architecture of the conformations, a notation analogous to that used by Mons and co-workers[41] is implemented in which the hydrogen-bonding behavior of NH groups will be represented from N- to C-terminus by either "F" meaning a free NH, uninvolved in an intramolecular hydrogen bond, or "n", where "n" is the number of atoms in the resulting hydrogen-bonded ring. So, for example, a structure having 4 NH groups might be described as F-F-10-10 meaning the NH groups from N- to C-terminus are free, free, C10, and C10.

4.3 Results

4.3.1 Z-Aib-OH

Resonant two-photon ionization (R2PI) and IR-UV hole-burning spectra for Z-Aib-OH are shown in Figure 4.2(a). The R2PI spectrum contains a single dominant

feature at 37602 cm^{-1} and two minor features at 37576 cm^{-1} and 37619 cm^{-1}. The IR-UV HB spectra identify the 37602 cm^{-1} and 37576 cm^{-1} transitions as S_0-S_1 origin transitions for two distinct conformations of Z-Aib-OH, labeled A and B, respectively. The peak at 37619 cm^{-1} is identified as a vibronic band, tentatively assigned to a butterfly motion of conformer A, involving the ring and backbone, based upon our IR assignments discussed below. The origin of conformer A is shifted just 1 cm^{-1} from the origin transition for Z-Gly-OH studied by Dean, et al. (37601 cm^{-1}). Additionally, the assigned vibronic activity is nearly identical to that for Z-Gly-OH suggesting that the two structures are very similar, with nearly equivalent environments for the Z-cap.[20]

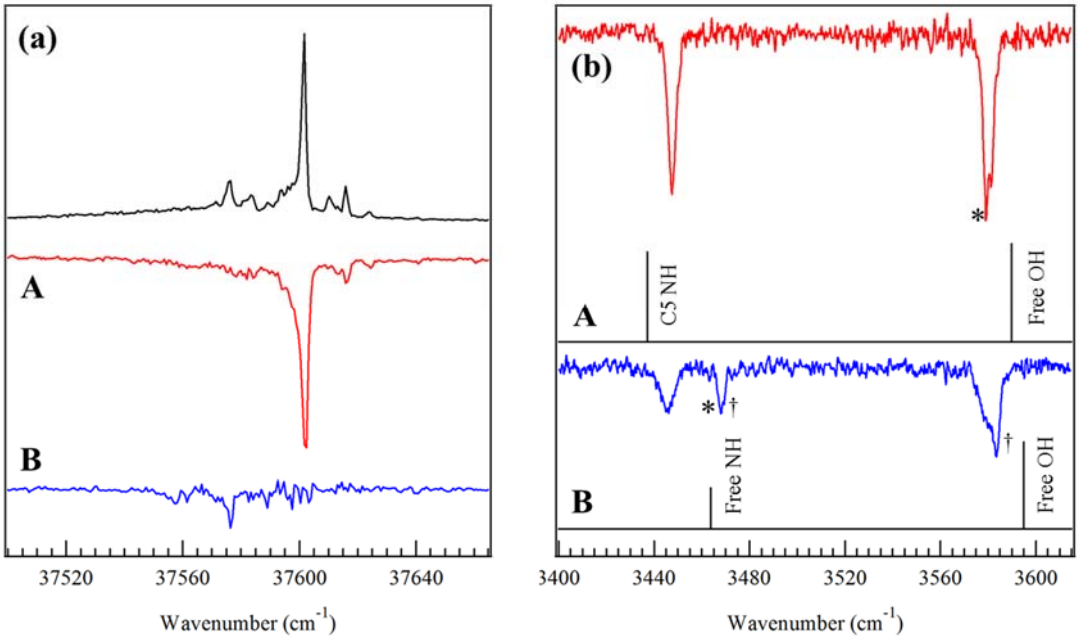

Figure 4.2: (a) R2PI (black) and IR-UV hole-burning spectra (red for A and blue for B) for Z-Aib-OH. Hole-burning spectra were recorded with the IR hole-burn laser fixed at 3579 cm^{-1} for A, and 3468 cm^{-1} for B. (b) RIDIR spectra for conformers A and B of Z-Aib-OH in the NH and OH stretch region. Scaled (*0.94), harmonic vibrational frequencies and infrared intensities for the assigned structures are shown as stick spectra below the experimental data, calculated at the DFT M05-2X/6-31+G(d) level of theory. The daggers indicate transitions specific to conformer B. Asterisks indicate frequencies used for IR-UV hole-burning experiments. See text for further discussion.

Resonant ion-dip infrared spectroscopy was used to record conformer-specific IR spectra in the NH and OH stretch regions for both conformers of Z-Aib-OH. The experimental spectra are compared with calculated, scaled, harmonic frequencies and IR intensities, depicted as stick spectra, in Figure 4.2(b). The RIDIR spectrum for conformer A shows two well-resolved transitions in the NH/OH stretching region. Comparison to computational results allows us to assign the transition at 3447 cm^{-1} to a C5 hydrogen-bonded NH group. The second transition, located at 3579 cm^{-1}, is assigned to a free OH stretch in the carboxylic acid group. The RIDIR spectrum for conformer B

is unusual in that it has two broadened transitions centered near those of conformer A as well as a pair of sharp transitions at 3468 cm^{-1} and 3583 cm^{-1}, (marked with daggers in Figure 4.2(b)). It is likely that the frequency of the UV monitor transition has contributions both from conformer B (responsible for the sharp transitions) and from a hot band of conformer A (responsible for the broadened bands centered on the transitions due to conformer A).

The assigned structures for conformers A and B are shown in Figure 4.3, and key structural parameters are summarized in Table 4.1. Conformer A is calculated to be the global minimum, among all computed structures, and contains an extended C5 interaction between the NH and C=O groups that span the Aib residue with ϕ, ψ = 180°, 180° and a *cis* carboxylic acid OH group. Conformer B is assigned to a significantly different structure in which neither of the C=O groups nor the NH group engage in hydrogen bonding. Instead, the steric crowding of the dimethylated α-carbon causes the two amide groups to orient with ϕ, ψ = -49°, -37°, values close to those found in a 3_{10}-helix.[10] Additionally, parallel alignment of the C=O groups produces a dipole moment that is twice the magnitude observed for conformer A (3.3 D in conformer B vs 1.5 D in conformer A). Since neither conformer contains an interaction between the carboxylic acid group and any other hydrogen-bonding sites along the backbone, we surmise that the methyl ester derivative (not studied here) would likely prefer similar structures, enabling direct comparison of the present Z-Aib-OH results with the methoxy-capped Z-$(Aib)_n$-OMe molecules with n = 2, 4.

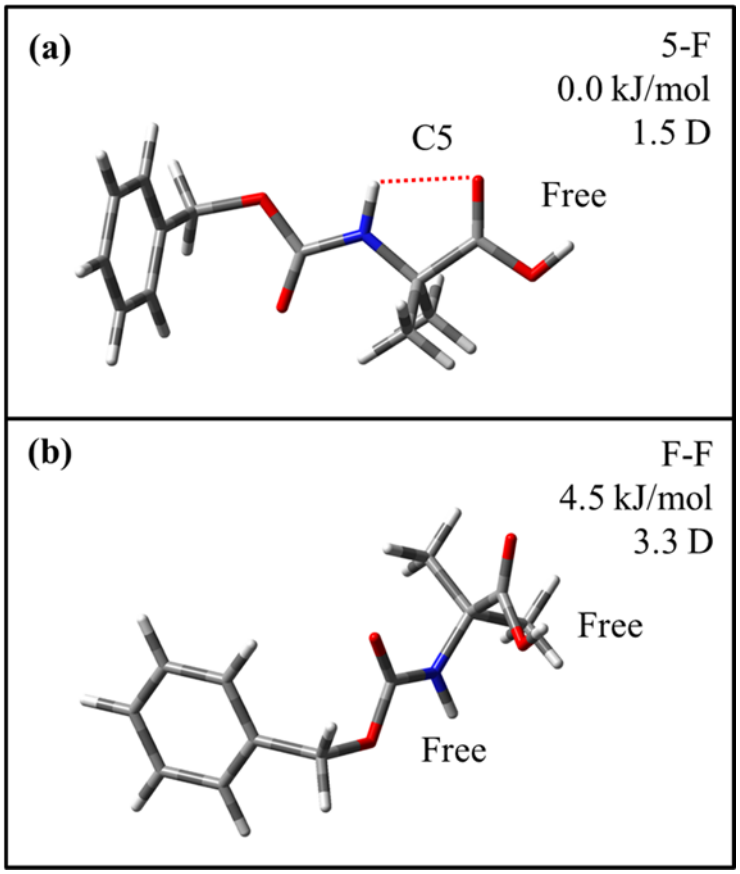

Figure 4.3: (a) Assigned structure for conformer A of Z-Aib-OH. The dotted red line indicates a C5 hydrogen-bonding interaction. (b) Assigned structure for conformer B of Z-Aib-OH. Structural families, computed (M05-2X/6-31+G(d)) relative energies (kJ/mol), and dipole moments (D) for the two conformers are listed.

4.3.2 Z-$(Aib)_2$-OMe

The R2PI and IR-UV HB spectra for Z-$(Aib)_2$-OMe are shown in Figure 4.4(a). Most of the intensity in the R2PI spectrum appears below 37500 cm^{-1}, significantly lower in energy than either of the origins for the two conformers of Z-Aib-OH (37602 and 37576 cm^{-1}). IR-UV hole-burning spectra identify three conformations labeled A, B, and C shown in red, blue, and green, respectively. The S_0-S_1 origin of conformer A is assigned to the peak at 37436 cm^{-1}. The hole-burning spectra for conformers B and C were a challenge to record due to the small intensity of their transitions relative to those

of conformer A, requiring significant signal averaging to pull their transitions out of the background. Therefore, it is difficult to identify the S_0-S_1 origin of conformer B with certainty, and the transition at 37545 cm^{-1}, the first transition relatively free of interference that shows up clearly in the R2PI spectrum, was used for RIDIRS. The S_0-S_1 origin of conformer C at 37604 cm^{-1}, is within 2 cm^{-1} of the origin for conformer A of Z-Aib-OH, indicating that the phenyl ring is likely located in an environment similar to the phenyl ring environment in conformer A of Z-Aib-OH.

The R2PI spectrum for Z-$(Aib)_2$-OMe is much more congested than that of Z-Aib-OH, due to the presence of several conformers and/or much stronger Franck-Condon activity in low-frequency modes. Specifically, a clear progression of peaks is seen in conformer A, beginning at 37436 cm^{-1}, with members separated by approximately 13 cm^{-1}. Vibrational assignments, discussed below, indicate that this progression is caused by an in-phase rocking motion involving the phenyl ring and the C-terminal end of the backbone.

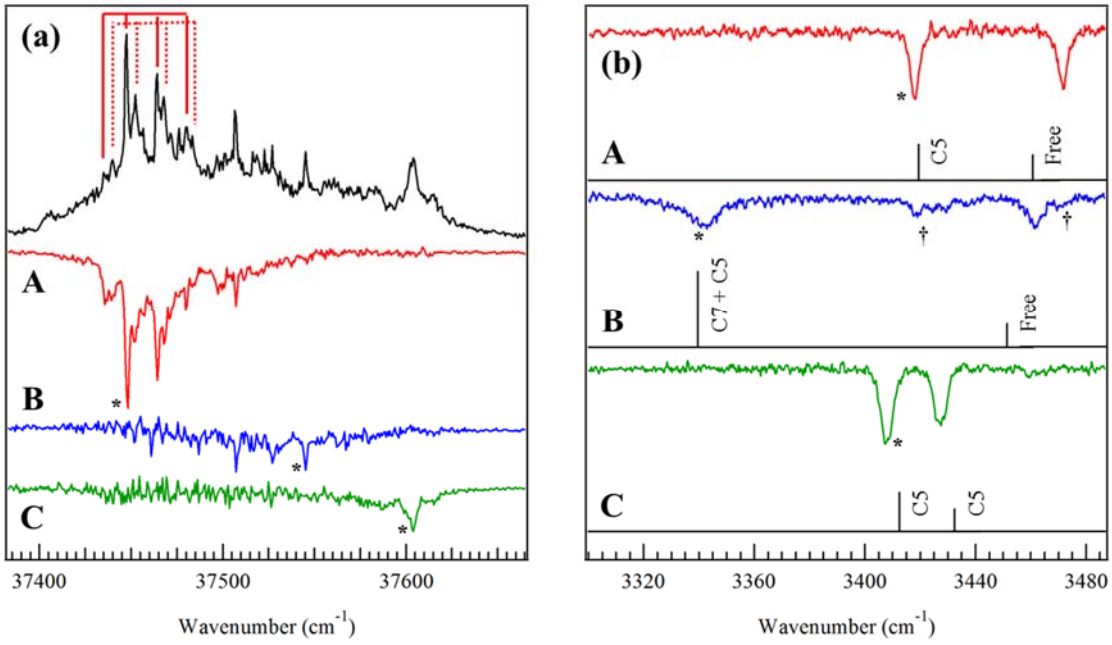

Figure 4.4: (a) R2PI (black) and IR-UV hole-burning spectra for conformers A, B, and C of Z-$(Aib)_2$-OMe. The hole-burning spectra were recorded with the IR hole-burning laser fixed at 3418 cm^{-1} for A, 3342 cm^{-1} for B, and 3407 cm^{-1} for C, marked with asterisks in (b). (b) RIDIR spectra for conformers A, B, and C of Z-$(Aib)_2$-OMe in the NH stretch region. Scaled (*0.94), harmonic, vibrational frequencies and infrared intensities for the assigned structures calculate at the M05-2X/6-31+G(d) level of theory are shown as stick spectra below experiment. Transitions used to record RIDIR spectra are marked with asterisks in (a).

Figure 4.4(b) presents RIDIR spectra of the three conformers of Z-$(Aib)_2$-OMe, recorded over the 3300-3500 cm^{-1} region where the amide NH stretch fundamentals are known to appear. Methoxy substitution removes the carboxylic acid OH, so scans above 3500 cm^{-1} were not necessary. The three IR spectra show distinct patterns characteristic of three structural types. Calculated (M05-2X/6-31+G(d)), scaled (*0.940), harmonic frequencies and IR intensities are shown below the experimental data as stick spectra.

The RIDIR spectrum of conformer A shows two well-resolved NH stretch fundamentals at 3418 cm^{-1} and 3472 cm^{-1}. The higher-frequency transition at 3472 cm^{-1}

is identified as the free stretch of the NH of the carbamate group resulting from the Z-cap. The lower-frequency peak at 3418 cm^{-1} is assigned to a C5 hydrogen-bonded NH stretch fundamental of the interior amide group. This peak is shifted significantly (-29 cm^{-1}) from the position of the assigned C5 NH stretch in the IR spectrum of Z-Aib-OH conformer A. The C5 structure of Z-Aib-OH contains an NH from a carbamate group, while the C5 structure of Z-$(Aib)_2$-OMe, conformer A, contains an NH of an amide group. Conformer A is thus assigned to the F-5 structure shown in Figure 4.5(a).

In the IR spectrum of conformer B, small transitions marked with daggers in Figure 4.4(b) appear at frequencies due to the two transitions of A, indicating a small overlap with a vibronic transition of conformer A at the UV wavelength chosen. Unique IR transitions at 3343 cm^{-1} and 3461 cm^{-1} are due to conformer B. The higher-frequency transition at 3461 cm^{-1} is assigned to the free (N-terminal) NH group, while the lower-frequency 3343 cm^{-1} peak is assigned to the central amide NH group that engages simultaneously in C7 and C5 hydrogen bonds with the Z-cap (carbamate) carbonyl and the C-terminal methyl ester carbonyl, respectively. The frequency of this NH stretch is close to that of other pure C7 hydrogen-bonded rings.[20,42] The stick diagram shows the calculated, scaled spectrum that best matches the experimental spectrum, arising from an F-7/5, bifurcated double-ring structure, shown in Figure 4.5(b).

The IR spectrum for conformer C contains two clearly resolved NH stretch fundamentals appearing at 3407 cm^{-1} and 3427 cm^{-1}. The computed structure that offers the best match to this experimental spectrum exhibits two C5 hydrogen-bonded NH groups. As previously observed, the phenyl ring adopts an orientation similar to the extended structure (conformer A) of Z-Aib-OH, consistent with the electronic origins of

these two structures being nearly identical. This structure is assigned as a fully-extended 5-5 structure. The N-terminal (carbamate) NH group is assigned to the lower-frequency transition at 3407 cm^{-1}, and the central amide NH group is assigned to the higher-frequency transition at 3427 cm^{-1}. This fully extended structure minimizes interaction between the side chains, backbone, and phenyl ring and has a dipole moment of 4.6 D. This is in line with the dipole moments calculated by Dean et al. for analogous extended structures of Z-Gly_n-OH.[20]

The assigned structures for conformers A-C, shown in Figure 4.5, possess the ϕ and ψ dihedral angles summarized in Table 4.1. It is noteworthy that the F-5 structure of conformer A, which is the global minimum structure, possesses Ramachandran angles (ϕ, ψ = -57°, -38°) about Aib[1] that are near those found in an idealized 3_{10}-helix (ϕ, ψ = -57°, -30°). The Ramachandran angles of Aib[2] allow for a C5 hydrogen-bonded structure. This same C-terminal C5 structure is found in the other two conformers, most likely because the C-terminal methyl ester possesses no NH group to participate in hydrogen bonding. The only other unique Ramachandran angles are those associated with the C7 γ-turn (ϕ_1, ψ_1 = +72°, -70°), which despite its strong H-bond (ν_{NH} = 3342 cm^{-1}) has an energy +7.2 kJ/mol above the F-5 structure.

The significantly shifted electronic origins of conformers A and B as well as the extensive low-frequency vibronic activity observed in their R2PI spectra lend additional support to the conformational assignments in Figure 4.5. Both structures fold the C-terminal end of the peptide back over the Z-cap, enabling a strong interaction so that upon π–π^* excitation, Franck-Condon activity is evident involving the low-frequency motions of the peptide backbone, ($\nu \sim 13$ cm^{-1}) against the aromatic ring.

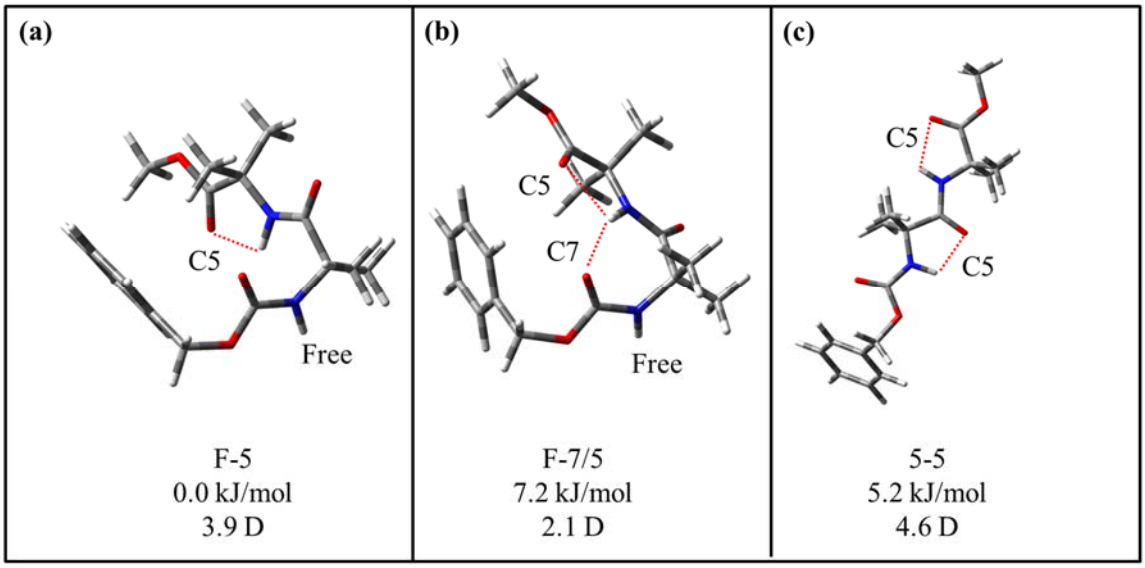

Figure 4.5: (a), (b), and (c) show the assigned structures for conformers A, B, and C of Z-(Aib)$_2$-OMe. Hydrogen bonds are indicated with dotted red lines. Structural families, relative energies (kJ/mol), and dipole moments (D) are listed.

4.3.3 Z-(Aib)$_4$-OMe

Figure 4.6 presents the R2PI and IR-UV hole-burning spectra of Z-(Aib)$_4$-OMe. The R2PI spectrum for Z-(Aib)$_4$-OMe shows significantly less congestion than that of Z-(Aib)$_2$-OMe. Even so, three unique conformations having origin transitions located at 37581 cm^{-1}, 37434 cm^{-1}, and 37629 cm^{-1} were identified based on hole-burning data, and are labeled A, B, and C, respectively. Based on the intensities of the S_0-S_1 origin transitions in the R2PI spectrum, conformer A appears to be the dominant conformation. The origin transition for conformer B appears only 2 cm^{-1} lower than the A origin in Z-(Aib)$_2$-OMe, suggesting a similar phenyl ring environment. Single-conformer UV spectra (lower traces of Figure 4.6) were obtained for conformers A and B. (Note that the feature in the IR-UV HB spectrum of conformer B which appears at a frequency identical to the origin transition of conformer A is due to incomplete subtraction in the gated

integrator.) However, a similar spectrum for conformer C was not available due to the weak intensity of its transitions. Instead, conformer C was identified by virtue of the fact that it was unaccounted for in the hole-burning scans of A or B, and by its possession of a unique IR spectrum.

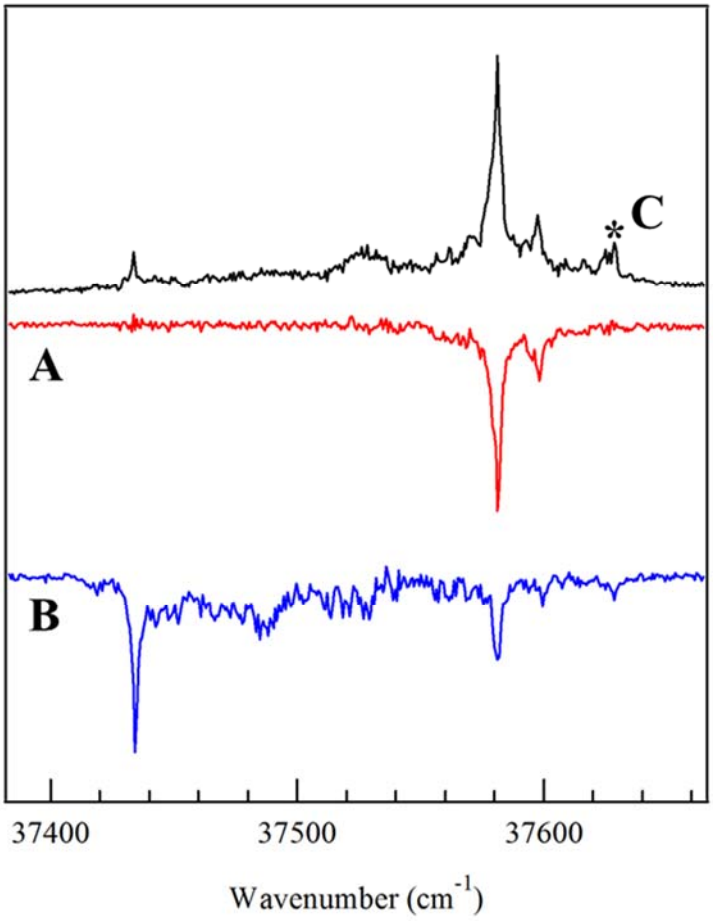

Figure 4.6: R2PI (black) and IR-UV hole-burning spectra for conformers A (red) and B (blue) of Z-$(Aib)_4$-OMe. The hole-burning spectra were recorded with IR hole-burning laser fixed at 3406 cm^{-1} for A, 3383 cm^{-1} for B, marked with asterisks in Figure 4.7(b).

RIDIR spectra of all three conformations collected in the C=O and NH stretching regions are shown in Figure 4.7(a) and 4.7(b), respectively. As with the peptides

examined above, calculated (M052X/6-31+G(d)), scaled(*0.940), harmonic frequencies and infrared intensities for the assigned conformers are shown below each experimental spectrum. A good spectral match between a computed spectrum for a low-energy conformer and the experimental spectrum with four NH stretch transitions, occurring as two closely-spaced pairs, allows us to assign two lower-frequency H-bonded NH fundamentals (3383 cm^{-1} and 3406 cm^{-1}) and two free NH stretch fundamentals (3464 cm^{-1} and 3478 cm^{-1}).

The calculated spectrum for the assigned structure associates a pair of C10-hydrogen-bonded NH groups with the low-frequency pair (3383 cm^{-1} and 3406 cm^{-1}), classifying the structure as F-F-10-10. The H-bonded NH stretch fundamentals appear within a few cm^{-1} of those found for the C10/C10 pair in the F-F-10-10 structure of Ac-Aib-Phe-Aib-NH_2 studied by Mons and co-workers.[22] This pattern of transitions indicates the first stages of a prototypical 3_{10}-helical structure in Z-$(Aib)_4$-OMe. Indeed, now all four Aib residues adopt local configurations characteristic of a full turn of a 3_{10}-helix (Table 4.1), with Ramachandran angles (ϕ, ψ) = (-61º, -27º), (-57º, -22º), (-57º, -35º), and (-48º, -40º). The slight variation of the ϕ, ψ angles of the C-terminal Aib residue is not surprising in light of the fact that the C-terminal ester group, lacking the capacity to function as a hydrogen-bonding donor, does not support the formation of additional hydrogen bonds.

Our calculated assignment for conformer A of Z-$(Aib)_4$-OMe is supported by the IR spectrum in the Amide I region shown in Figure 4.7(a), which shows two closely spaced sets of transitions occurring at 1701 cm^{-1} / 1707 cm^{-1} and 1727 cm^{-1} / 1739 cm^{-1}, as well as a single higher-frequency stretch at 1762 cm^{-1}. Assignments in the Amide I

region are complicated by the different functional groups (carbamate, amide, and ester) containing a C=O, and the coupling between C=O groups in the helix, which delocalizes the vibrational modes across more than one carbonyl. The labels in the figure identify the dominant contributor to each transition and the resulting hydrogen-bonded structure. These assignments match nicely with our established understanding of the Amide I region. Specifically, C=O groups involved in hydrogen bonding are shifted down in wavenumber from their otherwise free position. Note that ester and carbamate groups have C=O stretch fundamentals that are inherently higher in frequency by ~50 cm^{-1} than their amide C=O counterparts.[18] This difference in site frequencies of the various functional groups explains why a carbamate C=O appears at a higher frequency than a free, interior C=O, even though it participates in a hydrogen bond.

The range of calculated frequencies and intensities for the Amide I normal modes shown in Figure 4.7(a) reflects the variety of local electrostatic environments surrounding individual amide oscillators as well as the inter-amide coupling between local oscillators that gives rise to delocalized Amide I normal modes. Our gas phase spectra and their conformational assignments provide good tests for Hessian analysis, which seeks to extract local mode frequencies and inter-amide coupling constants.[43] Additionally, our solvent-free system could provide verification and/or calibration of the growing number of electrostatic maps, which have been developed for the purpose of Amide I band spectral prediction.[44]

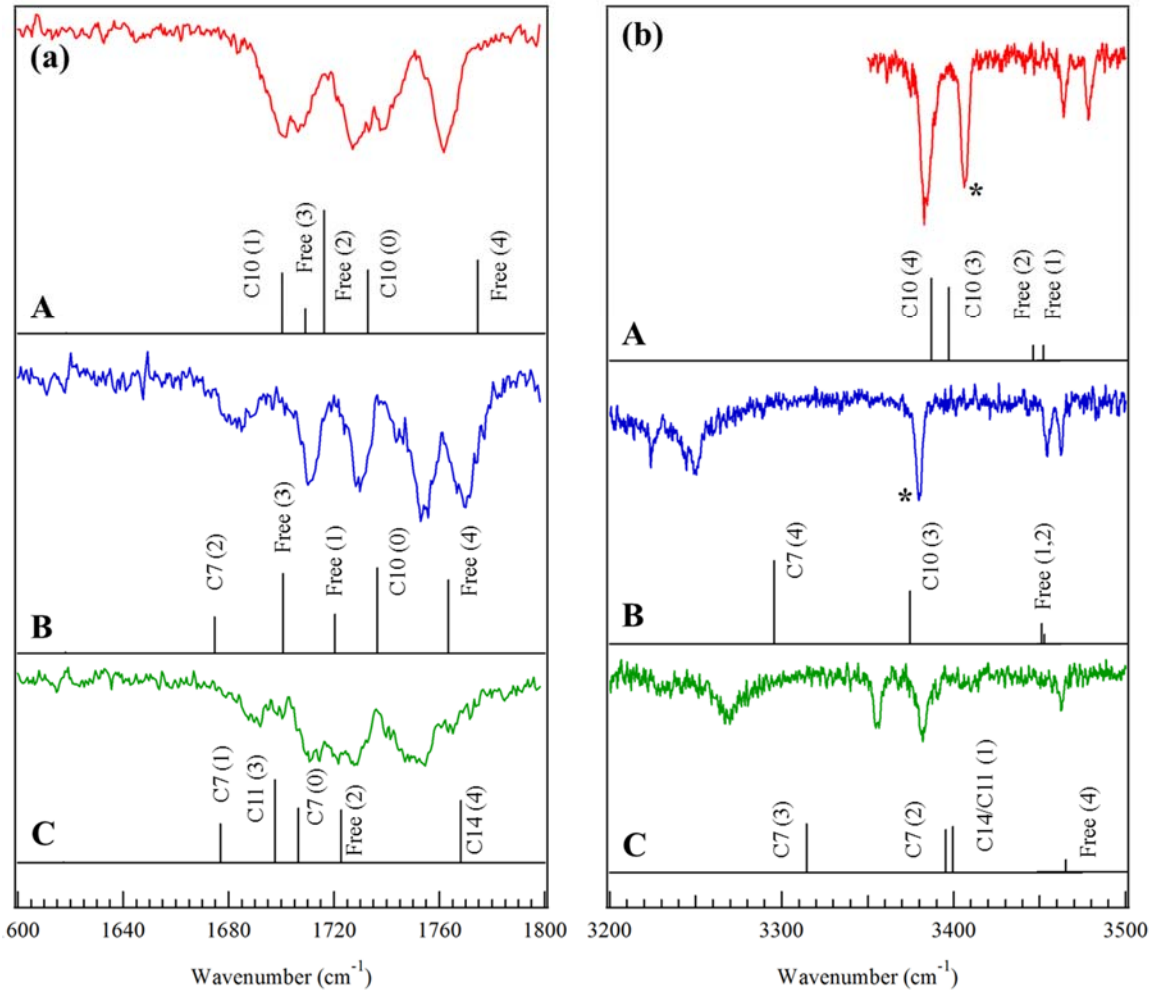

Figure 4.7: RIDIR spectra for conformers A, B, and C or Z-(Aib)$_4$-OMe in the (a) Amide I region and (b) NH stretch region. Asterisks indicate the transitions used for IR-UV hole-burning in Figure 4.6. Calculated, scaled (*0.94), harmonic, vibrational frequencies and infrared intensities for the assigned structures are shown as stick spectra below experiment.

The RIDIR spectrum of conformer B in the NH stretch region is shown as the middle trace (blue) in Figure 4.7(b). A good match with the calculated NH frequencies of an energy-minimized structure allows us to assign two higher-frequency, free NH stretch transitions, 3454 cm^{-1} and 3463 cm^{-1}, a single C10 H-bonded NH stretch transition, 3380 cm^{-1}, and a C7 hydrogen-bonded NH to the strongly shifted and broadened set of peaks near 3250 cm^{-1}. The calculated stick spectrum and the

experimental spectrum match well, leading to an assignment of conformer B to the F-F-10-7 structure shown in Figure 4.8(b). The higher-frequency free NH stretch, 3464 cm^{-1}, is due to the N-terminal carbamate NH. The transition at 3250 cm^{-1} is assigned to an NH participating in a C7 H-bond, which is calculated to have an NH•••O=C H-bond distance of just 1.94 Å, leading to its large shift of more than 120 cm^{-1} below the C10 NH stretch. This structure is intriguing, as it shares much in common with the F-F-10-10 structure of conformer A, but formally exchanges a final C10 H-bond for a C7. We will return in the discussion to a further consideration of this structure and its relationship to the 3_{10}-helix.

The good match between the experimental IR spectrum of conformer B in the Amide I region, Figure 4.7(a), with the calculated spectrum of the energy minimized structure confirms the assignment of an F-F-10-7 structure. The lowest frequency C=O stretch transition at 1681 cm^{-1} belongs primarily to the strongest hydrogen-bonded C=O [2] which is involved in a tight C7 hydrogen-bonded ring. This oscillator is also coupled to the free C=O stretch of the adjacent C=O[3] at 1710 cm^{-1}. The band at 1729 cm^{-1} is a free, interior C=O[1]. The C10 carbamate C=O[0] and free, ester C=O[4] are the two highest frequency Amide I fundamentals appearing at 1754 cm^{-1} and 1770 cm^{-1}. As discussed previously, the carbonyl stretch of the carbamate is a comparatively high frequency feature, despite its participation in hydrogen bonding.

Finally, the RIDIR spectrum for conformer C of Z-$(Aib)_4$-OMe in the NH stretch region is shown in green in Figure 4.7(a). The spectrum is unique, with a single free NH stretch at 3462 cm^{-1}, two intermediate-strength H-bonds, 3355 cm^{-1} and 3382 cm^{-1}, and a strong H-bond at 3270 cm^{-1}. The structure tentatively assigned to conformer C is shown in Figure 4.8(c), labeled as 14/11-7-7-F, with a predicted IR spectrum given in the stick

diagram below the experimental spectrum. The transition occurring at 3270 cm^{-1} is due to the strong C7[NH1] H-bond. The pair of transitions at 3355 cm^{-1} and 3382 cm^{-1} are delocalized combinations of the C14/C11 bonded NH and the NH involved in the weaker of the two C7 rings. The Amide I region of conformer C, Figure 4.7(a), is less well-resolved than Amide I regions of the other two conformers, having four broad bands centered around 1690 cm^{-1}, 1712 cm^{-1}, 1728 cm^{-1}, and 1752 cm^{-1}. The missing fifth band is likely hidden under the breadth of one of these other, much broader bands. The observed transitions are consistent with the stick diagram predicted for the assigned structure, which predicts the major C=O groups responsible for each absorption shown in the figure.

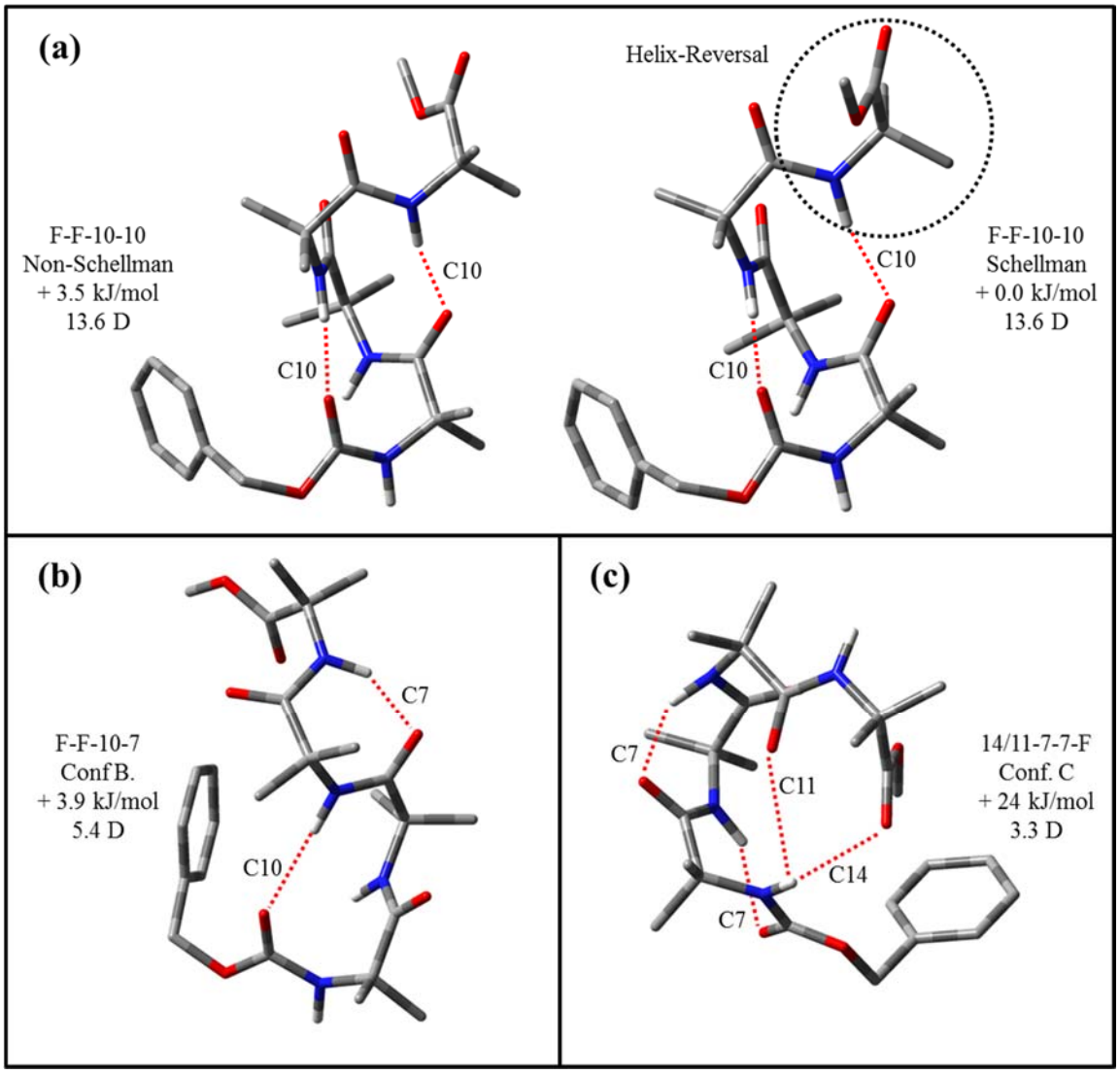

Figure 4.8: Assigned structures for conformers A, B, and C of Z-(Aib)$_4$-OMe. Both the Schellman and non-Schellman versions of conformer A have been shown. The dotted circle indicates the location of the Schellman helix reversal. Hydrogen-bonding interactions are shown with dotted red lines. Structural families, relative energies (M052X/6-31+G(d) , kJ/mol), and dipole moments (D) are listed. Non-amide hydrogen atoms have been removed for clarity.

4.4 Analysis and Discussion

The goal of this study is to evaluate the structural preferences of a series of Aib-based homopeptides of increasing size in the gas phase to determine whether their 3_{10}-helix forming propensity carries over from solution to the gas phase. We seek to extract

and evaluate the spectroscopic signatures of the 3_{10}-helix, if it is formed, identify possible competing structures, and understand how the Aib residue influences them.

Our Aib homopeptides (Z-Aib-OH, Z-$(Aib)_2$-OMe, and Z-$(Aib)_4$-OMe) vary in their propensity to adopt dihedral angles in the 3_{10}-helical region of the Ramachandran plot ($\phi \sim -57°$, $\psi \sim -30°$), and in their capacities to form a C10 hydrogen bond (i.e., $i \rightarrow i + 3$ hydrogen bond of a Type III β-turn) that is the structural hallmark of the 3_{10}-helix. For example, while the Z-Aib-OH molecule is incapable of forming a C10 intramolecular hydrogen bond, a minor conformer of Z-Aib-OH is seen to adopt Ramachandran angles that support such hydrogen bonds in larger members of the series. Conformer A of Z-$(Aib)_2$-OMe also displays a set of dihedral angles for the first Aib residue that are near those of a 3_{10}-helix, (ϕ, ψ = -57°, -30°), even though it also lacks the backbone length necessary to make a fully formed turn of the 3_{10}-helix. Indeed, the (ϕ, ψ) angles of the C-terminal Aib of conformer A of Z-$(Aib)_2$-OMe are fully extended ($\phi \sim -180°$, $\psi \sim -180^o$). Finally, the Z-$(Aib)_4$-OMe molecule, large enough to allow two intramolecular C10 hydrogen bonds, adopts a clear 3_{10}-helix as its dominant conformer, in which two C10 hydrogen bonds are formed, and all four residues adopt dihedral angles characteristic of the 3_{10}-helix (Table 4.1). Competing structures that incorporate C7, C11, and even C14 hydrogen-bonded rings form architectures classified as stalled or mixed helices, which make minor contributions to the R2PI spectrum. Even so, it is clear that in the gas-phase, free from intermolecular stabilization and solvent effects, Aib is a robust 3_{10}-helix former.

Table 4.1: Dihedral angles for all assigned conformations.[a] All angles are given in degrees. Relative energies are given in kJ/mol.

Molecule	Relative Energy (kJ/mol)	H-Bonding Pattern	Ring Orientation	ϕ(1)	ψ(1)	ϕ(2)	ψ(2)	ϕ (3)	ψ(3)	ϕ (4)	ψ(4)
Z-Aib-OH (A)	0	5	83	-180	-180						
Z-Aib-OH (B)	4.5	F-F	84	49	37						
Z-$(Aib)_2$-OMe (A)	0	F-5	71	-57	-38	-178	-179				
Z-$(Aib)_2$-OMe (B)	7.2	F-7/5	77	-72	70	180	179				
Z-$(Aib)_2$-OMe (C)	5.2	F-F	84	180	-180	180	180				
Z-(Aib)4-OMe (S)	0.0	F-F-10-10	74	-61	-26	-55	-27	-56	-31	51	40
Z-$(Aib)_4$-OMe (NS)	3.5	F-F -10-10	74	-61	-27	-57	-22	-57	-35	-48	-40
Z-$(Aib)_4$-OMe (B)	3.9	F-F-10-7	69	-63	-25	-58	-30	75	-74	-52	143
Z-$(Aib)_4$-OMe (C)	24.4	14-7-7-F	92	-82	34	68	-79	-53	151	43	49

[a]Due to the achiral nature of Aib, a second set of equivalent conformations exists in which the signs of all the dihedral angles are changed.

4.4.1 Energetics Analysis

An energy level diagram comparing the calculated structures for Z-Aib-OH is shown in the left-most column of Figure 4.9. The structures assigned for conformers A and B are labeled. The limited backbone length of Z-Aib-OH prohibits the formation of more complex hydrogen-bonding interactions, and all but four of the calculated structures fall within a 13 kJ/mol energy window, containing only free OH groups and free or C5 hydrogen-bonded NH groups. Conformer A, with a single C5 intramolecular hydrogen bond, was found to be the global minimum. Conformer B, with no intramolecular hydrogen bonding, is only 4.5 kJ/mol higher in energy. DFT calculations at the M052X/6-31+G(d) level of theory show two intervening conformers, plotted in the diagram, that are not observed experimentally. If the calculated energy ordering is correct, these two structures must have low energy barriers to isomerization to A, allowing their population to be removed during the cooling process in the expansion.

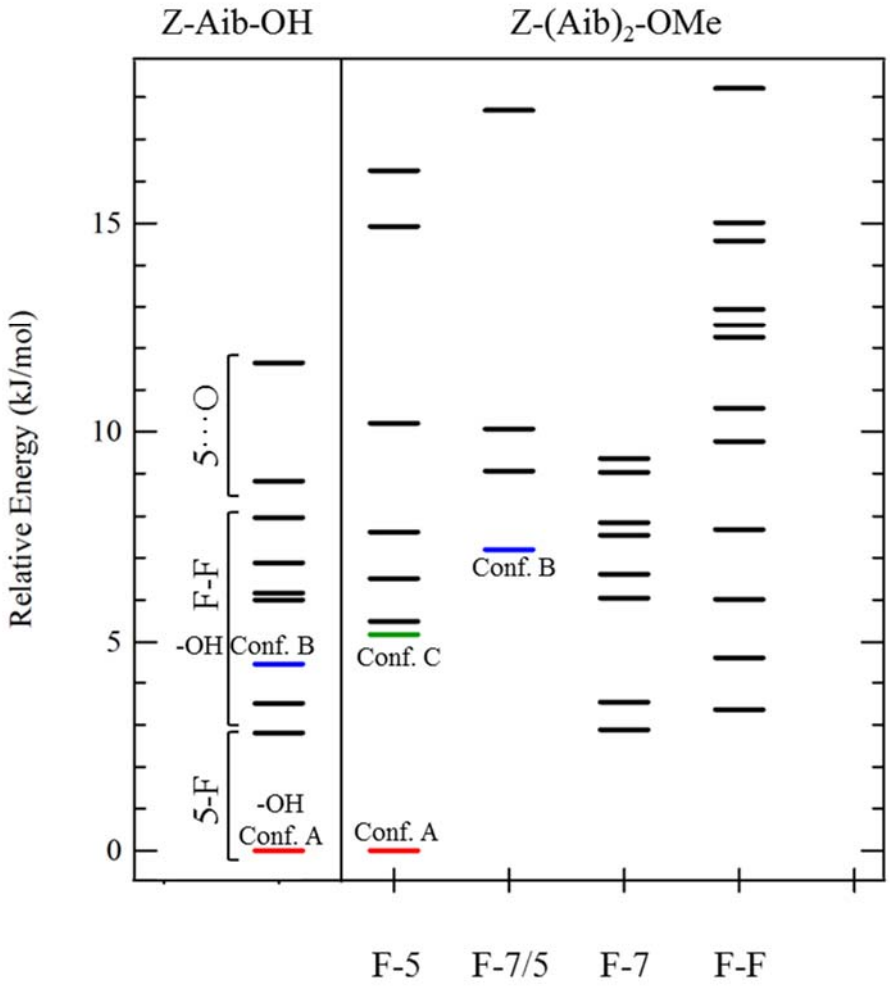

Figure 4.9: Energy level diagram for the relative, zero-point corrected energies (kJ/mol) of the conformational minima of Z-Aib-OH (left) and Z-(Aib)$_2$-OMe (right) calculated at the M052X/6-31+G(d) level of theory. The conformational families of Z-Aib-OH are bracketed and labeled. The conformational families of Z-(Aib)$_2$-OMe are labeled below their respective columns.

Not surprisingly, the energy level diagram for Z-(Aib)$_2$-OMe , displayed on the right-hand side of Figure 4.9, shows a larger number of low-energy structures than the diagram for Z-Aib-OH. Structural families are grouped by H-bonded features into columns; individual structures are ordered according to relative energy. A significant

number of the calculated structures contain one free NH group and one hydrogen-bonded NH group. The observed H-bond types include: (i) a C5 ring formed between the NH and C=O groups on a given Aib residue, characteristic of an extended peptide backbone, (ii) a C7 ring in which an NH group makes a more traditional, end-on interaction with the C=O of the adjacent Aib residue, and (iii) in a few cases, a special C5 in which the NH group of the second Aib residue interacts with the lone-pair on the backside of the backbone, methoxy-group oxygen. There is a single structure, assigned to conformer C, which contains two C5 hydrogen-bonded NH groups in a fully-extended peptide backbone geometry. In this sense, conformer C is the sole member of another conformational family (5-5), and could rightfully have its own column in the diagram, but has been grouped with the F-5 structures for efficient space utilization.

Conformer A, an F-5 structure, is found to be the global minimum, with its first Aib residue having Ramachandran angles close to that of a 3_{10} helix (Table 4.1). It is noteworthy that this structure, incorporating a single C5 ring, is lower in energy by 5.2 kJ/mol than conformer C, the fully extended structure, with its two weak C5 H-bonds. This energy stabilization of A over C must be attributed, at least in part, to the preference of the first Aib residue for the turn-like geometry (Figure 4.5(a)) observed in a 3_{10}-helix.

Conformer B, which is 7.2 kJ/mol above the global minimum, represents the first example of a C5/C7 bifurcated double ring in which a single NH group interacts with the nearest-neighbor C=O groups on either side of it. We have already noted that conformer C, the 5-5 structure, is the lowest (and only) example of a fully-extended structure. Thus, all three observed conformers of Z-$(Aib)_2$-OMe are the lowest-energy examples of three unique conformational families, suggesting that barriers between members of the same

family are relatively low, but inter-family barriers are substantial enough that collisional cooling between them is incomplete. The large intensity of conformer A in the R2PI spectrum relative to B and C is consistent with B and C being higher in energy, and therefore having smaller populations. Admittedly, other factors beyond population can affect relative sizes of peaks in the R2PI spectrum (e.g., Franck-Condon activity, S_1 lifetime, photoionization cross section). Once again, the lack of spectroscopic evidence for conformers of the F-7 and F-F conformational manifolds computed to have energies lower than those of assigned conformers B and C suggests that structures may have small barriers for isomerization to conformer A.

Figure 4.10(a) presents an energy level diagram for Z-$(Aib)_4$-OMe, the largest member of the present series of Aib homopeptides. Once again, the structures have been grouped into columns based on conformational/hydrogen-bonding family type. The first three columns have well-defined intramolecular hydrogen-bonding patterns; however the three columns to the right simply group the structures by the number of amide-amide H-bonds they possess.

The low-energy region of the energy level diagram for Z-$(Aib)_4$-OMe is remarkably sparse for a molecule this size, having only two competing structures within 10 kJ/mol of the global minimum. Both the global minimum and the second lowest-energy (+3.5 kJ/mol) structures are F-F-10-10 structures characteristic of a 3_{10}-helix, with very similar calculated IR spectra that are nominally consistent with the observed spectrum of conformer A, whose S_0-S_1 origin dominates the R2PI spectrum. Conformer B is assigned to the structure 3.9 kJ/mol above the global minimum, which is the lowest energy member of the F-F-10-7 family. Above 10 kJ/mol, there are many structures with

similar energies belonging to a wide variety of H-bonding architectures, none of which are observed experimentally.

Interestingly, the calculations predict a large number of structures, >11 kJ/mol above the calculated global minimum, trapped in F-F-10-10 conformational minima (left-most column of Figure 4.10(a). A C10 backbone hydrogen bond between the carbonyl oxygen of residue "*i*" and the amide hydrogen of residue "*i + 3*" is the defining characteristic of a β-turn, for which there is a taxonomy including many variations of ϕ and ψ backbone angles for residues i + 1 and i + 2.[45] Conformer A of Z-(Aib)$_4$-OMe exhibits "Type III" β-turns characteristic of 3_{10}-helices, for which (ϕ_2 and $\phi_3 \sim -57°$, ψ_2 and $\psi_3 \sim -30°$)[45,46] The higher-energy members of the F-F-10-10 manifold exhibit other classes of β-turn structures, differing in the dihedral angles along the incipient 3_{10}-helix, and in the strength of the C10 H-bonds that are formed.

The classically defined β-turn structure does not proscribe the ϕ, ψ angles of the i + 3 residue participating in a β-turn. The two lowest-energy F-F-10-10 conformers we calculated for Z-(Aib)$_4$-OMe exhibit ϕ, ψ angles for the C-terminal (i.e., fourth) residue that belong to the 3_{10}-helical region of the Ramachandran map. The major difference between these two low energy structures is that the minimum energy structure inverts the ϕ, ψ angles of its C-terminal residue. That is, the minimum energy structure exhibits a change of handedness for its fourth residue, as compared to preceding three residues. The second-lowest energy structure, 3.5 kJ/mol higher, however, maintains the same helical handedness for all four residues. This "helix reversal", known as a Schellman motif, is a common phenomenon at helix termini in protein structures and in the crystal structures of Aib oligomers.[47-50]

The structure assigned to conformer A, with an energy 3.5 kJ/mol above the calculated global minimum, maintains its handedness along the whole length of the peptide backbone (i.e., non-Schellman) and provides a slightly better spectroscopic fit to experiment. The calculated dipole moments of the Schellman and non-Schellman structures are nearly identical, differing by only 0.07 D. A comparison of these two calculated spectra with experiment is shown below in Figure 4.12.

Elsewhere in the diagram, Schellman/non-Schellman (S/NS) structural pairs appear. For instance, the F-F-10-10 structure at +17.5 kJ/mol differs from the global minimum by changes in the dihedrals about the first Aib residue (ϕ_1, ψ_1). (The energetic cost for this rearrangement is quite high.) Its NS counterpart is also observed, and appears at +20.5kJ/mol, as anticipated.

The conformational variations within the F-F-10-10 conformational manifold include deviations of ϕ and ψ of Aib[1] and/or Aib[4], and in the orientation of the phenyl ring of the Z-cap. These differences and combinations there-of have been annotated on the energy level diagram in Figure 4.10(a).

The orientation of the phenyl ring can also have a significant impact on the DFT-computed energy of a given structure. In Figure 4.10(a), structures annotated with "RF" incorporate a "ring flip" in which the phenyl ring is rotated by ~ 180º around the C-C(H2)-O-C(=O) dihedral angle of the Z cap, as compared to this dihedral's value for the rings in the two lowest energy structures. Such a geometry change comes at an energy cost of about 8 kJ/mol. The phenyl ring orientation may further destabilize the structure by adopting an *anti*-configuration in which the dihedral angle value falls between ±120º to ±180º. This orientation raises the energy of a given structure by approximately 12

kJ/mol. The isolated nature of these ring adjustments has been tested by manually changing the ring orientation, reoptimizing the structure at the DFT level, and comparing the resultant energies. In these tests, it was observed that adjusting the ring in this way only impacted the zero-point corrected energy of a particular structure and did not impact the predicted spectrum to any significant extent.

The remaining annotations, not explicitly discussed here, all occur at the ends of the molecule and primarily involve atoms that do not participate in intramolecular hydrogen bonding. By considering these geometry rearrangements individually and in concert with each other, the large number of unique structures within the F-F-10-10 family can be understood.

Conformer B is assigned as an F-F-10-7 structure. The F-F-10-7 structural manifold emerges from the F-F-10-10 structures by distortions of the dihedral angles in the third Aib residue away from their archetypal 3_{10}-helical values. There are nine structures within the first 25 kJ/mol that belong to this F-F-10-7 family. The lowest energy F-F-10-7 structure (i.e., conformer B) is almost 10 kJ/mol more stable than the next structure in this family. Just as in the F-F-10-10 structures, the other members of the F-F-10-7 family can be accounted for with combinations of ring flips, reversals of the Aib[3] Ramachandran angles, and modifications of ψ_4.

Conformer C is tentatively assigned to a compactly folded, mixed-helix structure containing three intramolecularly-hydrogen-bonded NH stretch transitions and a free NH stretch. This conformer appears near the top of Figure 4.10(a), in a column depicting the energy levels of conformations exhibiting 3 or 4 intramolecular hydrogen bonds. (The final two columns of Figure 4.10(a) indicate the energies of conformations found to

contain one or two intramolecular hydrogen bonds.) The structure assigned to conformer C, a 14/11-7-7-F conformation, is shown in Figure 4.8(c). While the fit between experiment and theory in Figure 4.7 is reasonable, the assigned structure is 24 kJ/mol above the global minimum, and keeps this assignment tentative. The combination of laser desorption with rapid collisional cooling in the supersonic expansion may be trapping a small portion of the population in this conformational well. Assignment of such a high-energy structure, while certainly uncommon, is not unprecedented. In fact, Dean, et al. made a similar argument to justify the assignment of a high energy conformation in their work on Z-$(Gly)_3$-OH.[20]

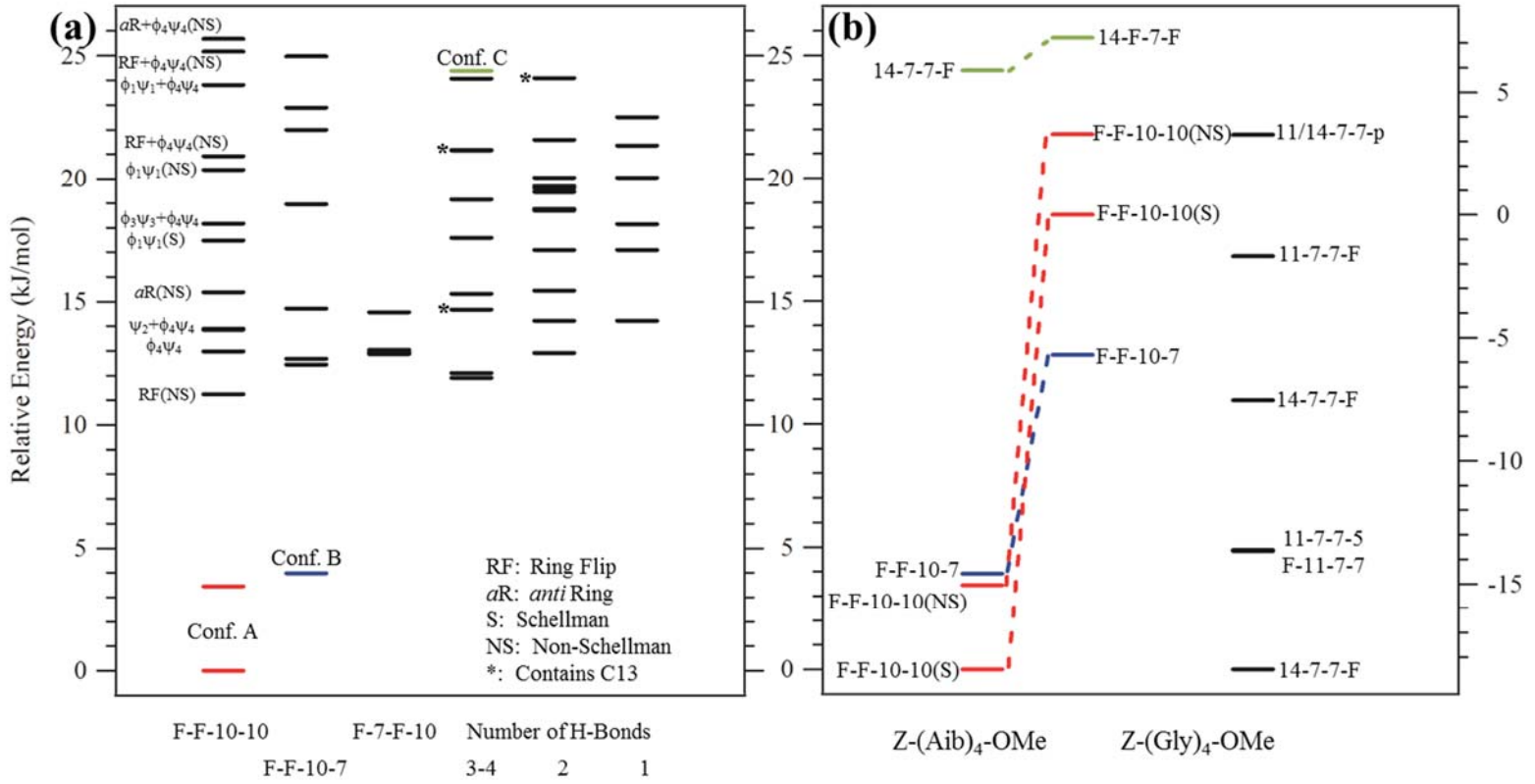

Figure 4.10: (a) Energy level diagram showing different structures of Z-(Aib)$_4$-OMe grouped by hydrogen-bonding family. Energies (kJ/mol) are relative to the calculated global minimum structure of Z-(Aib)$_4$-OMe. (b) Energy level diagram comparing the assigned structures for Z-(Aib)$_4$-OMe with their counterparts in Z-(Gly)$_4$-OMe and a selection of other low-energy Z-(Gly)$_4$-OMe structures. See text for further discussion. Energies (kJ/mol) on the left-hand column are relative to the calculated global minimum of Z-(Aib)$_4$-OMe or Z-(Gly)$_4$-OMe (as appropriate). Energies on the right-hand axis of (b) are relative to the F-F-10-10-(s) structure of Z-(Gly)$_4$-OMe.

4.4.2 Comparison of Z-$(Aib)_n$ with Z-$(Gly)_n$

A natural point of comparison exists between the present set of Aib homopeptides and their corresponding glycine (Gly) counterparts. One point of commonality between the two is that, unlike chiral amino acids, where formation of secondary structures such as helices occurs with a particular handedness (e.g., L-amino acids preferentially form right-handed helices).[45,51,52] Aib and Gly are both achiral, and therefore have allowed Ramachandran angles in which (+ϕ, +ψ) and (-ϕ, -ψ) are equivalent. Perhaps more importantly, Gly, with its two hydrogens, is the most flexible of the amino acids, with allowed Ramachandran angles that span the largest range of any of the amino acids.[53] By contrast, Aib, with its two methyl groups, shows much more restricted (ϕ, ψ) preferences localized around (+57°, +30°) and (-57°,-30°), and readily forms 3_{10}-helices in solution. Comparing the inherent conformational preferences of Aib and Gly homopeptides in the gas phase gives unique insight regarding the effects of dimethyl substitution, particularly in light of the accumulating macrodipole of the 3_{10}-helix that accompanies the spatial correlation of amide-group orientations.[54]

The structure observed for conformer A of Z-Aib-OH is strikingly similar to the assigned conformations for Z-Gly-OH in both its UV and IR spectroscopy. The limited backbone length of Z-X-OH, where X = Aib or Gly, provides very little conformational flexibility, and makes the extended C5 structure a highly favorable geometry. The similarity in the UV spectra between both molecules reflects their nearly identical phenyl ring environments. The frequencies of the OH and NH stretch oscillators also fall within a few cm^{-1} of each other, again as a consequence of the similar structures. However, conformer B of Z-Aib-OH does adopt a distinct conformation. The increased steric

impact of dual methyl sidechains causes a distortion of the fully extended structure and results in a backbone geometry with dihedral angles characteristic of the 3_{10}-helix. With only a single Aib residue, the nascent ability of the dimethylated peptide to induce this geometry is observed in Z-Aib-OH. The analogous Gly-based structure does not experience this steric burden, and the second, minor conformer observed in Z-Gly-OH retains the same dihedral angles as the major conformer and simply experiences a reorientation of its aromatic ring.[20]

The data for Z-$(Aib)_4$-OMe can be compared *qualitatively* to Z-$(Gly)_3$-OH, with the fourth amide group in Z-$(Aib)_4$-OMe having its NH group substituted for OH in Z-$(Gly)_3$-OH. Despite this nominal similarity, the dominant conformer of Z-$(Aib)_4$-OMe, the F-F-10-10, 3_{10}-helix, that has no low-energy counterpart in Z-$(Gly)_3$-OH. In order for the Gly-based molecule to form a second C10 H-bond the *cis*-OH in the COOH group would have to reconfigure to *trans*, an energetically costly isomerization. Instead, the major conformer A of Z-$(Gly)_3$-OH has an 11-7-7-OH•••π hydrogen-bonding pattern that is surprisingly similar to the 14/11-7-7-F pattern tentatively assigned to the minor conformer C in Z-$(Aib)_4$-OMe. The OH•••π hydrogen bond in conformer A of Z-$(Gly)_3$-OH would have its equivalent in an NH•••π H-bond in conformer C of Z-$(Aib)_4$-OMe, but formation of this π H-bond is blocked by the ester cap. Instead, the ester C=O[4] forms the second leg of a C14/C11 bifurcated double-ring with NH [1] in the Aib-based molecule.

One of the most striking results of the Z-$(Gly)_n$ studies occurred in the largest members of the series, Z-$(Gly)_5$-OH and Z-$(Gly)_5$-NHMe. While polyglycine peptides are known to adopt PGI/PGII structures in solution[55], Dean et al. discovered that these

molecules instead form 14/16 mixed helices in the gas phase.[20] Unlike α- or 3_{10}-helices, mixed helices incorporate H-bonds that include both N → C terminus and C → N terminus H-bonds that reduce the magnitude of the dipole moment which frequently accompanies helix formation.[20] In the gas phase, the calculated energies of polyglycine PGII or 3_{10}-helices increase relative to the 14/16 mixed helix as the helix length grows. Dean et al. postulated that the accumulating macrodipole of the polyglycine helices (PGII (9 Debye), 3_{10} (21 Debye)) destabilizes them in the non-polar environment of the gas phase relative to the low dipole moment of the mixed helix (μ = 2.8 D in Z-$(Gly)_5$-NHMe) leading to the preference for mixed helical structures.

The present work on Aib homopeptides shows the reverse to be true in Z-$(Aib)_4$-OMe. The F-F-10-10 structure, an emergent form of the 3_{10}-helix, is preferred over all alternatives, despite its sizable macrodipole of 13.6 D. We surmise on this basis that dimethyl substitution at C_α restricts the energetically allowed (ϕ, ψ) angles about each Aib residue to such an extent that 3_{10}-helix formation is observed in spite of its significant macrodipole.

While a direct experimental comparison between Z-$(Aib)_4$-OMe and Z-$(Gly)_4$-OMe is not currently available, it is possible to calculate the relative energies of optimized structures for Z-$(Gly)_4$-OMe at the same level of theory, and thus gain insight to the changes in relative energy that accompany dimethyl substitution of glycine residues. In addition, in order to place these structures for Z-$(Gly)_4$-OMe into a more appropriate context, a conformational search was performed on Z-$(Gly)_4$-OMe, and a set of the low energy structures discovered by the force field level search was submitted to

DFT geometry optimization and harmonic, vibrational frequency calculation. The results of these calculations are shown in the energy level diagram in Figure 4.10(b).

Several important deductions follow. Perhaps most startling is that the F-F-10-10 structure that is the emergent form of a 3_{10}-helix and the global minimum in Z-$(Aib)_4$-OMe is now more than 18 kJ/mol above the lowest energy structure calculated from our cursory search of Z-$(Gly)_4$-OMe. In contrast, the minimum energy Z-$(Gly)_4$-OMe structure is a 14-7-7-F structure, with its three hydrogen bonds pointing in both the N → C terminus and C →N terminus directions, while those in the 3_{10}-helix point only from C → N. It is worth emphasizing that we have not done an exhaustive search to find the global minimum structure in Z-$(Gly)_4$-OMe, so the true minimum may be even lower in energy than the 14-7-7-F structure. Nevertheless, the 14-7-7-F structure is an incipient form of the 14/16-helix observed in Z-$(Gly)_5$-NHMe, which had a full H-bonding pattern of F-14-7-7-16-7 using the present labeling scheme. The 14-7-7-F structure already has elements of a mixed-helix in that the C14 ring constitutes an $i \rightarrow i + 3$ H-bond, while the C7 rings are $i + 2 \rightarrow i$. The dipole moment of this structure is 5.2 D, while the dipole moment of the F-F-10-10 polyglycine structure is 12 D, consistent with the previous deduction that polyglycines in the gas phase preferentially fold into structures that reduce the dipole moment.

Substitution of Gly for Aib also has dramatic effects on the relative energies of the observed conformers of Z-$(Aib)_4$-OMe. For instance, the energy ordering of the assigned F-F-10-10 and F-F-10-7 structures switches upon substitution of Gly for Aib. In the Aib-based structures, conformer B, which incorporates a C7 hydrogen bond instead of a second C10 (i.e., F-F-10-7), is calculated to be approximately 4 kJ/mol *higher* in energy

than the global minimum (F-F-10-10) structure. When Gly residues compose the backbone instead, the F-F-10-7 structure becomes *lower* in energy than F-F-10-10(s) by ~6 kJ/mol, a relative energy shift of nearly 10 kJ/mol.

Even the high-energy 14-7-7-F structure tentatively assigned to conformer C (Figure 4.10(b)) of Z-(Aib)$_4$-OMe undergoes a significant shift in relative energy upon replacement of all the Aib residues with glycine residues. This structure sits 24 kJ/mol above the global minimum for Z-(Aib)$_4$-OMe case. When Gly residues are present instead, the significantly decreased steric crowding from the side chains, lowers the energy of the Gly version of conformer C by approximately 17 kJ/mol (relative to the F-F-10-10 structure), while maintaining the same overall structure. (There is a slight backbone dihedral adjustment that results in the breaking of the first C7 hydrogen bond. These dihedral angles are shown in Table 4.2.)

The observant reader will point out that the global minimum structure found by our cursory probe of the Z-(Gly)$_4$-OMe conformational space also adopts a 14-7-7-F geometry. Indeed, this is yet another instance in which adjustments to the dihedral angles along the backbone result in dramatic changes in energy. Upon substitution of Gly residues for Aib residues, the dihedral angles of conformer C change by no more than 20° at any given position. In fact most of the dihedrals change by less than 10°, indicating that the reduction in energy likely comes primarily from relief of the steric strain imposed by the methyl side chains. Comparing the dihedral angles of the higher energy 14-F-7-F (Gly-substituted Z-(Aib)$_4$-OMe conformer C) to the minimum energy 14-7-7-F structure of Z-(Gly)$_4$-OMe, on the other hand, reveals dihedral angles that differ to a much larger

extent (20°-100+°) at each position. Therefore, we conclude that the reduction in energy is associated with adoption of a geometry that is inherently preferred by the backbone.

Finally, there is one aspect of the energy level diagram that is relatively conserved within the Aib → Gly substitution; namely, the relative energy difference between the Schellman and non-Schellman structures for conformer A, which remains near 3 kJ/mol between the two molecules. Thus, it appears the energy requirement for flipping the C-terminal residue from one handedness does not arise from the dispersive/London forces of Aib's methyl side chains, but instead is due to the different electrostatic interaction of the polar ester group with the rest of the molecule.

Table 4.2: Shown below are the structures, relative energies, H-bonding patterns, and relevant dihedral angles for Gly-based analogues of the assigned structures for Z-(Aib)$_4$-OMe as well as the selected structures from our cursory conformational search on Z-(Gly)$_4$-OMe. Structures having a direct Z-(Aib)$_4$-OMe counterpart are listed as S and NS for Schellman and non-Schellman, B for conf. B, and C for conf. C. Non-analogous Z-(Gly)$_4$-OMe structures are simply numbered based up on their energy ordering. All angles are given in degrees.

Molecule	Relative Energy (kJ/mol)	H-Bonding Pattern	Ring Orientation	$\phi(1)$	$\psi(1)$	$\phi(2)$	$\psi(2)$	$\phi(3)$	$\psi(3)$	$\phi(4)$	$\psi(4)$
Z-(Gly)$_4$-OMe (S)	+18	F-F-10-10 (S)	67	-66	-12	-69	-6	-109	25	69	14
Z-(Gly)$_4$-OMe (NS)	+22	F-F-10-10 (NS)	66	-65	-16	-70	-5	-96	1	-71	-13
Z-(Gly)$_4$-OMe (B)	+13	F-F-10-7	62	-69	-13	-73	-19	80	-74	-104	-176
Z-(Gly)$_4$-OMe (C)	+26	14-7-7-F	85	-90	14	80	-80	-64	150	53	41
Z-(Gly)$_4$-OMe #1	0	14-7-7-F	99	-81	66	83	-67	-93	2	137	171
Z-(Gly)$_4$-OMe #2	+5	F-11-7-7	-85	57	-143	-89	69	81	-54	-122	-168
Z-(Gly)$_4$-OMe #3	+11	14-7-7-F	-84	80	-78	-85	70	121	-23	-103	60
Z-(Gly)$_4$-OMe #4	+17	11-7-7-F	-101	81	-78	-83	54	148	-165	-86	114
Z-(Gly)$_4$-OMe #5	+22	11/14-7-7-π	-169	77	-75	-79	75	127	-161	-92	66
Z-(Gly)$_4$-OMe #6	+27	F-11-7-7(OMe)	83	-55	140	91	-70	-81	54	135	13

4.4.3 Comparison with Crystal Structure

Figure 4.11 compares the calculated Schellman and non-Schellman structures for the F-F-10-10 conformer of Z-$(Aib)_4$-OMe with an available X-ray crystal structure of the same molecule taken from the work of Ranganathan et al.[56] Along most of the peptide backbone, the overlay between the gas phase F-F-10-10 and the X-ray crystal structure is excellent, indicating that even in the presence of close neighbors in the solid state, intramolecular forces dictate the structure of this molecule, and the crystal structure is essentially unperturbed from the gas phase minimum. The fact that the structure is stable regardless of its environment also speaks to the strong local structural preferences induced in the peptide backbone by the Aib residue, a rather remarkable result given the small size of the methyl groups.

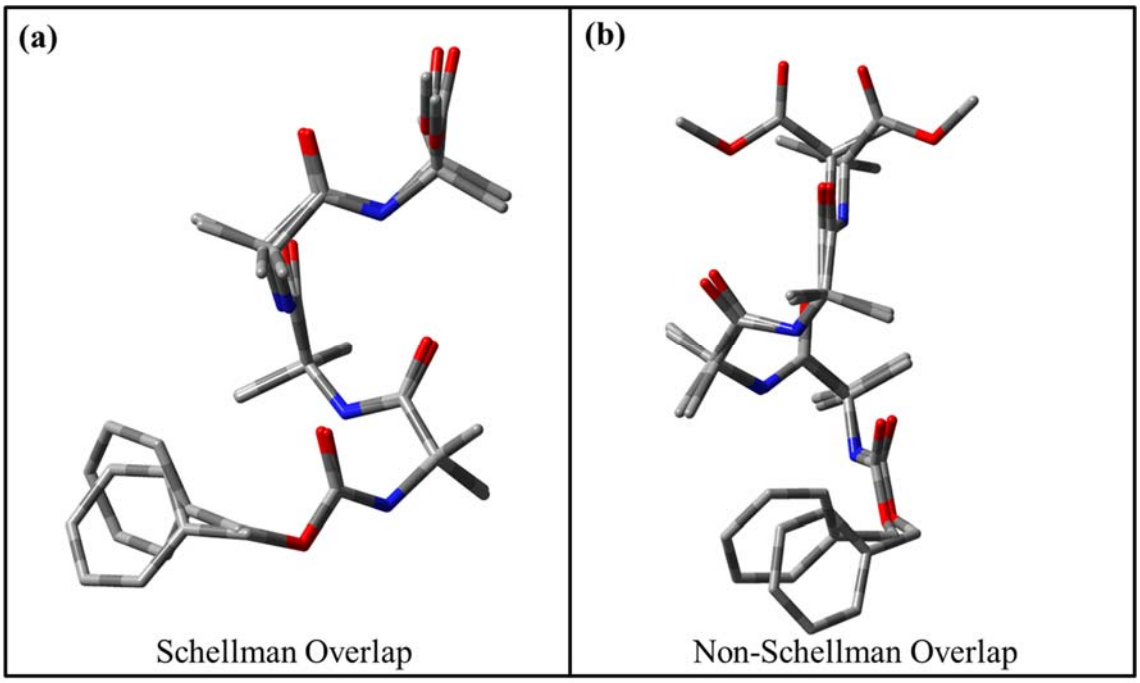

Figure 4.11: Schellman (a) and non-Schellman (b) versions of conformer A of Z-$(Aib)_4$-OMe overlaid with previously determined crystallographic structure for a Z-$(Aib)_4$-OMe oligomer possessing a 3_{10}-helical structure extracted from a unit cell. All hydrogen atoms have been removed to better show the backbone overlap.

One significant distortion is seen in the comparison between the non-Schellman structure and the crystal structure at the C-terminal end of the molecule. In the tentatively assigned (non-Schellman) gas-phase structure, the C-terminal Aib residue has dihedral angles that maintain the handedness of the helix, while in the crystal structure the handedness of the final residue is flipped. This difference is most clearly seen in the front view, shown in Figure 4.11(b). In the crystal phase, the Schellman motif enables formation of a pair of intermolecular NH•••C=O hydrogen bonds with each of two adjacent Aib oligomers within the unit cell. By aligning two 3_{10}-helical segments end to end, the free NH groups at the N-terminus of one oligomer interact with the free C=O

groups located at the C-terminus of the adjacent molecule. The isolated molecules probed by our experiment removes the possibility for intermolecular hydrogen bonding between Aib oligomers.

While the vibrational spectrum shows a slightly better fit with the standard 3_{10}-helix form of F-F-10-10, both structures are low in energy, with the Schellman version calculated to be the global minimum. Since the difference between the calculated infrared spectra for the two structures is subtle (see Figure 4.12), if the energy difference is real, it is likely that the experimentally observed structure is the Schellman version, in which case the correspondence between gas phase and crystal is near-perfect.

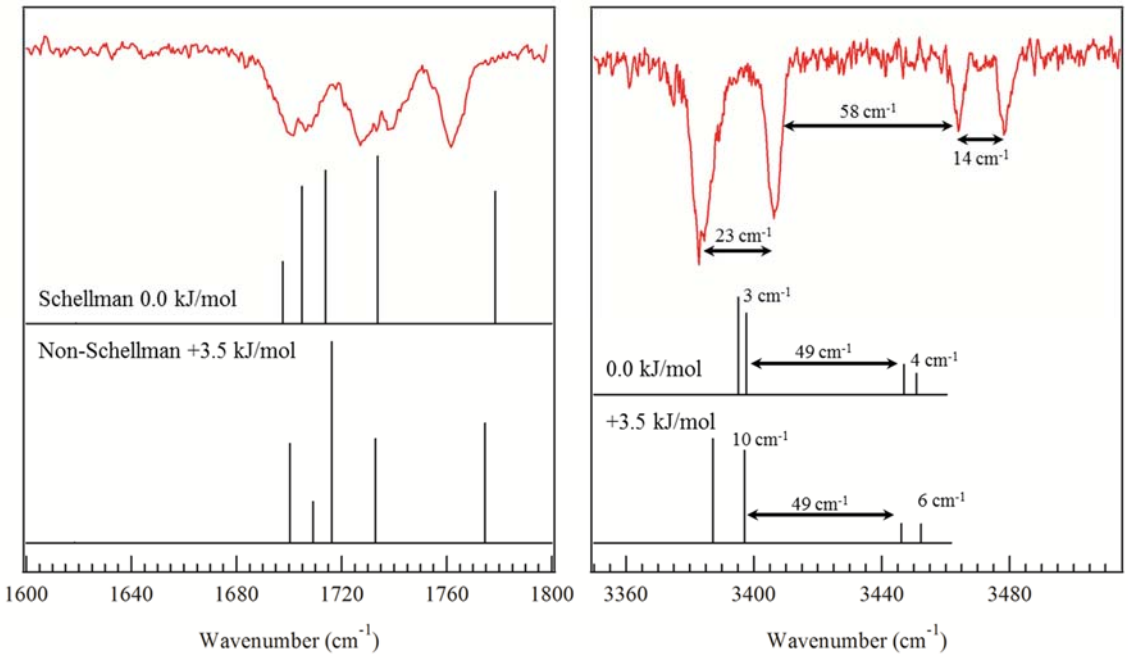

Figure 4.12: Presented here are the two lowest energy fits for conformer A of Z-$(Aib)_4$-OMe in the Amide I and Amide A regions. The splittings between individual transitions have been given in wavenumbers. The primary structural difference between the two is incorporation of the Schellman Motif[47] in the lower energy structure.

4.5 Conclusion

The work presented here investigates the folding propensities of a series of capped Aib-based homopeptides, Z-Aib-OH, Z-$(Aib)_2$-OMe, and Z-$(Aib)_4$-OMe. Single-conformation IR and UV spectra recorded under jet-cooled conditions in the gas phase are compared with harmonic, vibrational frequencies and infrared intensities calculated for the conformational minima of the molecules, leading to clear assignments. The achiral Aib residue is known to be a robust 3_{10}-helix former, with prototypical Ramachandran (ϕ, ψ) angles near (-57°, -30°) for a right-handed helix and (+57°, +30°) for a left-handed helix, which are energetically equivalent under isolated conditions. These local, residue-level angle preferences are observed to some degree already in Z-Aib-OH and Z-$(Aib)_2$-OMe, even though these homopeptides are too short to form the C10 H-bonds that serve as a spectroscopic marker for 3_{10}-helix formation. This indicates that the dimethyl substitution is inherently directing enough to produce a preference towards these angles even when supporting hydrogen bonds cannot be formed. However, alternative structures are also observed in these shorter members of the sequence.

When the backbone is extended to four residues in Z-$(Aib)_4$-OMe, an F-F-10-10 structure dominates the spectrum, with its peptide backbone constituting more than one full turn of the 3_{10}-helix. This is marked by both the hydrogen-bonding pattern of the NH groups, F-F-10-10, and the ϕ and ψ angles near -57° and -30°, respectively for each of the Aib residues in the molecule. Calculations predict that the two lowest energy structures for Z-$(Aib)_4$-OMe are both F-F-10-10 in type: the fully right/left-handed helix, and the helix which incorporates the Schellman motif at the last residue. A striking aspect of this result is that this strong energetic preference for the 3_{10}-helix formation occurs at the

earliest stages it can, with only two C10 H-bonds in place. Furthermore, the 3_{10}-helix is seen even though the macrodipole of these structures is 13.6 D, the largest of any of the calculated structures, which should bias against 3_{10}-helix formation. This is the reverse of what is seen in Z-$(Gly)_n$-NHMe, where a mixed 14/16-helix was favored in part because of its small dipole moment, a seeming advantage in the non-polar environment of the gas phase. Since this macrodipole continues to grow with helix length, it will be interesting to see whether the gas-phase preference for 3_{10}-helix formation continues in longer members of this series, a task left for future work.

4.6 References

(1) Beck, D. A. C.; Alonso, D. O. V.; Inoyama, D.; Daggett, V. *PROCEEDINGS OF THE NATIONAL ACADEMY OF SCIENCES OF THE UNITED STATES OF AMERICA* 2008, *105*, 12259.

(2) Best, R. B.; de Sancho, D.; Mittal, J. *Biophysical Journal* 2012, *102*, 1462.

(3) Moreau, R. J.; Schubert, C. R.; Nasr, K. A.; Török, M.; Miller, J. S.; Kennedy, R. J.; Kemp, D. S. *J. Am. Chem. Soc.* 2009, *131*, 13107.

(4) O'Neil, K.; DeGrado, W. *Science* 1990, *250*, 646.

(5) Padmanabhan, S.; Marqusee, S.; Ridgeway, T.; Laue, T. M.; Baldwin, R. L. *Nature* 1990, *344*, 268.

(6) Lyu, P.; Liff, M.; Marky, L.; Kallenbach, N. *Science* 1990, *250*, 669.

(7) Pauling, L.; Corey, R. B.; Branson, H. R. *PROCEEDINGS OF THE NATIONAL ACADEMY OF SCIENCES OF THE UNITED STATES OF AMERICA* 1951, *37*, 205.

(8) Andersen, C. A. F.; Rost, B. In *Structural Bioinformatics*; Gu, J., Weissig, H., Eds.; John Wiley & Sons, Inc.: Hoboken, 2003, p 339.

(9) Donohue, J. *PROCEEDINGS OF THE NATIONAL ACADEMY OF SCIENCES OF THE UNITED STATES OF AMERICA* 1953, *39*, 470.

(10) Toniolo, C.; Benedetti, E. *Trends in Biochemical Sciences* 1991, *16*, 350.

(11) Atilgan, C.; Gerek, Z. N.; Ozkan, S. B.; Atilgan, A. R. *Biophysical Journal* 2010, *99*, 933.

(12) Park, S. H.; Opella, S. J. *Protein Science : A Publication of the Protein Society* 2007, *16*, 2205.

(13) Marshall, G. R.; Hodgkin, E. E.; Langs, D. A.; Smith, G. D.; Zabrocki, J.; Leplawy, M. T. *PROCEEDINGS OF THE NATIONAL ACADEMY OF SCIENCES OF THE UNITED STATES OF AMERICA* 1990, *87*, 487.

(14) Toniolo, C.; Bonora, G. M.; Barone, V.; Bavoso, A.; Benedetti, E.; Di Blasio, B.; Grimaldi, P.; Lelj, F.; Pavone, V.; Pedone, C. *Macromolecules* 1985, *18*, 895.

(15) Bavoso, A.; Benedetti, E.; Di Blasio, B.; Pavone, V.; Pedone, C.; Toniolo, C.; Bonora, G. M. *PROCEEDINGS OF THE NATIONAL ACADEMY OF SCIENCES OF THE UNITED STATES OF AMERICA* 1986, *83*, 1988.

(16) Banerjee, R.; Basu, G. *Chembiochem* 2002, *3*, 1263.

(17) *Peptaibiotics: Fungal Peptides Containing alpha-Dialkyl alpha-Amino Acids*; Toniolo, C.; Bruckner, H., Eds.; VHCA, Wiley-VCH: Zurich, Weinheim, 2009.

(18) Maekawa, H.; Formaggio, F.; Toniolo, C.; Ge, N.-H. *J. Am. Chem. Soc.* 2008, *130*, 6556.

(19) Zeko, T.; Hannigan, S. F.; Jacisin, T.; Guberman-Pfeffer, M. J.; Falcone, E. R.; Guildford, M. J.; Szabo, C.; Cole, K. E.; Placido, J.; Daly, E.; Kubasik, M. A. *The Journal of Physical Chemistry B* 2014, *118*, 58.

(20) Dean, J. C.; Buchanan, E. G.; Zwier, T. S. *J. Am. Chem. Soc.* 2012, *134*, 17186.

(21) Chin, W.; Piuzzi, F.; Dognon, J. P.; Dimicoli, L.; Tardivel, B.; Mons, M. *J. Am. Chem. Soc.* 2005, *127*, 11900.

(22) Brenner, V.; Piuzzi, F.; Dimicoli, I.; Tardivel, B.; Mons, M. *Journal of Physical Chemistry A* 2007, *111*, 7347.

(23) James III, W. H.; Baquero, E. E.; Choi, S. H.; Gellman, S. H.; Zwier, T. S. *J. Phys. Chem. A.* 2010, *114*, 1581.

(24) Meijer, G.; Vries, M. S. d.; Hunziker, H. E.; Wendt, H. R. *Appl. Phys. B* 1990, *51*, 395.

(25) Dean, J. C., Purdue University, 2014.

(26) Lubman, D. M.; Rettner, C. T.; Zare, R. N. *Journal of Physical Chemistry* 1982, *86*, 1129.

(27) Levy, D. H. *Annual Review of Physical Chemistry* 1980, *31*, 197.

(28) Morse, M. D. *Experimental Methods in the Physical Sciences* 1996, *29*, 21.

(29) Lubman, D. M. *Mass Spectrometry Reviews* 1988, *7*, 559.

(30) Zwier, T. S. *Journal of Physical Chemistry A* 2001, *105*, 8827.

(31) Page, R. H.; Shen, Y. R.; Lee, Y. T. *Journal of Chemical Physics* 1988, *88*, 4621.

(32) Weiner, P. K.; Kollman, P. A. *Journal of Computational Chemistry* 1981, *2*, 287.

(33) Mohamadi, F.; Richards, N. G. J.; Guida, W. C.; Liskamp, R.; Lipton, M.; Caufield, C.; Chang, G.; Hendrickson, T.; Still, W. C. *J. Comput. Chem.* 1990, *11*, 440.

(34) Gaussian 09, R. A., Frisch, M. J.; Trucks, G. W.; Schlegel, H. B.; Scuseria, G. E.; Robb, M. A.; Cheeseman, J. R.; Scalmani, G.; Barone, V.; Mennucci, B.; Petersson, G. A.; Nakatsuji, H.; Caricato, M.; Li, X.; Hratchian, H. P.; Izmaylov, A. F.; Bloino, J.; Zheng, G.; Sonnenberg, J. L.; Hada, M.; Ehara, M.; Toyota, K.; Fukuda, R.; Hasegawa, J.; Ishida, M.; Nakajima, T.; Honda, Y.; Kitao, O.; Nakai, H.; Vreven, T.; Montgomery, Jr., J. A.; Peralta, J. E.; Ogliaro, F.; Bearpark, M.; Heyd, J. J.; Brothers, E.; Kudin, K. N.; Staroverov, V.N.; Kobayashi, R.; Normand, J.; Raghavachari, K.; Rendell, A.; Burant, J. C.; Iyengar, S. S.; Tomasi, J.; Cossi, M.; Rega, N.; Millam, N. J.; Klene, M.; Knox, J. E.; Cross, J. B.; Bakken, V.; Adamo, C.; Jaramillo, J.; Gomperts, R.; Stratmann, R. E.; Yazyev, O.; Austin, A.J.; Cammi, R.; Pomelli, C.; Ochterski, J. W.; Martin, R. L.; Morokuma, K.; Zakrzewski, V. G.; Voth, G. A.; Salvador, P.; Dannenberg, J. J.; Dapprich, S.; Daniels, A. D.; Farkas, Ö.; Foresman, J. B.; Ortiz, J.V.; Cioslowski, J.; Fox, D. J. Gaussian, Inc., Wallingford CT, 2009.

(35) Zhao, Y.; Truhlar, D. G. *Journal of Chemical Theory and Computation* 2007, *3*, 289.

(36) Walsh, P. S.; Kusaka, R.; Buchanan, E. G.; James III, W. H.; Fisher, B. F.; Gellman, S. H.; Zwier, T. S. *J. Phys. Chem. A*. 2013, *117*, 12350.

(37) Gord, J. R.; Walsh, P. S.; Fisher, B. F.; Gellman, S. H.; Zwier, T. S. *The Journal of Physical Chemistry B* 2014.

(38) Kusaka, R.; Zhang, D.; Walsh, P. S.; R., G. J.; Fisher, B. F.; Gellman, S. H.; Zwier, T. S. *J. Phys. Chem. A*. 2013, *117*, 10847.

(39) Li, J.; Sha, Y. *Molecules* 2008, *13*, 1111.

(40) Santagada, V.; Fiorino, F.; Perissutti, E.; Severino, B.; De Filippis, V.; Vivenzio, B.; Caliendo, G. *Tetrahedron Letters* 2001, *42*, 5171.

(41) Gloaguen, E.; Pollet, R.; Piuzzi, F.; Tardivel, B.; Mons, M. *Physical Chemistry Chemical Physics* 2009, *11*, 11385.

(42) Chin, W.; Piuzzi, F.; Dimicoli, I.; Mons, M. *Physical Chemistry Chemical Physics* 2006, *8*, 1033.

(43) Buchanan, E. G.; James III, W. H.; Choi, S. H.; Guo, L.; Gellman, S. H.; Müller, C. W.; Zwier, T. S. *J. Chem. Phys.* 2012, *137*, 094301.

(44) Sengupta, N.; Maekawa, H.; Zhuang, W.; Toniolo, C.; Mukamel, S.; Tobias, D. J.; Ge, N.-H. *Journal of Physical Chemistry B* 2009, *113*, 12037.

(45) De Poli, M.; De Zotti, M.; Raftery, J.; Aguilar, J. A.; Morris, G. A.; Clayden, J. *The Journal of Organic Chemistry* 2013, *78*, 2248.

(46) Venkatachalam, C. M. *Biopolymers* 1968, *6*, 1425.

(47) Schellman, C. In *Protein Folding: Proceedings of the 28th Conference of the German Biochemical Society*; Jaenicke, R., Ed.; Elsevier/North-Holland Biomedical Press: Univsersity of Regensburg: Regensburg, West Germany, 1979, p 53.

(48) Aurora, R.; Rose, G. D. *Protein Science* 1998, *7*, 21.

(49) Datta, S.; Shamala, N.; Banerjee, A.; Pramanik, A.; Bhattacharjya, S.; Balaram, P. *J. Am. Chem. Soc.* 1997, *119*, 9246.

(50) Pike, S. J.; Raftery, J.; Webb, S. J.; Clayden, J. *Organic & Biomolecular Chemistry* 2014, *12*, 4124.

(51) Creighton, T. E. *Proteins: Structure and Molecular Properties*; Second ed., 1993.

(52) Brown, R. A.; Marcelli, T.; De Poli, M.; Sola, J.; Clayden, J. *Angew. Chem. Int. Ed.* 2012, *51*.

(53) Read, R. J.; Adams, P. D.; Arendall, W. B., III; Brunger, A. T.; Emsley, P.; Joosten, R. P.; Kleywegt, G. J.; Krissinel, E. B.; Luetteke, T.; Otwinowski, Z.; Perrakis, A.; Richardson, J. S.; Sheffler, W. H.; Smith, J. L.; Tickle, I. J.; Vriend, G.; Zwart, P. H. *Structure* 2011, *19*, 1395.

(54) G., H. W. J. *Prog. Biophys. Mol. Biol.* 1985, *45*, 149.

(55) Bykov, S.; Asher, S. *Journal of Physical Chemistry B* 2010, *114*, 6636.

(56) Ranganathan, D.; Kurur, S.; Karle, I. L. *Biopolymers* 2000, *54*, 249.

CHAPTER 5
STEP-WISE SOLVATION OF 1,2-DIPHENYLETHANE•$(H_2O)_n$ CLUSTERS (n = 1-3)

5.1 Introduction

1,2-diphenylethane (DPE), shown in Figure 5.1, is a prototypical flexible bichromophore comprising two phenyl rings bound by an ethane bridge. Such molecules provide an opportunity to study the effects of vibronic coupling and charge transfer between the chromophores, which are of great importance in light-harvesting processes involving molecules like chlorophyll, under controlled laboratory conditions.[1,2] Specifically, the use of a supersonic jet expansion to cool and isolate flexible, multichromophore systems, and the application of single- and double-resonance laser spectroscopy techniques, have been implemented to elucidate the intrinsic conformational preferences of these molecules, thereby establishing the positions and orientations of the chromophores that interact in the molecules' excited states.[3-5] As an extension of this work, and enabled by the supersonic jet expansion environment, analogous experiments have been performed to elucidate the impact of cluster formation on these model systems. These efforts include studies of homomolecular dimer complexes[6] as well as studies in which a multichromophore system is perturbed by complexation with individual water molecules.[7] These studies are fascinating in their own right, since the aromatic 'solutes' offer binding sites to solvent molecules that can perturb the solute conformational

preferences and/or the solvent's interactions. This is especially true when the solvent is H_2O, which engages in water•••water hydrogen bonds and aromatic•••water π H-bonds.

1,2-Diphenoxyethane (DPOE) and 2,2,2-paracyclophane (TCP) have been studied extensively in their monomeric forms and under solvated conditions with $(H_2O)_n$ clusters (n = 1-5 for TCP and 1-4 for DPOE) in order to better understand their conformational preferences and electronic spectroscopy, both with and without the influence of water.[3,7-11]

One such investigation was performed by Buchanan et al. to characterize the impact of binding 1-5 water molecules in an aromatic-rich pocket created by the three equivalent, ethano-bound phenyl rings of the TCP. The authors determined that in all cases the primary interaction between TCP and the water molecule(s) was via double or single H-bond donation from one of the water molecules to the aromatic-rich interior pocket of TCP. In fact, Buchanan et al. report that in all cases, the water molecules adopt their preferred, non-complexed geometries and subsequently bind to the TCP pocket, rather than through some other "building-up" formation mechanism. Even so, spectroscopic investigation of the OH stretch modes of these H_2O clusters reveals that there are significant perturbations to the hydrogen-bonded water networks caused by interaction with TCP.[8]

In another work from Buchanan, et al., excitonic localization induced by the binding of H_2O to the *tgt* conformation of DPOE was observed. While the excitonic splitting in the DPOE monomer is only 1 cm^{-1}, a single H_2O molecule binds asymmetrically to the oxygen atom of one phenoxy ring and the π-cloud of the other phenoxy ring, breaking the symmetry of the two chromophores, and producing a 190 cm^{-}

^{1} splitting between the S_1 and S_2 states. Excited state, single-conformation IR spectroscopy revealed that S_0-S_1 excitation was localized on the π-bound ring while the S_0-S_2 excitation was localized on the oxygen bound ring. In fact, the water molecule proved to be a sensitive probe of the coupling between the two excited states, and dispersed fluorescence experiments confirmed extensive mixing between the S_1 and S_2 states.[7]

As an extension of this work, Walsh, et al. explored the impact of $(H_2O)_n$ clusters (n = 2-4) on the conformational preferences, electronic spectroscopy, and internal conversion between chromophores by probing both the ground and excited states of the complexes.[9,10]

Here, we have taken a simplifying step by eliminating one of the chromophores from TCP and both of the ether oxygens from DPOE to study the perturbative effects of water on 1,2-diphenylethane (DPE) within the cold, collision-free environment of a molecular beam in order to probe the impact of stepwise solvation on the geometry of DPE and its water-containing clusters. This study sets the stage for future work on the excited states by providing the starting structures for electronic excitation.

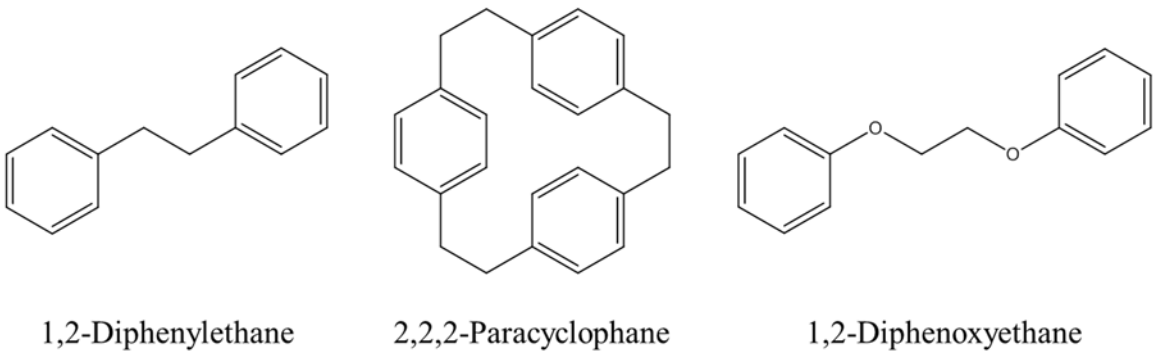

Figure 5.1: Chemical structures of 1,2-diphenylethane, 2,2,2-paracyclophane, and 1,2-diphenoxyethane.

5.2 Experimental Methods

5.2.1 Water Cluster Formation

In order to form DPE•$(H_2O)_n$ clusters, a gas manifold has been assembled that allows a partial pressure of H_2O to be incorporated into the carrier gas in a controlled way. The manifold splits the gas supply line coming from the cylinder into parallel lines equipped with dedicated flow meters as well as inlet and outlet valves. The primary line provides a direct pathway to the sample-holder and the backside of the pulsed valve. The secondary line passes through a vessel designed to hold a substantial amount of liquid water (or some other liquid-phase sample). By controlling the backing pressure and the relative flow through each portion of the gas manifold, the desired partial pressure can be achieved.

5.2.2 Resonant Two-Photon Ionization

Resonant two-photon ionization, described in detail already, was used to collect vibronic spectra for the DPE•H_2O clusters in question. By monitoring the ion signal at characteristic arrival times for the DPE monomer, DPE•H_2O, and DPE•$(H_2O)_2$ mass channels, all necessary R2PI spectra for the DPE•$(H_2O)_n$ clusters with n = 1-3 were able to be recorded. As we shall see, the vibronic spectra belonging to DPE•$(H_2O)_n$ neutral clusters appear most strongly in the DPE•$(H_2O)_{n-1}^+$ mass channels due to efficient fragmentation of the water cluster caused by a strong repulsive interaction between the DPE and the $(H_2O)_n$ cluster following a significant geometry rearrangement of the cluster upon photoionization of DPE. The nature of this fragmentation mechanism has been explored in detail elsewhere.[12]

5.2.3 Resonant Ion-Dip Infrared Spectroscopy

Resonant ion-dip infrared spectroscopy (RIDIRS) was used to record conformation specific IR spectra of each DPE•$(H_2O)_n$ cluster in the OH stretching region from approximately 3300 cm^{-1} to 3800 cm^{-1}. OH stretching modes provide a sensitive probe of the local environment and hydrogen bonding interaction of water molecules, and have been used to study a multitude of water-bound clusters.[7,13] To record a RIDIR spectrum, the UV laser, operating at 20 Hz, is tuned to a vibronic transition unique to a specific conformer within the supersonic expansion, providing a constant level of ion signal. An IR laser, operating at 10 Hz, is then spatially overlapped with the UV beam, but timed such that it interacts with the gas pulse approximately 200 ns prior to the arrival of the UV beam. Successive pulse sequences of “IR on” and “IR off” are subtracted by

an SRS gated integrator performing active baseline subtraction in order to produce a spectrum showing depletion in the ion signal of a single conformation as a function of IR wavelength.

5.2.4 IR-UV Hole-Burning Spectroscopy

IR-UV hole-burning spectroscopy was used to record conformation-specific UV spectra. By implementing the same overlap and timing scheme from RIDIRS, described above, fixing the IR laser on an OH stretch transition unique to one of the conformations observed, and scanning the UV laser, a spectrum showing ion dip as a function of UV wavelength can be recorded.

5.3 Results

Building upon the work reported previously on the 1,2-diphenylethane (DPE) monomer[3] in which both the *gauche* and *anti* conformations were characterized using IR and UV spectroscopy, R2PI spectra were recorded in the S_0-S_1 region of DPE•$(H_2O)_n$ complexes (n = 1-3) and are shown in Figure 5.2.

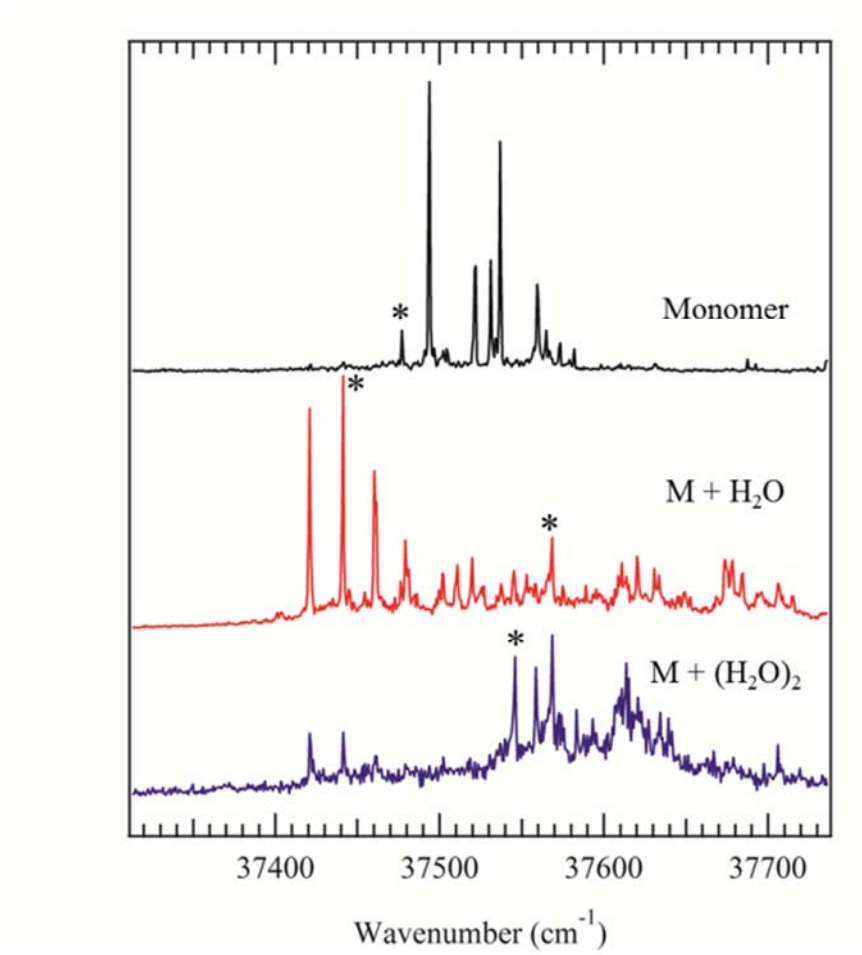

Figure 5.2: R2PI spectra in the region of the S_0-S_1/S_2 states of DPE with < 0.5% H_2O expansion in neon, while monitoring the (a) DPE monomer, (b) DPE•$(H_2O)_1^+$, and (c) DPE•$(H_2O)_2^+$ mass channels. Transitions due to the DPE monomer and DPE•$(H_2O)_n$ clusters with n = 1-3 are labeled. The transitions used for RIDIRS are marked with asterisks.

5.3.1 DPE•H_2O Complex

Origin transitions for both the *gauche*- and the *anti*-conformations were observed at 37494 cm^{-1} and 37559 cm^{-1} in the R2PI spectrum collected in the monomer mass channel, consistent with previous work in which they were identified and assigned.[3] A small transition occurring 17 cm^{-1} to the red of the *gauche* origin at 37477 cm^{-1} appeared

in the monomer mass channel when H_2O was added to the expansion. This transition is assigned to the DPE•H_2O complex, which can be detected in the monomer mass channel due to efficient fragmentation of the complex upon photoionization.[10,14,15] The observed spectral features from the DPE•H_2O cluster remain narrow and well-resolved because the absorption takes place within the cold, isolated neutral cluster, and it isn't until ionization that the fragmentation takes place. The transition at 37477 cm^{-1} was used as the monitor transition for collection of the single-conformation IR spectrum discussed below. Of note is the fact that the DPE•H_2O origin transition is red-shifted from both the *anti* and *gauche* monomer origins. Similar behavior was observed for TCP•$(H_2O)_n$ (n = 1-5) and certain cluster sizes of DPOE, however the benzene•H_2O cluster origin shifts in the opposite direction, blue of its respective monomer origin.[8,11,15,16]

The IR-UV hole-burning (IR-UV HB) spectrum, recorded by fixing the frequency of the hole-burn laser to the strong OH stretch transition of the complex at 3622 cm^{-1}, is shown as the red trace in Figure 5.3(a). It confirms the presence of a single DPE•H_2O conformer by burning out all non-monomer peaks observed in the R2PI spectrum. The monomer spectrum, presented as the middle trace in black, accounts for all remaining peaks present in the monomer mass channel. The hole-burning spectrum contains a series of weak vibronic transitions that are not observed in the R2PI spectrum for DPE•H_2O. This is due to the fact that hole-burn spectrum was recorded at higher UV laser power, where partial saturation increases the intensity of weak transitions relative to the electronic origin.

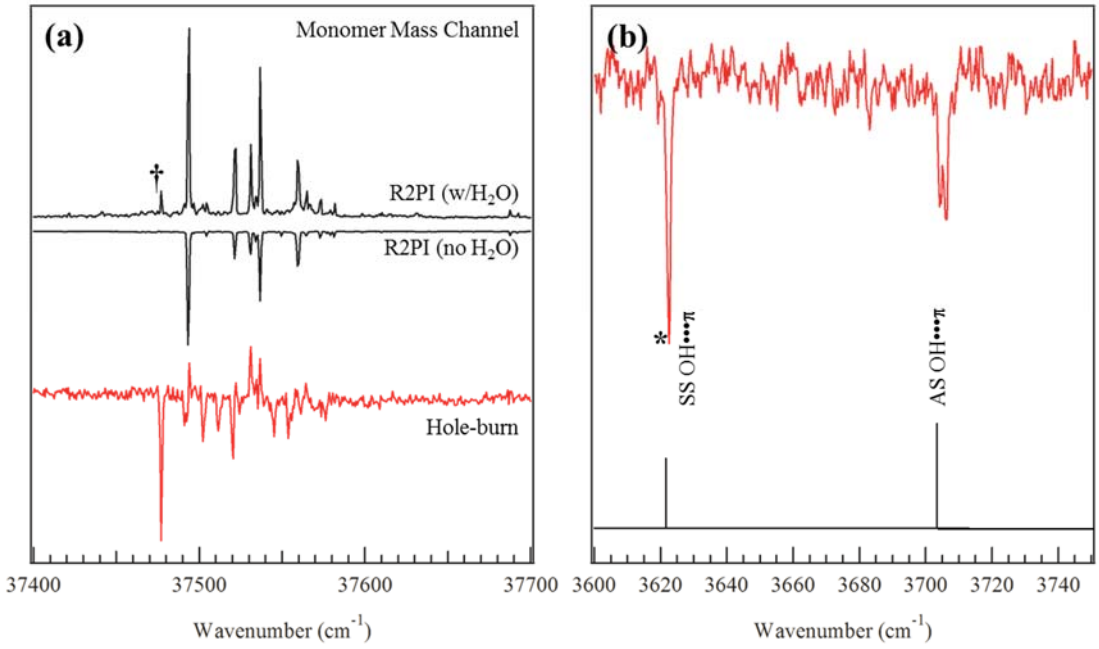

Figure 5.3: (a) R2PI spectra collected in the monomer mass channel with (top) and without (bottom) H_2O present in the expansion: The IR-UV hole-burning spectrum is shown in red. The dominant peak coming from DPE•H_2O is marked with a dagger. This is also the transition used to perform RIDIRS. (b) Assigned RIDIR spectrum for DPE•H_2O: The transition used to record the hole-burn spectrum is marked with an asterisk. Calculated (B3LYP/6-311+g(d,p)), scaled (*0.957), harmonic frequencies and IR intensities are given in the stick diagram.

The RIDIR spectrum of DPE•H_2O was recorded by fixing the UV laser on the vibronic peak located at 37477 cm^{-1} and monitoring depletion of the ion signal observed in the monomer mass-channel while the IR probe laser was tuned through the OH stretch region of the infrared from 3600 cm^{-1} to 3750 cm^{-1}. OH stretch transitions are observed at 3622 cm^{-1} and 3706 cm^{-1}, shifted down by -34 and -56 cm^{-1} from the OH stretch fundamentals of the H_2O monomer (3657 and 3756 cm^{-1}), as anticipated if π H-bond(s) are formed. Using the calculated (B3LYP/6-311+g(d,p)), scaled, harmonic frequencies and infrared intensities, we assign the DPE•H_2O IR spectrum to the structure shown in

Figure 5.4(a), built off the *gauche* monomer, in which the single water molecule binds symmetrically within the electron-rich pocket created between the two phenyl rings, using both its hydrogens to make two equivalent π hydrogen bonds to the two rings. This assignment allows us to identify the transitions at 3622 cm^{-1} and 3706 cm^{-1} as the symmetric and anti-symmetric OH stretch fundamentals, respectively. The peak at 3706 cm^{-1} actually appears as a closely spaced doublet (~2 cm^{-1} spacing), which is likely caused by large-amplitude motions of the H_2O molecule within the binding pocket, much as is observed in benzene•H_2O and TCP•H_2O.[8,14,17]

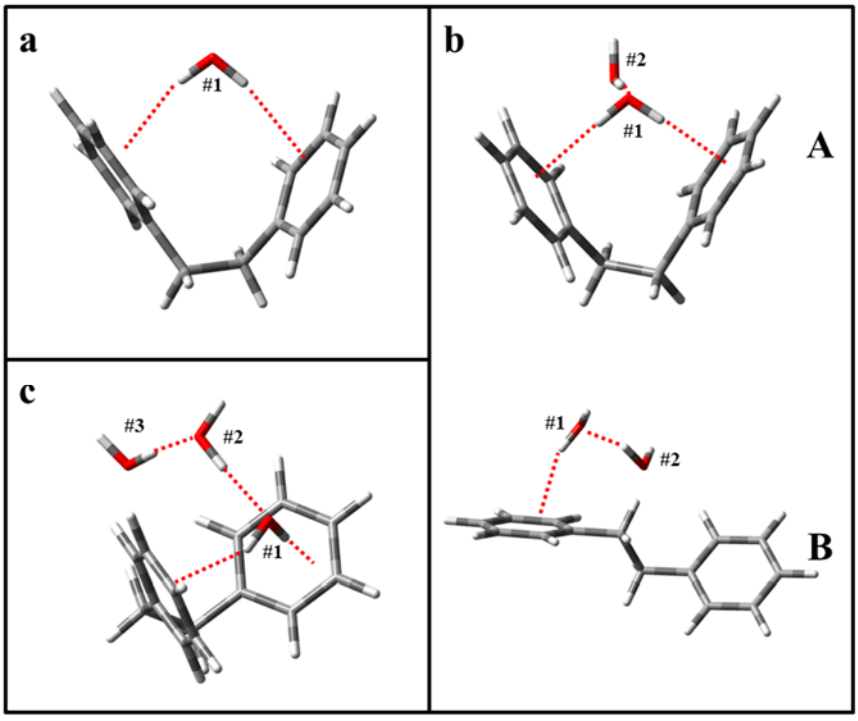

Figure 5.4: (a) Assigned structure for DPE•H_2O. (b) Assigned structures for conformers A and B of DPE•$(H_2O)_2$ built upon the *gauche* and *anti* conformations of DPE. (c) Assigned structure for DPE•$(H_2O)_3$.

5.3.2 DPE•$(H_2O)_2$ Complex

The R2PI spectrum of DPE•$(H_2O)_2$ was recorded in the DPE•H_2O mass channel and is shown in Figure 5.5(a). Again, detection of signal in the n-1 mass channel is due to efficient fragmentation of the DPE•$(H_2O)_2$ cluster by loss of one H_2O molecule following photoionization.[8,9,12] Transitions are observed near both the *gauche* and *anti* monomer origins. IR-UV hole-burning spectroscopy allows us to identify two conformations of DPE•$(H_2O)_2$ which, based on the locations of their origins, appear to be built on both the *gauche* and *anti* conformations of DPE. A vibronic progression beginning at 37421 cm^{-1} with three additional members spaced at 20 cm^{-1} intervals is observed. All four of these peaks are red-shifted from the *gauche* DPE monomer origin and are assigned to Conformer A of DPE•$(H_2O)_2$. Note that the H_2O induced red-shift observed for DPE•H_2O is seen again here. Included in the hole-burn spectrum for conformer A is a set of three small peaks, spaced at an interval of approximately 5 cm^{-1} that begins at 37676 cm^{-1}. Given its unique Franck-Condon profile, these transitions are likely candidates as S_0-S_2 transitions, however, the excited state spectroscopy of DPE and its H_2O clusters will not be explored further here.

The transition blue-shifted 9 cm^{-1} from the *anti* origin of the DPE monomer, located at 37569 cm^{-1}, is assigned to conformer B of DPE•$(H_2O)_2$. The H_2O induced blue-shift seen here is similar in direction and magnitude to the shifts observed in cases for DPOE•H_2O (+40 cm^{-1}) and benzene•H_2O (+55 cm^{-1}) complexes.[7,14,15] Two additional prominent transitions appearing at 37621 cm^{-1} and 37707 cm^{-1} are observed in the spectrum. One of these may possibly be identified as the S_0-S_2 origin, but further experimentation is needed to make a positive identification, and is a task for future work.

RIDIR spectra were recorded for both conformations of DPE•$(H_2O)_2$ within the $[DPE•H_2O]^+$ mass channel. The conformation-specific, IR spectra are shown in Figure 5.5(b). The spectrum for conformer A contains four transitions having frequencies of 3489 cm^{-1}, 3584 cm^{-1}, 3660 cm^{-1}, and 3710 cm^{-1}. Calculated (M052x/6-311++g(d,p)), scaled (*0.94), harmonic frequencies and IR intensities are used to assign these transitions to a single-donor OH stretch, the double-donor, symmetric stretch of a doubly π-bound H_2O, the double-donor, anti-symmetric stretch of the same doubly π-bound H_2O, and a free OH stretch, respectively. In the corresponding structure shown in Figure 5.4(b), one H_2O molecule, labeled #1, binds to DPE in similar fashion to the DPE•H_2O structure discussed above. It too is built off the *gauche* DPE monomer. The second H_2O molecule, labeled #2, serves as a single donor, making a hydrogen bond with the lone-pair electrons on the back side of H_2O #1, thereby forming a water dimer reminiscent of that found in pure $(H_2O)_2$ dimer. This structure is essentially formed by adding a second H_2O molecule on to the backside of the DPE•H_2O structure assigned above. The symmetric and anti-symmetric OH stretches belong to H_2O #1, while the single-donor and free stretches belong to H_2O #2. Note that the OH stretch involved in the water•••water hydrogen bond is shifted down in frequency from its value in $(H_2O)_2$ by 42 cm^{-1} due to the cooperative strengthening caused by the π H-bonds to DPE.[18]

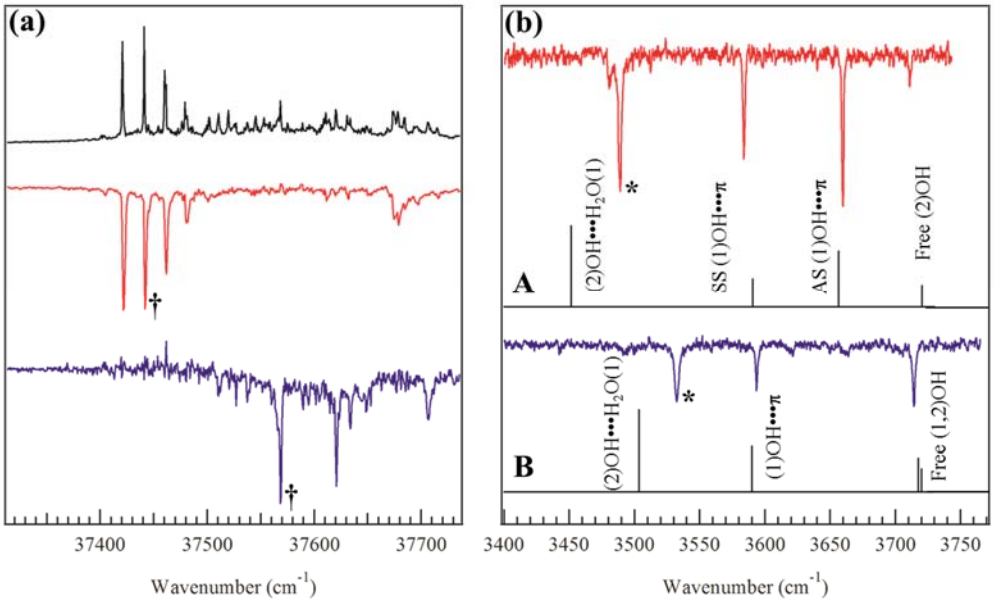

Figure 5.5: (a) R2PI and IR-UV hole-burning spectra for conformers A and B of DPE•$(H_2O)_2$: Transitions used to record RIDIR spectra are marked with daggers. (b) RIDIR spectra for conformers A and B of DPE•$(H_2O)_2$: Transitions used to collect IR-UV hole-burning spectra are marked with asterisks. Calculated (M052X/6-311++g(d,p)), scaled (*0.94), harmonic frequencies and IR intensities for the assigned structures are shown as stick diagrams.

The single-conformation IR spectrum of conformer B was recorded by fixing the UV laser on resonance at 37546 cm^{-1} and scanning the IR probe laser from 3400 cm^{-1} to 3770 cm^{-1}. The observed spectrum, shown in Figure 5.5(b), contains only three resolvable OH stretch transitions appearing at 3532 cm^{-1}, 3594 cm^{-1}, and 3714 cm^{-1}. The stick diagram below experiment is the best fit, arising from the lower structure shown in Figure 5.4(b), with an H_2O dimer forming a π H-bond with one of the phenyl rings of the *anti* DPE monomer. Calculated, scaled, harmonic frequencies and IR intensities indicate that the transition at 3532 cm^{-1} belongs to a single-donor OH involved in a water•••water hydrogen bond. In the next transition, at 3594 cm^{-1}, H_2O #1 makes a single-donor

hydrogen bond with the π-cloud above the phenyl ring. The final experimentally observed transition, having a frequency of 3714 cm^{-1}, contains contributions from both of the nearly-equivalent free OH stretches of H_2O molecules # 1 and #2.

5.3.3 DPE•$(H_2O)_3$ Complex

Finally, the R2PI and IR-UV hole-burning spectra of DPE•$(H_2O)_3$ were recorded by monitoring the ion signal in the DPE•$(H_2O)_2$ mass channel. These are shown in Figure 5.6(a). The second most prominent peak, occurring at 37546 cm^{-1}, is assigned to the only observed conformer of DPE•$(H_2O)_3$. The possibility of additional conformations is ruled out by the IR-UV hole-burning spectrum, which indicates that all transitions are accounted for between the signal coming from DPE•$(H_2O)_2$ and the signal from conformer A of DPE•$(H_2O)_3$. There are several additional transitions observed over the next 100 cm^{-1} that appear on top of a subtle background. Even so, the resolution of most individual transitions is not diminished by the background.

The RIDIR spectrum of DPE•$(H_2O)_3$ is shown in Figure5.6(b). A set of six OH stretch transitions were observed, as anticipated, having frequencies of 3380 cm^{-1}, 3471 cm^{-1}, 3576 cm^{-1}, 3650 cm^{-1}, 3712 cm^{-1}, and 3715 cm^{-1}, respectively. The stick diagram below the experimental spectrum is the best fit to experiment. It arises from the structure shown in Figure 5.4(c). In this assignment, the cluster structure is built off of the *gauche* conformation of DPE and has one water molecule which forms equivalent hydrogen bonds between the two phenyl rings, much as in DPE•H_2O and conformer A of DPE•$(H_2O)_2$. The remaining two water molecules bind to the DPE•H_2O structure and together form a water trimer chain extending out of the DPE pocket.

Based on this structural assignment, the broadened band at 3380 cm^{-1} is assigned to the H-bonded OH stretch of the single-donor/single-acceptor, H_2O #2, the central water in the water trimer chain. The next transition, with a frequency of 3471 cm^{-1}, is assigned to the H-bonded OH in the terminal water of the chain, H_2O #3. The third and fourth transitions are the symmetric (SS) and anti-symmetric (AS) OH stretch transitions of the single-acceptor/double-donor H_2O #1 that is bound to DPE. The SS and AS oscillators have frequencies of 3576 cm^{-1} and 3650 cm^{-1}, respectively. The remaining pair of frequencies, 3712 cm^{-1} and 3715 cm^{-1}, belong to the free OH stretch vibrations of H_2O #2 and #3.

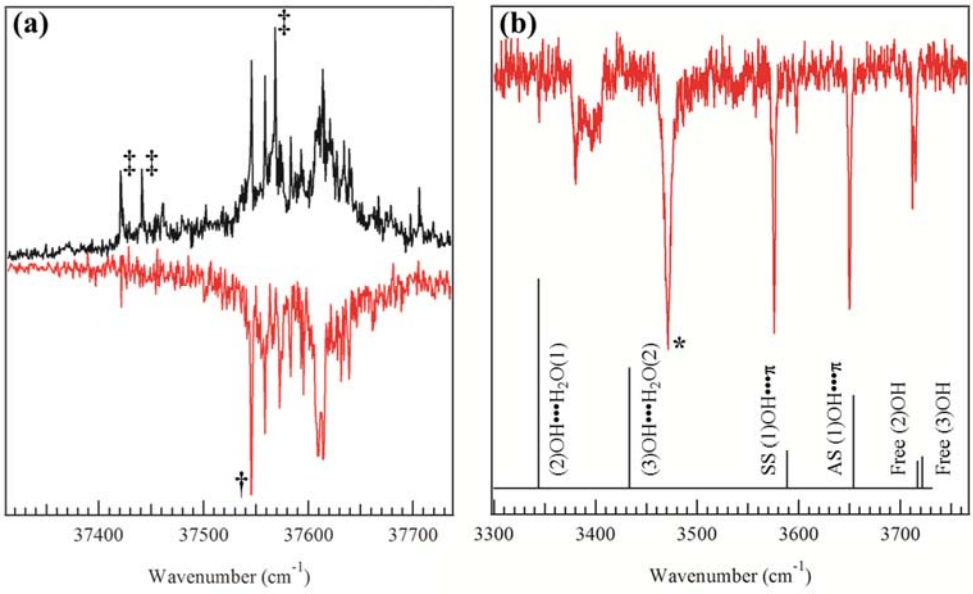

Figure 5.6: (a) R2PI and IR-UV hole-burning spectra for DPE•$(H_2O)_3$ recorded in the DPE•$(H_2O)_2$ mass channel: Transitions marked with double daggars belong to DPE•$(H_2O)_2$. The transition used to perform RIDIRS is marked with a single dagger. (b) RIDIR spectrum for the single observed conformation of DPE•$(H_2O)_3$: The vibration marked with an asterisk was used to perform IR-UV hole-burning. Calculated (M052X/6-311++g(d,p)), scaled (*0.94), harmonic frequencies and IR intensities for the assigned structure are presented as the stick diagram.

5.4 Discussion

Using a combination of double-resonance laser spectroscopy and theoretical exploration of the conformations, we have determined the preferred structures for DPE•$(H_2O)_n$ clusters with n = 1-3. The results are fascinating in that they shed light both on the effects of water on the conformations of DPE, and vice versa, on the effects of DPE on the $(H_2O)_n$ clusters. 1,2-diphenylethane (DPE) was known from previous work to exist in two conformations, *gauche* and *anti*, with transitions due to the *gauche* conformer significantly more intense (Figure 5.1). The major conformers of DPE•$(H_2O)_n$ also show this same dominance of *gauche* over *anti*. Indeed, only in n = 2 is there any evidence for clusters built off of the *anti* conformer.

DPE•H_2O was found to adopt a single conformation in which the water molecule bridges the two phenyl rings, making symmetric H-bonds with the π-clouds on either ring, maintaining the symmetry of the *gauche* conformation of DPE. After incorporating a second H_2O molecule, two conformations of DPE•$(H_2O)_2$ are observed. Conformer A is a chain structure that extends the observed conformation of DPE•H_2O by binding the second water molecule (H_2O #2) to the backside of the ring-bridging H_2O #1. The transitions of the SS and AS oscillators are red-shifted due to the cooperative strengthening induced by the binding of the second water molecule, transitioning H_2O #1 from being a “double-donor” to being a “double-donor, acceptor”. Conformer B adopts an entirely new geometry, building on the *anti* conformer of DPE. In this structure, H_2O #1 makes a single OH•••π bond, and H_2O #2 makes a single water•••water bond. Two nearly equivalent free OH stretches remain. Addition of a third H_2O molecule results in

adoption of a *gauche*-based chain structure that is a direct extension of the *gauche*, chain structures for the DPE•H_2O and DPE•$(H_2O)_2$ complexes.

5.4.1 Energetic Analysis

The assigned DPE•H_2O structure was found to be the minimum energy structure of all those calculated. A second low energy structure, located 1.3 kJ/mol higher in energy, in which the water molecule binds asymmetrically to the exterior of the DPE molecule was also considered, however, this structure was not assigned due to an inferior spectral fit; the relative splitting between the symmetric stretch (SS) and the anti-symmetric stretch (AS) is substantially greater in the exterior structure (82 cm^{-1} in the interior structure vs. 105 cm^{-1} in the exterior exterior) and matches poorly with our experimental spectrum. The observed structures for DPOE and TCP also informed this assignment.[8,11] No such exterior water structure was assigned for either of these similar molecules. In fact, in TCP, the predicted spectra show similar spectral patterns in which the SS/AS splitting is increased in the exterior structure relative to the assigned interior structure.[8] Interestingly, there are no low energy structures built off of the *anti* conformer of the DPE molecule.

The structure assigned to conformer A of DPE•$(H_2O)_2$ is the lowest energy structure of all those calculated. The energy level diagram, Figure 5.7, shows that there is another structure just 2 kJ/mol higher in energy that belongs to the same family as the assignment for conformer A. The difference between these two structures is a slight shortening of the hydrogen bond distances (~0.02-0.05 Å) in the lower energy structure.

A small gap between +2 kJ/mol and +6 kJ/mol is seen. All structures above this gap deviate from the lowest energy type structures in some way. These deviations primarily affect the arrangement of the DPE molecule, the arrangement of the water molecules, and the interaction between the H_2O and the DPE. Combinations of these energetically unfavorable modifications result in the plethora of structural families and energies. The energy level diagram groups calculated structures by conformational family, and orders them based on their relative energy when compared to the minimum energy structure. An example of each family is given in the area surrounding the diagram. Arrows are drawn to associate a given structural example to its column in the energy level diagram.

Conformer B appears approximately 10 kJ/mol higher in energy than conformer A and forms a water chain that make a π-hydrogen bond with one of the rings in a slightly twisted *anti* DPE monomer base. In making this assignment, we leap over top of a few intervening structures whose predicted spectra disagree with what we observe experimentally. We note that the most stable structure binding a water cluster to the *anti* conformation of the DPE monomer is still 7.5 kJ/mol higher in energy than the minimum energy structure.

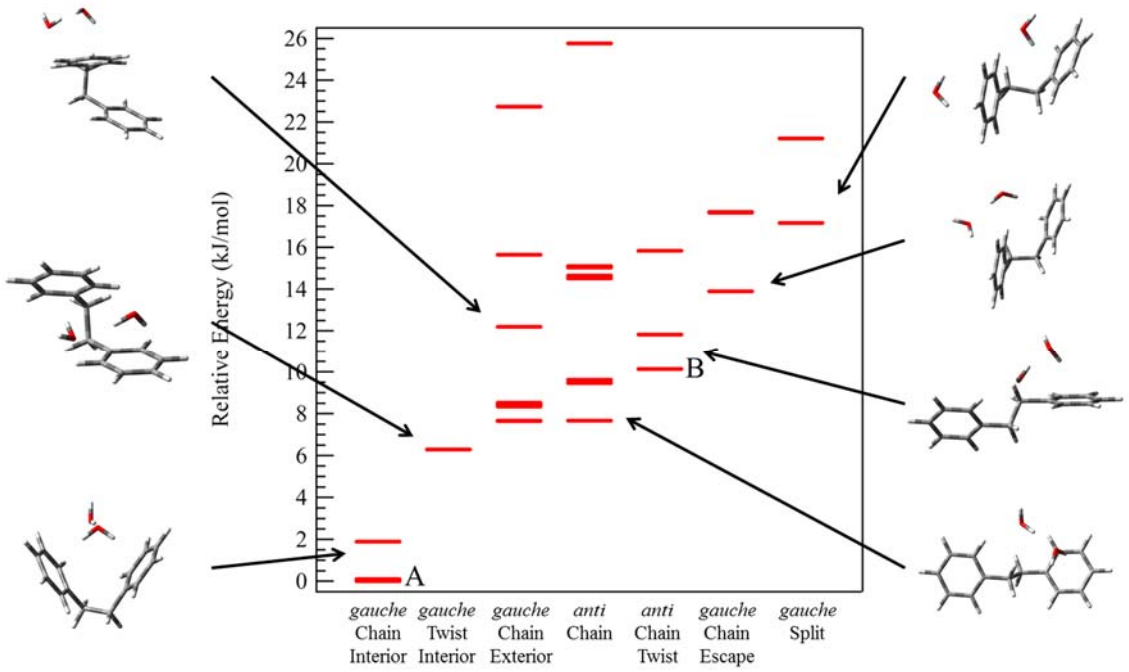

Figure 5.7: Shown here is the energy level diagram for DPE•$(H_2O)_2$ depicting the host of calculated (M052x/6-311++g(d,p)) structures, which have been grouped into columns according to major conformational differences. Structures are ordered according to relative energy on the Y-axis. The lines corresponding to the assigned structures have been labeled. Representative structures for each family have been depicted around the diagram and are matched to their columns with arrows.

Wrapping up our discussion of the potential energy surfaces, we look to the energy level diagram for DPE•$(H_2O)_3$, Figure 5.8. Immediately apparent is the large gap in energy between the two lowest energy structures and the next structure, 8 kJ/mol higher in energy. The lowest energy structure above the gap represents the first appearance of a structure that incorporates an $(H_2O)_3$ cycle. The structures above the energy gap occupy a wide distribution of conformations differing in similar fashion to the many structures displayed for DPE•$(H_2O)_2$. The most notable difference between the structures for DPE•$(H_2O)_2$ and DPE•$(H_2O)_3$ is the ability to form a water cycle, enabled by the addition of a third H_2O molecule.

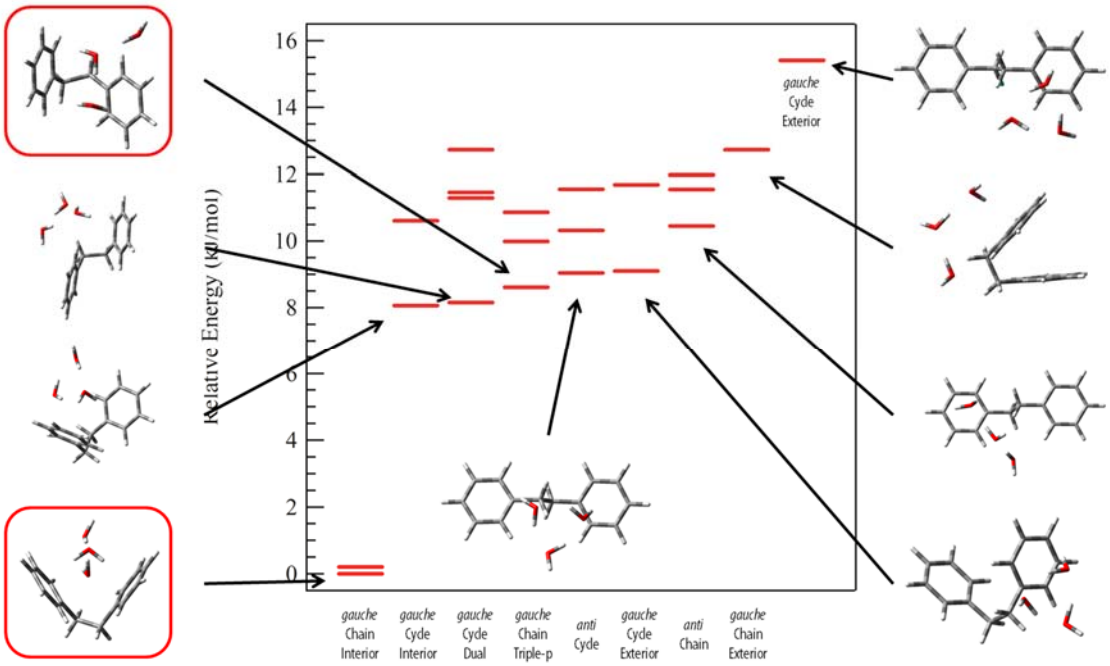

Figure 5.8: Shown here is the energy level diagram for DPE•$(H_2O)_3$ depicting the host of calculated (M052x/6-311++g(d,p)) structures, which have been grouped into columns according to major conformational differences. Structures are ordered according to relative energy on the Y-axis. The lines corresponding to the assigned structures have been labeled. Representative structures for each family have been depicted around the diagram and are matched to their columns with arrows.

5.4.2 Comparison with Benzene and TCP

DPE fits in nicely among benzene and TCP; it has two chromophores while the others have one and three, respectively. Even though DPOE also has two chromophores, its ability to form clusters with H_2O is complicated by the ether oxygen atoms in the linkage between phenyl rings. The lack of such oxygen atoms in DPE allows for a more direct comparison with benzene and TCP, discussed below.

5.4.2.1 H_2O Complex Comparisons

In the benzene•H2O complex, the water molecule serves as a double-donor, making two π H-bonds to the face of the benzene π-cloud. Figure 5.9 compares the OH stretch spectra for benzene•H_2O, DPE•H_2O, and TCP•H_2O. The large amplitude motions of the water molecule as it tumbles around on the π-surface result in the set of transitions near the expected location of the AS OH oscillator.[14,17] It is interesting to note that while a similar splitting is observed for the DPE•H_2O AS of benzene•H_2O, the spectrum is perturbed to a much smaller extent. Likely the presence of two equivalent π H-bonds locks in both sides of the H_2O molecule and prevents the large amplitude tumbling that is seen for the one and three ringed species. The splitting observed is due to the two equivalent orientations accessible through a 180° rotation of the water molecule. The splitting of the AS OH oscillator in the TCP•H_2O complex is more similar to that of benzene•H_2O. However, the degree of splitting is reduced, indicating that TCP "locks in" the water molecule to a greater extent than benzene, though still not quite as well as DPE. Also the similarity between the SS oscillators of all three species can be seen. Note that the SS oscillator of DPE•H_2O is shifted 8 cm^{-1} to the red of the SS oscillator in benzene•H_2O, and in TCP•H_2O, the SS oscillator is shifted an additional 7 cm^{-1}.

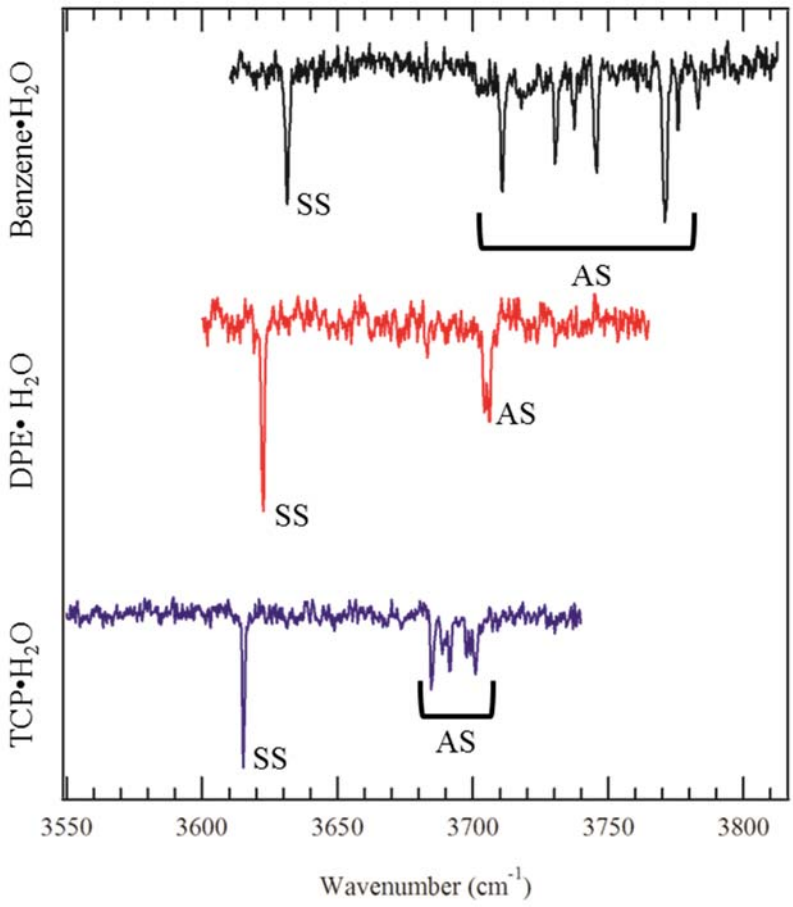

Figure 5.9: Comparison of the OH stretch, RIDIR spectra for the benzene•H_2O, DPE•H_2O, and TCP•H_2O clusters: Symmetric stretch and anti symmetric stretch oscillators have been labeled.

The flexibility of DPE allows the relative positioning of the two phenyl rings to be adjusted, thus allowing simultaneously access to two clear OH•••π binding sites for the coordinating H_2O molecules, i.e. the π-clouds on either phenyl ring. The geometry of TCP is much more constricted, and Buchanan et al. speculated that the geometry of TCP actually prevents the H_2O molecule from entering into the interior pore formed by the three phenyl rings, either due to a physical size limitation or to an impeding electron

density.[8] Consequently, the OH•••π binding takes place between the OH groups on the water molecule and the aggregate π-cloud that spills up out of the TCP cycle, thus the TCP•H_2O interaction is reminiscent of benzene•H_2O. Differences in hydrogen bonding susceptibility predicated based upon the geometric restrictions imposed by DPE and TCP influence the observed conformations as the number of water molecules increases.

5.4.2.2 $(H_2O)_2$ Complex Comparisons

Figure 5.10 compares the RIDIR spectra of both the *anti* and *gauche* conformations of DPE•$(H_2O)_2$ with the spectra for benzene•$(H_2O)_2$ and TCP•$(H_2O)_2$ (D:2, B:2, and T2, respectively). Two clear comparisons stand out; between the B:2 and D:2 *anti* complexes in which the water dimer interacts with a single phenyl ring and between the T:2 and D:2 *gauche* complexes in which the water dimer interacts with multiple phenyl rings. In the first comparison, the B:2 and D:2 *anti* free and SS stretch transitions are separated by 4 and 11 cm^{-1}, respectively; the water-bound OH stretches are shifted by 16 cm^{-1}. The D:2 *anti* OH stretches are those at lower frequencies in all cases.

The DPE *gauche* and TCP water dimer structures have incredibly similar spectra, indicating a similar conformation for the water dimer and mechanism of interaction between the water dimer and the monomer unit. Based on the increased frequency shifts of the AS and SS OH oscillators in T:2 vs D:2 *gauche*, H_2O #1 in T:2 appears to be more tightly bound. Cooperative strengthening also shifts the frequency of the water•••water interaction to lower frequency in T:2. All frequencies are listed in Table 5.1.

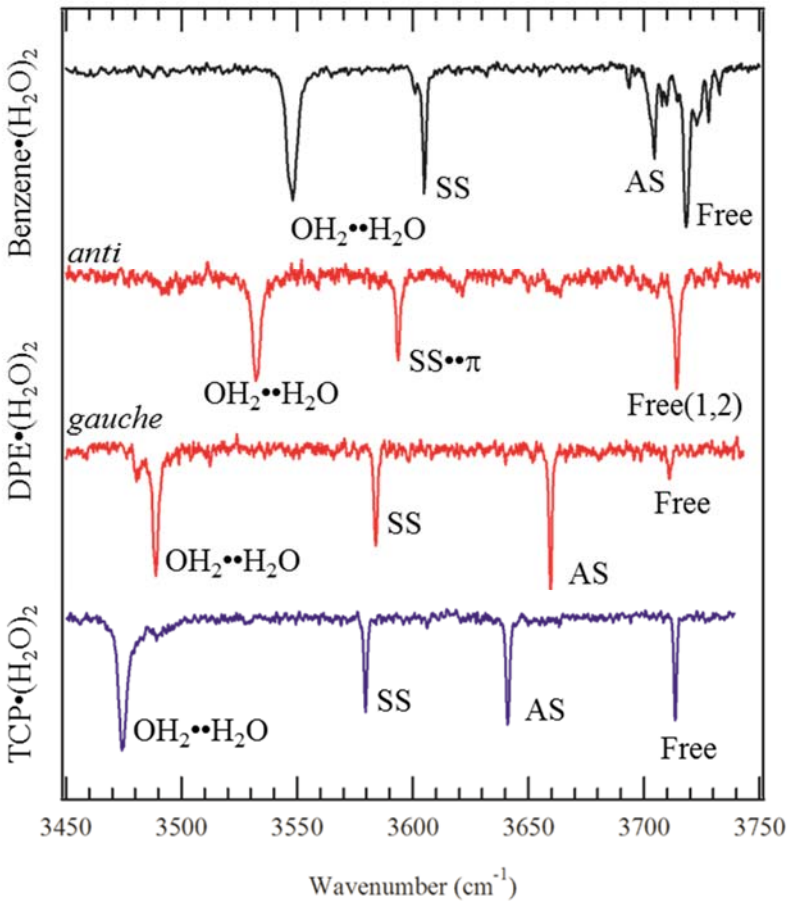

Figure 5.10: Comparison of the OH stretch, RIDIR spectra for the benzene•$(H_2O)_2$, DPE•$(H_2O)_2$, and TCP•$(H_2O)_2$ clusters: Symmetric stretch and anti symmetric stretch oscillators have been labeled, along with free OH stretches and water•••water interactions.

5.4.2.3 $(H_2O)_3$ Complex Comparisons

The similarity between the DPE•$(H_2O)_n$ and TCP•$(H_2O)_n$ or benzene•$(H_2O)_n$ structures ends at the point of n = 3. Here, the DPE system perturbs the water cluster, causing it to preferentially adopt a chain geometry rather than the preferred water-trimer, cycle geometry. TCP and benzene are not observed to have this perturbative impact; two

nearly equivalent (clockwise and counter-clockwise) water cycles were observed for TCP and a single water cycle is observed for benzene.[8,14] Buchanan, et al. reported that TCP appears to minimally perturb water's natural hydrogen bonding preferences. This is likely due to the use of an otherwise free OH to form the interaction between the water cluster and the TCP molecule. TCP, quite like benzene, provides an aromatic rich surface that is approximately flat to which water's preferred structures can bind. After forming their usual structures, especially when 3 or more water molecules are present, the water complex uses one of the OH groups that would otherwise be free, and binds into the aromatic surface.

With both TCP and benzene,[8,14,17] the nature of the π-systems is such that there are two equivalent surfaces to which the water complex can bind. However, these two surfaces are on opposite sides of the horizontal symmetry plane, and only one of the π-surfaces is typically accessible to the water cluster at a time. Because of water's innate desire to self-associate,[14,19] no structures were observed in which both surfaces were engaged in hydrogen bonding at the same time. With DPE, there are four π-surfaces that can be accessed by the binding water molecules. Further still, the two interior surfaces of the *gauche* conformation can be accessed simultaneously when a water molecule binds inside the *gauche* conformer pocket, as is demonstrated above in the assigned structures for all three (*gauche*) DPE•$(H_2O)_n$ complexes. This type of dual interaction is enabled by the flexibility of the linking ethane bridge which allows the distance between the two π-surfaces to adjust in order to better accommodate the guest water molecules. In TCP, on the other hand, the diameter of the aromatic rich pocket is fixed by the inherent cyclic nature of the trichromophore. Consequently the TCP•$(H_2O)_n$ (n = 3, 4, 5) structures all

formed their preferred water geometries, and then associated through a single OH•••π hydrogen bond. (In the n = 5 case, it was observed that the water-pentamer folds over the side of one of the phenyl rings and forms a second OH•••π bond.)

Figure 5.11(a) compares the OH stretch spectra for the $(H_2O)_3$ clusters of benzene, DPE and TCP. While some features here are conserved between all three spectra, the clear difference between chain and cycle structures can be seen. Specifically, spectra belonging to the benzene and TCP structures contain transitions belonging to the necessary three water•••water interactions required to form a cycle, while the DPE spectrum only shows two. In this case, the arrangement of the two phenyl rings in DPE preferentially stabilizes the chain structure, built within the electron-rich pocket of the *gauche* conformation.

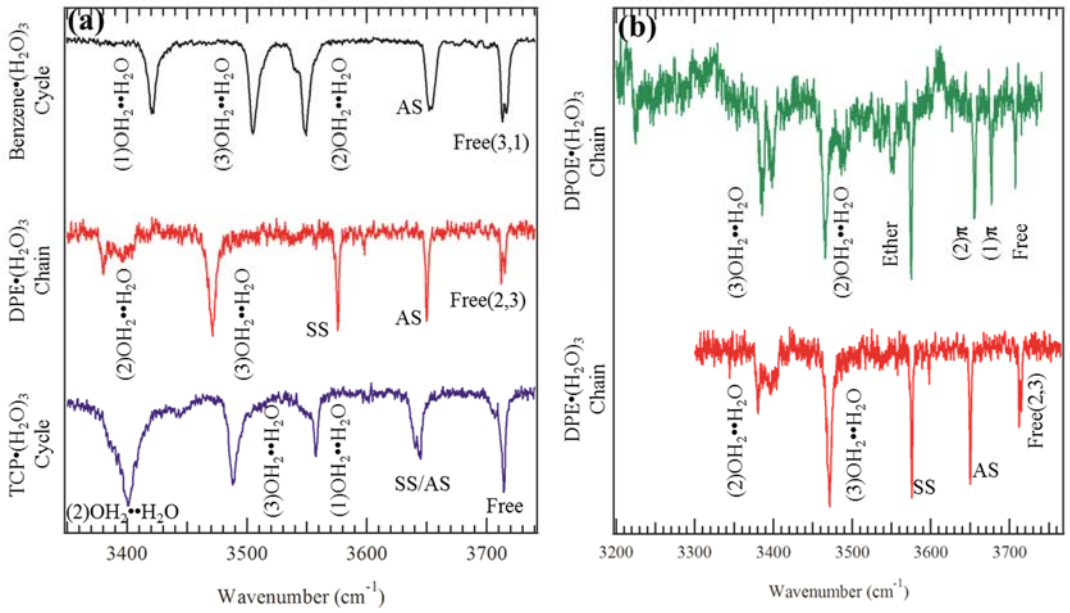

Figure 5.11: (a) Comparison of the OH stretch, RIDIR spectra for the benzene•$(H_2O)_3$, DPE•$(H_2O)_3$, and TCP•$(H_2O)_3$ clusters: Symmetric stretch and anti symmetric stretch oscillators have been labeled, along with free OH stretches and water•••water interactions. (b) Comparison of the OH stretch, RIDIR spectra for DPE•$(H_2O)_3$ and the chain structure of DPOE•$(H_2O)_3$. Symmetric stretch and anti-symmetric stretch oscillators have been labeled, along with free OH stretches and water•••water interactions.

The $(H_2O)_3$ cluster of DPOE adopts two conformations. The major conformer is a water trimer cycle in which one of the water molecules binds to the π-cloud of the phenyl ring, and another forms two OH•••ether bonds in which the same OH group is bound to both of the ether oxygen atoms. The remaining water molecule forms a single-donor, water•••water hydrogen bond and has a free OH stretch. In the DPOE•$(H_2O)_3$ chain structure the first water molecule binds asymmetrically, as in the water one and water two structures. The second water molecule makes one hydrogen bond with the back of the first water molecule, while simultaneously engaging in a second OH•••π hydrogen bond.

Finally, the third water molecule binds into the backside of the second, making a single-donor, water•••water bond. Walsh, et al. report that at the n = 4 point, there is a clear turn-over from a preference to form chain structures to a preference for cyclic water clusters.[10] A comparison of the OH stretch spectra for DPE•$(H_2O)_3$ and DPOE•$(H_2O)_3$ is shown in Figure 5.11(b). The two spectra have strikingly similar water•••water interaction regions, and the free OH oscillators appear at near-identical frequencies. The primary difference is in the mechanism of binding the water trimer chain to the monomer scaffold. This is to be expected, given the highly perturbative inclusion of oxygen atoms in the linking group between the DPOE rings.

Table 5.1: OH stretch frequencies and assigned bond types for the $(H_2O)_n$ clusters of Benzene, DPE, DPOE, and TCP.

Molecule	Structure	OH ν (cm^{-1})	OH Assign	OH ν (cm^{-1})	OH Assign	OH ν (cm^{-1})	OH Assign	OH ν (cm^{-1})	OH Assign	OH ν (cm^{-1})	OH Assign	OH ν (cm^{-1})	OH Assign
DPE•H_2O	N/A (*g*)	3623	(1)SS	3704/3706	(1)AS								
TCP•H_2O	N/A	3615	(1)SS	3684	(1)AS								
DPOE•H_2O	N/A	3597	(1)OH-O	3707	(1)OH••π								
Benzene•H_2O	N/A	3634	(1)OH••π	3713/33/40/ 48/74/85	Free								
(A) DPE•$(H_2O)_2$	Chain (*g*)	3489	(2)OH-(1)OH_2	3584	(1)SS	3660	(1)AS	3710	(2)Free				
(B) DPE•$(H_2O)_2$	Chain (*a*)	3532	(2)OH- (1)OH2	3594	(1)OH••π			3714	2xFree				
TCP•$(H_2O)_2$	Chain	3475	(2)OH-(1)OH_2	3580	(1)SS	3650	(1)AS	3712	(2)Free				
DPOE•$(H_2O)_2$	Chain	3486	(2)OH-(1)OH_2	3550	(1)OH••O	3683	(1)OH••π	3715	(2)Free				
Benzene•$(H_2O)_2$	Chain	3550	(2)OH-(1)OH_2	3608	(1)OH••π	3708	Free	3722	Free				
DPE•$(H_2O)_3$ †(A/B)	Chain (*g*) (cw & ccw)	3380	(2)OH-(1)OH_2	3471	(3)OH••(2)OH_2	3576	(1)SS	3650	(1)AS	3712	(2)Free	3715	(3)Free
TCP•$(H_2O)_3$ (A)	Chain	3401	$OH-OH_2$	3491	$OH••OH_2$	3557	OH••OH_2	3641	OH••π			3715	2xFree
DPOE•$(H_2O)_3$ (B)	Cycle	3384	$OH-OH_2$	3486	$OH••OH_2$	3563	OH••OH_2	3641	OH••O	3653	OH••π	3706	Free
DPOE•$(H_2O)_3$	Chain	3386/3398	$OH-OH_2$	3466	$OH••OH_2$	3575	OH••O	3655	OH••π	3677	OH••π	3707	Free
Benzene•$(H_2O)_3$	Cycle	3367	$OH-OH_2$	3427	$OH-OH_2$	3550	$OH-OH_2$	3657	OH••π	3716	Free		

5.4.3 The Effect of $(H_2O)_n$ on the Excited States of DPE

One of the original motivations for the previous study of the conformation-specific spectroscopy of DPE monomer was the opportunity it afforded for studying the vibronic coupling between the two identical phenyl ring chromophores, much as was done in studies of diphenylmethane (DPM) and 1,2-diphenoxyethane (DPOE).[11,20,21] With a simple conformational landscape, having two low-lying minima (*gauche* and *anti*), the two phenyl rings of DPE are placed at distinct positions relative to one another, affording two different views of the excitonic splitting and vibronic coupling between the close-lying and intermingled S_1/S_2 vibronic states. Interestingly, neither the UV hole-burning spectra of the two conformers nor their dispersed fluorescence spectra show evidence for two electronic origins.[3] This is as anticipated for the *anti* conformer, which has a C_{2h} symmetry that renders one of the transitions from S_0 forbidden. The *gauche* conformer (C_2 symmetry) has both S_0-S_1 and S_0-S_2 allowed and similar in size; yet, the two origins are not readily observed in the R2PI spectrum (Figure 5.2).

The DPE-$(H_2O)_n$ clusters studied here provide some additional insight regarding the excited states of DPE through the perturbations imposed on these excited states by the $(H_2O)_n$ clusters. The DPE•H_2O complex has been assigned to a structure in which the H_2O molecule bridges symmetrically across the two phenyl rings of the *gauche* conformer, and thus this binding provides no splitting in the uncoupled 'site' energies of the two electronic states due to the two aromatic rings. The IR-UV HB spectrum of DPE•H_2O complex (Figure 5.3(a)) is a shifted version of the *gauche* DPE monomer spectrum, without any apparent second electronic origin, just as in the monomer.

Two structures have been assigned for DPE•$(H_2O)_2$ based on the IR spectra, with conformer A assigned to a water dimer in which the water binds symmetrically to the two π-clouds of the DPE (*gauche*) conformer, as shown in Figure 5.4(a). Consistent with this assignment, the R2PI spectrum in Figure 5.5(a) shows a single Franck-Condon progression, but no evidence for two electronic origins.

By contrast, conformer B of DPE•$(H_2O)_2$ is assigned to the structure shown at the bottom right of Figure 5.4(b), in which the water dimer is bound to one ring. If this assignment is correct, it should lead to two distinct electronic origins with well-defined shifts relative to the *anti* conformer of DPE. This is indeed the case. As the IR-UV HB spectrum of conformer B shows (bottom trace of Figure 5.5(a)), the transition marked with a dagger at 37569 cm^{-1} is the S_0-S_1 origin, appearing only +10 cm^{-1} from that of DPE (*anti*) monomer, and consistent with its assignment to the phenyl ring not bound to water. A second UV transition at 37621 cm, is nearly as intense and has slightly increased Franck-Condon activity. This transition is shifted to the blue by +62 cm^{-1} from the DPE (*anti*) origin, a shift very similar to that in benzene•$(H_2O)_2$, where it is +75 cm^{-1}.[15] All evidence thus points to this blue-shifted transition as the S_0-S_2 origin of conformer B of DPE•$(H_2O)_2$ cluster, arising from a localized electronic excitation of the phenyl ring to which the water dimer is π-bound.

If these assignments hold true, they strongly suggest that in DPE monomer, the splitting between the S_1 and S_2 origins is so small as to not be resolved in the excitation spectrum, with a splitting of less than 1 cm^{-1}, much as occurred in 1,2-diphenoxyethane.[11] Leutwyler and co-workers have seen similarly small excitonic splittings in aromatic homodimers, and have elegantly described the reason that the purely excitonic splitting is

reduced due to Franck-Condon displacements.[6,22,23] It would be helpful to have high resolution UV spectra of the *gauche* conformer of DPE monomer to confirm the presence of two unresolved transitions contributing to the origin band. A similar overlap between the S_1 and S_2 origins should occur in the *gauche* conformers of DPE•$(H_2O)_{1-3}$ due to the symmetry of the H_2O binding to the two aromatic rings.

5.5 Conclusion

Four conformations were observed across the series of DPE•$(H_2O)_n$ clusters (n = 1-3). All four of these conformations were determined to incorporate chain water geometries using single-conformation IR spectroscopy. Considered within the context of TCP and benzene water-containing clusters, DPE provides an intermediate point of comparison having two phenyl rings while benzene and TCP have one and three, respectively. In the benzene and TCP•$(H_2O)_n$ structures, beginning at the n = 3 point, the observed water geometries were all seen to adopt cyclic conformations. In DPOE, at n = 3, both chain and cycle geometries were observed, and it wasn't until the n = 4 cluster that a clear preference for formation of cyclic water clusters was observed. DPE, however, demonstrated a clear preference for chain structures up to n = 3. (Higher order water clusters were not studied.)

The ability of DPE to support chain conformations of water is due to the flexibility of its two phenyl rings, and their capacity to compose an accommodating, electron-rich binding pocket that is capable of supporting two, highly stable OH•••π hydrogen bonds. By locking in the geometry of the DPE•H_2O complex and adding, stepwise, two additional water molecules, a solvated DPE is formed in which the

symmetry of the system is maintained. This structure is found to be significantly more stable than any other geometry; a surprising result given the established preference for water to form cyclic clusters at the point of n = 3+.[14]

We had hoped that the addition of water molecules to the symmetric DPE monomer would serve to localize the S_0-S_1 and S_0-S_2 excitations on one or the other of the phenyl rings. In fact, this effect was only observed in one of the four structures studied. Because the symmetry of the DPE•$(H_2O)_{1-3}$ chain structures is not broken, no localization is observed, and the S_0-S_2 origin remains unresolved. The DPE•$(H_2O)_2$ structure built off the *anti* conformation of the DPE monomer however, demonstrates this localization very clearly. Because the water dimer binds preferentially to one of the rings, the symmetry is broken and the S_0-S_1 excitation becomes localized on the unbound phenyl ring while the S_0-S_2 excitation becomes localized on the rings engaged by the water dimer. Much remains to be investigated about this solvated, bichromophore, work left for younger students.

5.6 References

(1) Engel, G. S.; Calhoun, T. R.; Read, E. L.; Ahn, T. K.; Mancal, T.; Cheng, Y. C.; Blankenship, R. E.; Fleming, G. R. *Nature* 2007, *446*, 782.

(2) Lee, H.; Cheng, Y. C.; Fleming, G. R. *Science* 2007, *316*, 1462.

(3) Buchanan, E. G.; Dean, J. C.; Zwier, T. S.; Sibert III, E. L. J. Chem. Phys. 2013, 138.

(4) Chattoraj, M.; Paulson, B.; Shi, Y.; Closs, G. L.; Levy, D. H. Journal of Physical Chemistry 1993, 97, 13046.

(5) Yip, W. T.; Levy, D. H.; Kobetic, R.; Piotrowiak, P. Journal of PHysical Chemistry A 1999, 103, 10.

(6) Ottiger, P.; Leutwyler, S. *Chimia* 2011, *65*, 228.

(7) Buchanan, E. G.; Gord, J. R.; Zwier, T. S. *J. Phys. Chem. Lett.* 2013, *4*, 1644.

(8) Buchanan, E. G.; Zwier, T. S. *J Phys Chem A* 2014, *118*, 8583.

(9) Walsh, P. S.; Buchanan, E. G.; Gord, J. R.; Zwier, T. S. J. Chem. Phys. 2015, 142, 154304.

(10) Walsh, P. S.; Buchanan, E. G.; Gord, J. R.; Zwier, T. S. J. Chem. Phys. 2015, 142, 154303.

(11) Buchanan, E. G.; Walsh, P. S.; Plusquellic, D. F.; Zwier, T. S. J. Chem. Phys. 2013, 138, 204313.

(12) Gord, J. R.; Garrett, A. W.; Bandy, R. E.; Zwier, T. S. Chemical Physics Letters 1990, 171, 443.

(13) Zwier, T. S. *Annual Review of Physical Chemistry* 1996, *47*, 205.

(14) Pribble, R. N.; Zwier, T. S. *Science* 1994, *265*, 75.

(15) Gotch, A. J.; Zwier, T. S. *Journal of Chemical Physics* 1992, *96*, 3388.

(16) Gotch, A. J.; Garrett, A. W.; Severance, D. L.; Zwier, T. S. Chemical Physics Letters 1991, 178, 121.

(17) Pribble, R. N.; Garrett, A. W.; Haber, K.; Zwier, T. S. Journal of Chemical Physics 1995, 103, 531.

(18) Huang, Z. S.; Miller, R. E. *Journal of Chemical Physics* 1989, *91*, 6613.

(19) Pugliano, N.; Saykally, R. J. *Science* 1992, *257*, 1937.

(20) Pillsbury, N. R.; Stearns, J. A.; Muller, C. W.; Plusquellic, D. F.; Zwier, T. S. Journal of Chemical Physics 2008, 129, 114301.

(21) Stearns, J. A.; Pillsbury, N. R.; Douglass, K. O.; Muller, C. W.; Zwier, T. S.; Plusquellic, D. F. Journal of Chemical Physics 2008, 129.

(22) Ottiger, P.; Leutwyler, S.; Koppel, H. Journal of Chemical Physics 2009, 131.

(23) Ottiger, P.; Frey, J. A.; Frey, H. M.; Leutwyler, S. Journal of Physical Chemistry A 2009, 113, 5280.

CHAPTER 6
ULTRAVIOLET AND INFRARED SPECTROSCOPY OF AN AMINOISOBUTYRIC ACID (AIB) HEXAPEPTIDE

6.1 Introduction

Our investigation of the homopeptide series Z-Aib-OH, Z-$(Aib)_2$-OMe, and Z-$(Aib)_4$-OMe in Chapter 4, laid out clear evidence that Aib is a strong 3_{10}-helix-former, being found to exert influence on the ϕ and ψ backbone dihedral angles as early as n = 1, inducing ϕ and ψ angles near -57° and -30°.[1,2] We discussed however, that one side effect of both α- and 3_{10}-helix formation is the accumulation of a significant macrodipole moment, which grows as the number of backbone residues increases, owing to the parallel alignment of the C=O groups. In fact, a study from Dean et al. discovered that polyglycine systems adopt mixed-helices in the gas phase in order to minimize the dipole moment and simultaneously maximize the number of hydrogen bonds that are formed between the backbone NH and C=O groups.[3] Interestingly, it was observed that this is not the case for the Aib-homopepetide systems discussed in Chapter 4, and in fact, 3_{10}-helices were observed despite having dipole moments of nearly 14 D. We speculated the reason that such a high dipole moment is not mitigated by adoption of some other geometry is because the steric influence of the dimethylated α-carbons and the stabilization of the C10 hydrogen bonds are more significant than the destabilizing effect of the macrodipole moment. This interpretation is supported by a series of calculations in which the Aib residues in our assigned structures for conformers A, B, and C of Z-$(Aib)_4$-

OMe were replaced with glycine residues and reoptimized at the DFT level. In particular, reoptimization of conformer C, which in the Aib case was found to adopt a structure similar to a mixed-helix, preserved the major hydrogen bonding features and dihedral angles of the original Aib-based structure, but saw a large reduction in its relative energy, likely due to the substantial decrease in steric strain accompanying the loss of the dual methyl side chains at each C_α.

Solution phase studies in which the partial charges accompanying any developed macrodipole moment can be satisfied by solvent interactions have been performed on a number of significantly larger Aib systems.[1,2,4] These studies have probed the effect of Aib residues when dispersed throughout the backbone to induce formation of 3_{10}-helices as well as under conditions in which the majority of the backbone comprises Aib units. They have found that under all conditions, Aib induces 3_{10}-helix formation. Studies of similarly large molecules in the gas phase have been exceptionally difficult to perform due to an inability to achieve sufficient vapor pressure, however, with the implementation of laser desorption as a mechanism of sample vaporization, studies of these larger systems have been realized.

In this short follow up to Chapter 4, we take one final look at the 3_{10}-helix forming ability of Aib, by studying the large molecule Z-$(Aib)_6$-OMe (simply called Aib6 moving forward). Weighing ~676 Da, Aib6 is the largest neutral species to have ever been studied in the Zwier Lab. Studying such a large molecule comes with the additional challenge that its mass falls outside the range of what our TOF mass spectrometer is able to cleanly resolve. Consequently, as will be discussed below, the collected spectra are less pure than is typical in cases where single-amu resolution allows contributions from

^{13}C containing species to be discriminated against. However, in this case, the monitored ion packet did contain signal from species incorporating one (or possibly more) ^{13}C atoms.

6.2 Experimental and Computational Methods

Experimental methods have already been discussed in detail, so only a cursory explanation will be given here. Laser desorption was implemented in order to generate gas-phase Aib6 molecules which could then be entrained in a supersonic expansion of argon.[5,6] With a molecular weight of 676 Da, Aib6 is the largest molecule to have ever been studied in the Zwier NSF chamber, and consequently required that extreme expansion conditions, i.e. high flow rates (~10 sccm) and high backing pressures (>6 bar), be used. Even under these conditions, the recorded UV spectrum still appears to be warm, containing broadened peaks indicative of higher internal temperatures as well as contributions from sequence and hot bands.[7,8]

Resonant two-photon ionization (R2PI) was used to record the ground state excitation spectrum of Aib6. Monitoring the appropriate mass channel was quite difficult; the ion-packet arrival time was spread over nearly 100 ns. Under normal conditions, ion-packet widths are typically on the order of 30-40 ns. In pushing the resolution limit of the instrument, it is likely the case that contributions from isotopically averaged species containing one or two ^{13}C atoms have contributed to the increased width of the observed vibronic transitions.

Single-conformation IR spectra were recorded by implementing resonant ion-dip infrared spectroscopy (RIDIRS) in the Amide I and Amide A regions, from 1600 cm^{-1} to

1800 cm^{-1} and 3200cm^{-1} to 3500 cm^{-1}, respectively. By fixing the UV laser to a specific feature in the R2PI spectrum and monitoring the ion signal at 20 Hz while scanning the IR laser through an appropriate frequency range at rep-rate of 10 Hz and performing active baseline subtraction, conformer-specific IR spectra were recorded in which dip in ion signal is plotted as a function of IR wavelength.

A conformational search similar to those described in Chapter 2 was performed. However, in this case, difficulty in determining an acceptable assignment for conformer A (to be discussed below) required additional search parameters and methodologies. Specifically, the number of Monte Carlo steps performed within each conformational search was increased from 1000 to 16,000, i.e. 1000 torsional steps per relevant, backbone dihedral rotation in order to access a larger portion of the potential energy surface. DFT calculations were then performed to determine optimized geometries and calculate harmonic frequencies and IR intensities for the most promising structures revealed by the conformational search.

6.3 Single-Conformation UV and IR Results

The R2PI spectrum for Z-$(Aib)_6$-OMe, recorded by tuning the UV laser through the characteristic Z-cap region from 37245 cm^{-1} to 37735 cm^{-1}, is shown below in Figure 6.1. Two main features centered about 37538 cm^{-1} and 37636 cm^{-1} are resolved, having full-widths at half-maximum (FWHMs) of 24 cm^{-1} and 15 cm^{-1}, respectively. The decreased spectral resolution is likely the result of multiple factors, discussed briefly above, including the addition of signal from ^{13}C containing species, as well as higher

vibrational and rotational temperatures which contribute to the observation of sequence and hot bands. Regardless, analysis of the collected spectrum identifies these two primary features as belonging to two different conformations, based on their respective IR spectra. The feature centered about 37636 cm^{-1} is assigned to conformer A, while the feature at 37538 cm^{-1} is assigned to conformer B. Comparing the frequencies of these features with those of the origin transitions for previously studied Aib homopeptides, reveals that the dominant feature for conformer A of Aib6 is blue-shifted by +7 cm^{-1} from the origin transition for conformer C of Z-$(Aib)_4$-OMe, which was determined to be a mixed-helical structure with a 14-7-7-F hydrogen bonding pattern. (This is the structure most similar to the mixed-helices observed by Dean, et al.[3]) The feature assigned to conformer B of Aib6 is shifted just -43 cm^{-1} to the red of the frequency for the A conformer of Z-$(Aib)_4$-OMe which was assigned to a well-formed 3_{10}-helix having a hydrogen bonding pattern of F-F-10-10.

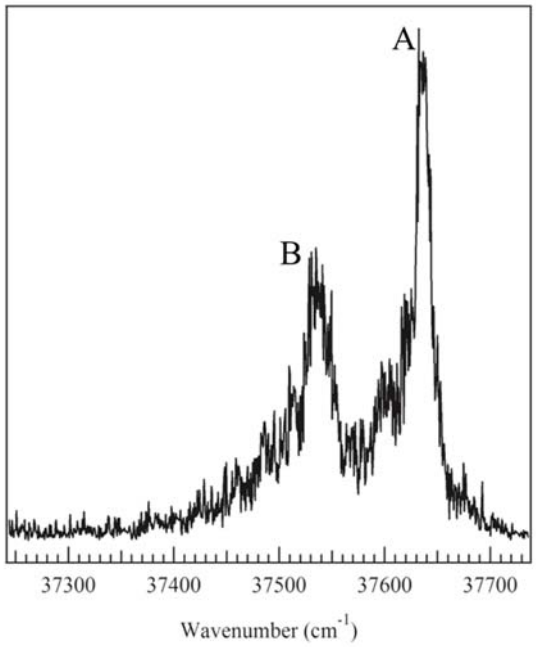

Figure 6.1: R2PI spectrum of Z-$(Aib)_6$-OMe: Features assigned to conformers A and B have been labeled accordingly.

Single-conformation IR spectra for conformers A and B, recorded using RIDIRS while monitoring ion signal from each of the major features and scanning through the Amide I (C=O stretch) and Amide A (NH stretch) regions of the IR, are shown below in Figure 6.2(a, b). The NH stretch spectrum recorded for conformer A, contains contributions from six features of varying breadths and intensities. Applying spectroscopic intuition, we can begin to make assignments for these peaks. The sharp transition located at 3475 cm^{-1} can likely be assigned to the vibration of a free NH group. The next transition at 3375 cm^{-1} appears very near to the location of C10 hydrogen bonded NHs groups that were observed in the IR spectra for Z-$(Aib)_4$-OMe conformers A and B. Admittedly, there are a number of hydrogen bonding motifs that would results in observation of a transition in this region. For example, another possible assignment for this transition comes from the C conformer of Z-$(Aib)_4$-OMe which showed a C14/C11

H-bonded NH group in this region with a frequency of 3381 cm^{-1}. The next transition appears at 3342 cm^{-1}, in the same frequency range as a weakly bound C7 NH group. The transition at 3315 cm^{-1} could also be assigned similarly. The two final transitions occur well below 3300 cm^{-1}, appearing at 3262 cm^{-1} and 3225 cm^{-1}. Both of these NH groups are involved in particularly strong hydrogen bonds, and may possibly be assigned as C7 hydrogen bonded NH groups.[3,9]

Five transitions are observed in the C=O stretch region, with measured frequencies of 1753 cm^{-1}, 1720 cm^{-1}, 1699 cm^{-1}, 1680 cm^{-1}, and 1665 cm^{-1}. Local mode coupling in the Amide I region makes it difficult to interpret spectra in this region and make assignments with certainty; however some features can be discerned. Specifically, the oscillator with a frequency of 1753 cm^{-1} is almost certainly a free, ester C=O. Also transitions recorded at and below 1720 cm^{-1} are often found to belong to backbone C=O groups engaging in hydrogen bonds.[9] To cleanly deconvolute this spectral region requires additional treatment using Hessian reconstruction analysis methods.[9,10]

A tentative fit for conformer A which nicely reproduces the pattern of the experimentally observed transitions, but fails to capture the extent of the shift experienced by the hydrogen bound NH groups, has been calculated using the M052X/6-31+G(d) level of theory. Based on this tentative assignment, the observed transition at 3475 cm^{-1} is indeed assigned to a free NH(2). The next peak, at 3375 cm^{-1}, belongs to a C10 bonded NH(3). The next two observed transitions belong to the out-of-phase and in-phase NH stretches of NH(4) and NH(5), which are involved in a C10 interaction and a C7 interaction, having frequencies of 3342 cm^{-1} and 3315 cm^{-1}, respectively. The coupled nature of these transitions helps explain why they are broadened into one

another. The remaining two transitions are attributed to a C20, NH(1), with an H-bond distance of 1.91 Å and a very strong C7, NH(6), with a hydrogen-bonding distance of 1.90 Å. The short, inter-atom distances of these interactions are reflected in the magnitude of the NH frequency shifts; these oscillators appear at 3262 cm^{-1} and 3225 cm^{-1}, respectively. The assigned structure is classified as 20-F-10-10-7-7, and is shown below in Figure 6.3(a).

Analysis of the Amide I region shows excellent agreement between calculation and experiment. The highest frequency C=O stretch at 1751 cm^{-1} is assigned to the ester group, which is involved in a C20 hydrogen bonded ring. The next transition, centered around 1720 cm^{-1}, belongs to the free stretch of C=O[2]. The transition at 1696 cm^{-1} contains contributions from the free stretch of C=O[5] and the C10 hydrogen bonded stretch of the carbamate C=O[0]. The next transition at 1679 cm^{-1} is broadened into the transitions on either side, and includes intensity from C=O[1], involved in a C10 hydrogen bonded ring, and C=O[4], which forms a C7 ring. Finally, the transition having a frequency of 1664 cm^{-1}, is assigned to C=O[3], involved in another C7 ring. The assigned structure is shown below in Figure 6.3(a)

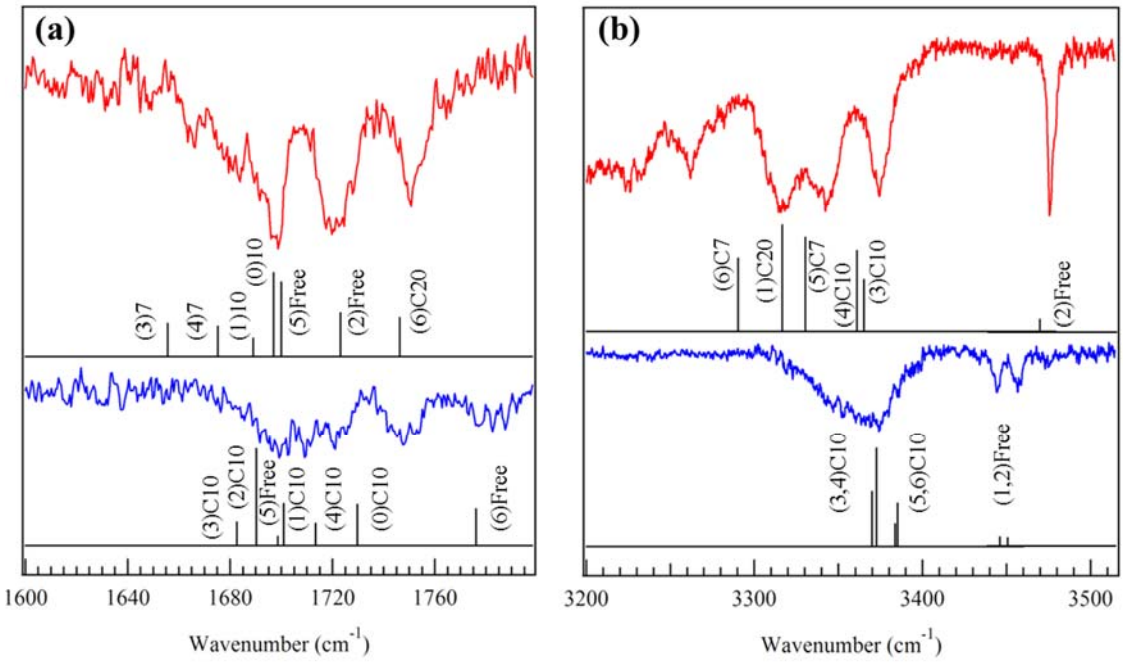

Figure 6.2: RIDIR spectra for conformers A and B of Z-$(Aib)_6$-OMe in the Amide I (a) and Amide A (b) regions. Calculated (M052x/6-31g(d)), scaled (*0.940), harmonic frequencies and IR intensities are given for the assigned structure of conformer B. Spectra for conformer A are shown in red, while spectra for conformer B are shown in blue.

A calculated spectrum having scaled, harmonic frequencies and IR intensities that match nicely with the observed experimental spectrum of conformer B is shown in the bottom portion of Figure 6.2(a,b). The two highest energy transitions are well resolved and have frequencies of 3445 cm^{-1} and 3455 cm^{-1}. Both of these are assigned as free NH stretches, in good agreement with spectral intuition as well as similar stretches in other peptides.[3,11-13] The remaining transition is a broad peak, spanning almost 80 cm^{-1}, centered near 3365 cm^{-1}. The scaled (*0.94), calculated spectrum shows four transitions appearing underneath this feature, all of which are assigned as C10 hydrogen-bound NH groups calculated to all fall between 3369 cm^{-1} and 3385 cm^{-1}. In the experimental

spectrum, the vibrations of the C10 H-bonded NH groups, being already closely spaced, are broadened, resulting in the observed, 80 cm^{-1} wide feature.

The experimental spectrum of conformer B in the Amide I region contains five somewhat resolved transitions appearing at 1700 cm^{-1}, 1710 cm^{-1}, 1720 cm^{-1}, 1750 cm^{-1}, and 1780 cm^{-1}. The highest frequency stretch at 1780 cm^{-1} is assigned to the free stretch of the C-terminal ester group, C=O[6]. The next stretch, 1750 cm^{-1}, belongs to the carbamate, C=O[0] group, which is engaged in a C10 hydrogen bonding interaction. The remaining five C=O oscillators, two of which are free, and three of which form C10 hydrogen-bonded rings, are all contained beneath the three remaining experimentally observed transitions. The highly coupled nature of the C=O oscillators makes assignment of this region quite difficult, especially given the resolution of the experimental spectrum. The assigned structure, with an F-F-10-10-10-10 hydrogen bonding pattern indicative of an archetypal 3_{10}-helix, is shown below in Figure 6.3(b).

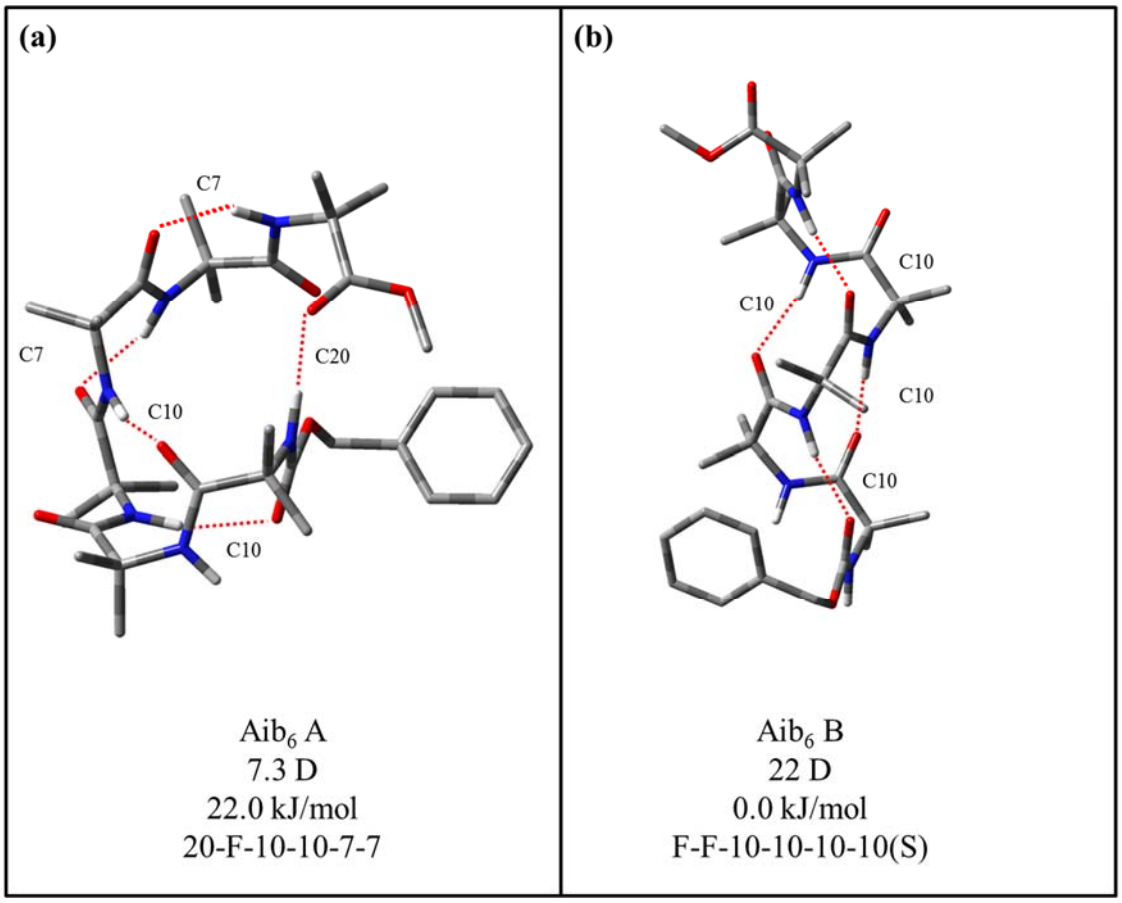

Figure 6.3: (a) assigned structure for conformer A of Aib6. (b) assigned 3_{10}-helical structure for conformer B of Aib6. Dipole moments, relative energies, and H-bonding patterns have been indicated. H-bonds have been labeled, and non-bonding hydrogens have been removed for clarity.

6.4 Discussion

The assigned structures for conformers A and B of Aib6 are shown above in Figure 6.3(a, b). Conformer B adopts the archetypal 3_{10}-helix geometry, having the characteristic ϕ and ψ dihedral angles, shown in Table 6.1, falling in the -57°, -30° range, four C10 hydrogen bonds, and a macrodipole moment of over 22 D. The C-terminal Aib residue adopts a Schellman motif.[14] Given our previously reported findings on the behavior of Aib as a strong 3_{10}-helix former, even when a significant dipole moment is

accumulated, this result is to be anticipated. Conformer A, on the other hand, incorporates a variety of different hydrogen bonding interactions in order to achieve a mixed-helical structure, forming hydrogen bonds in both the N → C and C → N directions. By adopting a mixed helical structure, conformer A dramatically reduces its dipole moment from 22 D in conformer B to just over 7 D. Given the seeming stability of gas-phase 3_{10}-helices observed previously, this is somewhat surprising. However, it is reasonable to predict that at some point the size of the accumulated macrodipole moment is no longer sustainable. At such a point, the peptide will seek out other low lying minima on the potential energy surface. It appears that in the gas phase, at n = 6 for Z-$(Aib)_n$-OMe, a crossover has occurred between a preference for 3_{10}-helical geometry and a preference for a dipole-minimized mixed-helix.

Table 6.1: Structural and energetic comparison of conformers A and B of Z-$(Aib)_6$-OMe: Dihedral angles are given in degrees.

Molecule	Relative Energy (kJ/mol)	H-Bonding Pattern	Ring	ϕ (1)	ψ (1)	ϕ (2)	ψ (2)	ϕ (3)	ψ (3)	ϕ (4)	ψ (4)	ϕ (5)	ψ (5)	ϕ (6)	ψ (6)
Z-$(Aib)_6$-OMe A	22	20-F-10-10-7-7	-97	-60	113	51	36	70	9	-77	33	69	-76	-58	136
Z-$(Aib)_6$-OMe B	0	F-F-10-10-10-10	73	-60	-28	-54	-28	-53	-30	-55	-30	-59	-28	50	40

6.4.1 Energetic Analysis

The energy level diagram for the calculated structures of Z-(Aib)$_6$-OMe within the first 32 kJ/mol of relative energy is given below in Figure 6.4. The available backbone dihedral torsions result in a large number of calculated structures, and clear groupings for conformational families are not observed, except for the F-F-10-10-10-10 family, which is shown in the first column of Figure 6.4. Consequently, structures have been grouped according to the number of hydrogen bonded NH stretches, five, four, or three, and are labeled accordingly in the diagram. No low energy structures having more than three free NH groups were calculated.

The lowest energy calculated structure, a 3_{10}-helix having a dipole moment of 22D, is assigned to conformer B of Aib6, and falls a full 10 kJ/mol lower in energy than the next lowest structure, indicating a clear energetic preference toward the archetypal 3_{10}-helix. However, similarly to the energy level diagram for Z-(Aib)$_4$-OMe (Figure 4.10), there are several structures calculated to adopt the F-F-10-10-10-10 hydrogen bonding pattern spread across a wide range of relative energies. As explained in Chapter 4, these energy differences are, in most cases, attributed to a combination of ring flips and rearrangements of the Aib[1] and Aib[6] residues. Two structures composing a Schellman/non-Schellman pair are also observed, having energies of +11 kJ/mol and +12 kJ/mol, respectively. Outside of the F-F-10-10-10-10 family, there is a paucity of low energy structures. In fact, no structures are calculated to be within 18 kJ/mol of the minimum energy structure.

Conformer A is assigned to a structure incorporating a single free NH group and has a calculated energy of +22 kJ/mol. This structure implements a combination of C20,

C10, and C7 hydrogen bonds to adopt a mixed-helical geometry with a minimized dipole moment of 7D. The remaining structures are spread across a wide variety of hydrogen bonding motifs, none of which presented calculated spectra having a reasonable match our experimentally determined IR data.

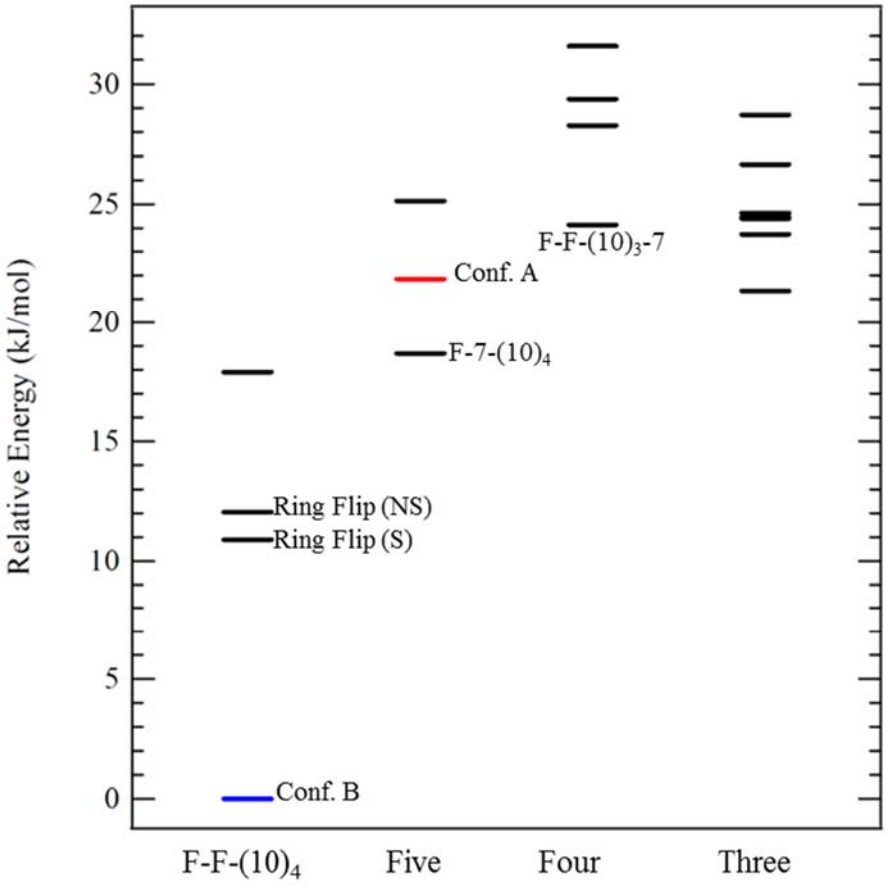

Figure 6.4: Energy level diagram for the calculated structures of Z-(Aib)$_6$-OMe. Structures have been sorted into columns according to the number of hydrogen bonded NH groups. Conformers A and B, along with a few notable structures, have been labeled.

6.4.2 Spectroscopic Analysis

We noted above that the frequency of the UV feature assigned to conformer A of Aib6 is indeed quite close to the frequency of the origin transition of conformer C of Z-(Aib)$_4$-OMe, the structure assigned for the n = 4 system that most resembled a mixed-helix. The appearance of NH stretch transitions within the IR spectrum spread across >200 cm^{-1} also supports this assignment. The feature in the UV spectrum assigned to conformer B is only slightly shifted from the frequency of the A origin in Z-(Aib)$_4$-OMe, which was assigned to a clear 3$_{10}$-helix. In the RIDIR spectrum, the appearance of two, baseline-resolved, free NH stretches, a common feature observed for the F-F-10-10 and F-F-10-7 families in Z-(Aib)$_4$-OMe, nicely reinforces the assignments made above. The breadth of the dominant feature in the RIDIR spectrum of conformer B increases our confidence in its assignment to four strong, C10-bound NH oscillators, all having similar frequencies.

6.4.3 Insights on Conformational Search Procedures

Identifying a suitable assignment for conformer A proved to be quite difficult. At the point of 100 atoms, DFT calculations require significant runtimes, and computational resources must be wisely managed to ensure that chemically realistic and non-redundant searches are being performed. Particularly, the starting structures selected on which to run DFT level calculations must be judiciously selected. As such, we have encountered difficulties based on the implementation of different force fields within our conformational searches. Specifically we found that the choice of force field can have a significant impact on the structures accessible to the conformational search. For

example, implementing the OPLS force field resulted in a set of Aib-based structures that were consistently non-helical.[15,16] In fact, none of the structures reported by the conformational search incorporated 3_{10}-helices. Instead, all were found to incorporate turn geometries that were not supportive of helix formation. Taken on its own, this is not necessarily a concern. However, when the Amber* force field was implemented, nearly 90% of the output structures were found to be helical.[17] Consequently, for the purposes of this investigation, it was necessary to use a mix of Amber* and OPLS results as starting structures for DFT level geometry optimization and frequency calculations. As systems of increasing size continue to be the objects of study, the importance of efficient and comprehensive conformational searches will increase.

6.5 Conclusion

UV and IR spectra of an Aib hexapeptide, Z-$(Aib)_6$-OMe, which is the largest neutral molecule ever studied in the Zwier lab, have been presented. Two dominant features in the UV spectrum are assigned to two fundamentally different conformations. Conformer-specific IR spectra identify the structures of conformers A and B as being a mixed-helix have a dipole moment of ~7 D, and a 3_{10}-Helix, having a macrodipole moment of >22 D. Evaluation of the UV spectrum indicates that the populations of the A and B conformers are in much closer proportion than was observed to be the case in Z-$(Aib)_4$-OMe, where there was a clear preference for formation of a 3_{10}-helix. We surmise that a transition point has been crossed, where the need to minimize the macrodipole moment competes with the structure-directing nature of the dimethylated Aib residues, giving way to significant portions of the population taking up mixed-helical

conformations. The interplay between dipole, electrostatic, and hydrogen-bonding forces is intriguing and merits further investigation, possibly with even larger systems.

6.6 References

(1) Toniolo, C.; Benedetti, E. *Trends in Biochemical Sciences* 1991, *16*, 350.

(2) Toniolo, C.; Bonora, G. M.; Barone, V.; Bavoso, A.; Benedetti, E.; Di Blasio, B.; Grimaldi, P.; Lelj, F.; Pavone, V.; Pedone, C. *Macromolecules* 1985, *18*, 895.

(3) Dean, J. C.; Buchanan, E. G.; Zwier, T. S. *J. Am. Chem. Soc.* 2012, *134*, 17186.

(4) Maekawa, H.; Formaggio, F.; Toniolo, C.; Ge, N.-H. *J. Am. Chem. Soc.* 2008, *130*, 6556.

(5) Meijer, G.; Vries, M. S. d.; Hunziker, H. E.; Wendt, H. R. *Appl. Phys. B* 1990, *51*, 395.

(6) Dean, J. C., Purdue University, 2014.

(7) Morse, M. D. *Experimental Methods in the Physical Sciences* 1996, *29*, 21.

(8) Levy, D. H. *Annual Review of Physical Chemistry* 1980, *31*, 197.

(9) Buchanan, E. G.; James III, W. H.; Choi, S. H.; Guo, L.; Gellman, S. H.; Müller, C. W.; Zwier, T. S. *J. Chem. Phys.* 2012, *137*, 094301.

(10) Choi, J. H.; Ham, S. Y.; Cho, M. *Journal of Physical Chemistry B* 2003, *107*, 9132.

(11) Gord, J. R.; Walsh, P. S.; Fisher, B. F.; Gellman, S. H.; Zwier, T. S. *The Journal of Physical Chemistry B* 2014.

(12) Kusaka, R.; Zhang, D.; Walsh, P. S.; R., G. J.; Fisher, B. F.; Gellman, S. H.; Zwier, T. S. *J. Phys. Chem. A.* 2013, *117*, 10847.

(13) Walsh, P. S.; Kusaka, R.; Buchanan, E. G.; James III, W. H.; Fisher, B. F.; Gellman, S. H.; Zwier, T. S. *J. Phys. Chem. A.* 2013, *117*, 12350.

(14) Schellman, C. In *Protein Folding: Proceedings of the 28th Conference of the German Biochemical Society*; Jaenicke, R., Ed.; Elsevier/North-Holland Biomedical Press: Univsersity of Regensburg: Regensburg, West Germany, 1979, p 53.

(15) Robertson, M. J.; Tirado-Rives, J.; Jorgensen, W. L. *Journal of Chemical Theory and Computation* 2015, *11*, 3499.

(16) Jorgensen, W. L.; Maxwell, D. S.; Tirado-Rives, J. *J. Am. Chem. Soc.* 1996, *118*, 11225.

(17) Cornell, W. D.; Cieplak, P.; Bayly, C. I.; Gould, I. R.; Jr., K. W. M.; Ferguson, D. M.; Spellmeyer, D. C.; Fox, T.; Caldwell, J. W.; Kollman, P. A. *J. Am. Chem. Soc.* 1995, *117*, 5179.

VITA

VITA

Joseph Ronald Gord was born on 29th November 1988, at Home Hospital in Lafayette, Indiana, to Dr. James R. and Renee F. Gord. He grew up in Dayton, OH, with his two brothers, Michael A. and Jeffrey A. Gord. After graduating valedictorian from Dayton Christian High School in 2007, Joseph attended Hillsdale College from whence he received his B.S. in Chemistry, graduating *cum laude* in 2011. From May of 2007 until August of 2011 Joseph worked at Wright-Patterson Air Force Base as a research contractor with Universal Technology Corporation. He was mentored by Drs. Christopher E. Bunker, William Lewis, and Sukesh Roy. In the fall of 2011, Joseph joined the research group of Dr. Timothy S. Zwier. While there, he implemented conformer-specific UV and IR spectroscopy to investigate the hydrogen bonding patterns of model peptide systems as well as solvation of multichromophore molecules. While at Purdue, Joseph met his wife, Kirsten A. (Salter) Gord. He received his Ph.D. in Chemistry in the summer of 2016 and joined the research groups of Drs. Gilbert Nathanson and Timothy Bertram as a post-doctoral researcher at the University of Wisconsin—Madison.

PUBLICATION

THE JOURNAL OF PHYSICAL CHEMISTRY B

Article

pubs.acs.org/JPCB

Mimicking the First Turn of an α-Helix with an Unnatural Backbone: Conformation-Specific IR and UV Spectroscopy of Cyclically Constrained β/γ-Peptides

Joseph R. Gord,[†] Patrick S. Walsh,[†] Brian F. Fisher,[‡] Samuel H. Gellman,[‡] and Timothy S. Zwier*,[†]

[†]Department of Chemistry, Purdue University, 560 Oval Drive, West Lafayette, Indiana 47907, United States

[‡]Department of Chemistry, University of Wisconsin-Madison, Madison, Wisconsin 53706, United States

Supporting Information

ABSTRACT: The folding preferences of two capped, constrained β/γ-dipeptide isomers, Ac-β_{ACPC}-γ_{ACHC}-NHBn and Ac-γ_{ACHC}-β_{ACPC}-NHBn, (designated $\beta\gamma$ and $\gamma\beta$, respectively), have been investigated using single- and double-resonance ultraviolet and infrared spectroscopy in the gas phase. These capped β/γ-dipeptides have the same number of backbone atoms between their N- and C-termini as a capped α-tripeptide and thus serve as a minimal structural unit on which to test their ability to mimic the formation of the first turn of an α-helix. Resonant two-photon ionization and UV−UV hole-burning spectroscopy were performed in the S_0-S_1 region, revealing the presence of three unique conformations of $\beta\gamma$ and a single conformation of $\gamma\beta$. Resonant ion-dip infrared spectra were obtained in the NH stretch region from 3300 to 3500 cm^{-1} and in both the amide I and amide II regions from 1400 to 1800 cm^{-1}. These infrared spectra were compared to computational predictions from density functional theory calculations at the M05-2X/6-31+G(d) level, leading to assignments for the observed conformations. Two unique bifurcated C8/C13 H-bonded ring structures for $\beta\gamma$ and a single bifurcated C9/C13 H-bonded ring structure for $\gamma\beta$ were observed. In all cases, the H-bonding patterns faithfully mimic the first full turn of an α-helix, most notably by containing a 13-membered H-bonded cycle but also by orienting the interior amide group so that it is poised to engage in a second C13 H-bond as the β/γ-peptide lengthens in size. The structural characteristics of the β/γ-peptide version of the 13-helix turn are compared with the α-helix counterpart and with a reported crystal structure for a longer β/γ-peptide oligomer.

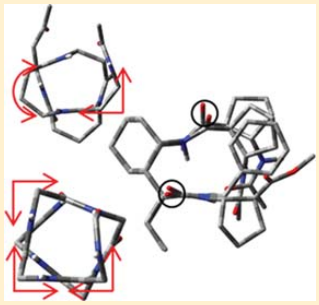

I. INTRODUCTION

One of the primary goals of the field of synthetic foldamers is to build into peptidomimetic structures folding propensities that either mimic those of naturally occurring α-peptides or differ from them in controllable ways that can be used in constructing new folding or binding paradigms. Among the most studied and promising classes of foldamers are β- and γ-peptides, which incorporate either two (β) or three (γ) backbone carbons between adjacent amide groups.[1−6] Their lengthened carbon backbones relative to α-peptides bring the potential for forming many conformations. However, the additional interamide carbons create the possibility of imposing conformational constraints by incorporating backbone carbon−carbon bonds into rings.

While foldamers comprising purely β- or purely γ-amino acid residues serve as important starting points for exploring the conformational properties of unnatural oligomers, heterogeneous backbones, which contain more than one type of residue, offer even greater possibilities for fine-tuning secondary structures and the positions of the side chains, thereby enabling foldamers to interact in specific ways with biomacromolecular targets.[5] β/γ-Peptides in which the β and γ residues alternate have a numerical congruency with α-peptides in that an α-tripeptide ($\alpha\alpha\alpha$) segment has the same number of backbone atoms as a β/γ-dipeptide ($\beta\gamma$ or $\gamma\beta$) segment.[7] The α-helix features a characteristic $i + 4 \rightarrow i$ N−H···O═C H-bonding pattern, and one of these 13-atom H-bonds can be formed by a capped α-tripeptide (e.g., Ac-$\alpha\alpha\alpha$-NHMe). An analogous 13-atom N−H···O═C $i + 3 \rightarrow i$ H-bond can be formed by a capped β/γ-dipeptide (e.g., Ac-$\beta\gamma$-NHMe or Ac-$\gamma\beta$-NHMe). This H-bond similarity has led to an interest in 1:1 β/γ-peptides with an alternating backbone pattern as potential structural mimics of an α-helix.[8]

Some efforts to mimic α-helical turns with β/γ segments have involved flexible subunits,[7,9,10] but Guo et al.[11] described β/γ-peptides in which both the β and γ subunits are cyclically constrained. That study included crystallographic analysis of a pentameric β/γ-peptide that displayed only C13 H-bonds in the solid state. NMR data for an analogous hexameric β/γ-peptide in a nonpolar solvent suggested a similar helical conformation. Vasudev et al.[12] described the crystal structure of

Special Issue: James L. Skinner Festschrift

Received: February 13, 2014
Revised: March 17, 2014
Published: April 2, 2014

ACS Publications © 2014 American Chemical Society

dx.doi.org/10.1021/jp5015884 | J. Phys. Chem. B 2014, 118, 8246−8256

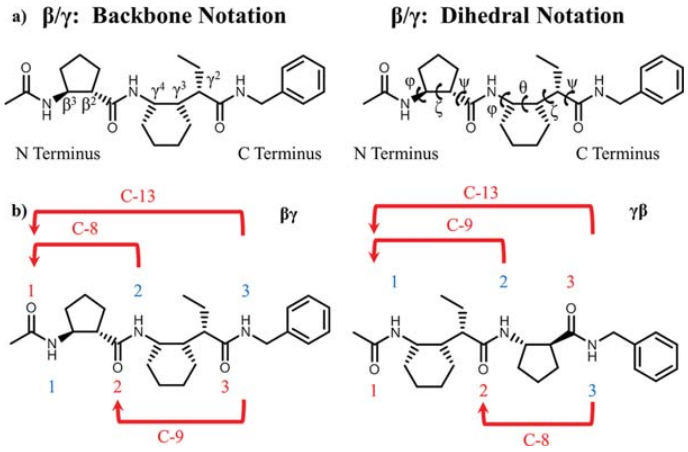

Figure 1. Schematic representation of the molecules to be studied in this work: (a) backbone and dihedral notation; (b) potential H-bonding patterns for $\beta\gamma$ and $\gamma\beta$.

a heterogeneous tripeptide displaying a C13 H-bond across a $\beta\gamma$-dipeptide unit, but other gabapentin-containing oligomers were found to display different H-bonding patterns.

The present work involves the study of the single-conformation spectroscopy of the two prototypical cyclically constrained, capped β/γ-dipeptides shown in Figure 1 in the gas phase. The goal of this work is to determine whether the preorganization in these small oligomers is sufficient to enable the formation of the first C13 H-bond or whether alternative structures containing different H-bonds are favored instead. Studying these molecules under jet-cooled conditions in the gas phase allows the inherent conformational preferences in the absence of solvent to be observed, and a direct comparison with calculations on isolated molecules can be made. Incorporation of an aromatic ring in the C-terminal benzyl cap enables the use of double-resonance laser spectroscopy to record single-conformation spectra both in the IR and UV regions.

This conformational analysis of β/γ-peptides in the gas phase builds on earlier studies of a similar nature focused on unconstrained β-peptides,[13,14] γ-peptides,[15,16] and mixed α/β-peptides.[2] In these cases, the simple backbone substitutions provided little in the way of strict steric constraints for the peptide backbone, producing a large number of conformational isomers that spanned a wide range of H-bonding patterns, including single-ring, sequential double-ring, and bifurcated double-ring structures. A subset of these conformers representing the full range of structures was used to create a test set of conformers for which the uncoupled site frequencies and amide I/I and amide II/II couplings could be determined.[17]

More recently, we have studied a series of small peptidic foldamers that contain cyclically constrained β or γ residues like those incorporated into the model foldamers considered here, including α/β-peptides,[18] γ-peptides,[19] and mixed α/γ-peptides.[2,13−16,18,20,21] In each case, an aromatic ring was incorporated into the structure to provide an ultraviolet chromophore for double-resonance spectroscopy. In the α/β-peptides, this was accomplished by a Phe side chain in the α-peptide subunit, while in the constrained γ- and α/γ-peptides and in the present study on constrained β/γ-peptides, the phenyl ring is a part of the C-terminal benzyl cap (Figure 1). This position of the phenyl cap at the end of the backbone enables a clearer look at the conformational preferences of the constrained backbones, an especially important aspect of the present work where cyclic constraints are built into both the β and γ subunits.

The β-amino acid *trans*-2-aminocyclopentanecarboxylic acid (ACPC) has the Cα−Cβ bond incorporated into a cyclopentyl ring. This cyclic constraint in our β/γ-peptides is intended to elicit a strong preference for an interior dihedral angle ζ in the 80−95° range for the Cα−Cβ bond.[22−24] With this constraint, the ACPC residue produces a gauchelike configuration for the two adjacent amide groups, thereby preorganizing the formation of a turn in the foldamer backbone. In the γ subunits, the Cβ−Cγ incorporated into a cyclohexyl ring (ACHC). This cyclic constraint in combination with the ethyl side chain at the Cα position (γ^2; Figure 1) predisposes the θ and ζ dihedral angles of the γ subunit to prefer gauche$^+$ configurations; the sequence of two consecutive gauche$^+$ torsion angles leads to a strong local turn-forming propensity.[25]

While the α/β- and α/γ-peptides containing ring−constrained β or γ residues showed some conformational diversity, a degree of preorganization was evident. The large C11 (α/β) and C12 (α/γ) single rings that represent the first H-bonded turn of an 11-helix or 12-helix, respectively, were among the structures observed, but these were in competition with conformers having different H-bonding architectures. In the recent study of γ-peptides with constrained residues, the corresponding capped triamide ($\gamma\gamma$) was almost entirely folded into a C14 single-ring structure that represents the first H-bonded turn of a 14-helix. Indeed, the peptide backbone of this C14 structure was calculated to be nearly identical to that of a di-γ-peptide segment within the 14-helix observed in the crystalline form of a constrained γ-peptide hexamer.[19,26] As shown below, the two cyclically constrained β/γ-peptides studied in the present work are almost entirely folded into C13 structures, thereby forming the H-bonded first turn of the β/γ-peptide analogue of the α-helix. The properties of this α-helix analogue will be considered in some detail relative to its natural counterpart.

dx.doi.org/10.1021/jp5015884 | *J. Phys. Chem. B* 2014, 118, 8246−8256

II. EXPERIMENTAL AND COMPUTATIONAL METHODS

Solid samples of the molecules of interest were placed in an oven located directly behind a pulsed valve with a 500 μm diameter orifice. Samples were heated to approximately 220 °C in order to generate the required vapor pressure. The sample was entrained in pure neon (~3 bar), and the pulsed valve was operated at a rate of 20 Hz. The supersonic expansion was passed through a 3 mm conical skimmer to form a molecular beam, which was subsequently interrogated in the ionization region of a 1 m linear time-of-flight (TOF) mass spectrometer.

The methods used here have been reported in detail elsewhere, so only a cursory explanation will be provided.[27] Electronic excitation spectra were obtained using resonant two-photon ionization (R2PI) by crossing the molecular beam at 90° in the ionization region of the Wiley–McLaren[28] linear TOF mass spectrometer using the doubled output of a Radiant Dyes NarrowScan dye laser (<1 mJ/pulse) pumped by the third harmonic of a Continuum Surelite II Nd:YAG laser. The ions arriving in the parent mass channel (m/z = 427) were detected with a microchannel plate ion detector. Action spectra in which the mass-resolved ion signal was plotted as a function of wavelength were then generated. These spectra contained contributions from all of the conformational isomers present in the expansion.

Single-conformation UV spectra were then obtained using UV–UV hole-burning (UVHB) spectroscopy. In this case, UVHB spectra were obtained by counterpropagating the doubled output of a second dye laser (Lambda-Physik ScanMate) operated at 10 Hz with the output from the 20 Hz probe laser. The two beams were spatially overlapped and temporally separated such that the hole-burning laser preceded the probe laser by 200 ns. The wavelength of the hole-burning laser was fixed on a specific vibronic transition identified in the R2PI spectrum, while the probe laser was scanned through the S_0–S_1 origin region. Depletion was monitored using the active baseline subtraction mode of a gated integrator (Stanford Research) to record the difference in ion intensity created by the hole-burning laser as the probe laser was tuned. When the probe laser was scanned to a vibronic transition originating from the same zero-point level as the isomer interrogated by the hole-burning laser, the depletion in ion signal was recorded.

Single-conformation infrared spectra were recorded via resonant ion-dip infrared (RIDIR) spectroscopy, a second double-resonance hole-burning technique, in which the hole-burning laser, now in the infrared, was produced by an optical parametric converter (LaserVision). In this case, the IR laser was tuned while the UV probe laser was fixed on a transition identified as being due to a particular conformational isomer. When the IR laser was resonant with a ground-state vibrational transition sharing the same ground-state level as that interrogated by the probe, molecules were removed from the ground state, and depletion was detected in the ion signal generated by the UV pulse. The difference between the ion signals for sequential IR "on" and IR "off" pulses was recorded as a function of wavenumber. Spectra in the NH stretching region from ~3300 to 3500 cm^{-1} were obtained with pulse energies of 3–10 mJ/pulse. Spectra in the amide I and II regions were obtained by frequency mixing of the signal and idler outputs in an additional $AgGaSe_2$ crystal in the final mixing stage to generate mid-IR output having pulse energies of ~300–500 μJ/pulse.

Computational predictions of spectra and geometry optimizations were determined by first performing a conformational search within the AMBER* force field using MacroModel[29] and a 100 kJ/mol energy window with no torsion check. The structures of approximately 50 of the lowest-energy conformations from each search were then optimized with Gaussian 09[30] using density functional theory (DFT) at the M05-2X/6-31+G(d) level.[31] Additional parameters were "int=grid=ultrafine" and "scf=tight". The harmonic vibrational frequencies and infrared intensities were calculated for all of the conformers and compared with the experimental values after scaling of the NH stretch region by 0.94 and the amide I/II region by 0.96.[32] The scaled calculated spectra most closely matching the intensity and frequency patterns in the observed experimental spectra were used to assign calculated structures to the experimental spectra. The relative energies of the calculated structures were then used as a sanity check to ensure that only energetically realistic structures were selected for assignments.

III. NOMENCLATURE

The nomenclature used to label different conformations is based on that used in our previous studies of constrained γ-peptides[19] and α/γ-peptides.[21] The various conformations are grouped into families that differ from one another first and foremost by their different H-bonding arrangements. Hydrogen bonds formed between amide NH and C=O groups are characterized primarily by the number of atoms in the cycle that is formed between the donor H and acceptor O group. This is done using a Cn notation, where n indicates the number of atoms in the cycle.[17] At times, a Cn ring of a given size can be formed from peptide backbones that differ in one or more of the backbone dihedral angles, with four unique angles (ϕ, θ, ζ, ψ) describing the γ-peptide subunit and three (ϕ, ζ, ψ) describing the β-peptide subunit (Figure 1a). The orientation of the ethyl side chain on the γ-peptide and the phenyl ring on the benzyl cap are also incorporated into the labeling scheme. The C_β–C_γ–$C_{ethyl,\alpha}$–$C_{ethyl,\beta}$ dihedral angle for the ethyl group and the C–N–C–C_{phenyl} dihedral angle for the phenyl ring are labeled as anti (a), gauche$^+$ (g+), or gauche$^-$ (g–) for dihedral angles measuring nominally ±180°, +60°, and −60°, respectively. A fully named structure would include the base name of the peptide, the H-bonding pattern, and then the orientations of the ethyl and phenyl rings, for example, $\beta\gamma$ C8/13 (a, g–).

IV. RESULTS AND ANALYSIS

A. Ac-β_{ACPC}-γ_{ACHC}-NHBn ($\beta\gamma$). The R2PI spectrum of $\beta\gamma$ from 37 240 to 37 750 cm^{-1} is shown as the top trace in Figure 2, with a series of UV–UV hole-burning spectra below it. Asterisks in the UVHB spectra indicate the transitions used for hole-burning in recording each spectrum. The R2PI spectrum is characterized by two clear sets of progressions, which the UVHB spectra below it identify as belonging to different conformational isomers. Conformer **A** has its S_0–S_1 origin transition at 37 420 cm^{-1} and has members of a Franck–Condon progression separated by ~18 cm^{-1}. This progression is due to a low-frequency torsional mode involving motion of both the ACPC and phenyl rings. The set of transitions assigned to conformer **B** begins 67 cm^{-1} to the red of **A**, with its S_0–S_1 origin at 37 353 cm^{-1}, and shows a somewhat shorter progression in a 20 cm^{-1} mode. The Franck–Condon activity

dx.doi.org/10.1021/jp5015884 | J. Phys. Chem. B 2014, 118, 8246–8256

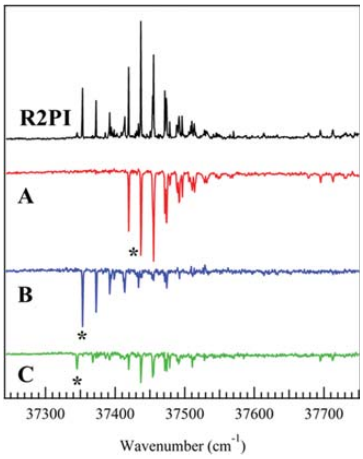

Figure 2. R2PI (black) and UVHB (red, blue, green) spectra taken in the S_0-S_1 region of $\beta\gamma$. Asterisks in A, B, and C indicate the vibronic transitions to which the hole-burn laser was set to collect UVHB spectra.

in these low-frequency modes indicates some degree of interaction between the phenyl ring and the rest of the molecule.

Transitions due to a third, minor conformer (conformer **C**) begin at 37 345 cm^{-1}. This peak was initially thought to be a hot band, but several attempts to induce intensity via warming of the expansion by modifying the expansion conditions (backing pressure, etc.) were unsuccessful, allowing us to tentatively assign it to an origin transition of a minor conformer. However, because of its weak intensity, no further investigation was carried out on it. It should be noted that the progression significantly blue-shifted from the origin is due to incomplete subtraction from the spectrum of conformer **A**.

The top traces in Figure 3a show RIDIR spectra obtained for conformations **A** (red) and **B** (blue) of $\beta\gamma$ in the amide I (1600−1800 cm^{-1}) and amide II (1450−1600 cm^{-1}) regions, while Figure 3b shows the analogous RIDIR spectra in the 3300−3500 cm^{-1} region associated with the amide NH stretch fundamentals. Only two of the three C═O stretch transitions are resolved in conformer **A**, while all three can be seen in **B**, with a closely spaced pair appearing at 1698 and 1705 cm^{-1}. Interestingly, in these spectra the transitions in the amide II region (nominally NH bend fundamentals) are significantly more intense than their amide I C═O stretch counterparts. In many circumstances, just the reverse is found.[17] Several small bands found in the 1400−1480 cm^{-1} region are tentatively assigned to CH bend fundamentals. The amide I/II regions of the two conformers are very similar to one another, suggesting that they are members of the same H-bonded family.

As expected on the basis of the number of amide groups, three NH stretch fundamentals are present in the spectrum of **A**, with a free amide NH stretch at 3467 cm^{-1}, a weakly H-bonded NH stretch at 3442 cm^{-1}, and a more strongly H-bonded NH stretch at 3372 cm^{-1}. The fact that the 3467 cm^{-1} peak is due to a free NH stretch is borne out by comparison with the free amide NH stretch fundamentals in the constrained γ-peptides[19] and α/γ-peptides[21] studied previously, which appear within a few cm^{-1} of this frequency. The NH stretch region of conformer **B** is generally similar to that of **A** but differs most substantially in having its lowest-frequency fundamental shifted up in frequency (3385 cm^{-1}) and its middle transition shifted down in frequency (3418 cm^{-1}) relative to **A**. The two spectra are quite similar in appearance and have a similar trade-off in frequency shifts as the two C9/C12 bifurcated double-ring structures of $\alpha\gamma$.[21]

Figure 3 also presents a comparison of the experimental RIDIR spectra with the predictions of M05-2X/6-31+G(d) DFT calculations for the best-fit vibrational frequencies and infrared intensities (shown as stick spectra below the experimental spectra). The structures associated with these simulated IR spectra are shown in Figure 4. Both structures are

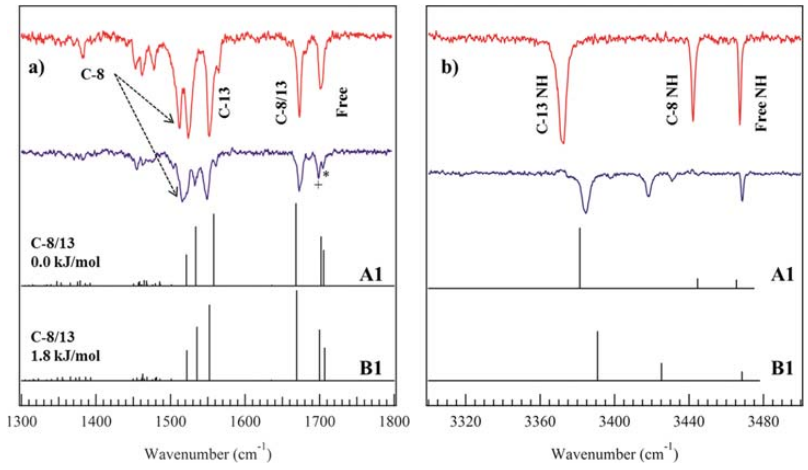

Figure 3. RIDIR spectra of conformers **A** (in red) and **B** (in blue) of $\beta\gamma$ in the (a) amide I/II and (b) NH stretch regions. Scaled calculated harmonic vibrational frequencies and IR intensities are given in the stick spectra. Harmonic frequencies were calculated using DFT at the M05-2X/6-31+G(d) level. Structural assignments of the transitions in each region are indicated. The scale factor in the amide I and II region (a) is 0.96, and the scale factor in the NH stretch region (b) is 0.94.

dx.doi.org/10.1021/jp5015884 | J. Phys. Chem. B 2014, 118, 8246−8256

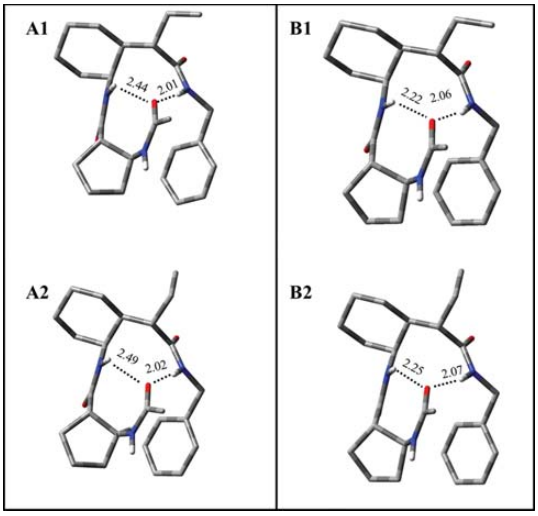

Figure 4. Assigned structures (hydrogens removed) based on computational fits to the RIDIR spectra of Ac-β_{ACPC}-γ_{ACHC}-NHBn. H-bonds are indicated with dashed lines, and their lengths are given in Å. Conformer **A1** was determined to be the global minimum. Conformers **B1** and **B2** are distinct from conformers **A1** and **A2** on the basis of their H-bonding patterns. Pairs **1** and **2** differ from each other primarily in the position of the ethyl group (anti and gauche, respectively) for both **A** and **B**.

C8/C13 bifurcated double rings that differ in subtle ways from one another. Structural pairs **A1**/**A2** and **B1**/**B2** differ along the 1/2 designation primarily in having different ethyl group orientations, while the **A** structures differ from the **B** structures in the length of the C8 and C13 H-bonds, with a shorter C13 bond (by ∼0.06 Å) and longer C8 bond (by ∼0.2 Å) in **A** than in **B**.

The close correspondence between experiment and calculation enables assignment of the observed infrared bands to particular aspects of the C8/C13 bifurcated double-ring structures responsible for them. In the NH stretch region (Figure 3b), the highest-frequency NH stretch transition of both conformers of $\beta\gamma$ is due to a free NH stretch of the N-terminal NH[1] group. The middle transition is due to NH[2], which forms a C8 H-bonded ring with C═O[1], while the lowest-frequency, most intense NH stretch transition is due to NH[3], which forms a C13 H-bond to the same C═O[1] group in closing the second segment of the bifurcated C8/C13 double-ring structure. The larger frequency shift and greater intensity of the C13 NH stretch transition relative to the C8 fundamental reflects the short, strong H-bond formed by the C13 ring.

The fact that C═O[1] acts as a double acceptor while the other two C═O groups are free is also borne out by the appearance of the spectrum in the amide I region. The amide I fundamentals due to the two free C═O groups appear at nearly identical frequencies, just above 1700 cm^{-1}. The transition due to C═O[1], which appears at 1673 cm^{-1}, is shifted down in frequency as is characteristic of such bifurcated double-ring acceptors.[17]

Finally, the amide II region shows reflection symmetry with respect to the NH stretch region. The highest-frequency amide II fundamental (1552 cm^{-1}) is associated with the strong C13 H-bond, as anticipated on the basis of a stiffening of the NH bend in the presence of a linear H-bond.[17] The free and C8 NH bends are close in frequency, reflecting the unusually weak nature of the C8 H-bond. Figure 4 shows the NH···O═C H-bond distances in the calculated structures. In the global-minimum structure, assigned to conformer $\beta\gamma$(**A**), the C13 H-bond length is 2.01 Å, while the C8 H-bond length is 2.44 Å. As anticipated, the lower frequency of the C13 NH stretch fundamental arises in part because of the short, strong H-bond formed.

The most striking difference in the spectrum of conformer $\beta\gamma$(**B**) relative to that of $\beta\gamma$(**A**) is the shift to lower frequency of the C8 NH stretch fundamental and the corresponding shift to higher frequency for the C13 NH stretch transition. These shifts are properly captured by both the **B1** and **B2** structures, which differ only in the ethyl group orientation, and we cannot distinguish between them with certainty. The structural changes accompanying these shifts are consistent with strengthening of the C8 H-bond, which is shortened from 2.44 to 2.24 Å, and a corresponding, but smaller, weakening of the C13 H-bond, which is elongated from 2.01 to 2.07 Å. On the basis of energetics, it is likely that the **A1** and **B1** structures are observed experimentally, but these structural differences are inconsequential relative to the firmly established C8/C13 bifurcated double ring that constitutes the first turn of a 13-helix.

The assigned structures make possible a clearer interpretation of the Franck−Condon activity observed in the R2PI spectrum. The long progressions in the R2PI/UVHB spectra involve the lowest-frequency modes of the molecules, in which the entire framework of the helix cycle rocks back and forth. The assigned structures lack a specific π H-bond with the ring (as evidenced by the IR spectra), and therefore, the interaction with the π cloud is via van der Waals interactions, which are unlikely to have a major effect on the relative energies of the structures even if the benzyl cap were removed.

B. Ac-γ_{ACHC}-β_{ACPC}-NHBn ($\gamma\beta$). The R2PI spectrum of $\gamma\beta$ from 37 380 to 37 750 cm^{-1} is shown as the top trace in Figure 5. The UVHB spectrum, shown below it, was recorded with the UVHB laser fixed on the transition at 37 483 cm^{-1}, marked by an asterisk in the figure. All of the transitions in the R2PI spectrum burn together, indicating that all of the transitions in this region are vibronic transitions due to a single conformational isomer of $\gamma\beta$, with its S_0−S_1 origin at 37 483 cm^{-1}. The extent of this Franck−Condon activity indicates substantial involvement of the aromatic ring with other parts of the molecule, with electronic excitation changing the geometry along these low-frequency modes in the excited state. Three progressions were identified in the spectrum, involving low-frequency modes with frequencies of 21, 31, and 37 cm^{-1}, labeled as Z, Y, and X, respectively, in Figure 5.

Figure 6a,b shows RIDIR spectra of the single conformer of $\gamma\beta$ in the amide I/II and NH stretch regions, respectively. In the spectrum for the amide I region, all three C═O stretch fundamentals are now well-resolved, while only a pair of transitions are resolved in the amide II region. The broadening of the low-frequency transitions at 1532 cm^{-1} suggests the possibility that a pair of unresolved transitions contributes to this breadth. The NH stretch region looks very similar to that of conformer **B** of $\beta\gamma$ (Figure 3b), having a free NH stretch fundamental at 3472 cm^{-1} and H-bonded NH stretch transitions at 3412 and 3370 cm^{-1}. The resemblance of the RIDIR spectrum of the single conformer of $\gamma\beta$ with the pair of

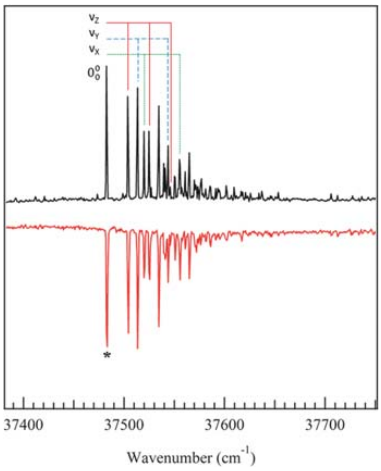

Figure 5. R2PI (black) and UVHB (red) spectra for Ac-γ_{ACHC}-β_{ACPC}-NHBn in the S_0−S_1 region of $\gamma\beta$ collected by monitoring the ion signal in the monomer mass channel. The asterisk indicates the transition to which the laser was set to collect the hole-burning spectrum. Progressions marked Z, Y, and X correspond to low-frequency modes with frequencies of 21, 31, and 37 cm^{-1}, respectively.

conformers observed for $\beta\gamma$ argues that it belongs to a similar bifurcated double ring conformational family.

This is borne out by the calculated IR spectrum of the global minimum structure for $\gamma\beta$, which is shown as the stick spectrum in Figure 6. The fit to experiment is excellent. As anticipated, the $\gamma\beta$ structure is a bifurcated double ring, but here it is a C9/C13 rather than a C8/C13 structure because the reversal of the β-peptide and γ-peptide subunits produces a C9 nearest-neighbor H-bond across the γ-peptide as the first segment of the bifurcated ring in $\gamma\beta$, rather than the C8 structure associated with the β-peptide subunit in $\beta\gamma$. The best-fit

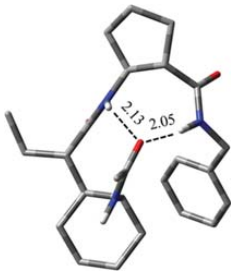

Figure 7. Assigned structure for Ac-γ_{ACHC}-β_{ACPC}-NHBn. H-bonds are indicated by dashed lines and NH···O distances are given in Å.

structure, shown in Figure 7, was also calculated to be the global minimum. As we might expect, similar to $\beta\gamma$, there is a pair of calculated structures share the same backbone conformation and differ only in the ethyl group orientation. However, in $\gamma\beta$, the energy cost is significantly higher (∼12 kJ/mol). This can be seen in Table 1. Again, however, there is a negligible impact on the calculated IR spectrum (Figure S4 in the Supporting Information), making an assignment to the C9/C13 H-bonding architecture firm. On the basis of energetics, in what follows we refer to structure $\gamma\beta$(**A1**) as the assigned structure for $\gamma\beta$.

The NH stretch fundamentals due to the C9 (NH[2]) and C13 (NH[3]) H-bonded rings have transitions appearing at 3412 and 3370 cm^{-1} respectively (Figure 6b). The C13 NH stretch is very near its value in the two conformers of $\beta\gamma$. However, as with their C8/C13 counterparts, the frequency of the C9 H-bond is almost 100 cm^{-1} above its value in an isolated C9 ring.[19] This is a consequence of the longer H-bond distance (2.13 Å vs 1.93 Å in γ) and the weakening associated with formation of a bifurcated double ring.

The spectra of $\gamma\beta$ in the amide I and II regions (Figure 6a) are also similar in appearance to their $\beta\gamma$ counterparts. However, in this case the two free C═O stretch transitions

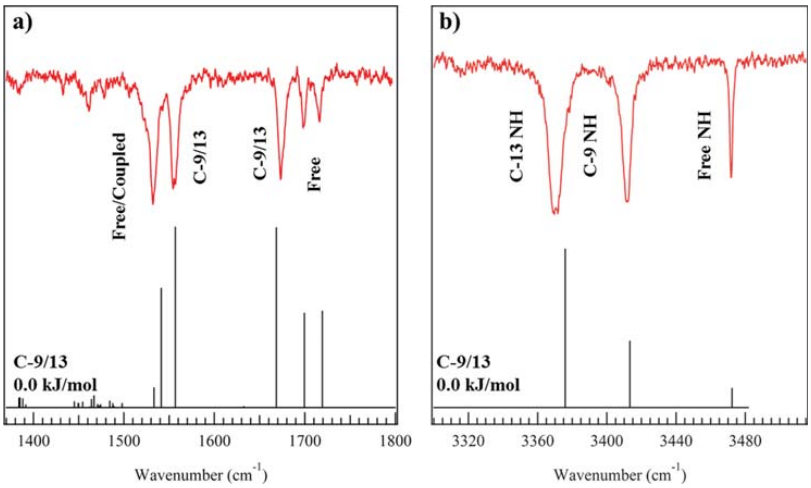

Figure 6. RIDIR spectra of $\gamma\beta$ (red) and scaled calculated harmonic vibrational frequencies and IR intensities of $\gamma\beta$ calculated using DFT at the M05-2X/6-31+G(d) level (stick spectra). Structural assignments of the transitions in each region are indicated. The scale factor in the amide I and II region (a) is 0.96, and the scale factor in the NH stretch region (b) is 0.94.

dx.doi.org/10.1021/jp5015884 | J. Phys. Chem. B 2014, 118, 8246−8256

Table 1. Structural and Energetic Comparison of Low-Energy Conformers of Foldamers $\beta\gamma$ and $\gamma\beta$

$\beta\gamma$ Molecules										
		dihedral angles (deg)[a]							H-bond lengths (Å)	
molecule	ΔE (kJ/mol)	φ_β	ζ_β	ψ_β	φ	θ	ζ	ψ	C13	C8
$\beta\gamma$ C8/C13 (*a*, *g*−) [**A1**]	0.00	−68	132	−103	−168	59	51	−122	2.01	2.44
$\beta\gamma$ C8/C13 (*g*−, *g*−) [**A2**]	5.92	−68	133	−104	−166	57	53	−131	2.02	2.49
$\beta\gamma$ C8/C13 (*a*, *g*−) [**B1**]	1.78	−70	127	−92	−171	58	48	−121	2.06	2.22
$\beta\gamma$ C8/C13 (*g*−, *g*−) [**B2**]	7.60	−70	126	−95	−168	57	51	−128	2.07	2.24
$\beta\gamma$ C8/C13 (*a*, *g*−)	0.32	−65	134	−103	−161	58	46	−115	1.97	2.4
$\beta\gamma$ C8/C13 (*a*, *a*)	1.40	−64	118	−128	−142	58	51	−112	1.93	2.94
$\beta\gamma$ C8/C13 (*g*−, *a*)	7.81	−66	135	−102	−161	57	49	−120	1.98	2.45

$\gamma\beta$ Molecules										
		dihedral angles (deg)[a]							H-bond lengths (Å)	
molecule	ΔE (kJ/mol)	φ	θ	ζ	ψ	φ_β	ζ_β	ψ_β	C13	C9
$\gamma\beta$ C9/C13 (*a*, *g*−) [**A1**]	0.00	−110	62	75	−115	−140	90	−90	2.04	2.13
$\gamma\beta$ C9/C13 (*g*+, *g*−)[**A2**]	11.78	−109	64	73	−117	−138	91	−90	2.04	2.14
$\gamma\beta$ C13 (*a*, *g*−)	2.16	−153	59	61	−113	−114	95	−112	1.97	N/A
$\gamma\beta$ C13 (*a*, *g*−)	6.53	−141	53	35	70	65	83	−127	1.95	N/A
$\gamma\beta$ C13 (*g*−, *g*−)	10.27	−155	59	58	−117	−103	93	−117	1.97	N/A

Additional Molecules								
		dihedral angles (deg)[a]						
molecule	family	φ_β	ζ_β	ψ_β	φ	θ	ζ	ψ
$\beta_{ACPC}\alpha$[b]	C7/C8a	~ −70	~130	~ −60				
β-γ-β-γ-β[c]	α-helix							
β_1		−108	93	−128				
γ_2					−135	60	60	−121
β_3		−134	114	−86				
γ_4					−147	58	47	−130
β_5		−168	141	−155				
γ[d]	C9				−106	66	75	−103
$\gamma\gamma$ (1)[d]	C14				−158	61	67	−115
$\gamma\gamma$ (2)[d]	C14 F/C9/C12				−161	59	56	−132
$\gamma\alpha$[e]					−105	62	71	−126
$\alpha\gamma$[e]	C5/F/C9				−103	66	76	−103

[a]Dihedral angles are defined in Figure 1. [b]Reference 18 (several structures, see reference). [c]Reference 11. [d]Reference 19. [e]Reference 21.

are well-separated from one another at 1716 cm^{-1} (C═O[3]) and 1698 cm^{-1} (C═O[2]). In the amide II region, the calculations predict that only two of the three NH bend fundamentals have appreciable intensity. In this case, the amide II vibrations are quite mixed, with significant amplitude on two of the three NH groups. The highest-frequency transition at 1554 cm^{-1} is assigned to an in-phase mixture of C13 and C9 NH motion. The band at 1532 cm^{-1} is primarily the free NH[1] bend, while the weak transition a few cm^{-1} below this (unresolved in the experimental spectrum) has out-of-phase contributions from the C9 NH[2] counteracted by out-of-phase motion of the C13 and free NH groups, leading to a near cancellation in its intensity.

It is worth noting that the assigned structure has its three lowest-frequency modes calculated at 28, 32, and 37 cm^{-1} (ground state), in good correspondence with the progressions Z, Y, and X observed in the R2PI spectrum, respectively. All three of these modes involve substantial motion of the cyclohexyl and phenyl rings relative to one another, as the single turn positions the two in close proximity to one another. Upon excitation of the π−π^* transition, the structure distorts along these low-frequency modes, giving rise to the observed Franck−Condon activity.

V. DISCUSSION

A. Conformational Preferences of $\beta\gamma$ and $\gamma\beta$. The present results on two prototypical β/γ-peptides provide a first look at the conformational preferences of the β/γ-peptide backbone in the gas phase. Unlike many of the early studies from our group on other homogeneous[13−16,19,20] and heterogeneous[2,18,21] foldamers, both the β and γ subunits studied are conformationally constrained by incorporation of a ring into the backbone: a cyclopentyl ring in the β subunit and a cyclohexyl ring in the γ subunit. As previously observed for other small foldamers containing ring-constrained subunits, the number of conformations observed in the expansion-cooled sample is small. In $\gamma\beta$, the conformational population is dominated by a single conformational isomer. In $\beta\gamma$, two conformers are observed, but these two structures belong to the same conformational family, with only minor differences between them.

Independent of the order of the β and γ subunits, the major intramolecular H-bond occurs in a 13-atom ring. This structure is secondarily stabilized by an additional NH···O═C H-bond involving NH[2] and C═O[1], forming either a C8 ($\beta\gamma$) or C9 ($\gamma\beta$) H-bonded ring, which in concert with the C13 H-bond results in a bifurcated double-ring structure. The C13 H-bond distance calculated for the assigned C9/C13 structure is almost

dx.doi.org/10.1021/jp5015884 | J. Phys. Chem. B 2014, 118, 8246−8256

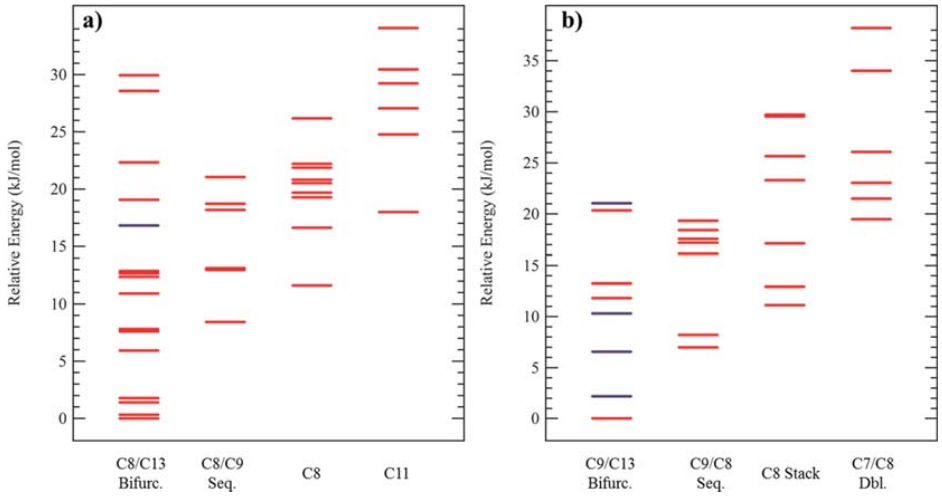

Figure 8. Energy level diagrams for the conformational minima of (a) $\beta\gamma$ and (b) $\gamma\beta$, calculated using DFT at the M05-2X/6-31+G(d) level. Columns are sorted by family (Bifurc. = bifurcated double ring, Seq. = sequential double ring, and Stack = amide-stacked). The blue markers indicate structures that contain only a C13 H-bond but otherwise have the characteristics of the C8/C13 bifurcated or C9/C13 bifurcated families.

identical to the C13 H-bond distance seen in both C8/C13 conformers **A** and **B** in $\beta\gamma$.

The different subunit order in $\beta\gamma$ versus $\gamma\beta$ leads to some interesting effects on the foldamer backbones and the dihedral angles they support (Table 1). Both the C8/C13 and C9/C13 bifurcated double-ring structures orient all three amide groups so that they point in the same direction, with the acceptor C═O on the N-terminal acyl cap accepting H-bonds from donor NH groups on the interior and C-terminal NHBn caps (Figure 1).

In $\beta\gamma$, the cyclopentyl bridges between amide groups are involved in a C8 H-bonded ring, with the C═O group of the γ residue oriented toward the NH of the benzyl cap. This arrangement produces a central ζ_β torsion angle (Cα−Cβ) near 130°, which is unusually large relative to ACPC residues in helical conformations.[22−24] In contrast, the ACPC residue in $\gamma\beta$ spans two amide groups that both act as NH donors, leading to ζ_β near 90°, which is in the range typically seen for ACPC residues within helical secondary structures.

The γ residue displays distinct dihedral preferences in response to the donor/acceptor nature of the neighboring amide groups. In contrast to the ACPC residues, the γ residues display central dihedral angles (θ, ζ) that are always near their optimal values of 60−70° whether they are involved in a C9 H-bond or not. However, the angle ϕ varies as a result of different sequence contexts for the γ residues, with values near −110° in $\gamma\beta$ conformations that form a C9 ring and opening up to values near −160° to −170° when both NH groups are involved in H-bonds, as in the C8/C13 double rings in $\beta\gamma$.

In assessing the degree to which our two constrained β/γ-peptides are locked into structures that support C13 H-bonds, we must compare the relative energies of the C13 structures with the energies of other structures that feature different H-bonding patterns. To that end, we carried out an exhaustive search of the potential energy surface and optimized all of the conformational minima in the first ∼40 kJ/mol using DFT at the M05-2X/6-31+G(d) level. The calculated relative energies of all of the conformational minima, grouped by conformational family, are summarized in the energy level diagrams for $\beta\gamma$ and $\gamma\beta$ shown in Figure 8a,b, respectively. Calculated structural families include bifurcated double rings, sequential double rings, single rings, and single-ring/amide-stacked composites. Analogues of these H-bonding patterns have been observed previously in both α-peptides and synthetic foldamers,[17] but for $\beta\gamma$ and $\gamma\beta$ they are expanded to ring sizes appropriate for the β/γ-peptides.

As Figure 8 nicely illustrates, structures that incorporate a C13 H-bond are clearly preferred over all alternatives, with energies at least 7 kJ/mol lower than those of the most stable C8/C9 or C9/C8 sequential double rings. The large number of low-energy C8/C13 structures for $\beta\gamma$ (Figure 8a) reflects the presence of two structural types (**A** and **B**) that differ in the strength of two H-bonds that share a common amide C═O acceptor group in what is otherwise a similar H-bonding architecture. In addition, for each backbone dihedral configuration, there are several conformations that differ in the position of the ethyl side chain, the orientation of the phenyl ring, and the cycle conformation.[18] The different phenyl ring orientations have energies spread over ∼2−5 kJ/mol, while reconfiguration of the ethyl group from its preferred *a* orientation to a *g*− orientation raises the energy of the conformer by ∼5.8 kJ/mol for $\beta\gamma$, while the analogous rotation of the ethyl group from *a* to *g*+ in $\gamma\beta$ comes at the cost of ∼12 kJ/mol.

In Figure 8b, we have combined the C9/C13 and single-ring C13 structures into a single column (the latter colored in blue). The fact that these single-ring structures are near in energy to their C9/C13 counterparts illustrates clearly how weak and nonoptimal the C9 H-bond is relative to its isolated counterpart (e.g., that in γ; Table 1).[19] The orientation most suited to the formation of the additional C9 H-bond occurs when the ϕ dihedral angles of the β and γ subunits approach 180° and −60° positions, respectively. In the cases where only a C13 H-bond is formed, these dihedral values are switched.

The C8/C9 and C9/C8 sequential double rings might be anticipated to compete effectively with the C13-containing

structures, which are held together principally by a single H-bond. The H-bond lengths of the C8/C9 rings are in the 1.9–2.0 Å range, a range similar to their distances in the absence of the cyclic constraints. In order to explore the role played by the cyclic constraints in dictating the preference for C8/C13 bifurcated rings over C8/C9 sequential rings, we optimized and compared the relative energies of each structural type with and without the cyclic constraints present, replacing these groups when appropriate with methyl groups. In the cases tested (Table S1 in the Supporting Information), the C8/C9 structures were always at least 7 kJ/mol higher in energy than their C8/C13 counterparts, indicating that the bifurcated structure is intrinsically more stable than the C8/C9 double-ring structure. This conclusion is somewhat surprising given the stability and prevalence of similar C7/C8 double-ring structures seen in work on α/β-peptides.[2,18]

Interestingly, one of the conformational families observed in $\gamma\beta$ is a hybrid structure that incorporates a C8 ring across the β subunit with an amide-stacked conformation across the γ subunit. Previous work showed that an amide-stacked conformation in unconstrained γ-peptides was nearly as stable as the C9 structure because of the combined effects of minimal steric strain involving the γ-peptide backbone and an energetically optimal antiparallel approach of the two amide groups engaged in the stacking interaction.[15,16,20,32] While the C8/stacked combination is about 10 kJ/mol less stable than the C9/C13 global minimum, it is nonetheless interesting to see that amide stacking leads to stable minima not far above the global minimum even in the presence of the cyclic constraint associated with the γ subunit employed in our studies. The C8/stacked structure differs from the C8/C13 global minimum in having the N-terminal amide group of the γ residue rotated 180° from its C8/C13 values as a result of differences in the dihedral angles ψ and ζ. Reorientation of the amide group leads to a dipole moment for the C8/stacked structure of ∼5 D, nearly 4 D less than the dipole moment of the C8/C13 counterpart, which has all of the amide groups pointing in the same direction.

B. Constrained γ-Peptide Series: α/γ-, β/γ-, and γ-Peptides. The results on constrained β/γ-peptides presented here complete a series of studies that includes the ring-constrained γ-peptide, α/β-peptide, and α/γ-peptide analogues. As a result, we can compare and contrast the types of conformational preferences imposed by the cyclohexyl ring and ethyl side chain constraints among the different peptidic backbones and the degree to which these constraints enforce a preference for a particular conformation.

The homogeneous constrained γ-peptides studied by Walsh et al.[19] have the same constraints as the γ subunit in the present work. This γ residue constraint led to clear and specific folding preferences among the γ-peptides previously examined. In the capped γ-diamide Ac-γ_{ACHC}-NHBn (labeled in shorthand simply as γ), all of the conformations contained a C9 H-bonded ring. In the capped triamide Ac-γ_{ACHC}-γ_{ACHC}-NHBn (labeled $\gamma\gamma$), the lone observed conformer contained a single C14 ring that constituted the first turn of a 14-helix. As Table 1 shows, the two central dihedral angles (θ and ζ) of the γ-peptide backbone are locked into angles near 60° ($g+$), producing a turn in the backbone. When combined in succession, the two turns bring the i + 3 NH group into close proximity with the i C═O group, forming an $i + 3 \rightarrow i$ C14 H-bond.

In the cyclically constrained α/β-peptides[18] and α/γ-peptides,[21] the α subunit, which cannot have a cyclic constraint without losing H-bond donor sites, was free to adopt multiple configurations with little energetic variation. Thus, while the cyclic constraint imposed restrictions on the γ or β subunit, several conformational families were observed for the heterogeneous α/β and α/γ backbones. C5/C8 bifurcated double rings were formed by the α/β-peptide $\alpha_L\beta_{ACPC}$, while in $\beta_{ACPC}\alpha_L$, both C8/$C7_{eq}$ sequential double rings and C11 single rings were observed.[18] In the α/γ-peptide analogues Ac-Ala-γ_{ACHC}-NHBn and Ac-γ_{ACHC}-Ala-NHBn (labeled simply as $\alpha\gamma$ and $\gamma\alpha$), a total of 10 conformations were observed, most of which contained a C9 ring across the γ subunit. Among them were three structures that incorporated a C12 ring, the first step in forming a 12-helix. By comparison, the β/γ-peptides studied in this work benefit from the restrictions imposed on the backbone by both the β and γ subunits. As a result, the preference for C13 structures in $\beta\gamma$ and $\gamma\beta$ appears to be as robust as the preference for C14 rings among fully constrained γ-peptides.

C. Comparison of the Single-Turn C13 Ring with the 13-Helix in β/γ- and α-Peptides. The present study allows us to compare in detail the structure of a prototypical turn of a β/γ-peptide 13-helix with the more fully formed 13-helix in longer β/γ-peptides and the α-helix formed by α-peptides. While there are no experimental data on $\beta\gamma$ and $\gamma\beta$ in solution or in crystalline form, previous studies by Guo et al.[11] on longer constrained β/γ-peptides provide a point of reference. The X-ray structure of the pentameric (β-γ-β-γ-β) foldamer reveals that some backbone dihedral angles vary along the backbone rather significantly. Nevertheless, the structural constraints imposed by the γ subunit appear to be quite robust, since the θ, ζ, and ψ angles in the pentamer crystal structure agree quite well with those found in the present gas-phase studies (Table 1).[11] The ϕ angles in the pentamer crystal structure (−135°, −147°) are intermediate between those found in $\beta\gamma$ and $\gamma\beta$ and are more consistent with the dihedral angles predicted for the single-ring C13 structures of $\gamma\beta$ (Table 1), which lack the distortions induced by the presence of a second H-bond (C8 or C9) imposed by the bifurcated double ring.

The dihedral angles for the β subunits in the crystalline pentamer show much greater variability than those of the γ subunits, a trend that is consistent with the significant differences among the ϕ_β, ζ_β, and ψ_β dihedral angles found in the β subunits of $\gamma\beta$ relative to those of $\beta\gamma$ (Table 1). Figure 9 presents an overlay of the $\beta\gamma$(**A**) C8/C13 structure determined in this work with the $\beta_3\gamma_4$ portion of the helical β/γ-pentapeptide from Guo et al.[11] The choice of this comparison is based on the fact that the dihedral angles of the $\beta\gamma$(**A**) structure most closely align at this point on the pentamer helix. As one can see, the C8/C13 structure differs from the more well-formed β/γ 13-helix primarily in the reorientation of the N-terminal amide group in order to form a C8 H-bond with the interior amide group, but it is still able to maintain a similar C13 H-bond distance.

Even with the adjustments noted above for the accommodation of the additional C8 H-bond, the dihedral angles calculated for the experimentally observed $\beta\gamma$ and $\gamma\beta$ structures are in surprisingly good agreement with computational predictions for the β/γ-hexapeptide 13-helix obtained by the Hofmann group in Germany.[8] The agreement is particularly noteworthy given that the calculations were conducted with β/γ-peptide oligomers completely lacking in side chains. It should

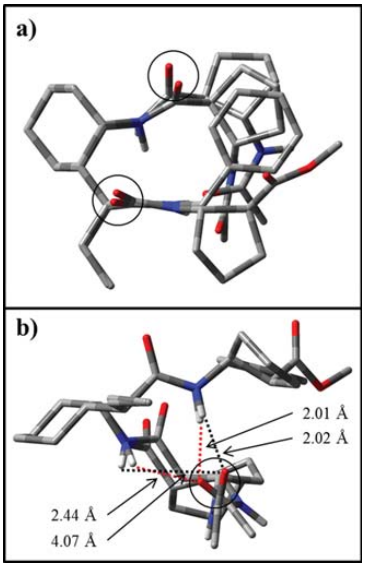

Figure 9. (a) Axial view and (b) side view of the structures of $\beta\gamma$(**A**) and the $\beta_3\gamma_4$ segment of the β/γ pentamer from Guo et al.[11] overlapped at the ACHC constraint to demonstrate the differences between the backbone dihedral angles of the two structures. The principal difference is found in the orientation of the N-terminal amide group, whose C═O acceptor is reconfigured to accommodate the C8 H-bond in $\beta\gamma$(**A**). Red and black dashed lines mark both the C8 and C13 hydrogen bonds formed in β/γ(**A**) and the $\beta_3\gamma_4$ segment, respectively. The associated bond lengths are listed and labeled.

be noted that the sign of each dihedral angle is switched in the Hofmann study relative to our work because the computational work involved helices with opposite handedness, formed from an achiral backbone, relative to the helical conformations specified by the subunit chirality in $\beta\gamma$ and $\gamma\beta$.

On the basis of their pentamer crystal structure, Guo et al. determined that the 13-helix formed from β/γ-peptides has a pitch (5.4 Å/turn) and radius (2.5 Å) very similar to those in the α-helix formed from α-peptides (pitch of 5.4 Å/turn, radius of 2.3 Å). Of course, the two helices differ significantly in the number of residues per turn (3.6 for the α-helix vs 2.6 for the β/γ-peptide 13-helix) since a β/γ-dipeptide has the same number of backbone atoms as an α-tripeptide. Figure 10 compares two views of the β/γ- and α-peptide 13-helices down the helical axes. In Figure 10, the side chains have been removed in order to better view the β/γ-peptide (Figure 10a) and α-peptide (Figure 10b) backbones. In an α-helix, the amide groups are evenly spaced and rotated by ~100° relative to one another (3.6 × 100° = 360° per turn). This arrangement in the α-helix causes the side chains to fan out around the helix periphery in a regularly spaced pattern, as shown in the bottom view in Figure 10b. By comparison, the backbone amide arrangement in the β/γ-peptide 13-helix must be less regular than in the α-helix because the foldamer helix is composed of two different types of subunit, with the γ-peptide subunit responsible for a larger angular change (~160°, semicircular arrow) than its β-peptide counterpart (~90°).

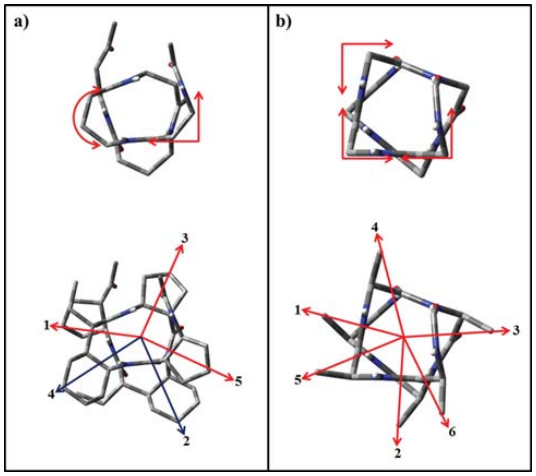

Figure 10. Comparison of the (top) backbone and (bottom) side-chain arrangements in (a) the β/γ-peptide 13-helix and (b) the α-helix. The numbering reflects the side-chain sequence from N-terminal to C-terminal. The arrows in the lower portions of both (a) and (b) show the arrangement of the side-chain groups. In the bottom portion of (a), the red arrows indicate the positions of the ACPC groups and the black arrows indicate the positions of the ACHC groups.

VI. CONCLUSION

Single-conformation spectroscopy of two prototypical β/γ-peptides in the gas phase has provided direct evidence that in the absence of solvent or intermolecular effects, the inherent structural preferences imposed by the cyclic constraints present in $\beta\gamma$ and $\gamma\beta$ are sufficient to lock in the population entirely in a structure held together principally by a single C13 H-bond. This conformation represents the first turn of a β/γ-peptide 13-helix that is closely analogous to the α-helices formed by α-peptides. It will be interesting in future work to extend the gas-phase studies to longer β/γ-peptides, in which the combined effects of successive C13 rings should show their effects in the NH stretch, amide I, and amide II regions, where they can be compared with the α-helix analogues. The effects of H_2O complexation on the conformational preferences and H-bonded networks formed also would be interesting subjects of future studies. Studies of β/γ-peptide analogues lacking residues with cyclic constraints should reveal the roles played by these constraints in determining the conformational preferences of this heterogeneous foldameric backbone.

■ ASSOCIATED CONTENT

Ⓢ Supporting Information

Frequency comparisons for all of the conformational families, influence of the side chain on sequential double rings, synthesis information, and the complete author list for ref 30. This material is available free of charge via the Internet at http://pubs.acs.org.

■ AUTHOR INFORMATION

Corresponding Author

*E-mail: zwier@purdue.edu.

Notes

The authors declare no competing financial interest.

■ ACKNOWLEDGMENTS

J.R.G., P.S.W., and T.S.Z. gratefully acknowledge support for this work from the National Science Foundation (NSF CHE 1213289). B.F.F. and S.H.G. also gratefully acknowledge support for this work from the National Science Foundation (NSF CHE 1307365). The authors thank Jacob Dean for his assistance during manuscript preparation.

■ REFERENCES

(1) Ramesh, V. V. E.; Puranik, V. G.; Sanjayan, G. J. Carbohydrate-derived conformationally restricted bicyclic dipeptides as potential hetero foldamer building blocks. *Tetrahedron: Asymmetry* **2012**, *23*, 1400−1404.

(2) James, W. H., III; Baquero, E. E.; Shubert, V. A.; Choi, S. H.; Gellman, S. H.; Zwier, T. S. Single-Conformation and Diastereomer Specific Ultraviolet and Infrared Spectroscopy of Model Synthetic Foldamers: α/β-Peptides. *J. Am. Chem. Soc.* **2009**, *131*, 6574−6590.

(3) Karle, I. L. Hydrogen bonds in molecular assemblies of natural, synthetic and "designer" peptides. *J. Mol. Struct.* **1999**, *474*, 103−112.

(4) Seebach, D.; Gardiner, J. β-Peptidic Peptidomimetics. *Acc. Chem. Res.* **2008**, *41*, 1366−1375.

(5) Horne, W. S.; Gellman, S. H. Foldamers with Heterogeneous Backbones. *Acc. Chem. Res.* **2008**, *41*, 1399−1408.

(6) Bouillere, F.; Thetiot-Laurent, S.; Kouklovsky, C.; Alezra, V. Foldamers Containing γ-Amino Acid Residues or Their Analogues: Structural Features and Applications. *Amino Acids* **2011**, *41*, 687−707.

(7) Karle, I. L.; Pramanik, A.; Banerjee, A.; Bhattacharjya, S.; Balaram, P. ω-Amino Acids in Peptide Design. Crystal Structures and Solution Conformations of Peptide Helices Containing a β-Alanyl-γ-Aminobutyryl Segment. *J. Am. Chem. Soc.* **1997**, *119*, 9087−9095.

(8) Baldauf, C.; Gunther, R.; Hofmann, H. J. Helix formation in α,γ- and β,γ-hybrid peptides: Theoretical insights into mimicry of α- and β-Peptides. *J. Org. Chem.* **2006**, *71*, 1200−1208.

(9) Araghi, R. R.; Jackel, C.; Colfen, H.; Salwiczek, M.; Volkel, A.; Wagner, S. C.; Wieczorek, S.; Baldauf, C.; Koksch, B. A β/γ-Motif To Mimic α-Helical Turns in Proteins. *ChemBioChem* **2010**, *11*, 335−339.

(10) Nyakatura, E. K.; Araghi, R. R.; Mortier, J.; Wieczorek, S.; Baldauf, C.; Wolber, G.; Koksch, B. An Unusual Interstrand H-Bond Stabilizes the Heteroassembly of Helical $\alpha\beta\gamma$-Chimeras with Natural Peptides. *ACS Chem. Biol.* **2013**, *9*, 613−616.

(11) Guo, L.; Almeida, A. M.; Zhang, W.; Reidenbach, A. G.; Choi, S. H.; Guzei, I. A.; Gellman, S. H. Helix Formation in Preorganized β/γ-Peptide Foldamers: Hydrogen-Bond Analogy to the α-Helix without α-Amino Acid Residues. *J. Am. Chem. Soc.* **2010**, *132*, 7868−7869.

(12) Vasudev, P. G.; Chatterjee, S.; Shamala, N.; Balaram, P. Gabapentin: A Stereochemically Constrained γ Amino Acid Residue in Hybrid Peptide Design. *Acc. Chem. Res.* **2009**, *42*, 1628−1639.

(13) Baquero, E. E.; James, W. H., III; Choi, S. H.; Gellman, S. H.; Zwier, T. S. Single-conformation ultraviolet and infrared spectroscopy of model synthetic foldamers: β-Peptides Ac-β^3-hPhe-NHMe and Ac-β^3-hTyr-NHMe. *J. Am. Chem. Soc.* **2008**, *130*, 4784−4794.

(14) Baquero, E. E.; James, W. H., III; Choi, S. H.; Gellman, S. H.; Zwier, T. S. Single-conformation ultraviolet and infrared spectroscopy of model synthetic foldamers: β-Peptides Ac-β^3-hPhe-β^3-hAla-NHMe and Ac-β^3-hAla-β^3-hPhe-NHMe. *J. Am. Chem. Soc.* **2008**, *130*, 4795−4807.

(15) Buchanan, E. G.; James, W. H., III; Gutberlet, A.; Dean, J. C.; Guo, L.; Gellman, S. H.; Zwier, T. S. Single-conformation spectroscopy and population analysis of model γ-peptides: New tests of amide stacking. *Faraday Discuss.* **2011**, *150*, 209−226.

(16) James, W. H., III; Buchanan, E. G.; Müller, C. W.; Dean, J. C.; Kosenkov, D.; Slipchenko, L. V.; Guo, L.; Reidenbach, A. G.; Gellman, S. H.; Zwier, T. S. Evolution of Amide Stacking in Larger γ-Peptides: Triamide H-Bonded Cycles. *J. Phys. Chem. A* **2011**, *115*, 13783−13798.

(17) Buchanan, E. G.; James, W. H., III; Choi, S. H.; Guo, L.; Gellman, S. H.; Müller, C. W.; Zwier, T. S. Single-conformation infrared spectra of model peptides in the amide I and amide II regions: Experiment-based determination of local mode frequencies and intermode coupling. *J. Chem. Phys.* **2012**, *137*, No. 094301.

(18) James, W. H., III; Baquero, E. E.; Choi, S. H.; Gellman, S. H.; Zwier, T. S. Laser Spectroscopy of Conformationally Constrained α/β-Peptides: Ac-ACPC-Phe-NHMe and Ac-Phe-ACPC-NHMe. *J. Phys. Chem. A* **2010**, *114*, 1581−1591.

(19) Walsh, P. S.; Kusaka, R.; Buchanan, E. G.; James, W. H., III; Fisher, B. F.; Gellman, S. H.; Zwier, T. S. Cyclic Constraints on Conformational Flexibility in γ-Peptides: Conformation Specific IR and UV Spectroscopy. *J. Phys. Chem. A* **2013**, *117*, 12350−12362.

(20) James, W. H., III; Buchanan, E. G.; Guo, L.; Gellman, S. H.; Zwier, T. S. Competition between Amide Stacking and Intramolecular H Bonds in γ-Peptide Derivatives: Controlling Nearest-Neighbor Preferences. *J. Phys. Chem. A* **2011**, *115*, 11960−11970.

(21) Kusaka, R.; Zhang, D.; Walsh, P. S.; Gord, J. R.; Fisher, B. F.; Gellman, S. H.; Zwier, T. S. Role of Ring-Constrained γ-Amino Acid Residues in α/γ-Peptide Folding: Single-Conformation UV and IR Spectroscopy. *J. Phys. Chem. A* **2013**, *117*, 10847−10862.

(22) Choi, S. H.; Guzei, I. A.; Spencer, L. C.; Gellman, S. H. Crystallographic characterization of helical secondary structures in α/β-peptides with 1:1 residue alternation. *J. Am. Chem. Soc.* **2008**, *130*, 6544−6550.

(23) Choi, S. H.; Guzei, I. A.; Spencer, L. C.; Gellman, S. H. Crystallographic Characterization of Helical Secondary Structures in 2:1 and 1:2 α/β-Peptides. *J. Am. Chem. Soc.* **2009**, *131*, 2917−2924.

(24) Choi, S. H.; Guzei, I. A.; Spencer, L. C.; Gellman, S. H. Crystallographic Characterization of 12-Helical Secondary Structure in β-Peptides Containing Side Chain Groups. *J. Am. Chem. Soc.* **2010**, *132*, 13879−13885.

(25) Guo, L.; Chi, Y. G.; Almeida, A. M.; Guzei, I. A.; Parker, B. K.; Gellman, S. H. Stereospecific Synthesis of Conformationally Constrained γ-Amino Acids: New Foldamer Building Blocks That Support Helical Secondary Structure. *J. Am. Chem. Soc.* **2009**, *131*, 16018−16020.

(26) Guo, L.; Zhang, W.; Reidenbach, A. G.; Giuliano, M. W.; Guzei, I. A.; Spencer, L. C.; Gellman, S. H. Characteristic Structural Parameters for the γ-Peptide 14-Helix: Importance of Subunit Preorganization. *Angew. Chem., Int. Ed.* **2011**, *50*, 5843−5846.

(27) Shubert, V. A.; Baquero, E. E.; Clarkson, J. R.; James, W. H., III; Turk, J. A.; Hare, A. A.; Worrel, K.; Lipton, M. A.; Schofield, D. P.; Jordan, K. D.; Zwier, T. S. Entropy-driven population distributions in a prototypical molecule with two flexible side chains: *O*-(2-acetamidoethyl)-*N*-acetyltyramine. *J. Chem. Phys.* **2007**, *127*, No. 234315.

(28) Wiley, W. C.; McLaren, I. H. Time-of-Flight Mass Spectrometer with Improved Resolution. *Rev. Sci. Instrum.* **1955**, *26*, 1150−1157.

(29) Mohamadi, F.; Richards, N. G. J.; Guida, W. C.; Liskamp, R.; Lipton, M.; Caufield, C.; Chang, G.; Hendrickson, T.; Still, W. C. Macromodel—An Integrated Software System for Modeling Organic and Bioorganic Molecules Using Molecular Mechanics. *J. Comput. Chem.* **1990**, *11*, 440−467.

(30) Frisch, M. J.; Trucks, G. W.; Schlegel, H. B.; Scuseria, G. E.; Robb, M. A.; Cheeseman, J. R.; Scalmani, G.; Barone, V.; Mennucci, B.; Petersson, G. A.; Nakatsuji, H.; et al. *Gaussian 09*, revision A.2; Gaussian, Inc.: Wallingford, CT, 2009.

(31) Zhao, Y.; Truhlar, D. G. Density functionals for noncovalent interaction energies of biological importance. *J. Chem. Theory Comput.* **2007**, *3*, 289−300.

(32) James, W. H., III; Müller, C. W.; Buchanan, E. G.; Nix, M. G. D.; Guo, L.; Roskop, L.; Gordon, M. S.; Slipchenko, L. V.; Gellman, S. H.; Zwier, T. S. Intramolecular Amide Stacking and Its Competition with Hydrogen Bonding in a Small Foldamer. *J. Am. Chem. Soc.* **2009**, *131*, 14243−14245.